Calcite dissolution kinetics at the sediment-water interface in an acidifying ocean

Thesis by

Olivier Sulpis

Department of Earth and Planetary Sciences

McGill University, Montreal

July 2019

A thesis submitted to McGill University in partial fulfillment of the requirements of the degree of Doctor of Philosophy

Acknowledgements

It is perhaps the most challenging part of writing this thesis to express my gratitude to all of those who helped, supported and inspired me all along the PhD road, but I will give it a try. First and foremost, I would like to thank my supervisor, Alfonso Mucci, for his wise guidance, ongoing support and encouragements during these four years. Al gave me the freedom to pursue my own path, while putting me back on track when I needed. I would also like to thank Bernard Boudreau for his precious advice and creative thinking that drove much of the research outputs presented here. I have learned so much from Al and Bernie, and they will remain a true scientific inspiration for the rest of my career. None of this work would have been possible without the help of my colleague and friend Claire Lix, who laid the foundations of the work on which this PhD is based. Many thanks go to Don Baker, who always came up with unexpected scientific ideas, encouraging words and made me discover the teaching experience. Carolina Dufour, who welcomed me in her group, and made me discover the wonderful world of models, is heartily thanked. For fruitful discussions and for their availability, I would like to thank Jeanne Paquette, Peter Douglas and Olivia Jensen. Thanks also go to Don Baker and Burke Hales for their careful and insightful review of this thesis. And to the McGill Earth and Planetary Sciences Department, I would like to express my gratitude for financial support.

To all of those who shared their ideas, data, samples or elbow grease, through email exchanges, conference meetings or phone calls, thank you infinitely. I am lucky to be a part of this welcoming oceanographic community. In particular, thanks go to Jess Adkins, who hosted me in his research group at Caltech, for a very enjoyable summer stay, for sharing his passion for science and always finding time for constructive discussions. I am also wholly indebted to John Trowbridge, for his invaluable help in understanding bottom flows. I thank Katherine Gombay, for her time and curiosity. She made the story of a dissolving seafloor accessible and understandable to all. For encouraging me to pursue my studies, and develop an interest in science, I thank my earlier supervisors, Sylvain Pichat, Amaelle Landais and Pierre Deschamps.

To Carlos, Sanita, Sanoop, Gloria, Shane, Duncan and, above all, Ashley, thank you for supporting me through the ups and downs of the first year, for the musical interludes, deep conversations and everlasting memories. To Monika, Longbo, Becky, Charlie, Jenny, Alexis, Pascale, Noah, Rob, Jethro, Jiaxin, Saad, Louise, Deneyn and Mathilde, my time at McGill would not have been as fun without you, and I will miss you dearly. Thanks go to Kamila, Cloé, Greg, Domitille, Fabien, Romain and Marie-Emilie, who encouraged me to give a try to the Canadian experience, and to all my friends from Bourges, Lyon and Marseille. I am happy to move back to the old continent, closer to you. Although they must still be wondering what I am doing studying the oceans, I would like to thank my parents for their love and ongoing support. I dedicate this thesis to my grandfather, James.

Abstract

Carbon dioxide (CO_2), produced and released to the atmosphere by human activities, has been accumulating in the oceans for approximately two centuries and will continue to do so well beyond the end of this century if emissions are not curbed. One direct consequence of CO_2 build-up in the atmosphere and its transfer to the ocean is the acidification of seawater. Calcite, a mineral secreted by many organisms living in the surface ocean to produce their shells and skeletons, covers a large part of the seafloor and acts as a natural anti-acid, neutralizing CO_2. Thus, a precise knowledge of the kinetics of this dissolution reaction is necessary to predict the ocean recovery time towards its pre-acidification state once anthropogenic CO_2 emissions are curbed. Over the past decades, numerous studies of calcium carbonate ($CaCO_3$) mineral dissolution kinetics have been performed in seawater. Despite this ongoing effort, the mechanisms controlling the dissolution rate of the two most common $CaCO_3$ minerals and polymorphs (calcite and aragonite) in seawater are still poorly understood and large discrepancies exist between results of in-situ and laboratory studies, most of which have been carried out under conditions (e.g., mineral suspensions) that are not representative of processes taking place at the seafloor. This thesis combines laboratory experiments, oceanographic measurements and model outputs to explore and unravel the mechanisms that control calcite dissolution at the sediment-water interface (SWI) on the seafloor in the context of current anthropogenic ocean acidification.

Using a newly developed temperature-controlled rotating-disk reactor, as well as a stirred reactor, we were able to measure the rate of dissolution of simulated and natural sediment disks of variable calcite content under environmental and hydrodynamic conditions representative of deep-sea benthic environments. These experiments revealed that, in contrast to the reigning paradigm that calcite dissolution kinetics in seawater is surface reaction-controlled and of high order, calcite dissolution at the SWI and under deep-sea conditions is linearly dependent on the undersaturation state of the overlying seawater with respect to calcite and controlled by the presence of a diffusive-boundary layer (DBL) above the sediment bed. The DBL is a thin layer of fluid at the interface with a solid surface, in which frictional forces cause molecular diffusion to become the dominant mode of solute transport and whose thickness is inversely correlated with the turbulence of the fluid above or the speed of bottom currents. Therefore, irrespective of the mineralogy and sediment properties, the dissolution rate is simply a function of the saturation state of the overlying seawater with respect to calcite, the calcite content of the sediment, and hydrodynamics at the seafloor.

From these observations, using a compilation of seawater chemical variables in the global ocean, corresponding sediment calcite content and rain rates, as well as recently modeled bottom current velocities, we have been able to identify the loci of current anthropogenic calcite dissolution and its rate. We found that significant anthropogenic dissolution of calcite at the seafloor currently occurs in the western North Atlantic, where the bottom waters are youngest, and at various hot spots in the southern Atlantic, Indian and Pacific Oceans. Using model projections for the 21st century, under a "business as usual" scenario, we found that while seawater will become

more corrosive to this mineral, calcite dissolution at the seafloor will decrease in intensity because bottom currents will slow down and the amount of calcite particles delivered to the seafloor will diminish. These results indicate that the neutralization of human-made CO_2 by calcite dissolution at the seafloor may take longer than previously thought. The amount of anthropogenic CO_2 currently neutralized each year by seafloor or water-column calcite dissolution is negligible, less than 1% of the current CO_2 emission rate, and will remain so throughout the 21st century.

These findings are of critical interest to the scientific community and the public, as these results have far reaching implications for ocean acidification mitigation, to the fate of benthic communities living under increasing environmental stress, and to geologists contemplating both present and past records of ocean acidification.

Résumé

Le dioxyde de carbone (CO_2), produit et libéré à l'atmosphère par les activités humaines, s'est accumulé dans les océans depuis environ deux siècles et continuera ainsi bien après la fin du siècle si les émissions actuelles ne sont pas freinées. Une des conséquences directes de cette accumulation de CO_2 dans l'atmosphère et son transfert aux océans est l'acidification de l'eau de mer. La calcite, un minéral secrété par de nombreux organismes vivant à la surface des océans afin de former leur coquille ou squelette, recouvre une large partie du plancher océanique et agit comme un antiacide naturel, neutralisant le CO_2. De ce fait, une connaissance précise de la cinétique de cette réaction de dissolution est requise afin de prédire le temps nécessaire à l'océan de retrouver son état pré-acidification une fois que les émissions de CO_2 anthropiques ralentiront. Durant les décennies passées, de nombreuses études de la cinétique de dissolution des carbonates de calcium ($CaCO_3$) ont été effectuées dans l'eau de mer. Malgré cet effort continu, les mécanismes contrôlant la dissolution des deux plus communs minéraux et polymorphes du $CaCO_3$ (calcite et aragonite) dans l'eau de mer ne sont toujours pas bien compris, et il existe de larges différences entre les résultats d'études *in situ* et en laboratoire, dont la plupart ont été effectuées sous des conditions (par exemple, des minéraux gardés en suspension) qui ne sont pas représentatives des processus ayant lieu au niveau du plancher océanique. Cette thèse rassemble les résultats d'expériences en laboratoire, des données océanographiques et des sorties de modèles afin d'explorer les mécanismes contrôlant la vitesse de dissolution de la calcite à l'interface eau-sédiment (IES) sur les fonds océaniques, et dans le contexte actuel d'acidification des océans.

En utilisant un nouveau réacteur à disque rotatif, sous température contrôlée, ainsi qu'un réacteur mélangé, nous avons été capables de mesurer les taux de dissolution de disques de sédiment contenant des quantités variées de calcite, sous des conditions hydrodynamiques et environnementales représentatives des environnements benthiques profonds. Ces expériences ont montré que, au contraire du paradigme selon lequel la cinétique de dissolution de la calcite dans l'eau de mer est contrôlée par des processus à la surface des grains et d'ordre élevé, la dissolution de la calcite à l'IES et sous des conditions d'océan profond est une fonction linéaire de l'état de sous-saturation de l'eau de mer surnageante par rapport à la calcite, et contrôlée par la présence d'une couche limite de diffusion (CLD) au-dessus du sédiment. La CLD est une mince couche de fluide à l'interface d'une surface solide dans laquelle les forces de friction font de la diffusion moléculaire le mode de transport dominant pour les espèces en solution, et dont l'épaisseur est inversement proportionnelle à la turbulence du fluide ou la vitesse des courants de fond. Par conséquent, indépendamment de la minéralogie ou des propriétés des sédiments, la vitesse de dissolution est simplement une fonction de l'état de saturation de l'eau de mer par rapport à la calcite, du contenu en calcite des sédiments, et des conditions hydrodynamiques au niveau du plancher océanique.

A partir de ces observations, une compilation de variables chimiques de l'eau de mer à travers l'océan global, des teneurs en calcite des sédiments et de taux d'accumulation de calcite,

ainsi que des vitesses de courant de fond récemment modélisées, nous avons identifié les lieux où la dissolution anthropique de calcite a lieu, ainsi que sa vitesse. Nous avons trouvé qu'une dissolution significative de calcite s'effectuait présentement au niveau du plancher océanique dans l'Atlantique nord, où les eaux de fond sont jeunes, ainsi qu'à divers points chauds dans le sud des océans Atlantique, Indien et Pacifique. Par la suite, en utilisant des prédictions de modelés pour le 21ème siècle, sous un scenario de « statut quo », nous avons déterminé que bien que l'eau de mer deviendra davantage corrosive pour la calcite, la dissolution de ce minéral au plancher océanique allait décroitre en intensité parce que les courants de fond ralentiront, et que la quantité de particules de calcite livrée au plancher océanique diminuera. Ces résultats indiquent que la neutralisation du CO_2 d'origine humaine par la dissolution de calcite du plancher océanique pourrait prendre plus de temps que prévu. La quantité de CO_2 anthropique présentement neutralisée par la dissolution de calcite dans la colonne d'eau ou dans les sédiments est négligeable, inférieure à 1% des émissions de CO_2 actuelles, et il en sera ainsi durant tout le 21ème siècle.

Ces trouvailles sont d'un intérêt capital pour la communauté scientifique aussi bien que pour le grand publique, car elles ont d'importantes implications pour l'atténuation de l'acidification des océans, le devenir des communautés benthiques vivant sous des conditions environnementales qui se dégradent, et pour les géologues étudiant à la fois les enregistrements sédimentaires présents et passés de l'acidification des océans.

Table of contents

List of figures

List of tables

Contribution of Authors

Chapter 1

Olivier Sulpis wrote this chapter with feedbacks from Alfonso Mucci.

Chapter 2

Olivier Sulpis wrote the manuscript with notable inputs from Bernard P. Boudreau and Alfonso Mucci. Olivier Sulpis, Bernard P. Boudreau and Alfonso Mucci interpreted the results. Olivier Sulpis and Claire Lix performed the experiments and analyses. All authors contributed to the project conception/design as well as manuscript edition and discussions.

Chapter 3

Olivier Sulpis wrote the manuscript with notable inputs from Alfonso Mucci and Bernard P. Boudreau. Olivier Sulpis, Bernard P. Boudreau and Alfonso Mucci interpreted the results. Olivier Sulpis performed all the experiments and analyses. Mark A. Barry and Bruce D. Johnson advised on the design of the rotating-disk reactor. All authors contributed to the manuscript edition and discussions.

Chapter 4

Olivier Sulpis wrote the manuscript with notable inputs from Alfonso Mucci. Olivier Sulpis, Pascale Daoust and Deneyn White performed the experiments and analyses. All authors contributed to the interpretation of the results as well as editing and discussions.

Chapter 5

Olivier Sulpis and Bernard P. Boudreau wrote the manuscript with notable inputs from Alfonso Mucci. Olivier Sulpis, Bernard P. Boudreau and Alfonso Mucci contributed to the interpretation of the results. Olivier Sulpis performed the modelling work. David S. Trossman and Brian K. Arbic contributed the bottom velocity fields used in this study as well as advised about the usage of these fields. Chris Jenkins provided the global carbonate content sediment data. Robert M. Key advised on the use of the GLODAP data and on the use of CFC-11 tracer data. All authors contributed to the manuscript editing and discussions.

Chapter 6

Olivier Sulpis wrote the manuscript with notable inputs from Carolina O. Dufour, Alfonso Mucci and John P. Dunne. Olivier Sulpis and Carolina O. Dufour conceived the study. Olivier Sulpis performed the modelling work. David S. Trossman and Brian K. Arbic contributed the bottom-water velocity fields used in this study, and advised about the use of these fields. David S. Trossman compiled the current-meter data. Andrea J. Fassbender advised on the use of the CMIP5 model data. All authors contributed to the interpretation of the results as well as manuscript editing and discussions.

Chapter 7

Olivier Sulpis wrote this chapter with inputs from Alfonso Mucci and Bernard P. Boudreau. Olivier Sulpis designed the research and performed the modelling work. Olivier Sulpis and Alfonso Mucci interpreted the results.

Chapter 1

Ocean acidification and $CaCO_3$ dissolution at the deep seafloor

1.1 Anthropogenic CO_2 and ocean acidification

1.1.1 Atmospheric CO_2 emissions

The growing interference of mankind with the Earth System over the past century has become a topic of concern to all nations. The term Anthropocene was suggested by Crutzen and Stoermer (2000) to underscore the role of mankind as a recognizable force that significantly impacts its surroundings. Human population has increased 10-fold over the past 3 centuries, reaching an estimated 7.5 billion people in 2015, and is projected to exceed 11 billion by 2100 (McNeill, 2001; United Nations, 2017). Along with technological and economic progress arose the need for energy. Fossil fuels (petroleum, natural gas, and coal) are currently the major and the cheapest sources of energy. The remaining reserves of fossil fuel carbon available for energy are estimated at about 5000 Gt C (Archer, 2005). Most of it is found in the form of coal, whereas extractable oil resources are evaluated at about 250 Gt C, and traditional natural gas reserves represent about 200 Gt C, with the potential to expand these reserves several times if unconventional sources such as oil sands or methane hydrates are considered (Milkov, 2004; Rogner, 1997). Projections for anthropogenic carbon release to the atmosphere usually do not exceed 2100. Although very speculative, the worst-case scenario would call for the burning of the totality of the 5000 Gt C available for energy production.

Anthropogenic CO_2 emissions to the atmosphere were 555 ± 85 Pg C between 1750 and 2011. Of this amount, fossil fuel combustion and cement production contributed 375 ± 30 Pg C and land use change (including deforestation and reforestation) contributed 180 ± 80 Pg C (Ciais et al., 2013), see also ***Fig. 1.1a***. The annual mean growth rate of the atmospheric CO_2 concentration, as measured at Mauna Loa, has more than doubled between 1960 and 2015, reaching a value of 2 parts per million (ppm) per year. The atmospheric CO_2 concentration was ~280 ppm in 1750 (Joos and Spahni, 2008), reached 405 ppm in 2017 (Dlugokencky and Tans,

2018), and may exceed 1000 ppm by 2100 according to the "business as usual" Representative Concentration Pathway 8.5 (RCP8.5, van Vuuren et al. (2011)), a high-CO_2 emission scenario developped by the Intergovernmental Panel on Climate Change (IPCC) in which no specific climate mitigation action is taken (Riahi et al., 2011). The pCO_2 for the RCP8.5 scenario is shown in ***Fig. 1.1b***.

Between 1960 and 2015, atmospheric CO_2 concentrations increased at only 43% of the rate of fossil fuel emissions, the rest being either dissolved in the oceans or taken up by the terrestrial reservoir (Le Quéré et al., 2016). Oceanic uptake plays a major role in the regulation of the atmospheric CO_2 budget, accounting for ~26 % of the annual anthropogenic CO_2 emissions (Le Quéré et al., 2016). Without this oceanic uptake, atmospheric pCO_2 concentrations would be 55 ppm higher than today (Sabine et al., 2004). The ocean takes up anthropogenic CO_2 at a rate of about 10^6 tons of CO_2 per hour, meaning that if these emissions were partitioned equally per capita, each human would be contributing 4 kg of CO_2 per day to the ocean (Brewer and Peltzer, 2009; Orr, 2011).

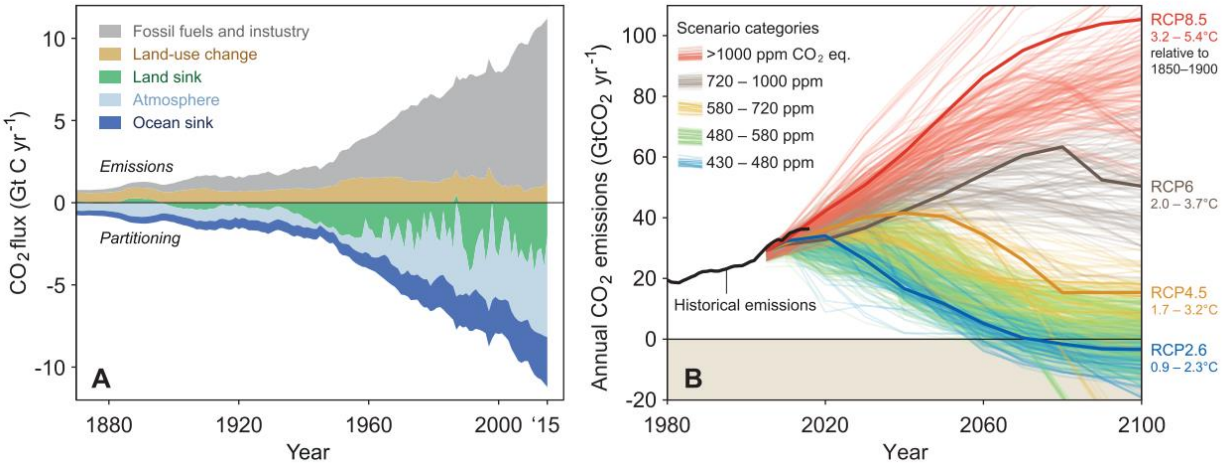

Fig. 1.1 | *a) Annual anthropogenic CO_2 emissions and their partitioning among the atmosphere, land and ocean (Gt C a^{-1}) reservoirs from 1870 to 2015. The emissions and their partitioning only include fluxes that have changed since 1750, and not the natural CO_2 fluxes between the atmosphere, land and ocean reservoirs that existed before that time and still exist today (source: Le Quéré et al., 2016). b) Measured annual CO_2 emissions between 1980 and 2015 and predicted emissions between 2006 and 2100 for various RCP scenarios (source: Global Carbon Budget, 2016).*

One of the consequences of massive CO_2 dissolution in the ocean is ocean acidification. Absorption of anthropogenic CO_2 by the oceans is lowering surface ocean water pH, and, according to the business-as-usual scenario, a pH change larger than any inferred from the geological record of the past 300 Ma (with the possible exception of those resulting from extreme/catastrophic events such as impacts of celestial objects or massive methane hydrate degassing) is predicted by the end of this century (Caldeira and Wickett, 2003). Before discussing the chemistry of ocean acidification and its impact on marine ecosystems, I will review the chemistry of the carbonate system in seawater and factors that control the dissolution of anthropogenic CO_2 in the ocean.

1.1.2 The carbonate system

A strong acid, once in solution, is very nearly completely dissociated into its constituent ions except in very concentrated solutions (in water, one mole of strong acid yield one mole of protons and one mole of the conjugate base). Conversely, a weak acid undergoes only partial dissociation in water, the extent of which is dependent on pH and can be described by a mass-action law or equilibrium reaction (Pauling, 1970). Upon the dissolution of CO_2 in seawater, CO_2 takes on the form of solvated CO_2 ($CO_{2\,(aq)}$ or $CO_2 \cdot H_2O$) or carbonic acid (H_2CO_3). As carbonic acid can successively, but partially shed two protons, it is considered a weak diacid. The reactions that describe these dissociations are:

$$\boldsymbol{CO_{2\,(aq)} + H_2O \leftrightarrow H_2CO_3^*} \quad \textbf{(1.1)}$$

$$\boldsymbol{H_2CO_3^* \overset{K_1}{\leftrightarrow} H^+ + HCO_3^-} \quad \textbf{(1.2)}$$

$$\boldsymbol{HCO_3^- \overset{K_2}{\leftrightarrow} H^+ + CO_3^{2-}} \quad \textbf{(1.3)}$$

where K_1 and K_2 are the first and second dissociation constants of carbonic acid. If defined in terms of the ratio of the activities (effective concentrations) of the products over the reactants, they are referred to as thermodynamic constants (K°, conventionally denoted by a naught). Thermodynamic constants vary with temperature and pressure, but not solution composition. On the other hand, the activity of the carbonic acid species cannot readily be measured directly and must be derived from concentrations and model estimates of the activity coefficients (coefficients that reflect their deviation from ideal behavior) of each species. To avoid estimating activity

coefficients, marine scientists have developed a set of stoichiometric equilibrium constants to represent the state of the system for a given pressure, temperature and salinity. To describe the carbonate system, K_1^* and K_2^* or stoichiometric constants (conventionally denoted by a uppercase star) are defined in terms of the concentrations of the different species:

$$\boldsymbol{K^*_1} = \frac{[\boldsymbol{HCO_3^-}][\boldsymbol{H^+}]}{[\boldsymbol{H_2CO_3^*}]} \quad \textbf{(1.4)}$$

$$\boldsymbol{K^*_2} = \frac{[\boldsymbol{CO_3^{2-}}][\boldsymbol{H^+}]}{[\boldsymbol{HCO_3^-}]} \quad \textbf{(1.5)}$$

We use H_2CO_3* to represent the sum of H_2CO_3 and $CO_{2\ (aq)}$ since they can only be readily be distinguished by infra-red spectrometry, but the true acid only makes up ~ 0.3% of the H_2CO_3*.

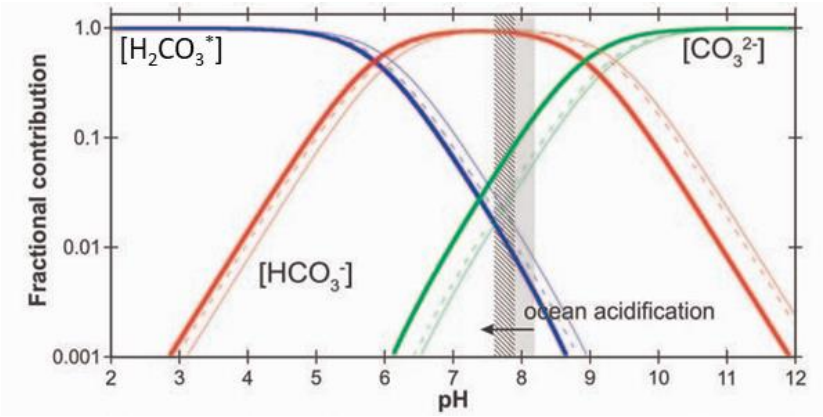

Fig. 1.2 | *Speciation (Bjerrum) diagram of the carbonate system in seawater, for different temperatures, salinities and pressures (heavy curves are for S=35, T=25ºC, P=0bar, narrow curves are S=35, T=0ºC, P=0bar, dashed curves are S=35, T=0ºC, P=300bar). The shaded region reflecting the range of modern (annual average) ocean surface, with the hashed region reflecting the corresponding projected year 2010 range (source: Barker and Ridgwell, 2012).*

Using these stoichiometric equilibrium constants, we can calculate the relative quantities of the dissolved inorganic carbon species, as plotted on the speciation (or Bjerrum) diagram as a function of pH (***Fig. 1.2***). According to this diagram, if a strong acid is added to seawater, CO_3^{2-} and HCO_3^- ions will be successively converted to H_2CO_3*. Upon this conversion, the pH will remain between 6 and 8, and, given the total alkalinity of normal seawater (~ 2.4 mmol/kg at a practical salinity (S_P) of 35), will drop appreciably only after 3 mmol of protons are added per kg of seawater (Zeebe and Wolf-Gladrow, 2001). If a weak acid like CO_2 is added to seawater, most

of the protons released to solution following the dissociation of the carbonic acid will be neutralized by reaction with the carbonate ions. Thus, the carbonate system is a natural buffer for the seawater pH (Sillén, 1967).

To understand what limits the capacity of seawater to absorb anthropogenic CO_2, it is necessary to first define the basic variables of the carbonate system. Two conservative tracers (in closed systems, i.e., isolated from the atmosphere) are commonly used to describe the carbonate system: the dissolved inorganic carbon (DIC) and the total alkalinity (TA).

$$\boldsymbol{DIC = [H_2CO_3{}^*] + [HCO_3{}^-] + [CO_3{}^{2-}]} \quad \textbf{(1.6)}$$

$$\boldsymbol{TA = [HCO_3{}^-] + 2[CO_3^{2-}] + [B(OH)_4{}^-] + [OH^-] - [H^+]} \quad \textbf{(1.7)}$$

DIC is the sum of the dissolved inorganic carbon species (**Eq. 1.6**), and TA represents a measurable parameter that reflects the acid neutralizing capacity of seawater. The formula presented here (**Eq. 1.7**) for TA approximates the definition provided by Dickson (1981), who defined the total alkalinity as "the number of moles of hydrogen ion equivalent to the excess of proton acceptors over proton donors in one kilogram of sample", taking in account the carbonate, borate, phosphate, silicate, hydrogen sulfide and ammonia acid-base systems. In more practical terms, it is the sum of all bases that are titratable with a strong acid to an equivalence point corresponding to the conversion of HCO_3^- to H_2CO_3. In open ocean waters at low nutrient concentrations, when the pH is around 8, the alkalinity of natural seawater can be approximated by ***Eq. 1.7*** (Zeebe and Wolf-Gladrow, 2001). Irrespective, this is generally not true in sediment porewaters or where phosphate, silicate and dissolved organic carbon concentrations are elevated.

Given that H_2CO_3* contributes little to DIC at pH > 8 (see ***Fig. 1.2***), these two variables can be combined to provide estimates (within a 10% uncertainty, as explained in Sarmiento and Gruber (2006)) of the concentrations of inorganic carbon species:

$$\boldsymbol{[CO_3^{2-}] \approx TA - DIC} \quad \textbf{(1.8)}$$

$$\boldsymbol{[HCO_3^-] \approx 2DIC - TA} \quad \textbf{(1.9)}$$

The concentration of CO_3^{2-} ions in seawater decreases with acidification, as the ions react with protons released upon the dissociation of the added carbonic acid and buffers the pH change. As a result**,** ***reaction 1.3*** is driven to the left, which can be represented by the overall acid-base neutralization reaction:

$$CO_2 + H_2O + CO_3^{2-} \leftrightarrow 2\,HCO_3^- \quad \textbf{(1.10)}$$

The equilibrium of ***reactions 1.1*** to ***1.3*** shifts when the pH of the solution is changed (see ***Fig. 1.2***). The pH, on the total proton concentration scale, in the surface ocean is usually around 8. Consequently, the bicarbonate ion is the most abundant dissolved inorganic carbon species, as shown in ***Fig. 1.2***. ***Reaction 1.10*** demonstrates that, when CO_2 dissolves in seawater (i.e., DIC is increased), most of it is converted to bicarbonate. This phenomenon explains why the CO_2 (or H_2CO_3*) concentration in solution increases only slightly upon the addition of anthropogenic CO_2 in the surface ocean, because the system is buffered by CO_3^{2-} ions (Zeebe and Wolf-Gladrow, 2001).

1.1.3 Air-sea CO_2 flux

A common model used to represent the process of gas exchange at the air-sea interface is the stagnant boundary model. This model assumes a well-mixed atmosphere and a well-mixed surface ocean separated by a thin stagnant film through which gas exchange is controlled by molecular diffusion across a concentration gradient and turbulence (Bolin, 1960; Broecker and Peng, 1971; Liss and Slater, 1974). In the stagnant boundary layer, molecular diffusion transport is described by Fick's first law as:

$$F = -D_{CO_2}\left(\frac{\Delta[CO_2]}{\delta}\right) \quad \textbf{(1.11)}$$

where D_{CO2} is the molecular diffusion coefficient, a function of the nature of the gas and temperature (= 1.86×10^{-5} cm^2/s for CO_2 at 25°C; Broecker and Peng (1974)), δ is the thickness of the stagnant film, and $\Delta[CO_2]$ is the concentration gradient within the film. The water at the top of the stagnant film is assumed to be in equilibrium with the atmosphere, and its CO_2 concentration can be computed using the solubility of CO_2 in seawater, a function of its salinity, temperature and pCO_2 in the atmosphere, as determined by Henry's law:

$$[CO_2]_{sw} = K_H\, pCO_2 \quad \textbf{(1.12)}$$

where $[CO_2]_{sw}$ is the concentration of CO_2 in the aqueous phase in mol L^{-1}, K_H is Henry's law constant or the solubility constant at a given temperature and salinity (3.4×10^{-2} mol L^{-1} atm^{-1} in pure water under standard conditions - 1 bar and 298 K - as determined by Morgan and Maass

(1931), and 2.84 x 10^{-2} mol L^{-1} atm^{-1} in seawater at 298 K and a S_P of 35.00 as determined by Weiss (1974)), and pCO_2 is the partial pressure of CO_2 expressed in atm in the gas phase.

The thickness of the stagnant boundary at the air-sea interface has been parameterized as a function of wind speed by several authors (Bates et al., 2011; Deacon, 1980; Liss and Merlivat, 1986; Takahashi et al., 2002; Tans et al., 1990). The expression used by Wanninkhof (1992) is:

$$\delta = \frac{D}{0.39\, U_{10}{}^2 \left(\frac{Sc}{660}\right)^{-0.5}} \qquad \textbf{(1.13)}$$

where U_{10} is the wind speed corrected to 10-m elevation, and *Sc* is the Schmidt number for CO_2, a dimensionless number defined as the ratio of the kinematic viscosity and the mass diffusivity (see Bergman et al. (2011) and Wanninkhof (1992) for further information). From ***Eq. 1.13***, it can be inferred that strong winds decrease the thickness of the stagnant boundary, which enhances the diffusive flux (***Eq. 1.11***).

1.1.4 Anthropogenic CO_2 penetration to the deep ocean

Regions where deep-water formation takes place are very limited geographically (e.g., Antarctic or Northern Atlantic) and critically important as they act as windows through which anthropogenic CO_2 can enter the deep ocean (Sigman and Boyle, 2000).

Main deep-water formation areas include the Southern Ocean and the North Atlantic. Recent paleo-oceanographic studies have highlighted large changes in the rates of deep-water formation and of deep-ocean circulation patterns in response to current climate changes (Clark et al., 2002; Lynch-Stieglitz et al., 2007; Oke and England, 2003). Dense water is formed by buoyancy loss, due to heat loss across the air-sea interface, sea-ice formation, or caballing (mixing of two water masses of equal density resulting in a denser fluid; Bullister et al., 2013). For instance, rapid sea-ice formation increases the salinity of the underlying waters, which may promote their sinking and carry anthropogenic CO_2 to depth.

In the North Atlantic, as a part of the Atlantic meridional overturning circulation (AMOC), two separate source regions for deep-water formation can be identified, one is located in the Labrador Sea and the other is at the southeastern tip of Greenland, as shown in ***Fig. 1.3***. Upper North Atlantic Deep Water is formed in the Labrador Sea by deep convection in late winter when

the density stratification is erased in the upper 1000-2500 meters of the water column (Bullister et al., 2013; Marshall and Schott, 1999). In general, deep convection, favoring the formation of deep waters, takes place in areas near land where cold continental air flows over the surface ocean and leads to high heat loss, and where surface ocean circulation is weakly cyclonic, helping to maintain the convection (Lazier, 2001).

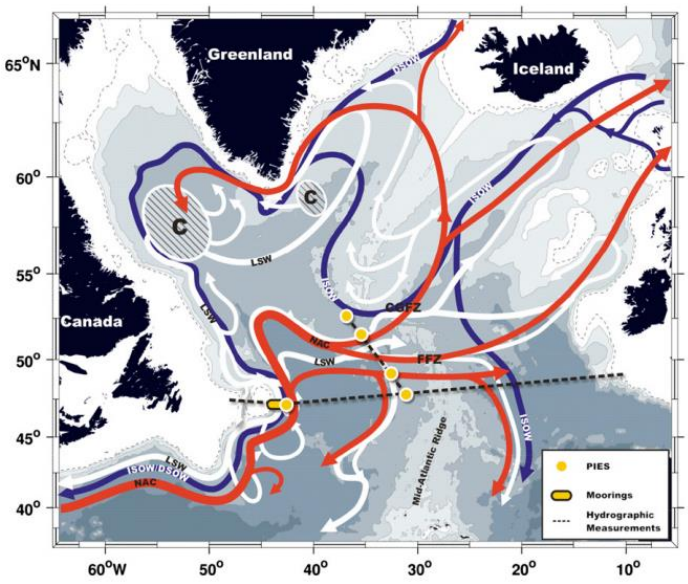

Fig. 1.3 | *Schematic representation of the Atlantic meridional overturning circulation (AMOC). The counter-clockwise circulation between 45°N and 60°N is called the subpolar gyre. NAC: North Atlantic Current, LSW: Labrador Sea Water, ISOW: Iceland Scotland Overflow Water, DSOW: Denmark Strait Overflow Water, C: convection regions (Rhein et al., 2011).*

In addition, anthropogenic CO_2 can also be brought to the deep-ocean through the 'biological pump'. The latter refers to the biologically-driven processes that sequester CO_2 in surface waters and transfer it to the deep ocean (Passow and Carlson, 2012). Phytoplanktonic organisms produce organic matter from DIC through photosynthesis. In order to grow, they require three essential resources: light, nutrients and turbulence (Cullen et al., 1992; Kirk, 1992). Turbulence is essential because it impacts the position of the organisms in the water column and it redistributes nutrients within the surface mixed-layer as well as brings them up from depth to the surface through upwelling. According to the "law of the minimum" popularized by Liebig and Playfair (1840), growth of phytoplankton is limited by the least abundant resource. Some factors influence the efficiency and the rate at which organisms can use these resources, such as temperature or the intrinsic capacities of organisms (e.g., pigments, anatomy, and morphology). In the modern ocean, photosynthetic DIC fixation by marine phytoplankton leads to the formation of about 45 Gt of organic carbon per year (Falkowski et al., 1998).

` As a part of the food web, phytoplankton are grazed upon by zooplankton and undigested material is packaged into fecal pellets. These pellets can sink from surface waters to the abyss in only a few days or weeks (Fowler and Small, 1972; Smayda, 1969). Some particulate organic carbon also aggregates in marine snow (i.e., an assemblage of particulate organic matter and bacteria often held together by a mucus formed of exopolymeric substances; (Passow et al., 2012)) or adsorbs onto mineral particles that carry them down to the deep ocean (ballasting) (Fowler and Knauer, 1986). Finally, sinking zooplankton carcasses also participate to this organic carbon transfer from the surface to the deep ocean (Frangoulis et al., 2011). This sinking particulate organic matter is used as a source of food for organisms living in deep waters and on the deep-sea floor (Eppley and Peterson, 1979) or remineralized to CO_2.

1.2 $CaCO_3$ chemistry in the marine environment

1.2.1 $CaCO_3$ dissolution

Ocean acidification perturbs the $CaCO_3$ oceanic cycle, impeding biogenic calcification and promoting the dissolution of biogenic carbonates (Delille et al., 2005; Feely et al., 2004). One of the most important geochemical reactions regulating pH in marine and fresh waters on short time scales (decades to millenia, while the CO_2-H_2O buffer described in ***section 1.1.2*** is nearly instantaneous, on the time scale of gas exchange) is the equilibrium with calcium carbonate minerals. The dissolution of these minerals can be described by the following reaction:

$$\boldsymbol{CaCO_3 \leftrightarrow Ca^{2+} + CO_3^{2-}} \qquad \textbf{(1.14)}$$

The saturation state of seawater with respect to calcium carbonate minerals is defined by:

$$\Omega = \frac{(\boldsymbol{Ca^{2+}})(\boldsymbol{CO_3^{2-}})}{\boldsymbol{K^{\circ}_{sp}}} = \frac{[\boldsymbol{Ca^{2+}}][\boldsymbol{CO_3^{2-}}]}{\boldsymbol{K^{*}_{sp}}} \qquad \textbf{(1.15)}$$

where K°_{sp} and K^{*}_{sp} are, respectively, the thermodynamic and stoichiometric solubility constants of calcite or aragonite at a given temperature and pressure, (i) are the ion activities, and [i] are total ion concentrations.

$$\boldsymbol{K^0_{sp} = (Ca^{2+})_{eq}(CO_3^{2-})_{eq}} \qquad \textbf{(1.16)}$$

$$K_{sp} = \gamma_{T,Ca^{2+}}[Ca^{2+}]_{eq}\,\gamma_{T,CO3_2^-}[CO_3^{2-}]_{eq} = K_{sp}{}^{*}\,\gamma_{T,Ca^{2+}}\gamma_{T,CO_3^{2-}} \quad \textbf{(1.17)}$$

where $\gamma_{T(i)}$ are total ion activity coefficients. In strong electrolyte solutions, electrostatic interactions between solutes and water molecules bias their solubility behavior. The activity, or effective concentration of an electrolyte, is related to its concentration by a factor that accounts for its deviation from ideal behavior. This factor is called the activity coefficient and can be estimated by various models, depending on the range of ionic strengths and complexity of the solution investigated (Garrels and Thompson, 1962; Kester and Pytkowicz, 1969; Millero and Pierrot, 1998; Millero and Schreiber, 1982; Pytkowicz and Hawley, 1974; Pitzer, 1973; Pitzer and Kim, 1974). To avoid the use of these activity coefficients, stoichiometric equilibrium constants are commonly used in marine sciences, as they represent the state of the system for a given pressure, temperature and salinity.

The saturation state (Ω) represents the thermodynamic potential for the mineral of interest to precipitate or to dissolve. If $\Omega < 1$, the solution is undersaturated with respect to the mineral and, thus, the mineral should normally dissolve if exposed to this solution. Conversely, if $\Omega > 1$, the solution is supersaturated with respect to the mineral and the latter should spontaneously precipitate from the solution. Finally, if $\Omega = 1$, the solution is in equilibrium with the mineral, and there should be no net dissolution or precipitation. The most common calcium carbonate minerals in marine environments are calcite and aragonite. Calcite is the most stable polymorph of $CaCO_3$ under Earth surface conditions, predominates in deep-sea sediments and crystallizes in the hexagonal crystallographic system, with a rhombohedral unit cell. Aragonite, which is often most abundant in shallower and warmer waters, belongs to the orthorhombic system, has a structure significantly denser and topologically far more complex than that of calcite, and is metastable under Earth surface conditions. Nevertheless, in reality, the precipitation of a stable phase, such as calcite in the contemporary surface ocean, is most often preceded by the formation of amorphous phases or metastable polymorphs, such as aragonite, a theory that is known as Ostwald's step rule. As explained by Sun et al. (2015), in today's ocean, due to its lower surface energy and the inhibitory effect of Mg^{2+}ions in seawater, the nucleation rate of the metastable aragonite can surpass that of the more stable calcite.

The influence of salinity and temperature on the stoichiometric solubility constants of aragonite and calcite in seawater was studied by Mucci (1983) at 1 bar total pressure. The

stoichiometric solubility constants increase systematically with salinity and decrease slightly with temperature. Given that seawater has nearly the same relative composition in all open oceans, these constants are expressed as a simple function of salinity rather than a detailed solution composition. Salinity in the pelagic ocean, below a few hundred meters depth, is nearly constant and its value is around 35 (Schlitzer, 2000).

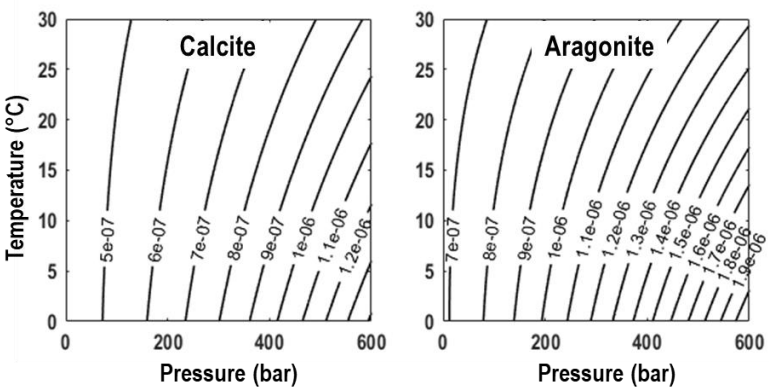

Fig. 1.4 | *Stoichiometric solubility products (in mol² kg⁻²) of aragonite and calcite in seawater, with a S_P of 35, for various pressures and temperatures. Based on the equations of Mucci (1983) and Millero (1995).*

Increasing pressure and, to a lesser extent, decreasing temperature, increase the solubility of $CaCO_3$ minerals in the deep ocean. Millero (1995) used the molal volume and compressibility changes for the dissociation reactions of $CaCO_3$ minerals to quantify the pressure dependence of the $CaCO_3$ solubility.

$$\ln\left(\frac{K_i^P}{K_i^0}\right) = -\left(\frac{\Delta V_i}{RT}\right)P + \left(\frac{0.5\Delta\kappa_i}{RT}\right)P^2 \qquad \textbf{(1.18)}$$

where K_i^P and K_i^0 are, respectively, the solubility constants of aragonite or calcite at the applied pressure (P, in bars) and at atmospheric pressure, ΔV_i and $\Delta\kappa_i$ are, respectively, the molal volume and compressibility change for ***reaction 1.14*** and can be estimated as a function of temperature for both aragonite and calcite (refer to Millero (1995) for more details), and R is the gas constant and equal to 83.131 cm^{-3} mol^{-1} bar deg^{-1}. Note that the effect of pressure on the solubility of aragonite and calcite in seawater was also determined experimentally, including by Ingle (1975). The equation of Millero (1995), along with the temperature effect parameterized by Mucci (1983) were used to draw ***Fig. 1.4***, for a S_P of 35. The greater solubility of aragonite relative to that of calcite is observable on this figure. Furthermore, that pressure has a greater influence than temperature on

the solubility constants over the range of temperatures and pressures encountered in the open ocean is clearly represented.

Injection of anthropogenic CO_2 in seawater decreases the pH and shifts the equilibria of ***reactions 1.1*** to ***1.3***, causing a measurable decrease in CO_3^{2-} concentration in seawater (see the Bjerrum diagram depicted on ***Fig. 1.2***) and leading to a lowering of the saturation state of seawater with respect to calcium carbonate minerals. Once the latter becomes smaller to 1, seawater is undersaturated with respect to calcium carbonate minerals and their dissolution occurs. Thus, combining ***Eqs. 1.1*** to ***1.3*** and ***Eq. 1.14***, we can write the overall reaction:

$$\boldsymbol{CaCO_3 + CO_{2\,(aq)} + H_2O \leftrightarrow 2HCO_3^- + Ca^{2+}} \qquad \textbf{(1.19)}$$

According to ***Eq. 1.25***, $CaCO_3$ dissolution releases one Ca^{2+} ion and one CO_3^{2-} ion to seawater and leads to an increase in TA and DIC in a ratio of 2:1 (***Eqs. 1.6*** and ***1.7***). The direct consequence of this is a higher buffer capacity of seawater and an acceleration of anthropogenic CO_2 uptake. $CaCO_3$ precipitation, such as it occurs during biogenic calcification, has the reverse effect, decreasing DIC and TA and counterintuitively increasing [CO_2] in seawater. It has been determined by Zeebe and Wolf-Gladrow (2001) that under surface ocean conditions, [CO_2] increases by ~0.03 µmol per µmol of $CaCO_3$ precipitated.

The projected changes in seawater chemistry due to ocean acidification may have deleterious consequences for calcifying organisms. Smith and Buddemeier (1992) suggested that, even under supersaturated conditions, a decrease in the saturation state of seawater with respect to calcium carbonate minerals would cause a decrease in biogenic calcification rates, implying a competitive advantage for non-calcifying reef organisms. Whether they are composed of calcite or aragonite, the increasing scarcity of CO_3^{2-} ions makes it harder for calcifying organisms to access it and build their shell, as $CaCO_3$ precipitation will require greater Gibb's free energy.

1.2.2 Inhibitors and catalysts of $CaCO_3$ dissolution

The adsorption of foreign ions or impurities on mineral surfaces, or their co-precipitation with the mineral, are known to have a significant influence on the reactivity of $CaCO_3$ minerals (Terjesen et al., 1961). In this section, the role of magnesium, soluble reactive phosphate and dissolved organic carbon as inhibitors or catalysts of $CaCO_3$ dissolution are briefly reviewed.

Under Earth surface conditions, high Mg-calcite minerals are thermodynamically metastable and persist owing to kinetic constraints (Andersson et al., 2008; Goldschmidt, 1983). Furthermore, surface waters are often supersaturated with respect to these minerals, promoting their formation (Andersson et al., 2008). High Mg-calcites whose magnesium content exceed 12 mol% are more soluble than aragonite (see ***Fig. 1.5*** and Bischoff et al. (1987)).

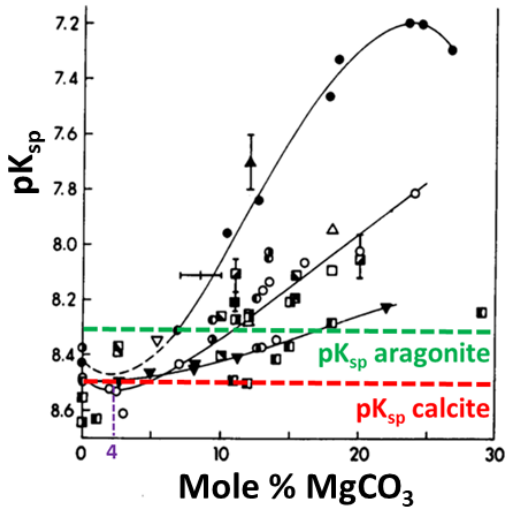

Fig. 1.5 | *Compilation of experimental determinations of magnesian calcite solubilities as a function of the $MgCO_3$ mole fraction. The minimum solubility is reached for a $MgCO_3$ mole fraction of ~4%. The solubilities of calcite and aragonite are taken from Plummer and Busenberg (1982). For a detailed description of the experimental conditions under which each dataset was generated, see the original article by Mucci and Morse (1990).*

Calcifying organisms are a major component of all marine ecosystems. The composition of the shells, tests or skeletons of these organisms can vary widely in shallow water sediments. Some organisms precipitate calcium carbonate minerals containing significant amounts of magnesium (see ***Fig. 1.6***). In the case of calcite, low to high Mg-calcites occur in shallow marine environments. They are usually distinguished on the basis of their $MgCO_3$ content with a boundary at typically 4 mol%, a value that is representative of the Mg-calcite of minimum solubility, as depicted in ***Fig. 1.5*** (Mackenzie et al., 1983; Reeder, 1983). Chave (1954) analyzed the composition of a large number of calcareous organisms, highlighting a strong taxonomic control of the magnesium content of calcitic tests. The most important and common - due to their ubiquity – Mg-calcite producers are the red coralline algae, benthic foraminifera, bryozoans and echinoderms, crustaceans or brachiopods (Andersson et al., 2008; Chave, 1954). The Mg-calcite composition of these species ranges from a few mol% to as much as 30 mol%. In addition, Mg^{2+} is also found to occur in abiotic calcite, upon the formation of Mg-calcite cements or overgrowths (Mucci and Morse, 1983; Mucci et al., 1985).

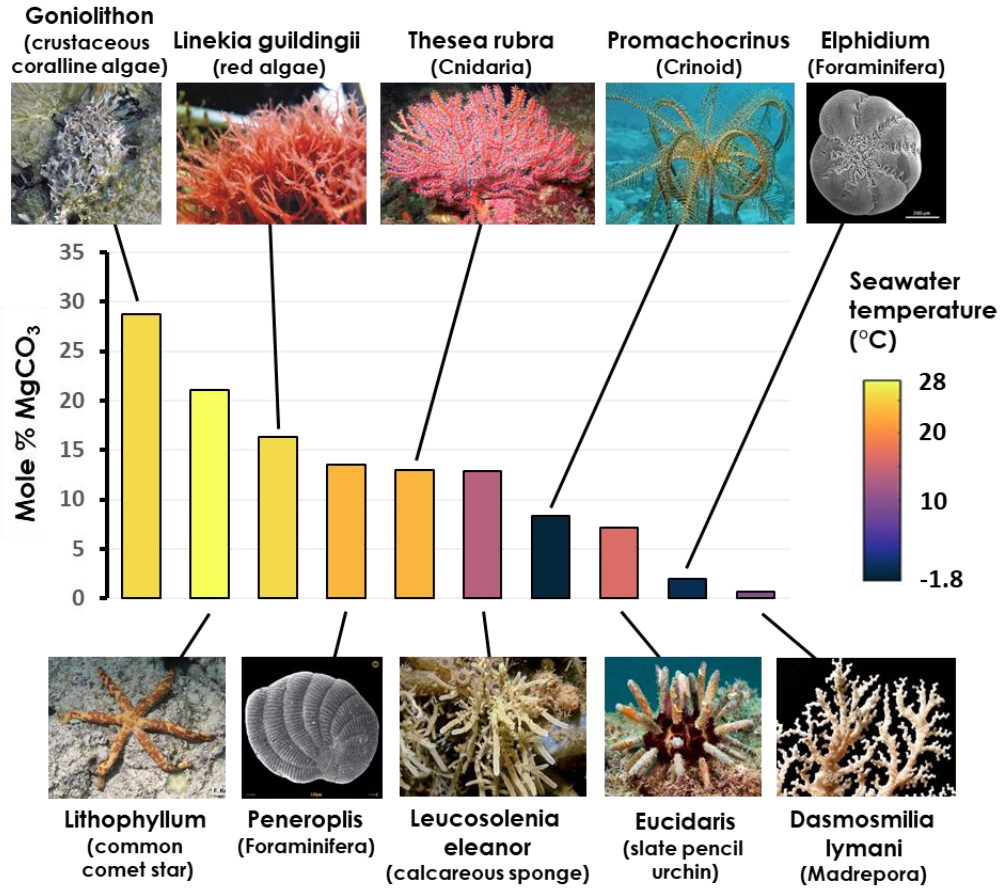

Fig. 1.6 | *Histogram showing the magnesium content of biogenic calcites in a selection of marine species that proliferate at various locations and temperatures. From the data of Chave (1954). Pictures are taken from (left to right) Wikimedia, Enature.qa, Benison Media, Foraminifera.eu, marinespecies.org, Habitas, Oikonos, Reeflex, Wikimedia and Wikimedia.*

Today, the Mg:Ca molar ratio of seawater is ~5.2 (Villiers and Nelson, 1999) and is controlled by the differential supply and removal of these elements in the oceanic reservoir. Rivers carry Mg and Ca originating from continental weathering to the oceanic reservoir, and the precipitation of carbonate minerals or evaporites is a sink for these elements. Hydrothermal activity plays an important part in the oceanic cycle of Mg and Ca. The Ca input from ridge crest hydrothermal activity was estimated at ~1.8 x 10^{12} mol/a whereas Mg removal was evaluated as ~2.2 x 10^{12} mol/a (Arvidson et al., 2013). In fact, high-temperature hydrothermal circulation through mid-ocean ridge crust can remove 20-60% of the river input of Mg to the oceans and is consequently a major Mg sink (Mottl and Wheat, 1994; Elderfield and Schultz, 1996; Arvidson et al., 2013). The river input flux of Ca is estimated at ~1.2 x 10^{13} mol/a (Elderfield and Schultz,

1996), and is consequently the major source of Ca to the oceans, approximately 7 times greater than the hydrothermal Ca flux calculated by Arvidson et al. (2013). Over the Phanerozoic eon, the Mg:Ca ratio in seawater has oscillated between ~1.3 and 5.0 (Hardie, 1996; Mackenzie and Andersson, 2013). Given the kinetic inhibition and thermodynamic destabilization of calcite by the magnesium ion, the dominant carbonate mineralogy of shelf sediments has oscillated between calcite and aragonite ("calcite seas" and "aragonite seas"). These variations (seawater Mg:Ca ratio and dominant $CaCO_3$ mineralogy) are thought to be correlated with the rate of seafloor spreading, atmospheric CO_2 concentration, sea-level fluctuations and "greenhouse" or "icehouse" conditions (Dickson, 2002; Sandberg, 1983; Wilkinson et al., 1985; Kump, 2013). Hence, the average Mg:Ca ratio in shallow-water calcium carbonate sediments is heterogeneous, and its value varies over geological history.

The ocean is currently in an "aragonite sea" episode. Calcite in tropical shelf sediments of the ocean is particularly rich in Mg, with Mg contents often exceeding 12 mol% (Chave, 1954). Under the business-as-usual CO_2 emission scenario, models predict that tropical surface seawater could become undersaturated with respect to calcite minerals with a magnesium content > 12 mol% by the end of the century (Andersson et al., 2008). Thus, high Mg-calcite-rich shelf sediments will be the "first responders" to ocean acidification, and anthropogenic emissions of CO_2 may ultimately lead the oceans towards a "calcite sea" episode, as modelled by Morse et al. (2006).

Soluble reactive phosphate (SRP) has been recognized as a strong inhibitor of both calcite precipitation and dissolution (Berner and Morse, 1974; Morse, 1974a; Nancollas et al., 1981; Reddy, 1977). All living organisms require phosphorus to synthetize nucleotides and nucleic acids. Orthophosphate, the main biologically-available form of phosphorus in the ocean, originates from continental weathering and is brought to the oceans by rivers. It displays a nutrient-type vertical distribution profile in the oceanic water column (Levitus et al., 1993; Redfield, 1958). Phosphorus compounds in seawater occur as organic or inorganic, particulate or dissolved forms. Dissolved inorganic species include phosphate (PO_4^{3-}), hydrogen phosphate (HPO_4^{2-}) and dihydrogen phosphate ($H_2PO_4^-$) ions. In surface seawater, at $pH_T = 8.1$, $S_P = 35$ and 25°C, their respective proportions are 20.4 %, 79.2 % and 0.5 %, making HPO_4^{2-} the dominant species. In deep waters, at a pressure of 500 bar (~5000 m depth), the relative concentration of PO_4^{3-} increases slightly due

to the effect of pressure on the dissociation constants, but the decrease in pH with depth (resulting for the accumulation of metabolic CO_2) overcompensates this effect and HPO_4^{2-} remains the dominant species (see ***Fig. 1.7*** and Millero (2013)). Ocean waters usually contain only traces of soluble reactive phosphate (SRP), on average only about 3 µM (Turekian, 1976), but in marine sediment pore waters, organic matter decomposition/remineralization increases this concentration to values as high as 30 µM, with the effective concentration on carbonate mineral surfaces being even higher as phosphate strongly adsorbs onto these surfaces (Burton and Walter, 1990; Krom and Berner, 1980).

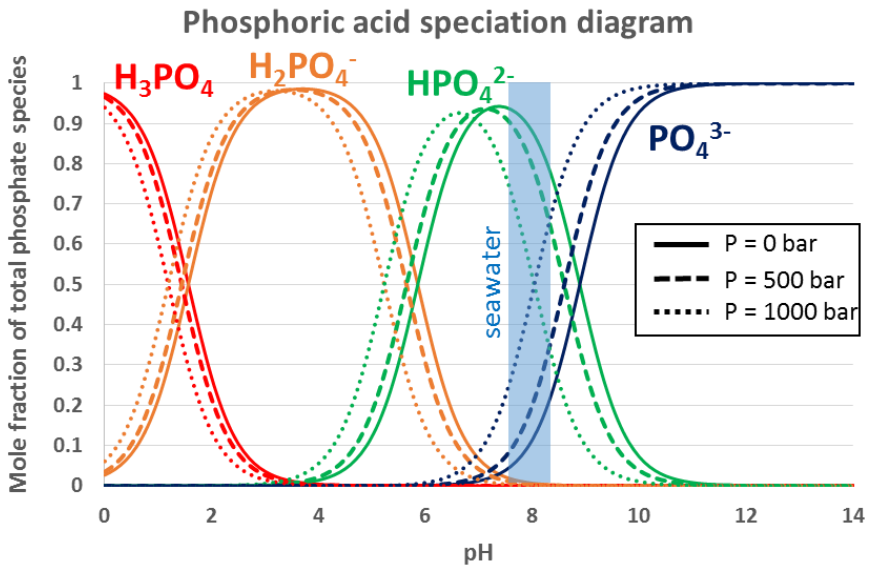

Fig. 1.7 | *Speciation diagram of the orthophosphate species showing the effect of pressure. The dissociation constants and the effect of pressure are computed for a temperature of 25°C and are taken from Millero (2013).*

The inhibition of calcite precipitation and dissolution by SRP is attributed to its adsorption at high-energy sites (e.g., steps, kinks, dislocations) on the calcite mineral surface (Alkattan et al., 2002; Millero et al., 2001). Svensson and Dreybrodt (1992) studied the differential effect of SRP on the dissolution of a synthetic and natural (limestone) calcite in CO_2-H_2O solutions containing 10 µM of SRP. Whereas they observed an inhibition of the synthetic calcite dissolution rate, no significant inhibition by phosphate was observed on the dissolution rates of natural samples. Their interpretation of this differential behavior was that other "unknown inhibitors" similar to phosphate were already present on the surface of the natural calcite samples.

Mucci (1986) and Burton and Walter (1990) demonstrated a pH-dependency of the calcite precipitation inhibition by SRP at a fixed calcite supersaturation, identifying which of the orthophosphate species is mostly responsible for the inhibition. They concluded that for calcite, precipitation rates were inhibited by both PO_4^{3-} and HPO_4^{2-}, whereas only PO_4^{3-} influenced aragonite precipitation rates.

Finally, dissolved inorganic carbon (DOC) is a well-known $CaCO_3$ precipitation/dissolution inhibitor and many researchers studied its role in the precipitation of $CaCO_3$ minerals (Carter and Mitterer, 1978; Chave and Suess, 1970; Kitano and Hood, 1965; Lebron and Suarez, 1996). Murray and Renard (1891) first suggested that organic coatings initially act as a protection for coccoliths and other marine calcitic organisms against dissolution by undersaturated seawater. Morse (1974b) carried out a quantitative study of the $CaCO_3$ dissolution inhibition in the presence of various dissolved aliphatic organic compounds (the DOC concentrations were greater than 250 µM C in each solution). He found that when the DOC concentration is increased in solution by a factor of 5, the $CaCO_3$ dissolution inhibition is also increased by a factor of 5.

1.2.3 $CaCO_3$ marker horizons in the water column

The effect of seawater saturation state with respect to $CaCO_3$ on the fate of biogenic $CaCO_3$ in the water column is an old problem that has been studied since the *HMS Challenger* expedition in the Atlantic, Antarctic, Pacific and Indian Oceans. Murray and Renard (1891) observed that pteropods (i.e., marine organisms that secrete an aragonitic shell) were slowly dissolved at rather shallow depths. During the *Meteor* oceanographic expedition in the Atlantic and Antarctic Oceans between 1925 and 1927, a team of German scientists determined the saturation state of seawater with respect to $CaCO_3$ throughout the water column and related it to pCO_2, pH, alkalinity, salinity, temperature and pressure (Barth et al., 1939).

Whereas surface ocean waters are generally supersaturated with respect to calcite and aragonite, cold deep-ocean waters are typically undersaturated with respect to both minerals, mainly because $CaCO_3$ solubility increases with increasing water depth (pressure, see ***Eq. 1.18***) (Mackenzie and Lerman, 2006) and pH decreases as metabolic CO_2 accumulates and DIC increases as the water masses age. The injection of anthropogenic CO_2 to the deep ocean results in

a further decrease in both pH and CO_3^{2-} ion concentrations which, in turn, reduces the saturation state of seawater with respect to aragonite and calcite (see ***Eq. 1.15***) and raises the depth at which the waters become undersaturated (the saturation depth/level). The degree of undersaturation (1 - Ω) with respect to each mineral is the thermodynamic driving force behind $CaCO_3$ dissolution.

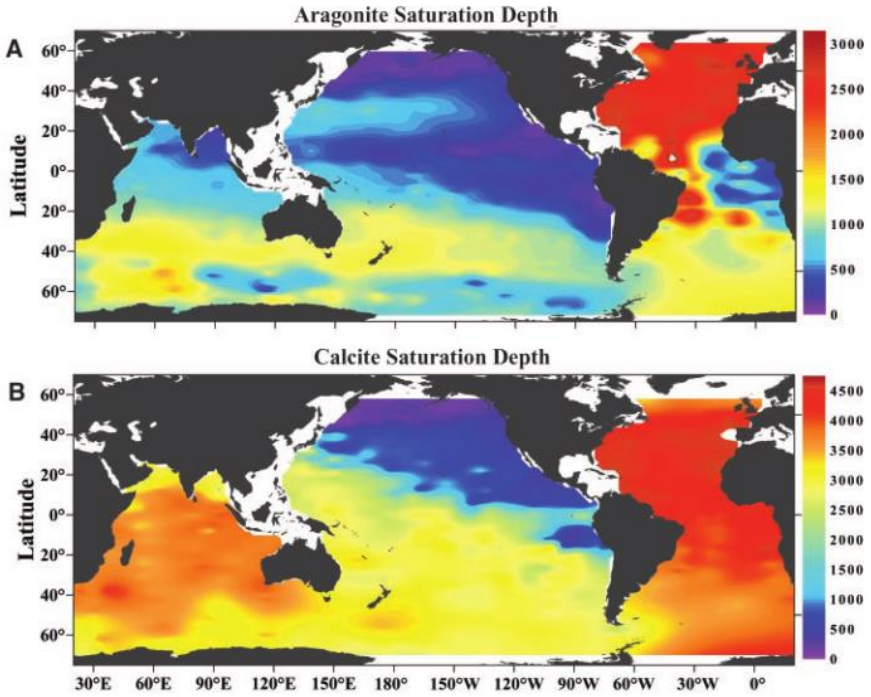

Fig. 1.8 | *Distribution of aragonite (A) and calcite (B) saturation depths (Ω=1) in the global oceans. Data are from the US Joint Global Ocean Flux Study that took place between 1989 and 1996 (Feely et al., 2004).*

As shown in ***Fig. 1.8***, the saturation level sits at a greater depth for calcite (Ω_C=1, ~4000 m deep in Atlantic, ~500 m deep in the Northern Pacific; Feely et al. (2004)) than for aragonite (Ω_A=1, ~2500 m deep in the Atlantic, ~300 m deep in the Northern Pacific; Feely et al. (2004)) because aragonite is 1.5 times more soluble than calcite (ratio of their respective solubility product from Mucci (1983)) at any given pressure, salinity and temperature encountered in the ocean (Berner, 1981; Drever, 1997; Millero, 2013). The difference in the depth of the saturation level between the Atlantic and Northern Pacific is a manifestation of the thermohaline circulation pattern, Northern Pacific deep waters being older and having accumulated more metabolic CO_2 than the young and recently ventilated Northern Atlantic deep waters. Assuming that TA is conservative, we can approximate [CO_3^{2-}] to the difference between TA and DIC (see ***Eq. 1.8***).

Accordingly, as DIC increases with the age of the water mass or with anthropogenic CO_2 injection, $[CO_3^{2-}]$ decreases and, thus, the saturation state of the waters is reduced.

The $CaCO_3$ content of deep-sea sediments varies considerably throughout the oceans, higher carbonate contents being found in sediments accumulated on topographic highs (Chester and Jickells, 2012). The geochemical behavior of aragonite in the water column is close to what would be predicted based on thermodynamic principles, i.e., significant dissolution occurs once the sinking particles reach undersaturated seawater with respect to aragonite, below the aragonite saturation depth (ASD; $\Omega_A = 1$). Thus, the ASD typically coincides with the depth below which little or no aragonite accumulates in the sediments, more commonly referred to as the aragonite compensation depth (ACD) (Morse and Mackenzie, 1990).

Calcite has a more complex behavior and a multiple calcite dissolution marker horizons have been defined, causing much confusion amongst marine geochemists. Throughout this document, I will use three different calcite marker horizons, the calcite saturation depth (CSD), the calcite compensation depth (CCD) and the snowline, defined in the following manner. The CSD is a thermodynamic marker, defined as the water-column depth(s) below which seawater is undersaturated with respect to calcite. The CCD is the water-column depth in the oceans at which the rate of calcite accumulation equals its rate of dissolution. Below the CCD, little or no calcite accumulates in the sediment (Bramlette, 1961). The snowline denotes the depth below which no calcite is found in the sediment (Boudreau et al., 2018). At steady-state, the snowline and the CCD coincide. These markers are represented in ***Fig. 1.9***.

Whereas seawater is corrosive to calcite below its saturation depth, calcite still accumulates in deep-sea sediments down to the CCD. In the Atlantic, the CCD can be as much as 2 km below the calcite saturation level. Thus, both thermodynamic and kinetic factors affect the distribution and preservation of $CaCO_3$ sinking to the seafloor. The balance between the calcite flux from the surface to the deep ocean and the dissolution rate is the dominant factor that determines the distance that separates the CCD from the CSD. In areas of low productivity, the CCD will be close to the CSD. Conversely, there can be a considerable separation of the two horizons below fertile regions where the supply of calcitic material is abundant (e.g., tropical regions).

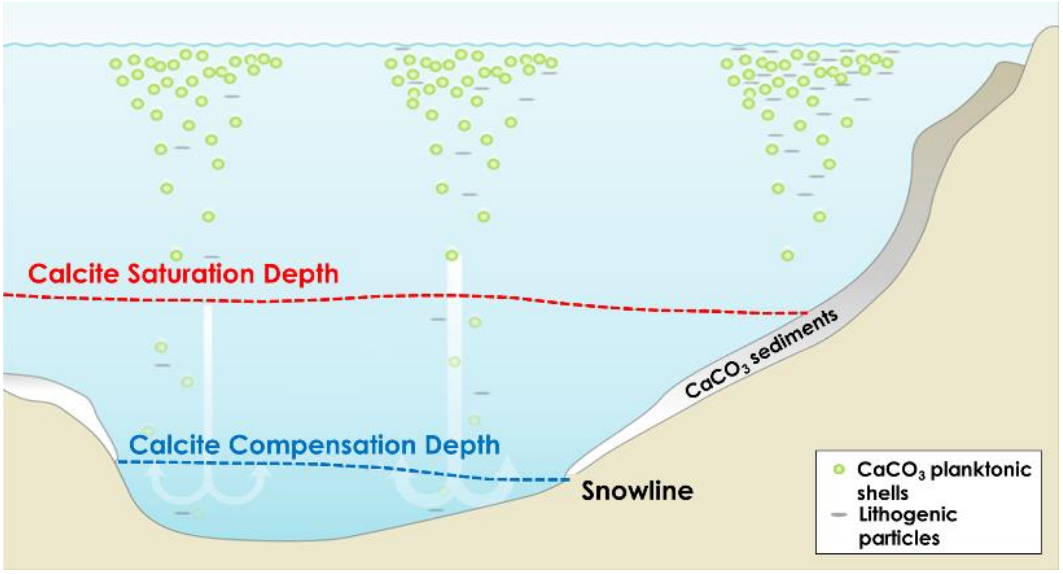

Fig. 1.9 | *Schematic representation of calcite dissolution marker horizons (adapted from Boudreau et al., 2018).*

It should be noted that dissolution of both calcite and aragonite may take place in sediments that are overlain by supersaturated waters, as the microbial degradation of sedimentary organic matter within sediments releases metabolic CO_2 (see ***reaction 1.20***), acidifies and lower the saturation state of the porewaters (Berger et al., 1982; Schulte and Bard, 2003).

$$(CH_2O)_{106}(NH_3)_{16}H_3PO_4 + 138O_2 \rightarrow H_3PO_4 + 16HNO_3 + 106CO_2 + 122H_2O \quad \textbf{(1.20)}$$

Porewaters depth profiles of O_2, pH and $CO_{2\,(aq)}$ reveal that microbial respiration can take place even in deep-sea sediments and that most of it is located in the oxic layer, within a few millimeters of the sediment-water interface where most of the reactive organic matter is found (Hales, 2003; Hales and Emerson, 1997a). Likewise, but to a smaller extent, and limited to continental shelf and slope sediments, the oxidation of reduced iron or manganese, diffusing up from the suboxic and anoxic zones of the sediment (Burdige, 1993; Emerson et al., 1982; Tebo and Emerson, 1986; Tebo et al., 2005), produces protons that acidify the porewaters and further reduces their saturation state, triggering $CaCO_3$ dissolution (Emerson and Bender, 1981). The hypothesis of significant respiration-driven dissolution above the CSD has been criticized (Broecker and Clark, 2003) and early models taking into account respiration and dissolution rates

failed to reproduce TA and Ca^{2+} fluxes observed from deep-sea benthic chamber incubations carried out in the North Atlantic and western equatorial Pacific Oceans (Archer et al., 1989a; Archer et al., 1989b; Archer and Maier-Reimer, 1994; Jahnke et al., 1994). Nevertheless, Gehlen et al. (1999), using a first-order kinetic expression to describe calcite dissolution, developed a model that successfully reproduces the observed porewater distribution of DIC and Ca^{2+}, and allows a quantification of the TA flux induced by metabolic CO_2 released to porewaters within deep-sea sediments. Jahnke and Jahnke (2004) proposed that, in $CaCO_3$-rich sediments overlain by supersaturated seawater, precipitation of fresh $CaCO_3$ at the sediment surface masks the influence of breathing organisms, but that respiration-driven dissolution occurs deeper in response to the accumulation of metabolic CO_2.

Conversely, deviations from an ideal thermodynamic behaviour also occur through the preservation of $CaCO_3$ below the saturation level. Fecal pellets and aggregates of calcitic organisms account for most of the mass flux of sinking $CaCO_3$ particles to the deep sea (Alldredge and Silver, 1988; Honjo, 1976). The rapid settling of fecal pellets and encapsulation allows $CaCO_3$ particles to reach the deep-sea floor – assuming a 5 km water column – in a few days (versus from 50 to 150 years for individual coccoliths; Honjo, 1976) and be preserved below the CSD. On the other hand, Harris (1994) observed that only 27-50% of the coccolith tests ingested by copepods (zooplankton) in the surface ocean where egested and encapsulated in fecal pellets, the remainder being dissolved in the copepod guts and in the water column above the CSD. As it is processed through each of these steps, the calcitic-shell assemblage is modified, since the reactive surface area of shells varies among species and shells have variable vulnerabilities with respect to dissolution (Peterson and Prell, 1985). Alternatively, Morse (1974a) proposed that SRP concentrations in the deep sea inhibit calcite dissolution (discussed later). Finally, the dissolution of most of the $CaCO_3$ reaching the seafloor allows some of it to be preserved by maintaining the saturation state of the porewaters at or near saturation until the particles are isolated from the undersaturated overlying waters.

1.2.4 Shoaling of the aragonite and calcite marker horizons

Early studies of the response of ocean carbonate chemistry to future increases in atmospheric anthropogenic CO_2 concentrations assumed equilibrium between the atmosphere and

surface ocean waters at their *in situ* TA, temperature and salinity (Broecker et al., 1979; Feely et al., 1988; Feely et al., 1984). Under these assumptions, undersaturation of surface waters with respect to aragonite will occur too soon (Orr et al., 2005). In reality, the oceanic response to anthropogenic CO_2 emissions lags that of the atmosphere and, thus, a non-equilibrium approach is required to model future changes in ocean chemistry. Orr et al. (2005) modelled the impact of anthropogenic ocean acidification on the vertical migration of $CaCO_3$ marker horizons. Under a "business-as-usual" scenario, by 2100, the average tropical surface ocean [CO_3^{2-}] will have dropped by 45% relative to preindustrial levels, corresponding to a decline from ~330 µmol kg^{-1} to 149 ± 14 µmol kg^{-1}. Despite this change, surface waters will remain supersaturated with respect to aragonite over most of the oceans, as shown in ***Fig. 1.10***. In the Southern Ocean (below 60°S), [CO_3^{2-}] will decrease to 55 ± 5 µmol.kg^{-1} in surface waters, a value that is 18% below the aragonite saturation threshold (66 µmol.kg^{-1}). These changes are not limited to the surface and may extend to the entire water column. In fact, according to the model of Orr et al. (2005), the Southern Ocean's ASD will shoal from its present average depth of ~800 m to the surface by 2100. A shoaling of the ASD is also predicted to occur in the subarctic Pacific (from 120 m deep to the surface by 2100) and in the North Atlantic (from 2600 m to 115 m below the surface by 2100), under a "business-as-usual" scenario. According to the same model, calcite saturation depths will show less pronounced changes, and the average CSD will remain below 2200m, although the Weddell Sea could become slightly undersaturated with respect to calcite by the end of the century (Orr et al., 2005). More recently, Negrete-García et al. (2019), using GLODAP observations and seawater chemistry predictions under the RCP8.5 scenario, confirmed the sharp ASD shoaling to occur in the Southern Ocean during the 21st century and estimated that more than 80% of the Southern Ocean surface waters will be undersaturated with respect to aragonite by 2100.

Using their coupled climate-carbon Earth system model, Dunne et al. (2012) were able to model calcite exports through the water column and its burial in deep-sea sediments. Their results match observations of deep-sea sediment distributions (Chester and Jickells, 2012; Murray and Renard, 1891) and calcite dissolution horizons in the water column (Feely et al., 2004; Feely et al., 2002). Dunne et al. (2012) assumed that the sinking flux of calcite is proportional to the particulate organic carbon export (although regional variations in the $Ca:C_{org}$ utilization ratios exist, as described in Sarmiento et al. (2002)) and were able to model the $CaCO_3$ burial rate and content in deep-sea sediments. Highest estimated $CaCO_3$ fluxes to the seafloor are found in the

equatorial upwelling zones, the sub-Antarctic zones and in the Northern Pacific. These are areas of high primary productivity, in agreement with satellite-based estimates of sea surface temperatures and chlorophyll concentrations. The Eastern Equatorial Pacific is also an area of high primary productivity, high $CaCO_3$ burial flux and high $CaCO_3$ sediment content, in apparent contradiction with the presence of undersaturated bottom waters shown in ***Fig. 1.11***. It emphasizes the kinetic control exerted on the spatial distribution of calcitic sediment discussed in the previous section, as a balance between sinking and dissolution rates.

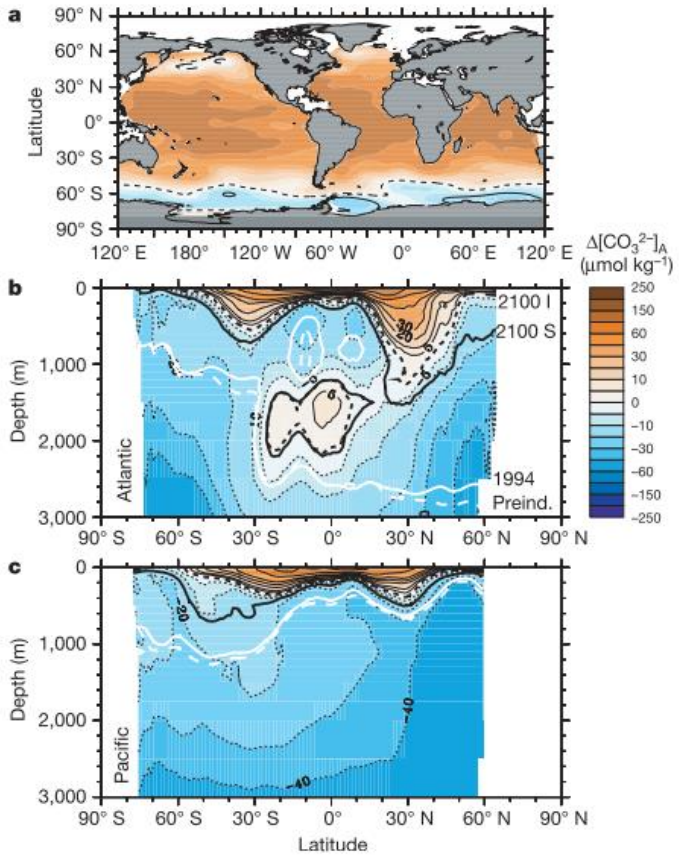

Fig. 1.10 | *Predicted aragonite saturation states in 2100 under the IS92a scenario as indicated by $\Delta[CO_3^{2-}]_A$, the in situ $[CO_3^{2-}]$ minus that for aragonite saturation, all other variables (TA, S_P, T) being equal: a) surface map, b) Atlantic Ocean and c) Pacific Ocean zonal averages. Thick lines represent the ASD in 1765 (white dashed line), 1994 (white solid line) and 2100 (black solid line for a "stabilization" scenario, black dashed line for a "business-as-usual" scenario) (source: Orr et al., 2005).*

1.3 Dissolution of shallow and deep-sea sediments

1.3.1 $CaCO_3$ sediments dissolution

Shallow-water (<200 m) carbonate-rich sediments represent a major $CaCO_3$ reservoir that is particularly vulnerable to ocean acidification and the resulting decrease in the saturation state of seawater with respect to carbonate minerals. In low latitude shallow-water carbonate-rich

sediments, most calcites are magnesium-rich >12 mol% $MgCO_3$ and, given their higher solubility (higher than aragonite, see ***Fig. 1.4***), are considered to likely be the ocean's first responders to ocean acidification. The median Mg content of both abiotic (cements) and biogenic tropical and subtropical calcites is about 13-15 mol% $MgCO_3$ (Morse et al., 2006). Morse et al. (2006) estimated that seawater will become undersaturated with respect to 18 mol% Mg-calcite once the surface ocean pCO_2 reaches 1414 ppmv, a value that may be reached before 2200 if we keep pace with the IPCC business-as-usual scenario depicted in ***Fig. 1.1***. (Meinshausen et al., 2011).

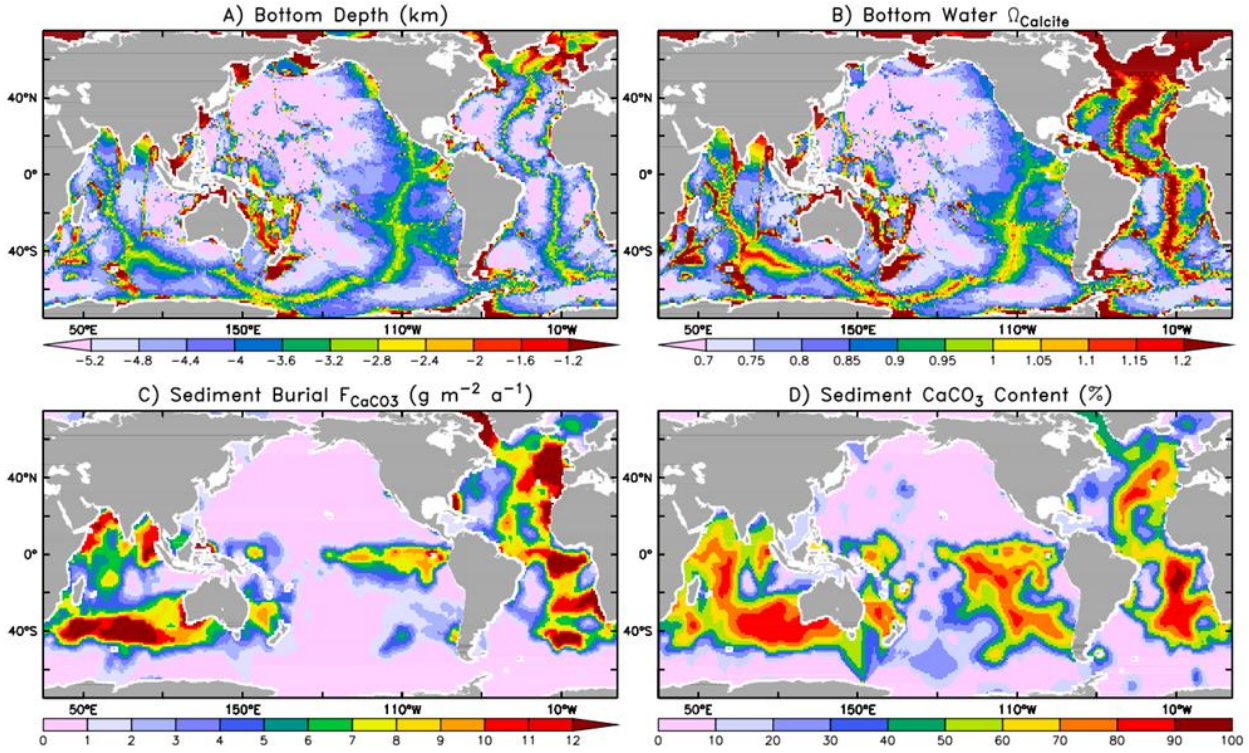

Fig. 1.11 | *Observation-based oceanic bottom-water properties and fluxes. A) Bathymetry. B) Calcite saturation state of bottom water. C) Burial flux of $CaCO_3$ based on sediment observations. D) $CaCO_3$ content of sediment. (Dunne et al., 2012).*

In this section, the role of deep-sea $CaCO_3$-rich sediments as the ultimate sink for anthropogenic CO_2 is reviewed. The deep sea represents all marine domains that extend seaward of the continental shelf break, an area that covers 63.6% of the Earth's surface (Mulder et al., 2011). Deep-sea sediments consist of clastic particles derived from eroded rocks and sediments, volcanic particles, biogenic compounds, and particles formed by chemical precipitation of elements dissolved in seawater (referred to as authigenic sediments).

Mekik et al. (2002) identified three main variables that control the preservation of $CaCO_3$ in deep-sea sediments: bottom-water chemistry and its saturation state, carbonate flux to the seafloor, and organic carbon flux from the surface euphotic zone. A fast burial of the sinking calcitic particles and a high $CaCO_3$:organic carbon flux ratio are as important to $CaCO_3$ preservation as is the bottom-water chemistry (Archer et al., 1989a; Emerson and Bender, 1981; Hales and Emerson, 1997a, b).

Only a small fraction of the particulate organic carbon (POC) produced in the surface ocean reaches the deep seafloor, and most of it is oxidized upon burial. In the open oceans, it is estimated that 0.014% of the POC produced at the surface is buried in the sediments (Seiter et al., 2004). As discussed before, a high flux of $CaCO_3$ particles causes a greater distance between the CSD and the CCD. Above the latter, pelagic sediments are composed mostly of biogenic constituents, predominantly carbonates or mixed carbonate/siliceous components. Below the CCD, they consist of siliceous tests and detrital sediments (Hesse and Schacht, 2011). In areas of low surface productivity, very little biogenic material reaches the deep-sea floor and sediments are formed of brown abyssal clay (which can turn red upon the conversion of iron-hydroxide to hematite) that typically accumulate at rates of less than 5m per million years (Hesse and Schacht, 2011). In comparison, biogenic pelagic sediments can accumulate at rates of up to 200m per million years (Scholle et al., 1983). A detailed description of the classification and the composition of deep-sea sediments is beyond the scope of this document, but an excellent review is provided by Chester and Jickells (2012).

Nearly one third of the ocean floor is covered by $CaCO_3$-rich sediments (>30% w/w) (Morse and Mackenzie, 1990). Their distribution is a function of the surface productivity (production factor), the saturation state of the overlying waters (dissolution factor) and potential dilution by terrigenous, atmospheric, authigenic or other biogenic solids (dilution factor).

Coccoliths dominate the surface sediment composition in the oligotrophic gyres of the South Atlantic. In fact, coccolithophores, in their haploid form (i.e., a cell that contains a single set of chromosomes), have a relatively high level of tolerance for nutrient-depleted media and, thus, tend to thrive in oligotrophic habitats where other phytoplankton would not survive (Houdan et al., 2006). Conversely, the contribution of planktonic foraminifera to surface sediments is highest in regions of elevated fertility, like the mesotrophic equatorial divergence zone (Hüneke

and Henrich, 2011). Pteropods, which have shells composed of aragonite, dominate regionally (Bednaršek et al., 2012). The pteropod carbon biomass is high along the margin of the western Atlantic, reaching up to 50% in the underlying surface sediments, as depicted in ***Fig. 1.12*** (Baumann et al., 2003).

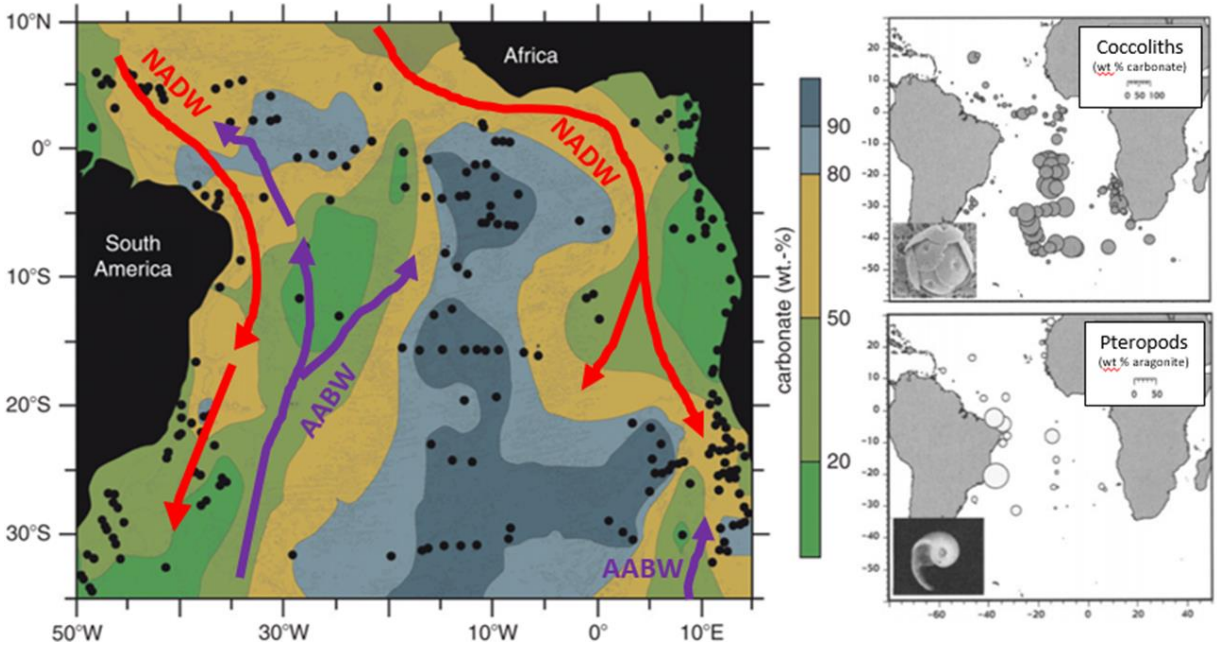

Fig. 1.12 | *Total carbonate, coccolith (calcite) and pteropod (aragonite) content in surface sediments of the South Atlantic (modified from Baumann et al. (2003)). NADW: North Atlantic Deep Waters; AABW: Antarctic Bottom Waters. The deep-water flow paths are drawn from Henrich et al. (2003).*

The location of $CaCO_3$-rich surface sediments highlighted in ***Fig. 1.12*** corresponds roughly to the mid-Atlantic ridge. This area of high topography allows calcitic particles to accumulate in sediments above the CCD. On each side of the ridge, cold and dense corrosive deep-waters (from the North Atlantic and Antarctica) circulate. Note that in ***Fig. 1.12*** the relatively $CaCO_3$-poor sediments near the African coastline are partially explained by the huge discharge of non-carbonate particles brought by the Niger and Congo Rivers to the coast (dilution factor; Dai and Trenberth (2002)). The depth at which the calcite content of sediments starts to drop is encountered at a depth of 3500 m at 35°S and becomes gradually deeper northward (3900 m at 25°S), as the contact between the North Atlantic deep waters and the underlying undersaturated Weddell Sea deep waters becomes deeper. The saturation states of bottom waters with respect to calcite and aragonite

are represented in ***Fig. 1.11***. A comparison between these two maps reveals that the most $CaCO_3$ depleted surface sediments are overlain by the lowest saturation state waters.

1.3.2 Future projections for $CaCO_3$ dissolution

As a consequence of ocean acidification, the ability of organisms to produce $CaCO_3$ could decrease while the rates of bioerosion and $CaCO_3$ dissolution could increase (Andersson and Gledhill, 2013; Langdon et al., 2003; Morse et al., 2006). It is estimated that, at present, coral reefs produce 0.9 Pg $CaCO_3$ per year, of which 0.7 Pg is accumulating in reef areas and the remainder (0.2 Pg) is exported or dissolved (Andersson and Gledhill, 2013; Iglesias-Rodriguez et al., 2002). Observations of net community dissolution (gross dissolution minus reef calcification) under various environmental and experimental (*in situ* vs laboratory studies) conditions show dissolution rates varying from $1x10^{-14}$ to nearly $7x10^{-10}$ mol cm^{-2} s^{-1} (Burdige and Zimmerman, 2002; Conand et al., 1997). The extent of $CaCO_3$ dissolution can vary widely because it is controlled by a number of parameters that are highly variable in sediments, including their organic matter content and porosity (or permeability). For instance, $CaCO_3$ dissolution rates in sediments have been demonstrated to be linearly correlated with seagrass density (Burdige and Zimmerman, 2002). Therefore, predicting the rate of $CaCO_3$ dissolution is a complicated task and has been the focus of numerous studies.

The degree of supersaturation (Ω-1) or undersaturation (1-Ω) of seawater with respect to $CaCO_3$ minerals is a measure of the thermodynamic potential of a reaction towards a state of equilibrium (Ω=1, the rate of dissolution is equal to the rate of precipitation). When seawater is undersaturated, $CaCO_3$ minerals should dissolve if exposed to this solution. Nevertheless, the dissolution reaction is not instantaneous, and a kinetic description is necessary to predict the evolution of the system towards equilibrium. The dissolution rate of calcite is commonly fitted to an empirical kinetic expression of the form (Morse and Berner, 1972):

$$\boldsymbol{r = -\frac{dm_{calcite}}{dt} = k(1-\Omega_c)^n} \qquad \textbf{(1.21)}$$

where k is the dissolution rate constant, Ω_C is the saturation state, and n is the reaction order. Unfortunately, predicting the dissolution rate of deep-sea sediments from the undersaturation state of bottom waters (see ***Fig. 1.11***) is not straightforward, because the dissolution rate constant (k)

and the reaction order (n) in ***reaction 1.21*** are not well constrained. In fact, kinetic studies carried out to date on synthetic (Keir, 1980, 1983; Morse et al., 1979; Subhas et al., 2015; Walter and Morse, 1985) and biogenic (Keir, 1980; Walter and Morse, 1985; Subhas et al., 2018) calcite and aragonite, as well as on deep-sea sediments (Gehlen et al., 2005; Keir, 1980, 1983; Morse, 1978; Walter and Morse, 1985), show huge discrepancies in the magnitude of the dissolution rates and in reaction orders (from linearity to high reaction orders of up ~7; Morse (1978)), as reviewd later in section 1.4.

If the rate of dissolution of $CaCO_3$ minerals as a function of the saturation state of seawater and the surface area of $CaCO_3$ material available for dissolution were known, it would be possible to model the response time of $CaCO_3$ dissolution induced by the penetration of anthropogenic CO_2 into the deep ocean. Smith and Mackenzie (2016) recently elaborated a comprehensive $CaCO_3$ budget in the oceans. They estimated the total visible reef area in the world oceans at about 0.15 x 10^{12} m^2, the carbonate banks and bays cover an area of 0.8 x 10^{12} m^2, and the extratropical high-carbonate shelves extend over 1.3 x 10^{12} m^2. Sedimentary shelf areas to a depth of ~100 m for the tropical and extratropical oceans were estimated to occupy 7.7 x 10^{12} and 11.7 x 10^{12} m^2, respectively. Smith and Mackenzie (2016) then computed the $CaCO_3$ production rates for each of these environments (expressed in mol m^{-2} a^{-1}), along with the plankton production. By comparing the $CaCO_3$ production fluxes to its accumulation in shelves and pelagic sediments, they estimated their respective dissolution fluxes. According to their calculations, more than 90% of the planktonic $CaCO_3$ production dissolves in the water column or in the sediments. Given an estimated global ocean $CaCO_3$ production of 175 x 10^{12} mol a^{-1} and a total accumulation rate of 31 x 10^{12} mol a^{-1}, an average of 144 x 10^{12} moles of $CaCO_3$ are currently dissolving in the world ocean every year.

According to ***reaction 1.19***, for each mole of $CaCO_3$ dissolved, one mole of CO_2 is consumed. Nevertheless, because of the weak buffer capacity of the CO_2-H_2O system described in ***section 1.1.2***, ***reaction 1.19*** is a quantitatively inappropriate representation of $CaCO_3$ dissolution and precipitation (Lyman, 1958). The carbonate buffer capacity of the ocean decreases with increasing pCO_2. Thus, the larger the cumulative anthropogenic CO_2 emissions, the higher the remaining atmospheric fraction (Eby et al., 2009; Joos et al., 2013). Frankignoulle et al. (1994) introduced the molar ratio of $CaCO_3$ dissolved to CO_2 neutralized, referred to as ψ, to represent

the net CO_2 flux associated with $CaCO_3$ dissolution/precipitation reactions such that it can be empirically represented by the following equation (Smith and Mackenzie, 2016):

$$\boldsymbol{CaCO_{3\,(s)} + \psi CO_{2\,(aq)} + H_2O_{\,(l)} \leftrightarrow (1+\psi)HCO_3^-{}_{(aq)} + Ca^{2+}{}_{(aq)} + (1-\psi)OH^-} \qquad \textbf{(1.22)}$$

Because some of the bicarbonate ions (HCO_3^-) produced by this reaction will react with protons to generate CO_2, in the deep-sea (below a depth of 1000 m, where dissolution, estimated at 144 x 10^{12} mol $CaCO_3$ a^{-1}, takes place (Smith and Mackenzie (2016)) and under current conditions, ψ is ~0.85 and shows a positive correlation with seawater pCO_2, implying that the efficiency of the $CaCO_3$ dissolution reaction to sequester CO_2 will increase as ocean acidification persists and intensifies (Smith and Gattuso, 2011; Smith and Mackenzie, 2016). In the contemporary surface ocean, where an estimated 175 x 10^{12} mol $CaCO_3$ a^{-1} are precipitated, ψ is ~0.66. Thus, a comparison of ψ and the $CaCO_3$ precipitation / dissolution balance in these two reservoirs (surface and deep oceans) yields an estimate of the net $CaCO_3$-mediated CO_2 uptake into the ocean of 7 x 10^{12} mol a^{-1}. In comparison, for the decade 2005-2014, the mean ocean CO_2 sink due to fossil fuel (amount of CO_2 absorbed by the oceans in response to these emissions), cement production and land-use change emissions was about 240 x 10^{12} mol a^{-1}. Thus, the anthropogenic CO_2 influx is substantially higher than the small net CO_2 flux driven by oceanic C + $CaCO_3$ metabolism (Smith and Mackenzie, 2016). Moreover, $CaCO_3$ dissolution is expected to increase in the next centuries/millennia as anthropogenic CO_2 penetrates the deep-ocean and is brought in contact with $CaCO_3$-rich deep-sea sediments.

In a modelling study, Gehlen et al. (2008) assessed changes in bottom-water chemistry and benthic $CaCO_3$ dissolution under a scenario where atmospheric pCO_2 is increased 4-fold over a 140-year period. Although they note that their model likely overestimates bottom-water saturation states, they report bottom-water [CO_3^{2-}] decreases by up to -100 μmol kg^{-1} in the North Atlantic and Arctic Oceans. The modelled $CaCO_3$ content of surface sediments drops by up to 5% over the same period, in the North Atlantic and Southern Oceans, due to a combination of enhanced $CaCO_3$ dissolution and reduced $CaCO_3$ flux to the bottom.

Ridgwell and Hargreaves (2007), using an Earth system model (GENIE-1) that takes in account the preservation and burial of $CaCO_3$ in deep-sea sediments, modelled the response of

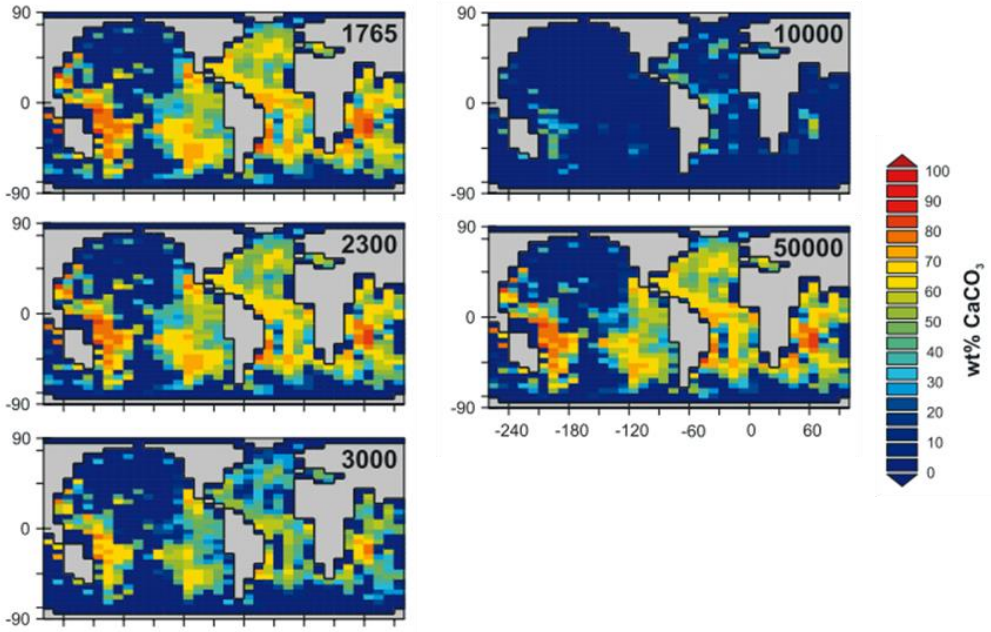

Fig. 1.13 | *Evolution of sediment $CaCO_3$ surface content in response to fossil fuel CO_2 release to the atmosphere for the calendar years 1765, 2300, 3000, 10000 and 50000 (Ridgwell and Hargreaves, 2007).*

deep-sea sediments to a massive release of anthropogenic CO_2 on multi-millennial timescales. The deep-sea sediment module in their model considers that bioturbation effectively homogenizes a 5-cm-thick surface sediment layer that sits on top of a series of 1-cm-thick sub-layers. Dissolution only takes place in the surface layers of the simulated sediment, but bioturbation and advective transport bring new material to the surface in case of surface deficit (i.e., dissolution). They used an empirical function to represent the depth variation of the porosity profile which decreased from 0.95 at the surface of the sediments and leveled off at ~0.7 at 5 cm-depth (Ridgwell, 2001). The results of their model in terms of the long-term fate of fossil fuel CO_2 are presented in ***Figure 1.13***. Assuming a peak of CO_2 release in 2400 followed by an instantaneous cut in emissions (the "rapid" emission scenario described in Lenton et al. (2006)), the surface sediment $CaCO_3$ content decreases as dissolution occurs. In the calendar year 10000, $CaCO_3$ nearly disappears from surface sediments, although some rare $CaCO_3$-rich areas remain, mostly in shallow-tropical platforms. Upon the release of bicarbonate ions in seawater due to $CaCO_3$ dissolution, ocean acidification is more strongly buffered, and dissolution eventually reaches a steady state. The timescale of drawdown is much longer and, in the year 50000, anthropogenic CO_2 stored by the ocean will

account for 92.4% of the total atmospheric CO_2 emissions, mostly stored in $CaCO_3$-rich sediments whose areal distribution would be similar to today's.

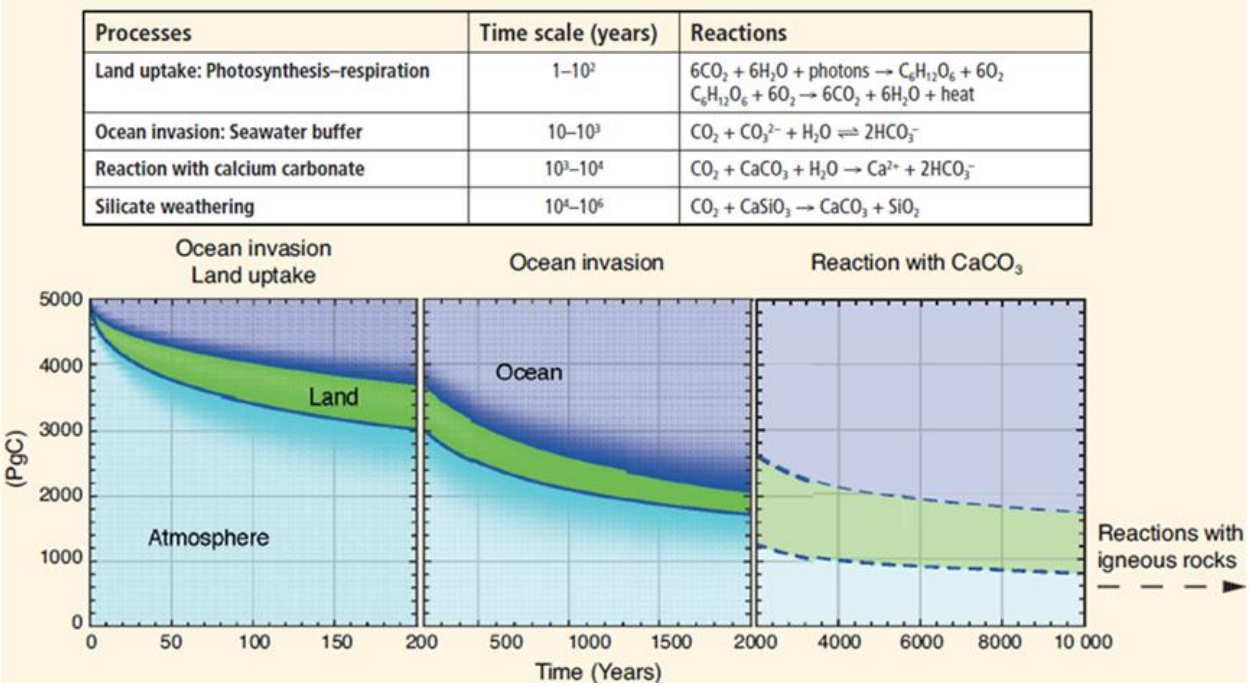

Fig. 1.14 | *Table:* *The main natural processes that remove CO_2 following a large emission pulse to the atmosphere, their atmospheric CO_2 adjustment time scales, and the main (bio)chemical reactions involved.* ***Plot:*** *Decay of 5000 Pg C-CO_2 emitted at time zero into the atmosphere, and its subsequent redistribution into the land and ocean reservoirs as a function of time, computed by coupled carbon-cycle climate models. The width of the colour bands is proportional to the carbon uptake by each reservoir. The first two panels show a multi-model mean from a model inter-comparison project (Joos et al., 2013). The last panel shows the longer-term redistribution of CO_2-C, including ocean dissolution of carbonate sediments as computed with an Earth System Model of Intermediate Complexity (after Archer et al. (2009)) (Ciais et al., 2013).*

The main natural processes and the time scales over which CO_2 is removed from the atmosphere following a large pulse are summarized in ***Fig. 1.14***. In the first 2 centuries after the pulse, about one third of the CO_2 goes into the land and ocean, while the remainder stays in the atmosphere. As anthropogenic CO_2 invades the deep ocean, and within a thousand years, the fraction of an initial pulse of 5000 Gt remaining in the atmosphere would be about 40%. Within a few thousands of years, the decrease in ocean pH is restored by dissolution of $CaCO_3$ minerals on the seafloor, partly replenishing the buffer capacity of the ocean and removing a further 3-8% of added CO_2 from the atmosphere on a timescale of 8-10 ka (Archer et al., 1998; Ciais et al., 2013;

Lenton and Britton, 2006). Archer (1996) estimated that the total sedimentary $CaCO_3$ inventory available to neutralize anthropogenic CO_2 is approximately 1600 Gt C, a quantity that may be exceeded by the amount of fossil fuels potentially burnable in the next centuries. Ultimately, within several hundreds of thousands of years, the remainder of the anthropogenic CO_2 will be neutralized by silicate weathering and other igneous minerals (Ridgwell and Zeebe, 2005; Tyrrell et al., 2007; Walker and Kasting, 1992).

1.4 Calcite dissolution kinetics

1.4.1 Brief literature review

Oceanic uptake plays a major role in the regulation of the atmospheric CO_2 budget, mitigating climate change. The dissolution of anthropogenic CO_2 in seawater and transfer to the deep ocean results in a decrease in the pH, $[CO_3^{2-}]$ and Ω, triggering the dissolution of $CaCO_3$ minerals. The dissolution of the latter represents the strongest short-term (decades to millennia) pH buffering mechanism in the oceans, and is commonly referred to as the ultimate sink of anthropogenic CO_2, for which an estimate of the response time requires a quantitative description of the dissolution kinetics.

The first study of calcite dissolution kinetics was performed by Gortikov and Panteleva (1937) who measured the rate of dissolution of calcite crystals mounted on a disk that was rotated at high speed in an acidic solution. They observed a positive, linear correlation between the rotation speed and the dissolution rate until the dissolution rate asymptotically approached a value of about ~3150 mol/m^2/a. Weyl (1958), based on results of his dissolution experiments of a porous limestone in a CO_2-saturated aqueous solution, proposed that the leveling-off of the dissolution rate might be attributed to 1) the dissociation of $CaCO_3$ at the mineral-water interface, 2) the conversion of CO_3^{2-} to HCO_3^-, 3) the outgassing of $CO_{2\,(aq)}$ or 4) the transport of the various species through the solution. He found that the $CaCO_3$ dissolution rate increased linearly with the flow velocity and reported maximum rates of dissolution well above those observed by Gortikov and Panteleva (1937). The conical shape of the depression that formed at the surface of the crystal where the water flow was greatest, lead Weyl to conclude that the rate of dissolution is not limited by the rate of dissolution at the mineral-water interface but by diffusion. Furthermore, based on the results of Shternina and Frolova (1952), who observed an increased rate of calcite dissolution

with increasing stirring and CO_2-gas bubbling, Weyl (1958) stated that the calcite dissolution rate depends solely on the rate of solute transport away from the dissolving solid. Later, Weyl (1961, 1967) developed a method to measure the degree of departure of a solution from equilibrium with respect to the mineral of interest, which he called the carbonate saturometer. Solid calcium carbonate was added to a solution and dissolved until equilibrium was reached. The evolution of the reaction was followed with a pH-sensitive electrode and the pH excursion served as a measure of the disequilibrium. A version of this method is still in use today and referred to as the free-drift technique. Alternatively, another experimental approach was established in which a constant degree of disequilibrium is maintained in solution through the metered or constant injection of an acidic solution, allowing the dissolution kinetics of carbonate minerals to be studied at close to constant undersaturations (Morse, 1974b, 1978). This technique is referred to as the pH-stat or the chemostatic method.

Great strides in the study of calcium carbonate mineral dissolution kinetics in seawater were made by John W. Morse and Robert A. Berner in the 70's. Their preliminary studies (Berner and Morse, 1974; Morse and Berner, 1972) dealt with the relationship between calcite dissolution kinetics and the lysocline (that they define as the depth in the ocean below which the calcite dissolution rate increases substantially) as well as the theoretical interpretation of their results in terms of rate controlling mechanisms in relation to the saturation state of the solution, a concept introduced earlier by Larson et al. (1942). Studies of calcite dissolution rates carried out in artificial and natural seawater, using both the pH-stat (Morse, 1978; Walter and Morse, 1985) and the free-drift methods (Keir 1980, 1983), reported highly nonlinear dissolution kinetics. The most heralded study to date was performed by Keir (1980) who found the dissolution kinetics of suspended calcite powders to be strongly nonlinear and reported a reaction order, n, of 4.5 (see ***Eq. 1.21***). High reaction orders were observed for synthetic calcite (Keir, 1980, 1983), biogenic calcite (Keir, 1983; Walter and Morse, 1985), and for natural calcite-rich sediments. The latter, recovered from sediment cores taken at sea, were washed and kept resuspended (Keir, 1980; Morse, 1978) or spread at the bottom of a reactor and overlaid by seawater (Keir, 1983). Morse et al. (1979) used the pH-stat method to investigate the dissolution kinetics of synthetic aragonite in seawater. They found a dissolution reaction order of 2.93 close to equilibrium and a reaction order of 7.27 at greater undersaturations. They compared the dissolution rates obtained for synthetic samples with those of pteropods, organisms with aragonitic shells. The rates of pteropod dissolution were more

than 30 times slower than those of synthetic aragonite. They ascribed the discrepancy to the fact that only a small fraction of the pteropod surface is directly exposed to seawater. The high reaction order for the dissolution kinetics of pteropods and synthetic aragonite was later confirmed by Keir (1980) using the free-drift method, and by Walter and Morse (1985) on various organisms with aragonitic skeletons. It is interesting to note that, although all these authors consistently reported high reaction orders for both the aragonite and calcite dissolution kinetics, the measured rates of dissolution (reaction order and rate constants) showed important discrepancies, as discussed later and highlighted in ***Table 1.1***.

Table 1.1 | *Summary of the main dissolution kinetics studies carried out in natural or artificial seawater, as reported by their respective authors.*

Compilation of results of calcite dissolution kinetics studies, as reported by their respective authors

Author	*Material*	*Method*	*Solution*	*Rate constant*	*Rate constant unit*	*Reaction order*
Morse, 1978	Indian Ocean sediment	pH-stat	Natural seawater	**$10^{4.3}$**	%/day	**5.2**
Keir, 1980	Reagent grade calcite	Free drift	Artificial seawater	**1.31×10^{-3}**	%/day	**4.5**
Keir, 1983	Synthetic calcite	Free drift	Artificial seawater	**0.16**	day^{-1}	**4.5**
Walter & Morse, 1985	Low Mg-synthetic calcite	pH-stat	Natural seawater	**3.39×10^{3}**	µmoles g^{-1} hr^{-1}	**2.96**
Walter & Morse, 1985	Mg-calcite: Goniolithon	pH-stat	Natural seawater	**5.37×10^{2}**	µmoles g^{-1} hr^{-1}	**3.20**
Gehlen et al., 2005	Sierra Leon Rise natural sediments	Free drift	Artificial seawater	**0.346**	meq/m^2/day	**2.1**
Subhas et al., 2015	Synthetic calcite	$\Delta^{13}C$	Artificial seawater	**$7.2 \pm 0.6 \times 10^{-4}$**	g/cm^2/day	**3.9 ± 0.1**

Compilation of results of aragonite dissolution kinetics studies as reported by their respective authors

Author	*Material*	*Method*	*Solution*	*Rate constant*	*Rate constant unit*	*Reaction order*
Morse, 1979	Synthetic aragonite	pH-stat	Natural seawater	**110**	%/day	**2.93**
Keir, 1980	Synthetic aragonite	Free drift	Artificial seawater	**1.32×10^{4}**	%/day	**4.2**
Keir, 1980	Pteropods	Free drift	Artificial seawater	**3.18×10^{2}**	%/day	**3.5**
Walter & Morse, 1985	Biogenic aragonites	pH-stat	Natural seawater	**7.79×10^{2}**	µmoles g^{-1} hr^{-1}	**2.484**

Keir (1983) determined the dissolution rate of calcite in a stirred-flow reactor with (non-suspended) beds of synthetic and natural carbonate sediments. Considering a reaction order similar to his previous experiments on suspended sediment (n=4.5; Keir, 1980), the dissolution rate constant was approximately two orders of magnitude lower. Keir (1983) proposed that the presence of a diffusive boundary layer (DBL) at the sediment-water interface (SWI) might explain the discrepancy between his experimental results. The DBL is defined as a thin layer of fluid between the solid (possibly porous) surface and the bulk solution, within which molecular diffusion dominates over turbulent transport and whose thickness is influenced by the hydrodynamic conditions (Schlichting, 1979). The DBL can behave as a region of mass-transfer resistance and thus may limit the dissolution at the solid-water interface (Boudreau and Guinasso, 1982; Dade, 1993; Jørgensen and Revsbech, 1985; Santschi et al., 1983; Steinberger and Hondzo, 1999). Later, Boudreau (2013) showed that the dissolution rates, measured by Keir (1983) on (non-suspended) beds of synthetic and natural carbonate sediments, were in fact linearly dependent on the undersaturation states of the solution. A linear relationship would be easier to implement in oceanographic or geochemical models and was adopted by Hales and Emerson (1997b) and Dunne et al. (2012). First-order calcite dissolution kinetics appear to be more consistent with results of *in situ* studies of $CaCO_3$ dissolution in the deep sea (Hales and Emerson, 1996, 1997a, b), but diagenetic processes, such as metabolic CO_2 production and bioturbation, may significantly influence these *in situ* rate measurements. It is important to note and keep in mind that, while studies focusing on the dissolution of suspended particles (e.g., Keir, 1980; Walter and Morse, 1985; Subhas et al., 2015) report their rates as a function of the grain surface area, sediment-based studies (e.g., Keir, 1983 and as in the experimental data reported in this document) conveniently use the SWI-surface area to normalize the dissolution rate.

More recently, Gehlen et al. (2005) measured an average reaction order of 2.3 ± 4 for the dissolution of calcitic sediment particles suspended in seawater. Subhas et al. (2015) found a reaction order of 3.9 ± 0.1, based on the dissolution rate measurements of ^{13}C-enriched calcite under near steady-state conditions, as monitored by changes in the $\delta^{13}C$ of the dissolved inorganic carbon (DIC) with time using a cavity ringdown spectrometer (CRDS). Recently, Naviaux et al. (2019), based on laboratory dissolution experiments on ^{13}C-enriched calcites and variations of the reaction order with the degree of undersaturation ($1 - \Omega_C$), proposed that close to equilibrium ($\Omega_C > 0.9$), dissolution is limited to the retreat of pre-existing steps, kinks and adatoms on the calcite

surface, further away from equilibrium ($0.9 > \Omega_C > \sim 0.75$), defect-assisted dissolution dominates, and below $\Omega_C \sim 0.75$, the measured rates show a sharp increase, as undersaturation is high enough to allow dissolution to occur homogeneously across the mineral surface. This apparent criticality in the mineral-solution system might explain the nonlinear dissolution behaviors observed by several authors for calcite grains kept in suspension in seawater.

When dissolution of a sediment at the seafloor is controlled by the combined solid-solution reaction and transport rates within the sediment, then "deep" solute gradients develop within the sediment, on a scale far greater than the thickness of the DBL; the DBL is typically one millimeter thick under deep-sea conditions but can be thinner in a reactor. In this document, we will refer to transport and surface reaction limitations that take place within the sediment as "sediment-side control" and to diffusion limitation through the DBL above the bed as "water-side control". This distinction is adopted because transport across the DBL will be affected by benthic currents, whereas control by processes within the sediments (transport through the pore network, reactions involving the minerals that compose the sediment, respiration or degradation of organic matter, adsorption/desorption, etc.) will be impervious to such effects (baring resuspension or flow penetration). Note that dissolution controlled by water-side processes (DBL transport) are inherently linear, as dictated by Fick's first law of diffusion (e.g., ***Eq. 1.11***), which would stand in stark contrast to past assertions of high-order nonlinearity for calcite dissolution rates and be consistent with the linear calcite dissolution kinetics of the experiments of Keir (1983) on calcite-rich sediments. If controlled by diffusive transport through the DBL, the calcite dissolution rate at the SWI should also be dependent on the bottom-current velocity, as the air-sea CO_2 diffusive flux discussed above is a function in the wind speed, see ***Eq. 1.13***. Yet, most sediment models published to date either ignore the presence of a DBL above the sediment-water interface (Van Cappellen and Wang, 1996; Archer et al., 2002; Hales, 2003; Munhoven, 2007; Tschumi et al., 2011) or consider a DBL with a thickness set to a constant arbitrary value (Boudreau, 1996; Heinze et al., 1999). Instead, the DBL thickness should be expressed as a function of current-speed, as formulated by various authors (Boudreau and Guinasso, 1982; Levich, 1962; Higashino and Stefan, 2004) and confirmed by experimentalists (Larkum et al., 2003; Lorke et al., 2003; Santschi et al., 1983; Santschi et al., 1991).

1.4.2 Scope and outline of the dissertation

With the exception of Keir (1983), all previous laboratory-based $CaCO_3$ dissolution studies avoided the role of water-side processes by re-suspending the sediment in seawater in order to expose all the mineral surfaces and minimize the boundary layer around each grain (Gehlen et al., 2005; Keir, 1980; Morse, 1978; Walter and Morse, 1985). Although these studies provide good insights on calcite dissolution kinetics in the water column (after normalization to the exposed surface area), they are not representative of sediment dissolution conditions (Boudreau, 2013). Thus, current kinetic expressions cannot be applied to the seafloor because transport conditions that are specific to sediments (i.e., the presence of a continuous DBL between the grains, the transport of solutes and reactions products through the pore network, a different conception of surface area normalization) are disregarded in dissolution experiments carried out on suspended materials. There is no proper quantification nor understanding of the mechanisms controlling $CaCO_3$ mineral dissolution kinetics at the seafloor. Although mathematical formulations of $CaCO_3$ mineral dissolution kinetics in marine sediments exist in the literature, they have never been compared with laboratory or *in situ* observations.

The overarching hypothesis to be tested in this Ph.D. thesis is the following: *calcite dissolution kinetics in deep-sea sediments are a linear function to the saturation state of the overlying waters and water-side transport-controlled.* The hypothesis will be tested by reaching the following three main objectives:

1) Determine the dissolution rate of synthetic calcite and aragonite at the interface between natural seawater and a synthetic sediment of various porosities and calcium carbonate content.
2) Qualitatively and quantitatively describe the rate controlling mechanism(s) under conditions that simulate the range of hydrodynamic conditions encountered at the seafloor.
3) Using bottom-seawater chemistry and bottom-current databases, as well as the calcite dissolution rate laws derived from laboratory experiments, compute the calcite dissolution rate at the seafloor on a global scale.

In ***Chapter 2***, a stirred flow-through reactor is used to measure the dissolution rates of a synthetic sediment disk placed at the bottom of the reactor and overlain by natural, acidified seawater, under a range of undersaturation states and seawater stirring rates. The dissolution rates,

normalized to the interfacial area of the sediment disks, are linear functions on the undersaturation state of the experimental seawater solution and display a square-root dependence on the calcite content, under both quiescent and stirred conditions. The rate of release of reaction products from the sediment to the solution increases with stirring rate, i.e., shear stress, until it becomes invariant at higher stirring rates. This latter result argues that calcite dissolution is transport (water-side) controlled for shear stress levels known to exist at the seafloor, which advises a simpler kinetic description of benthic calcite dissolution.

In ***Chapter 3,*** we describe a novel, simple temperature-controlled rotating-disk reactor that is suitable for use with natural sediments and capable of generating thick DBLs such as those encountered in deep-sea conditions. In this reactor, water overlying the rotating sediment can be sampled discretely or continuously to monitor the chemical reaction progress. The worthiness of the reactor is tested by dissolving a foraminiferal sand bed in natural seawater. The results (1) show that measured dissolution fluxes agree with those predicted by theory and (2) confirm that the dissolution of calcite under seafloor-like hydrodynamic conditions is controlled by mass transfer across the DBL above the bed. Guidelines for best practices under various experimental conditions, possible future developments, and the theoretical equations to compute the DBL thickness and diffusive fluxes in this reactor are described.

Chapter 4 presents a large dataset of dissolution experiments carried out using the newly designed flow-through rotating-disk reactor and simulated deep-sea sediment disks, to provide a quantitative description of the calcite dissolution kinetics under quantitatively well-constrained and seafloor-representative hydrodynamic conditions and unravel the mechanisms that control this dissolution. Among all the investigated oceanographic variables that may potentially influence the dissolution rate, i.e., sediment porosity, permeability, grain size and specific surface area, biogenic or synthetic particles, seawater temperature, current speed and carbonate ion concentration [CO_3^{2-}], results show that only seawater [CO_3^{2-}] and the current speed have a statistically significant influence on calcite dissolution rates. The current-speed dependency is explained by the presence of a diffusive boundary layer (DBL) above the SWI. Based on these observations, it is argued that geologically long- or medium-term changes in bottom-current velocities, such as those that may be induced by changes in continental positions or evolving climate, should be considered along

with variations of calcite deposition fluxes or seawater acidification when interpreting calcite preservation data through time.

In ***Chapter 5***, recent databases of bottom-water chemistry, benthic currents, and $CaCO_3$ content of deep-sea sediments are combined with our rate model to derive the global distribution of benthic calcite dissolution rates and obtain primary confirmation of an anthropogenic component. By comparing preindustrial with present-day rates, it is determined that significant anthropogenic dissolution now occurs in the western North Atlantic, accounting for 40–100% of the total seafloor dissolution at its most intense locations. At these locations, the calcite compensation depth has risen ~300 m. Increased benthic dissolution is also revealed at various hot spots in the southern extent of the Atlantic, Indian, and Pacific Oceans.

The aim of ***Chapter 6*** is to test the paradigm that seafloor $CaCO_3$ dissolution will spread spatially and accelerate as ocean acidification persists and intensifies. Results from a range of Earth System and climate models run under high-CO_2 emission scenarios and at various resolutions are used to test the paradigm. Following the "business-as-usual" RCP8.5 scenario, which is a high anthropogenic CO_2 emission scenario in which no specific climate mitigation action is taken, results show that while $CaCO_3$ dissolution will increase over the 21st century in some areas of the deep ocean, such as the eastern central Pacific Ocean, it is projected to decrease in the Northern Pacific and abyssal Atlantic Oceans. The decrease is due to reduced $CaCO_3$ delivery to the seafloor, as well as slower bottom-water circulation, which leads to thicker diffusive boundary layers above the sediment bed and a consequent stronger kinetic barrier to the dissolution reaction. Although a projected weakening of bottom currents is consistent over most of the seafloor into the 21st century, irrespective of the model, strong discrepancies exist in the magnitude of predicted bottom-current speeds among models. Modern bottom-current speeds returned by most models consistently underestimate observations made by current meters, and the discrepancy between model results and observations narrows as the model resolution increases. The poor performance of most models in representing bottom velocities, as well as the large disparities encountered across bottom-water chemical variables, reduce our ability to estimate the magnitude and temporal evolution of anthropogenic $CaCO_3$ dissolution rates and the accompanying carbon neutralization.

Finally, ***Chapter 7*** summarizes the main results from this thesis and places them into the broader context of the marine $CaCO_3$ cycle in the Anthropocene. Implications for our

understanding and quantification of water-column $CaCO_3$ dissolution and $CaCO_3$ burial in sediments are discussed. Future methodological improvements for the study of calcite dissolution kinetics at the SWI in the laboratory, and perspectives for future research are presented.

References

Alkattan, M., Oelkers, E.H., Dandurand, J.-L. and Schott, J. (1998) An experimental study of calcite and limestone dissolution rates as a function of pH from -1 to 3 and temperature from 25 to 80°C. *Chemical Geology*, 151, 199-214, https://doi.org/10.1016/S0009-2541(98)00080-1

Alldredge, A.L. and Silver, M.W. (1988) Characteristics, dynamics and significance of marine snow. *Progress in Oceanography*, 20, 41-82.

Andersson, A.J., Mackenzie, F.T. and Bates, N.R. (2008) Life on the margin: implications of ocean acidification on Mg-calcite, high latitude and cold-water marine calcifiers. *Marine Ecology Progress Series*, 373, 265-273.

Andersson, A.J. and Gledhill, D. (2013) Ocean acidification and coral reefs: effects on breakdown, dissolution, and net ecosystem calcification. *Annual Reviews of Marine Science*, 5, 321-348.

Archer, D., Emerson, S. and Reimers, C. (1989a) Dissolution of calcite in deep-sea sediments: pH and O_2 microelectrode results. *Geochimica et Cosmochimica Acta*, 53(11), 2831-2845.

Archer, D., Emerson, S. and Smith, C.R. (1989b) Direct measurement of the diffusive sublayer at the deep sea floor using oxygen microelectrodes. *Nature*, 340, 623-626.

Archer, D. and Maier-Reimer, E. (1994) Effect of deep-sea sedimentary calcite preservation on atmospheric CO_2 concentration. *Nature*, 367, 260-263.

Archer, D. (1996) A data-driven model of the global calcite lysocline. *Global Biogeochemical Cycles*, 10, 511-526, https://doi.org/10.1029/96GB01521.

Archer, D., Kheshgi, H. and Maier-Reimer, E. (1998) Dynamics of fossil fuel CO_2 neutralization by marine $CaCO_3$. *Global Biogeochemical Cycles*, 12, 259-276, https://doi.org/10.1029/98GB00744

Archer, D.E., Morford, J.L. and Emerson, S.R. (2002) A model of suboxic sedimentary diagenesis suitable for automatic tuning and gridded global domains. *Global Biogeochemical Cycles*, 16(1), 17-1-17-21, https://doi.org/10.1029/2000GB001288

Archer, D. (2005) Fate of fossil fuel CO_2 in geologic time. *Journal of Geophysical Research*, 110(C09S05).

Archer, D., Eby, M., Brovkin, V., Ridgwell, A., Cao, L., Mikolajewicz, U., Caldeira, K., Matsumoto, K., Munhoven, G., Montenegro, A. and Tokos, K. (2009) Atmospheric Lifetime of Fossil Fuel Carbon Dioxide. *Annual Review of Earth and Planetary Sciences*, 37, 117-134, https://doi.org/10.1146/annurev.earth.031208.100206

Arvidson, R.S., Mackenzie, F.T. and Guidry, M.W. (2013). Geologic history of seawater: A MAGic approach to carbon chemistry and ocean ventilation. *Chemical Geology*, 362, 287-304, https://doi.org/10.1016/j.chemgeo.2013.10.012

Barker, S. and Ridgwell, A. (2012) Ocean acidification. *Nature Education Knowledge*, 3(10), 21

Barth, T.F.W., Correns, C.W., and Eskola, P. (1939) Die Entstehung der Gesteine, Berlin, Springer-Verlag, 424 pp.

Bates, N.R., Mathis, J.T. and Jeffries, M.A. (2011) Air-sea CO_2 fluxes on the Bering Sea shelf. *Biogeosciences*, 8(5), 1237-1253.

Baumann, K.-H., Bockel, B., Donner, B., Gerhardt, S., Henrich, R., Vink, A., Volbers, A., Willems, H. and Zonneveld, K.A.F. (2003) Contribution of calcareous plankton groups to the carbonate budget of South Atlantic surface sediments. In Wefer, G., Mulitza, S., and Ratmeyer, V. [Eds], The South Atlantic in the Late Quaternary: Berlin, Springer-Verlag.

Bednaršek, N., Možina, J., Vogt, M., O'Brien, C., and Tarling, G. A. (2012) The global distribution of pteropods and their contribution to carbonate and carbon biomass in the modern ocean. *Earth System Science Data*, 4(1), 167-186.

Berger, W.H., Bonneau, M.C. and Parker, F.L. (1982) Foraminifera on the deep-sea floor: lysocline and dissolution rate. *Oceanologica Acta*, 5(2), 249-258.

Bergman, T.L., Lavine, A.S., Incropera, F.P. and DeWitt, D.P. (2011) Fundamentals of heat and mass transfer, 7th edition, Wiley Global Education, 1072 pp.

Berner, R.A. and Morse, J.W. (1974) Dissolution kinetics of calcium carbonate in sea water: IV. Theory of calcite dissolution. *American Journal of Science*, 274(2), 108-134.

Berner, R.A. (1981) Pelagic sedimentation of aragonite: Its geochemical significance. *Science*, 211, 940-942.

Bischoff, W.D., Mackenzie, F.T. and Bishop, F.C. (1987) Stabilities of synthetic magnesian calcites in aqueous solution: Comparison with biogenic materials. *Geochimica et Cosmochimica Acta*, 51(6): 1413-1423.

Bolin, B. (1960) On the exchange of carbon dioxide between the atmosphere and the sea. *Tellus*, 7(3), 174-184.

Boudreau, B.P. and Guinasso Jr., N.L. (1982) The influence of a diffusive boundary layer on accretion, dissolution, and diagenesis at the sea floor. In: Fanning, K.A., Manheim, F.T. [Eds.]. *The Dynamic Environment of the Ocean Floor*. Lexington Books, Lexington, pp. 115-145.

Boudreau, B.P. (1996) A method-of-lines code for carbon and nutrient diagenesis in aquatic sediments. *Computers & Geosciences*, 22(5), 479-496, https://doi.org/10.1016/0098-3004(95)00115-8

Boudreau, B.P. (2013) Carbonate dissolution rates at the deep ocean floor. *Geophysical Research Letters* 40, 744-748, https://doi.org/10.1029/2012GL054231

Boudreau, B.P., Middelburg, J.J. and Luo, Y. (2018) The role of calcification in carbonate compensation. *Nature Geoscience*, 11, 84-890,

Bramlette, M.N. (1961) Pelagic sediments. In: Sears, M. [Ed.], Oceanography. *Publications of the American Association for the Advancement of Science*, 67, pp. 345-366.

Brewer, P.G. and Peltzer, E.T. (2009) Limits to marine life. *Science*, 324, 347-348.

Broecker, W.S. and Peng, T.H. (1971) The vertical distribution of radon in the Bomex area. *Earth and Planetary Science Letters*, 11, 99-108.

Broecker, W.S., Takahashi, T., Simpson, H.J. and Peng, T.H. (1979) Fate of fossil fuel carbon dioxide and the global carbon budget. *Science*, 206(4417), 409-418.

Broecker, W.S. and Clark, E. (2003) Pseudo dissolution of marine calcite. *Earth and Planetary Science Letters*, 208(3-4), 291-296.

Bullister, J.L., Rhein, M. and Mauritzen, C. (2013) Deepwater formation. In Siedler, G., Gould, J., and J., C. [Eds.] Ocean Circulation and Climate: A 21st Century Perspective. 2nd Ed.: Oxford, GB, Academic Press, pp. 227-253.

Burdige, D.J. (1993) The biogeochemistry of manganese and iron reduction in marine sediments. *Earth-Science Reviews*, 35, 249-284.

Burdige, D.J. and Zimmerman, R.C. (2002) Impact of sea grass density on carbonate dissolution in Bahamian sediments. *Limnology and Oceanography*, 47(6), 1751-1763.

Burton, E.A. and Walter, L.M. (1990) The role of pH in phosphate inhibition of calcite and aragonite precipitation rates in seawater. *Geochimica et Cosmochimica Acta*, 54(3), 797-808.

Caldeira, K. and Wickett, M.E. (2003) Anthropogenic carbon and ocean pH. *Nature* 425, 365-365, https://doi.org/10.1038/425365a

Carter, P.W. and Mitterer, R.M. (1978) Amino acid composition of organic matter associated with carbonate and non-carbonate sediments. *Geochimica et Cosmochimica Acta* 42(8), 1231-1238.

Chave, K.E. (1954) Aspects of the biogeochemistry of magnesium 1. Calcareous marine organisms. *The Journal of Geology* 62(3), 266-283.

Chave, K.E. and Suess, E. (1970) Calcium carbonate saturation in seawater: effects of dissolved organic matter. *Limnology and Oceanography* 15(4), 633-637.

Chester, R. and Jickells, T.D. (2012) Marine Geochemistry: Second Edition, New York, John Wiley & Sons, 436pp.

Ciais, P., Sabine, C., Bala, G., Bopp, L., Brovkin, V., Canadell, J., Chhabra, A., DeFries, R., Galloway, J., Heimann, M., Jones, C., Le Quéré, C., Myneni, R.B., Piao, S. and Thornton, P. (2013) Carbon and Other Biogeochemical Cycles. In: Stocker, T.F., D. Qin, G.-K. Plattner, M. Tignor, S.K. Allen, J. Boschung, A. Nauels, Y. Xia, V. Bex and P.M. Midgley [Eds.] Climate Change 2013: The Physical Science Basis. Contribution of Working Group I to the Fifth Assessment Report of the Intergovernmental Panel on Climate Change. Cambridge University Press, Cambridge, United Kingdom and New York, NY, USA.

Clark, P.U., Pisias, N.G., Stocker, T.F. and Weaver, A.J. (2002) The role of the thermohaline circulation in abrupt climate change. *Nature* 415, 863-869.

Conand, C., Chabanet, P., Cuet, P. and Letourneur, Y. (1997) The carbonate budget of a fringing reef in La Reunion Island (Indian Ocean): sea urchin and fish bioerosion and net calcification. In Lessios, H.A. and Macintyre, I.G. [Eds.] Proceedings of the 8th International Coral Reef Symposium Vol. 1. Smithsonian Tropical Research Institute, Panama.

Crutzen, P.J. and Stoermer, E.F. (2000) The "Anthropocene". *IGBP Newsletter* 41, 17-18.

Cullen, J., Yang, X. and MacIntyre, H.L. (1992) Nutrient limitation and marine photosynthesis. In Falkowski, P. G., and Woodhead, A.D. [Eds.] Primary Productivity and Biogeochemical Cycles in the Sea: New York, Springer Science+Business Media, p. 69-88.

Dade, W.B. (1993) Near-bed turbulence and hydrodynamic control of diffusional mass transfer at the sea floor. *Limnology and Oceanography* 38, 52-69, https://doi.org/10.4319/lo.1993.38.1.0052

Dai, A. and Trenberth, K.E. (2002) Estimates of freshwater discharge from continents: Latitudinal and seasonal variations. *Journal of Hydrometeorology* 3, 660-687.

Deacon, E.L. (1980) Sea-air gas transfer: the wind speed dependance. *Boundary-Layer Meteorology* 21, 31-37.

Delille, B., Harlay, J., Zondervan, I., Jacquet, S., Chou, L., Wollast, R., Bellerby, R.G.J., Frankignoulle, M., Borges, A.V., Riebesell, U. and Gattuso, J.-P. (2005) Response of primary production and calcification to changes of pCO_2 during experimental blooms of the coccolithophorid Emiliania huxleyi. *Global Biogeochemical Cycles* 19(GB2023).

Dickson, A.G. (1981) An exact definition of total alkalinity and a procedure for the estimation of alkalinity and total inorganic carbon from titration data. *Deep Sea Research* 28A(6), 609-623.

Dickson, J.A.D. (2002) Fossil echinoderms as monitor of the Mg/Ca ratio of Phanerozoic Oceans. *Science* 298, 1222-1224.

Dlugokencky, E. and Tans, P. (2018) *Trends in atmospheric carbon dioxide*. National Oceanic and Atmospheric Aministration, Earth System Research Laboratory (NOAA/ESRL).

Drever, J.I. (1997) The Geochemistry of Natural Waters: Surface and Groundwater Environments (3rd Edition), Upper Saddle River, New Jersey, Prentice Hall.

Dunne, J.P., Hales, B. and Toggweiler, J.R. (2012) Global calcite cycling constrained by sediment preservation controls. *Global Biogeochemical Cycles* 26(3), https://doi.org/10.1029/2010GB003935.

Eby, M., Zickfeld, K., Montenegro, A., Archer, D., Meissner, K.J. and Weaver, A.J. (2009) Lifetime of anthropogenic climate change: Millennial time scales of potential CO_2 and surface temperature perturbations. *Journal of Climate* 22(10), 2501-2511.

Elderfield, H., and Schultz, A. (1996) Mid-ocean ridge hydrothermal fluxes and the chemical composition of the ocean. *Annual Review of Earth and Planetary Sciences* 24, 191-224.

Emerson, S. and Bender, M. (1981) Carbon fluxes at the sediment-water interface of the deep-sea: calcium carbonate preservation. *Journal of Marine Research* 39, 139-162.

Emerson, S., Kalhorn, S., Jacobs, L., Tebo, B.M., Nealson, K.H. and Rosson, R.A. (1982) Environmental oxidation rate of manganese(II): bacterial catalysis. *Geochimica et Cosmochimica Acta* 46(6), 1073-1079.

Eppley, R.W. and Peterson, B.J. (1979) Particulate organic matter flux and planktonic new production in the deep ocean. *Nature* 282, 677-680.

Falkowski, P.G., Barber, R.T. and Smetacek, V. (1998) Biogeochemical controls and feedbacks on ocean primary production. *Science* 281, 200-206.

Feely, R.A., Byrne, R.H., Acker, J.G., Betzer, P.R., Chen, C.-T.A., Gendron, J.F. and Lamb, M.F. (1988) Winter-summer variations of calcite and aragonite saturation in the Northeast Pacific. *Marine Chemistry* 25(3), 227-241.

Feely, R.A., Sabine, C.L., Lee, K., Millero, F.J., Lamb, M.F., Greeley, D., Bullister, J.L., Key, R.M., Peng, T.H., Kozyr, A., Ono, T. and Wong, C.S. (2002) In situ calcium carbonate dissolution in the Pacific Ocean. *Global Biogeochemical Cycles* 16, 91-91-91-12, https://doi.org/10.1029/2002GB001866

Feely, R.A., Sabine, C.L., Lee, K., Berelson, W., Kleypas, J., Fabry, V.J. and Millero, F.J. (2004) Impact of Anthropogenic CO_2 on the $CaCO_3$ System in the Oceans. *Science* 305(5682), 362-366.

Fowler, S.W., and Small, L.F. (1972) Sinking rates of Euphausiid fecal pellets. *Limnology and Oceanography* 17(2), 293-296.

Fowler, S.W. and Knauer, G.A. (1986) Role of large particles in the transport of elements and organic compounds through the oceanic water column. *Progress in Oceanography* 16(3), 147-194.

Frangoulis, C., Skliris, N., Lepoint, G., Elkalay, K., Goffart, A., Pinnegar, J.K. and Hecq, J.-H. (2011). Importance of copepod carcasses versus faecal pellets in the upper water column of an oligotrophic area. *Estuarine, Coastal and Shelf Science* 92(3), 456-463, https://doi.org/10.1016/j.ecss.2011.02.005

Frankignoulle, M., Canon, C., and Gattuso, J.-P. (1994) Marine calcification as a source of carbon dioxide: Positive feedback of increasing atmospheric CO_2. *Limnology and Oceanography*, 39(2), 458-462.

Garrels, R.M. and Thompson, M.E. (1962) A chemical model for sea water at 25 degrees C and one atmosphere total pressure. *American Journal of Science* 260, 57-66.

Gehlen, M., Mucci, A. and Boudreau, B. (1999) Modelling the distribution of stable carbon isotopes in porewaters of deep-sea sediments. *Geochimica et Cosmochimica Acta* 63(18), 2763-2773.

Gehlen, M., Bassinot, F.C., Chou, L. and McCorkle, D. (2005) Reassessing the dissolution of marine carbonates: II. Reaction kinetics. *Deep Sea Research Part I: Oceanographic Research Papers* 52(8), 1461-1476.

Gehlen, M., Bopp, L. and Aumont, O. (2008) Short-term dissolution response of pelagic carbonate sediments to the invasion of anthropogenic CO_2: A model study. *Geochemistry, Geophysics, Geosystems*, 9(2), https://doi.org/10.1029/2007gc001756

Global Carbon Budget (2016) More information, data sources and data files at http://www.globalcarbonproject.org/carbonbudget/

Goldschmidt, J.R. (1983) Phase relations of rhombohedral carbonates. In Reeder, R.J. [Ed.] Carbonates: mineralogy and chemistry: Washington DC, Mineralogical Society of America, p. 49-76.

Gortikov, V.M. and Panteleva, L.I. (1937) Kinetics of solvation of calcium carbonate. *J. Gen. Chern. USSR* 1(7) 56-64.

Hales, B. and Emerson, S. (1996) Calcite dissolution in sediments of the Ontong-Java Plateau: In situ measurements of pore water O_2 and pH. *Global Biogeochemical Cycles* 10(3), 527-541.

Hales, B. and Emerson, S. (1997a) Calcite dissolution in sediments of the Ceara Rise: In situ measurements of porewater O_2, pH, and $CO_{2\,(aq)}$. *Geochimica et Cosmochimica Acta* 61(3), 501-514.

Hales, B. and Emerson, S. (1997b) Evidence in support of first-order dissolution kinetics of calcite in seawater. *Earth and Planetary Science Letters* 148(1), 317-327.

Hales, B. (2003) Respiration, dissolution, and the lysocline. *Paleoceanography and Paleoclimatology* 18: https://doi.org/10.1029/2003PA000915.

Hardie, L.A. (1996) Secular variation in seawater chemistry: An explanation for the coupled secular variation in the mineralogies of marine limestones and potash evaporites over the past 600 m.y. *Geology* 24(3), 279-283.

Harris, R. P. (1994) Zooplankton grazing on the coccolithophore Emiliania huxleyi and its role in inorganic carbon flux. *Marine Biology* 119, 431-439.

Heinze, C., Maier-Reimer, E., Winguth, A.M.E. and Archer, D. (1999) A global oceanic sediment model for long-term climate studies. Global Biogeochemical Cycles 13(1), 221-250, https://doi.org/10.1029/98GB02812

Hendriks, I.E., Duarte, C.M., Marbà, N. and Krause-Jensen, D. (2017) pH gradients in the diffusive boundary layer of subarctic macrophytes. *Polar Biology* 40: 2343-2348.

Hesse, R. and Schacht, U. (2011) Early Diagenesis of Deep-Sea Sediments. In Hüneke, H., and Mulder, T. [Eds.] Deep-Sea Sediments: Amsterdam, Elsevier.

Higashino, M., and Stefan, H. G. (2004) Diffusive boundary layer development above a sediment-water interface. *Water Environment Research* 76: 292-300, https://doi.org/10.2175/106143004X141870.

Honjo, S. (1976) Coccoliths: Production, transportation and sedimentation. *Marine Micropaleontology* 1, 65-79.

Houdan, A., Probert, I., Zatylny, C., Véron, B. and Billard, C. (2006) Ecology of oceanic coccolithophores. I. Nutritional preferences of the two stages in the life cycle of Coccolithus braarudii and Calcidiscus leptoporus. *Aquatic Microbial Ecology* 44, 291-301.

Hüneke, H., and Henrich, R. (2011) Pelagic Sedimentation in Modern and Ancient Oceans. In Hüneke, H., and Mulder, T. [Eds.] Deep-Sea Sediments: Amsterdam, Elsevier.

Iglesias-Rodriguez, M.D., Armstrong, R., Feely, R., Hood, R., Kleypas, J., Milliman, J.D., Sabine, C. and Sarmiento, J. (2002) Progress made in study of ocean's calcium carbonate budget. *EOS, Transactions American Geophysical Union* 83(34), 365-375.

Ingle, S.E. (1975) Solubility of calcite in the ocean. *Marine Chemistry* 3(4), 301-319.

Jahnke, R.A., Craven, D.B. and Gaillard, J.-F. (1994) The influence of organic matter diagenesis on $CaCO_3$ dissolution at the deep-sea floor. *Geochimica et Cosmochimica Acta* 58(13), 2799-2809.

Jahnke, R.A. and Jahnke, D.B. (2004) Calcium carbonate dissolution in deep sea sediments: reconciling microelectrode, pore water and benthic flux chamber results. *Geochimica et Cosmochimica Acta* 68(1), 47-59.

Joos, F. and Spahni, R. (2008) Rates of change in natural and anthropogenic radiative forcing over the past 20,000 years. *Proceedings of the National Academy of Sciences of the United States of America* 105, 1425-1430, https://doi.org/10.1073/pnas.0707386105

Joos, F., Roth, R., Fuglestvedt, J.S., Peters, G.P., Enting, I.G., von Bloh, W., Brovkin, V., Burke, E.J., Eby, M., Edwards, N.R., Friedrich, T., Frölicher, T.L., Halloran, P.R., Holden, P.B., Jones, C., Kleinen, T., Mackenzie, F.T., Matsumoto, K., Meinshausen, M., Plattner, G.K., Reisinger, A., Segschneider, J., Shaffer, G., Steinacher, M., Strassmann, K., Tanaka, K., Timmermann, A. and Weaver, A.J. (2013) Carbon dioxide and climate impulse response functions for the computation of greenhouse gas metrics: a multi-model analysis. *Atmospheric Chemistry and Physics* 13(5), 2793-2825.

Jørgensen, B.B. and Revsbech, N.P. (1985) Diffusive boundary layers and the oxygen uptake of sediments and detritus. *Limnology and Oceanography* 30, 111-122.

Keir, R.S. (1980) The dissolution kinetics of biogenic calcium carbonates in seawater. *Geochimica et Cosmochimica Acta* 44(2), 241-252.

Keir, R.S. (1983) Variation in the carbonate reactivity of deep-sea sediments: determination from flux experiments. *Deep-Sea Research* 30, 279-296.

Kester, D.R. and Pytkowicz, R.M. (1969) Sodium, magnesium, and calcium sulfate ion-pairs in seawater at 25C. *Limnology and Oceanography* 14, 686-692.

Kirk, J.T.O. (1992) The nature and measurement of the light environment in the ocean. In Falkowski, P.G. and Woodhead, A.D. [Eds.] Primary Productivity and Biogeochemical Cycles in the Sea: New York, Springer Science+Business Media, p. 9-30.

Kitano, Y. and Hood, D.W. (1965) The influence of organic material on the polymorphic crystallization of calcium carbonate. *Geochimica et Cosmochimica Acta* 29(1), 29-41.

Krom, M.D. and Berner, R.A. (1980) Adsorption of phosphate in anoxic marine sediments. *Limnology and Oceanography* 25(5), 797-806.

Kump, L.R. (2013) The Role of Seafloor Hydrothermal Systems in the Evolution of Seawater Composition During the Phanerozoic. In Lowell, R.P., Seewald, J.S., Metaxas, A. and Perfit, M.R. [Eds.] Magma to Microbe: Modeling Hydrothermal Processes at Ocean Spreading Centers, Volume 178, https://doi.org/10.1029/178GM14

Langdon, C., Broecker, W.S., Hammond, D.E., Glenn, E., Fitzsimmons, K., Nelson, S.G., Peng, T.-H., Hajdas, I., and Bonani, G. (2003) Effect of elevated CO_2 on the community metabolism of an experimental coral reef. *Global Biogeochemical Cycles* 17(1)

Larkum, A.W.D., Koch, E.M.W., and Kühl, M. (2003) Diffusive boundary layers and photosynthesis of the epilithic algal community of coral reefs. *Marine Biology* 142: 1073-1082, https://doi.org/10.1007/s00227-003-1022-y.

Larson, T. E., Buswell, A. M., Ludwig, H. F., & Langelier, W. F. (1942). Calcium carbonate saturation index and alkalinity interpretations [with Discussion]. *Journal (American Water Works Association)* 34(11), 1667-1684.

Lazier, J.R.N. (2001) Deep convection. In Siedler, G., Church, J., and Gould, J. [Eds.] Ocean Circulation and Climate, Academic Press, p. 387-400.

Le Quéré, C., Andrew, R. M., Canadell, J. G., Sitch, S., Korsbakken, J. I., Peters, G. P., Manning, A. C., Boden, T. A., Tans, P. P., Houghton, R. A., Keeling, R. F., Alin, S., Andrews, O. D., Anthoni, P., Barbero, L., Bopp, L., Chevallier, F., Chini, L. P., Ciais, P., Currie, K., Delire, C., Doney, S. C., Friedlingstein, P., Gkritzalis, T., Harris, I., Hauck, J., Haverd, V., Hoppema, M., Klein Goldewijk, K., Jain, A. K., Kato, E., Körtzinger, A., Landschützer, P., Lefèvre, N., Lenton, A., Lienert, S., Lombardozzi, D., Melton, J. R., Metzl, N., Millero, F., Monteiro, P. M. S., Munro, D. R., Nabel, J. E. M. S., Nakaoka, S., O'Brien, K., Olsen, A., Omar, A. M., Ono, T., Pierrot, D., Poulter, B., Rödenbeck, C., Salisbury, J., Schuster, U., Schwinger, J., Séférian, R., Skjelvan, I., Stocker, B. D., Sutton, A. J., Takahashi, T., Tian, H., Tilbrook, B., van der Laan-Luijkx, I. T., van der Werf, G. R., Viovy, N., Walker, A. P., Wiltshire, A. J., and Zaehle, S. (2016) Global carbon budget 2016. *Earth System Science Data* 8, 605-649, https://doi.org/10.5194/essd-8-605-2016

Lebron, I., and Suarez, D.L. (1996) Calcite nucleation and precipitation kinetics as affected by dissolved organic matter at 25°C and pH > 7.5. *Geochimica et Cosmochimica Acta* 60(15), 2765-2776.

Lenton, T.M. and Britton, C. (2006) Enhanced carbonate and silicate weathering accelerates recovery from fossil fuel CO_2 perturbations. *Global Biogeochemical Cycles*, 20(3).

Lenton, T.M., Williamson, M.S., Edwards, N. R., Marsh, R., Price, A. R., Ridgwell, A. J., Shepherd, J. G., and Cox, S. J. (2006) Millennial timescale carbon cycle and climate change in an efficient Earth system model. *Climate Dynamics* 26(7-8), 687-711.

Levich, V. G. (1962) *Physicochemical Hydrodynamics*, Prentice-Hall.

Levitus, S., Conkright, M. E., Reid, J. L., Najjar, R. G. and Mantyla, A. (1993) Distribution of nitrate, phosphate and silicate in the world oceans. *Progress in Oceanography* 31(3), 245-273.

Liebig, J.V. and Playfair, L. (1840) Organic chemistry in its application to agriculture and physiology, London, Taylor and Walton, 418 pp.

Liss, P. S., and Merlivat, L. (1986) Air-sea gas exchange rates: Introduction and synthesis. In Buat-Ménard, P. [Ed.] The Role of Air-Sea Exchange in Geochemical Cycling: Dordrecht, D. Reidel, p. 113-129.

Liss, P. S., and Slater, P. G. (1974) Flux of gases across the air-sea interface. *Nature* 247, 181-184.

Lorke, A., Müller, B., Maerki, M. and Wüest, A. (2003) Breathing sediments: The control of diffusive transport across the 530 sediment-water interface by periodic boundary-layer turbulence. *Limnology and Oceanography* 48: 2077-2085, https://doi.org/10.4319/lo.2003.48.6.2077.

Lyman, J. (1958) Buffer Mechanism of Sea Water. University of California [PhD thesis].

Lynch-Stieglitz, J., Adkins, J. F., Curry, W. B., Dokken, T., Hall, I. R., Herguera, J. C., Hirschi, J. J.-M., Ivanova, E. V., Kissel, C., Marchal, O., Marchitto, T. M., McCave, I. N., McManus, J. F., Mulitza, S., Ninnemann, U., Peeters, F., Yu, E.-F., and Zahn, R. (2007) Atlantic Meridional Overturning Circulation during the Last Glacial Maximum. *Science* 316, 66-69.

Mackenzie, F. T., Bischoff, W. D., Bishop, F. C., Loijens, M., Schoonmaker, J., and Wollast, R. (1983) Mg-calcites: low temperature occurrence, solubility and solid-solution behavior. In Reeder, R. J. [Ed.] Carbonates: Mineralogy and Chemistry, Volume 11: Washington DC, Mineralogical Society of America, p. 97-143.

Mackenzie, F. T. and Lerman, A. (2006) Carbon in the Geobiosphere: - Earth's Outer Shell-. Springer Science & Business Media, Dordrecht, 402 pp., Dordrecht, Springer Science & Business Media.

Mackenzie, F. and Andersson, A. (2013) The Marine Carbon System and Ocean Acidification during Phanerozoic Time. *Geochemical Perspectives*, 1-227, https://doi.org/10.7185/geochempersp.2.1

Marshall, J., and Schott, F., 1999, Open-ocean convection: Observations, theory, and models. *Reviews of Geophysics* 37(1), 1-64.

McNeill, J. R. (2001) Something New Under the Sun: An Environmental History of the Twentieth-Century World, New York, W. W. Norton.

Meinshausen, M., Smith, S.J., Calvin, K., Daniel, J.S., Kainuma, M.L.T., Lamarque, J.F., Matsumoto, K., Montzka, S.A., Raper, S.C.B., Riahi, K., Thomson, A., Velders, G.J.M. and van Vuuren, D.P.P. (2011) The RCP greenhouse gas concentrations and their extensions from 1765 to 2300. *Climatic Change* 109, 213-241, https://doi.org/10.1007/s10584-011-0156-z

Mekik F. A., P. W. Loubere, and D. E. Archer, 2002 Organic carbon flux and organic carbon to calcite flux ratio recorded in deep-sea carbonates: Demonstration and a new proxy. *Global Biogeochemical Cycles* 16, https://doi.org/10.1029/2001GB001634.

Milkov, A. V. (2004) Global estimates of hydrate-bound gas in marine sediments: how much is really out there? *Earth-Science Reviews* 66(3-4), 183-197.

Millero, F. J. and Schreiber, D. R. (1982) Use of the ion pairing model to estimate activity coefficients of the ionic components of natural waters. *American Journal of Science* 282(9), 1508-1540.

Millero, F. J., and Pierrot, D. (1998) A chemical equilibrium model for natural waters. *Aquatic Geochemistry* 4(1), 153-199.

Millero, F.J. (1995) Thermodynamics of the carbon dioxide system in the oceans. *Geochimica et Cosmochimica Acta* 59, 661-677, https://doi.org/10.1016/0016-7037(94)00354-O

Millero, F., Huang, F., Zhu, X., Liu, X. and Zhang, J.-Z. (2001) Adsorption and desorption of phosphate on calcite and aragonite in seawater. *Aquatic Geochemistry* 7(1), 33-56.

Millero, F. J. (2013) Chemical Oceanography, Fourth Edition, Boca Raton, CRC Press - Taylor & Francis Group, 591 pp.

Morgan, O. M. and Maass, O. (1931) An investigation of the equilibria existing in gas-water systems forming electrolytes. *Canadian Journal of Research* 5, 162-199.

Morse, J.W. and Berner, R.A. (1972) Dissolution kinetics of calcium carbonate in sea water: I, A kinetic origin for the lysocline. *American Journal of Science* 272(9), 840-851.

Morse, J.W. (1974a) Dissolution kinetics of calcium carbonate in seawater: V. Effects of natural inhibitors and the position of the chemical lysocline. *American Journal of Science* 274, 638-647.

Morse, J. W. (1974b) Dissolution kinetics of calcium carbonate in sea water: III. A new method for the study of carbonate reaction kinetics: *American Journal of Science* 274(2), 97-107.

Morse, J.W. (1978) Dissolution kinetics of calcium carbonate in sea water: VI. The near-equilibrium dissolution kinetics of calcium carbonate-rich deep sea sediments. *American Journal of Science* 278(3): 344-353.

Morse, J. W., Kanel, J. D. and Harris, K. (1979) Dissolution kinetics of calcium carbonate in seawater: VII. The dissolution kinetics of synthetic aragonite and pteropod tests. *American Journal of Science* 279, 488-502.

Morse, J.W. and Mackenzie, F.T. (1990) Geochemistry of Sedimentary Carbonates. Elsevier, Amsterdam.

Morse, J. W., Andersson, A. J. and Mackenzie, F. T. (2006) Initial responses of carbonate-rich shelf sediments to rising atmospheric pCO_2 and "ocean acidification": Role of high Mg-calcites. *Geochimica et Cosmochimica Acta* 70(23), 5814-5830.

Mottl, M. J. and Wheat, C. G. (1994) Hydrothermal circulation through mid-ocean ridge flanks: Fluxes of heat and magnesium. *Geochimica et Cosmochimica Acta* 58(10), 2225-2237.

Mucci, A. (1983) The solubility of calcite and aragonite in seawater at various salinities, temperatures and one atmosphere total pressure. *American Journal of Science* 283, 780-799, http://doi.org/10.2475/ajs.283.7.780

Mucci, A. and Morse, J.W. (1983) The incorporation of Mg^{2+} and Sr^{2+} into calcite overgrowths: influences of growth rate and solution composition. *Geochimica et Cosmochimica Acta* 47(2), 217-233.

Mucci, A., Morse, J.W. and Kaminsky, M.S. (1985) Auger spectroscopy analysis of magnesian calcite overgroths precipitated from seawater and solutions of similar composition. *American Journal of Science* 285(4): 289-305.

Mucci, A. (1986) Growth kinetics and composition of magnesian calcite overgrowths precipitated from seawater: Quantitative influence of orthophosphate ions. *Geochimica et Cosmochimica Acta* 50(10): 2255-2265.

Mucci, A., and Morse, J. W. (1990) Chemistry of low-temperature abiotic calcites: Experimental studies on coprecipitation, stability, and fractionation. *Aquatic Sciences*, 3(2-3), 217-254.

Mulder, T., Hüneke, H., and Loon, A. J. V. (2011) Progress in Deep-Sea Sedimentology. In Hüneke, H., and Mulder, T. [Eds.] Deep-Sea Sediments: Amsterdam, Elsevier, p. 1-24.

Munhoven, G. (2007) Glacial–interglacial rain ratio changes: Implications for atmospheric CO_2 and ocean–sediment interaction. Deep Sea Research Part II: Topical Studies in Oceanography 54(5-7), 722-746, https://doi.org/10.1016/j.dsr2.2007.01.008

Murray, J. and Renard, A. F. (1891) Report on deep-sea deposits based on the specimens collected during the voyage of H.M.S. Chalenger in the years 1872 to 1876: Her Majesty's Stationery Office.

Nancollas, G. H., Kazmierczak, T. F., and Schuttringer, E. (1981) A controlled composition study of calcium carbonate crystal growth: The influence of scale inhibitors. *Corrosion* 37(2), 76-81.

Naviaux, J.D., Subhas, A.V., Rollins, N.E., Dong, S., Berelson, W.B. and Adkins, J.F. (2019). Temperature dependence of calcite dissolution kinetics in seawater. *Geochimica et Cosmochimica Acta* 246: 363-384, https://doi.org/10.1016/j.gca.2018.11.037

Negrete-García, G., Lovenduski, N.S., Hauri, C., Krumhardt, K.M. and Lauvset, S.K. (2019) Sudden emergence of a shallow aragonite saturation horizon in the Southern Ocean. Nature Climate Change 9, 313-317, https://doi.org/10.1038/s41558-019-0418-8

Oke, P. R. and England, M. H. (2003) Oceanic response to changes in the latitude of the Southern Hemisphere subpolar westerly winds. *Journal of Climate* 17, 1040-1054.

Orr, J.C., Fabry, V.J., Aumont, O., Bopp, L., Doney, S.C., Feely, R.A., Gnanadesikan, A., Gruber, N., Ishida, A., Joos, F., Key, R.M., Lindsay, K., Maier-Reimer, E., Matear, R., Monfray, P., Mouchet, A., Najjar, R.G., Plattner, G.K., Rodgers, K.B., Sabine, C.L., Sarmiento, J.L., Schlitzer, R., Slater, R.D., Totterdell, I.J., Weirig, M.F., Yamanaka, Y. and Yool, A. (2005) Anthropogenic ocean acidification over the twenty-first century and its impact on calcifying organisms. *Nature* 437, 681-686, https://doi.org/10.1038/nature04095

Orr, J.C., 2011, Recent and future changes in ocean carbonate chemistry. In Gattuso, J.-P. and Hansson, L. [Ed.] Ocean Acidification: Oxford, Oxford University Press, p. 41-66.

Passow, U. and Carlson, C.A. (2012) The biological pump in a high CO_2 world. *Marine Ecology Progress Series* 470, 249-271.

Passow, U., Ziervogel, K., Asper, V., and Diercks, A. (2012) Marine snow formation in the aftermath of the Deepwater Horizon oil spill in the Gulf of Mexico. *Environmental Research Letters* 7(3), https://doi.org/10.1088/1748-9326/7/3/035301

Pauling, L. (1970) General Chemistry, 3rd edition, New York, Dover Publications, 992 pp.

Peterson, L. C. and Prell, W. L. (1985) Carbonate dissolution in recent sediments of the Eastern Equatorial Indian Ocean: preservation patterns and carbonate loss above the lysocline. *Marine Geology* 64, 259-290.

Pitzer, K. S. (1973) Thermodynamics of electrolytes. I. Theoretical basis and general equations. *The Journal of Physical Chemistry* 77(2), 268-277.

Pitzer, K. S., and Kim, J. J. (1974) Thermodynamics of electrolytes. IV. Activity and osmotic coefficients for mixed electrolytes. *Journal of the American Chemical Society* 96(18), 5701-5707.

Pytkowicz, R. M., and Hawley, J. E. (1974) Bicarbonate and carbonate ion-pairs and a model of seawater at 25°C. *Limnology and Oceanography* 19, 223-234.

Reddy, M. M. (1977) Crystallization of calcium carbonate in the presence of trace concentrations of phosphorus-containing anions. *Journal of Crystal Growth* 41, 287-295.

Redfield, A. C. (1958) The biological control of chemical factors in the environment. *American Scientist* 46(3), 205-221.

Reeder, R. J. (1983) Crystal chemistry of the rhombohedral carbonates. In Reeder, R. J. [Ed.] Carbonates: Mineralogy and Chemistry: Washington DC, Mineralogical Society of America, p. 1-47.

Rhein, M., Kieke, D., Hüttl-Kabus, S., Roessler, A., Mertens, C., Meissner, R., Klein, B., Böning, C. W., and Yashayaev, I. (2011) Deep water formation, the subpolar gyre, and the meridional overturning circulation in the subpolar North Atlantic. *Deep Sea Research Part II: Topical Studies in Oceanography* 58(17-18), 1819-1832.

Riahi, K., Rao, S., Krey, V., Cho, C., Chirkov, V., Fischer, G., Kindermann, G., Nakicenovic, N. and Rafaj, P. (2011) RCP 8.5-A scenario of comparatively high greenhouse gas emissions. *Climatic Change* 109, 33-57, https://doi.org/10.1007/s10584-011-0149-y

Ridgwell, A. J. (2001) Glacial-Interglacial Perturbations in the Global Carbon Cycle, Ph.D. thesis: University of East Anglia, 146 p.

Ridgwell, A. and Zeebe, R. (2005) The role of the global carbonate cycle in the regulation and evolution of the Earth system. *Earth and Planetary Science Letters* 234(3-4), 299-315.

Ridgwell, A. and Hargreaves, J.C. (2007) Regulation of atmospheric CO_2 by deep-sea sediments in an Earth system model. *Global Biogeochemical Cycles* 21, https://doi.org/10.1029/2006GB002764

Rogner, H.-H. (1997) An assessment of world hydrocarbon resources. *Annual Review of Energy and the Environment* 22, 217-262.

Sabine, C. L., Feely, R. A., Gruber, N., Key, R. M., Lee, K., Bullister, J. L., Wanninkhof, R., Wong, C. S., Wallace, D. W. R., Tilbrook, B., Millero, F. J., Peng, T.-H., Kozyr, A., Ono, T., and Rios, A. F. (2004) The oceanic sink for anthropogenic CO_2. *Science* 305, 367-371.

Sandberg, P. A. (1983) An oscillating trend in Phanerozoic non-skeletal carbonate mineralogy. *Nature* 305, 19-22.

Santschi, P. H., Bower, P., Nyffeler, U. P., Azevedo, A. and Broecker, W. S. (1983) Estimates of the resistance to chemical transport posed by the deep-sea boundary layer. *Limnology and Oceanography* 28: 899-912, https://doi.org/10.4319/lo.1983.28.5.0899.

Santschi, P.H., Anderson, R.F., Fleisher, M.Q. and Bowles, W. (1991) Measurements of diffusive sublayer thicknesses in the ocean by alabaster dissolution, and their implications for the measurements of benthic fluxes. *Journal of Geophysical Research: Oceans* 96, 10641-10657, https://doi.org/10.1029/91JC00488

Sarmiento, J. L., Dunne, J., Gnanadesikan, A., Key, R. M., Matsumoto, K. and Slater, R. (2002) A new estimate of the $CaCO_3$ to organic carbon export ratio. *Global Biogeochemical Cycles* 16(4), 54-51-54-12.

Sarmiento, J.L. and Gruber, N. (2006) Ocean Biogeochemical Dynamics. Princeton University Press, Princeton, NJ.

Schlichting, H. (1979) Boundary Layer Theory. McGraw-Hill, New York.

Schlitzer, R. (2000) Electronic atlas of WOCE hydrographic and tracer data now available. *EOS, Transactions American Geophysical Union* 81(5), 45.

Scholle, P. A., Arthur, M. A., and Ekdale, A. A. (1983) Pelagic environment. In Scholle, P. A., Bebout, D. G., and Moore, C. H. [Eds.] Carbonate Depositional Environments, American Association of Petroleum Geologists, p. 708.

Schulte, S., and Bard, E. (2003) Past changes in biologically mediated dissolution of calcite above the chemical lysocline recorded in Indian Ocean sediments. *Quaternary Science Reviews* 22(15-17), 1757-1770.

Seiter, K., Hensen, C., Schröter, J. and Zabel, M. (2004). Organic carbon content in surface sediments - defining regional provinces. *Deep Sea Research Part I: Oceanographic Research Papers* 51(12), 2001-2026, https://doi.org/10.1016/j.dsr.2004.06.014

Shternina, E. B., and Frolova, E. V. (1952) The solubility of calcite in the presence of CO_2 and NaCl: Izv. sektor. fiz.-khim. anal., obschchei neorg. kim. *Akad. Nauk SSSR* 21, 271-287.

Sigman, D. M. and Boyle, E. A. (2000), Glacial/interglacial variations in atmospheric carbon dioxide. *Nature* 407, 859-869.

Sillén, L. G. (1967) The ocean as a chemical system. *Science* 156, 1189-1197.

Smayda, T. J. (1969) Some measurements of the sinking rate of fecal pellets. *Limnology and Oceanography* 14(4), 621-625.

Smith, S. V., and Buddemeier, R. W. (1992) Global change and coral reef ecosystems. *Annual Review of Ecology and Systematics* 23, 89-118.

Smith, S. V. and Gattuso, J.-P. (2011) Balancing the oceanic calcium carbonate cycle: Consequences of variable water column Ψ. *Aquatic Geochemistry* 17, 327-337

Smith, S.V., Mackenzie, F.T. (2016) The role of $CaCO_3$ reactions in the contemporary oceanic CO_2 cycle. *Aquatic Geochemistry* 22, 153-175.

Steinberger, N. and Hondzo, M. (1999) Diffusional mass transfer at sediment-water interface. *Journal of Environmental Engineering* 125, 192-200, https://doi.org/10.1061/(ASCE)0733-9372(1999)125:2(192)

Subhas, A.V., Rollins, N.E., Berelson, W.M., Dong, S., Erez, J. and Adkins, J.F. (2015) A novel determination of calcite dissolution kinetics in seawater. *Geochimica et Cosmochimica Acta* 170, 51-68.

Subhas, A.V., Rollins, N.E., Berelson, W.M., Erez, J., Ziveri, P., Langer, G. and Adkins, J.F. (2018) The dissolution behavior of biogenic calcites in seawater and a possible role for magnesium and organic carbon. *Marine Chemistry* 205, 100-112.

Sun, W., Jayaraman, S., Chen, W., Persson, K. A. and Ceder, G. (2015) Nucleation of metastable aragonite $CaCO_3$ in seawater. *Proceedings of the National Academy of Sciences of the U.S.A* 112(11): 3199-3204, https://doi.org/10.1073/pnas.1423898112

Svensson, U. and Dreybrodt, W. (1992) Dissolution kinetics of natural calcite minerals in CO_2-water systems approaching calcite equilibrium. *Chemical Geology* 100, 129-145.

Takahashi, T., Sutherland, S.C., Sweeney, C., Poisson, A., Metzl, N., Tilbrook, B., Bates, N., Wanninkhof, R., Feely, R.A., Sabine, C., Olafsson, J. and Nojiri Y. (2002) Global sea–air CO_2 flux based on climatological surface ocean pCO_2, and seasonal biological and temperature effects. *Deep Sea Research Part II: Topical Studies in Oceanography* 49(9-10), 1601-1622, https://doi.org/10.1016/S0967-0645(02)00003-6

Tans, P. P., Fung, I. Y., and Takahashi, T. (1990) Observational constraints on the global atmospheric CO_2 budget. *Science* 247, 1431-1438.

Tebo, B. M., and Emerson, S. (1986) Microbial manganese(II) oxidation in the marine environment: a quantitative study. *Biogeochemistry* 2(2), 149-161.

Tebo, B. M., Johnson, H. A., McCarthy, J. K., and Templeton, A. S. (2005) Geomicrobiology of manganese(II) oxidation. *Trends in Microbiology* 13(9), 421-428.

Terjesen, S. G., Erga, O., Thorsen, G., and Ve, A. (1961) Phase boundary processes as rate determining steps in reactions between solids and liquids: The inhibitory action of metal ions on the formation of calcium bicarbonate by the reaction of calcite with aqueous carbon dioxide. *Chemical Engineering Science* 14(1), 277-288.

Tschumi, T., Joos, F., Gehlen, M. and Heinze, C. (2011) Deep ocean ventilation, carbon isotopes, marine sedimentation and the deglacial CO_2 rise. *Climate of the Past* 7(3), 771-800, https://doi.org/10.5194/cp-7-771-2011

Turekian, K. K. (1976) Oceans, Upper Saddle River, New Jersey, Prentice-Hall, 149 pp.

Tyrrell, T., Shepherd, J. G. and Castle, S. (2007) The long-term legacy of fossil fuels. *Tellus B* 59(4), 664-672.

United Nations, Department of Economic and Social Affairs, Population Division (2017) World Population Prospects: The 2017 Revision, Key Findings and Advance Tables. Working Paper No. ESAPWP/248.

Van Cappellen, P. and Wang, Y. (1996) Cycling of iron and manganese in surface sediments; a general theory for the coupled transport and reaction of carbon, oxygen, nitrogen, sulfur, iron, and manganese. American Journal of Science 296(3), 197-243, https://doi.org/10.2475/ajs.296.3.197

van Vuuren, D.P., Edmonds, J., Kainuma, M., Riahi, K., Thomson, A., Hibbard, K., Hurtt, G.C., Kram, T., Krey, V., Lamarque, J.-F., Masui, T., Meinshausen, M., Nakicenovic, N., Smith, S.J. and Rose, S.K. (2011) The representative concentration pathways: an overview. *Climatic Change* 109, 5-31, https://doi.org/10.1007/s10584-011-0148-z

Villiers, S. D., and Nelson, B. K. (1999) Detection of low-temperature hydrothermal fluxes by seawater Mg and Ca anomalies. *Science* 285, 721-723.

Walker, J. C. G., and Kasting, J. F. (1992) Effects of fuel and forest conservation on future levels of atmospheric carbon dioxide. *Palaeogeography, Palaeoclimatology, Palaeoecology* 97(3), 151-189.

Walter, L.M. and Morse, J.W. (1985) The dissolution kinetics of shallow marine carbonates in seawater: A laboratory study. *Geochimica et Cosmochimica Acta* 49(7): 1503-1513.

Wanninkhof, R. (1992) Relationship between wind speed and gas exchange over the ocean. *Journal of Geophysical Research* 97(C5), 7373-7382.

Weiss, R. F. (1974) Carbon dioxide in water and seawater: the solubility of a non-ideal gas. *Marine Chemistry* 2, 203-215.

Weyl, P. K. (1958) The solution kinetics of calcite. *The Journal of Geology* 66(2), 163-176.

Weyl, P. K. (1961) The carbonate saturometer. *The Journal of Geology*, 69(1), 32-44.

Weyl, P. K. (1967) The solution behavior of carbonate minerals in sea water. *Studies in Tropical Oceanography* 5, 178-228.

Wilkinson, B. H., Owen, R. M., and Carroll, A. R. (1985) Submarine hydrothermal weathering, global eustasy, and carbonate polymorphism in Phanerozoic marine oolites. *Journal of Sedimentary Petrology* 55(2), 171-183.

Zeebe, R. E., and Wolf-Gladrow, D. (2001) CO_2 in Seawater: Equilibrium, Kinetics, Isotopes, Amsterdam, Elsevier Science, Elsevier Oceanography Series, 346 pp.

Preface to Chapter 2

The absorption, or uptake, of anthropogenic CO_2 by the oceans results in a decrease in pH and carbonate ion concentration, $[CO_3^{2-}]$; as a consequence, the saturation state of seawater with respect to $CaCO_3$ minerals (calcite, aragonite) falls, leading to a shallowing of their saturation depths and triggering an increase in their dissolution at the seafloor. Nearly one-third of the seabed is composed of $CaCO_3$-rich sediments (> 30% $CaCO_3$), and their dissolution is the ultimate short-term (millennia) marine sink of anthropogenic CO_2. Despite numerous past studies, much confusion and uncertainty still surround our understanding of factors that control the rates $CaCO_3$ dissolution at the deep seafloor. Results from *in situ* studies disagree with those of laboratory studies, most of which have been carried out under conditions, e.g., mineral suspensions, that are not representative of processes at the seafloor.

Herein, we report measurements of the dissolution rate of calcite, formed into synthetic sediment disks by mixing various amounts of this mineral with a purified montmorillonite. These disks were placed in a stirred-flow reactor and exposed to a range of saturation states and shear stress conditions to simulate conditions at the sediment-water interface. The dissolution rates, normalized to the interfacial area of the sediment disks, were linearly dependent on the undersaturation state of the experimental seawater solution and displayed a square-root dependence on the calcite content of the synthetic sediment, under both quiescent and stirred conditions. The rate of release of reaction products from the sediment increased with stirring rate, i.e., shear stress, until it became invariant at higher stirring rates. This latter result argues that calcite dissolution is transport (water-side) controlled for shear stress levels known to exist at the seafloor, which advises a simpler kinetic description of benthic calcite dissolution.

Chapter 2

Calcite dissolution kinetics at the sediment-water interface in natural seawater*

Olivier Sulpis[1], Claire Lix[1], Alfonso Mucci[1] and Bernard P. Boudreau[2]

[1]GEOTOP and Department of Earth and Planetary Sciences, McGill University, Montreal QC, Canada

[2]Department of Oceanography, Dalhousie University, Halifax NS, Canada

**Published in Marine Chemistry*, doi:10.1016/j.marchem.2017.06.005

Abstract

The absorption, or uptake, of anthropogenic CO_2 by the oceans results in a decrease in pH and carbonate ion concentration, $[CO_3^{2-}]$; as a consequence, the saturation state of seawater with respect to $CaCO_3$ minerals (calcite, aragonite) falls, leading to a shallowing of their saturation depths and triggering an increase in their dissolution at the seafloor. Nearly one-third of the seabed is composed of $CaCO_3$-rich sediments, and their dissolution is the ultimate marine sink of anthropogenic CO_2. Despite numerous past studies, much confusion and uncertainty still surround our understanding of the rates and kinetics of $CaCO_3$ dissolution at the deep seafloor. Results from in situ studies disagree with laboratory studies, most of which have been carried out under conditions, e.g., mineral suspensions, that are not representative of processes at the seafloor. Herein, we report measurements of the dissolution rate of calcite, formed into synthetic sediment disks by mixing various amounts of this mineral with montmorillonite. These disks were placed in a stirred-flow reactor and exposed to a range of saturation states and shear stress conditions to simulate conditions at the sediment-water interface. The dissolution rates, normalized to the interfacial area of the sediment disks, were linearly dependent on the undersaturation state of the experimental seawater solution and displayed a square-root dependence on the calcite content, under both quiescent and stirred conditions. The rate of release of reaction products from the sediment increased with stirring rate, i.e., shear stress, until it became invariant at higher stirring rates. This latter result argues that calcite dissolution is transport (water-side) controlled for shear

stress levels known to exist at the seafloor, which advises a simpler kinetic description of benthic calcite dissolution.

2.1 Introduction

In 2014, the global atmospheric CO_2 concentration first reached 400 ppm (Tans and Keeling, 2016), exceeding any recorded level for at least the past 800,000 years (Lüthi et al., 2008). Between 1959 and 2008, atmospheric CO_2 concentrations increased at only 43% of the rate of fossil fuel emissions, the rest being either dissolved in the oceans or taken up by the terrestrial reservoir (Le Quéré et al., 2009). The ocean is the largest reservoir of carbon dioxide on Earth and, thus, the largest sink for anthropogenic CO_2 (Gehlen et al., 2007). Consequently, oceanic uptake plays a major role in the regulation of the atmospheric CO_2 budget, mitigating climate change. Whereas it was estimated that ~26% of the anthropogenic CO_2 emitted to the atmosphere between 1960 and 2012 was absorbed by the ocean (Gattuso and Hansson, 2011; Sabine and Feely, 2007), the mean anthropogenic CO_2 uptake rate by the ocean increased significantly from 1.2 ± 0.5 Gt C yr^{-1} between 1960 and 1969 to 2.9 ± 0.5 Gt C yr^{-1} in 2012 (Le Quéré et al., 2014).

One of the consequences of massive CO_2 uptake in the ocean is ocean acidification, as absorbed anthropogenic CO_2 is lowering surface ocean water pH. At the end of this century, the pH of surface ocean waters is expected to drop by an average of 0.4 pH unit (Ciais et al., 2013), reaching values as low as those estimated in the surface waters of the Jurassic and Cretaceous oceans (Hönisch et al., 2012). Anthropogenic ocean acidification will perturb the oceanic $CaCO_3$ cycle, impeding biogenic calcification and promoting its dissolution (Delille et al., 2005; Feely et al., 2004). The dissolution of $CaCO_3$-rich sediments is the ultimate marine sink of anthropogenic CO_2 and, if anthropogenic emissions were to cease, would restore the pH of the oceans back to its pre-anthropogenic value on timescales on the order of 10 kyr (Archer, 2005).

The uptake of CO_2 induces $CaCO_3$ dissolution by lowering the carbonate ion concentration, $[CO_3^{2-}]$, and consequently, the saturation state of seawater with respect to calcium carbonate minerals:

$$\Omega = \frac{[Ca^{2+}][CO_3^{2-}]}{K_{sp}^{*}} \qquad \textbf{(2.1)}$$

where the square brackets indicate total concentrations in mol kg^{-1} of seawater and K_{sp}* is the stoichiometric solubility constant of the mineral of interest (calcite, aragonite, mol^2 kg^{-2} seawater) at ambient temperature, pressure and salinity (Millero, 1979; Mucci, 1983).

Whereas surface ocean waters are generally supersaturated with respect to calcite and aragonite, cold deep ocean waters are typically undersaturated with respect to both minerals, mainly because $CaCO_3$ solubility increases with increasing water depth (pressure) (Millero, 1979) and metabolic CO_2 accumulates as deep waters age. Anthropogenic CO_2 invasion in the deep-sea is dictated by the rate at which biologically-driven processes that sequester CO_2 in the surface waters transfer it to the deep ocean (biological pump, see Passow and Carlson (2012)) and the rate at which anthropogenic CO_2 absorbed by the surface ocean is advected to the deep ocean (physical/solubility pump). Thus, the acidification of the deep ocean lags behind that of the surface ocean. For instance, if today's rate of anthropogenic CO_2 emissions were doubled by the end of this century, Ridgwell and Hargreaves (2007) predict that it would take a thousand years before the deep ocean reached near-equilibrium with the atmospheric CO_2. The injection of anthropogenic CO_2 to the deep ocean results in a further decrease in CO_3^{2-} ion concentrations, which in turn reduces the saturation state of seawater (***equation 2.1***) and raises the depth at which the waters become undersaturated. When overlying waters are undersaturated, biogenic aragonite or calcite reaching the seafloor can dissolve. The degree of undersaturation ($1 - \Omega$) with respect to each mineral is the driving force behind this dissolution. As the calcite saturation depth ($\Omega_c = 1$) rises, the area of the seafloor covered by calcitic sediments and overlain by calcite-undersaturated seawater will increase, triggering additional dissolution. The present study aims to characterize the dissolution kinetics of calcite-bearing sediments or how fast the calcite-component of these sediments will dissolve in response to ocean acidification.

$CaCO_3$-rich sediments (>30 wt%), which constitute nearly a third of the ocean floor (Morse and Mackenzie, 1990), will ultimately serve to neutralize a large part of the anthropogenic CO_2 delivered to the deep ocean according to the overall reaction (Archer et al., 1998),

$$\boldsymbol{CaCO_3 + CO_{2\,(aq)} + H_2O \leftrightarrow 2HCO_3^- + Ca^{2+}} \qquad \textbf{(2.2)}$$

The time required for neutralization of the anthropogenic CO_2 is dependent on the CO_2 transfer rate from the surface ocean to the deep ocean, as well as benthic $CaCO_3$ dissolution kinetics (Boudreau, 2013; Caldeira and Wickett, 2003; Tyrrell, 2011).

The kinetics of calcite dissolution are often expressed by a simple empirical equation of the form:

$$\boldsymbol{r = k(1-\Omega_c)^n} \qquad \textbf{(2.3)}$$

where r is the dissolution rate normalized to the mass (mol g^{-1} yr^{-1}) or surface area (mol m^{-2} yr^{-1}) of the mineral, k is the dissolution rate constant (mol g^{-1} yr^{-1} or mol m^{-2} yr^{-1}), Ω_c is the saturation state of the solution with respect to calcite, see ***Eq. 2.1***, and n is the reaction order.

Rate constants (k) and reaction orders (n) derived from laboratory studies diverge widely. Keir (1980) derived a high reaction order (n = 4.5) to represent the dissolution rates of suspended biogenic and synthetic calcites in seawater. Likewise, Walter and Morse (1985) obtained a high order dependence (n = 3) from their study of synthetic calcite dissolution rates in seawater. However, several researchers have argued recently that calcite dissolution kinetics is linearly dependent (i.e., n = 1) on the seawater undersaturation (Boudreau, 2013; Hales and Emerson, 1997b). First-order calcite dissolution kinetics appear to be more consistent with results of *in situ* studies of $CaCO_3$ dissolution in the deep-sea (Hales and Emerson, 1996, 1997a,b), but diagenetic processes, such as metabolic CO_2 production and bioturbation, may significantly influence these *in situ* rate measurements.

Keir (1983) determined the dissolution rate of calcite in a stirred-flow reactor with (non-suspended) beds of synthetic and natural carbonate sediments. Although his calculated reaction order was nearly the same as found with previous kinetic experiments on suspended sediment (Keir, 1980), the dissolution rate constant was approximately two orders of magnitude lower. Keir (1983) proposed that the presence of a diffusive boundary layer (DBL) at the sediment-water interface (SWI) of his samples might explain the discrepancy in the experimental results.

The DBL is a thin layer of fluid between a solid (possibly porous) surface and a flowing bulk solution, within which molecular diffusion dominates over turbulent transport and whose thickness is determined by the hydrodynamic conditions (Schlichting, 1979). The DBL behaves as a region of mass-transfer resistance and, thus, may limit the dissolution at a solid-water interface (Boudreau and Guinasso, 1982; Dade, 1993; Jørgensen and Revsbech, 1985; Santschi et al., 1983; Steinberger and Hondzo, 1999).

When dealing with a single crystal or suspended grains, calcite dissolution can be broken up into several processes or steps taking place concurrently near the dissolving mineral grain, as described in Morse and Arvidson (2002). In such a scheme, one or more reactions occur at the grain surface, while reactants and products must be transported to or from the grain surface. The slowest of these steps determines the rate of the overall reaction, giving rise to the concept of transport versus reaction control.

The transport-reaction "geometry" for the sediment disks in our reactor or for sediments at the seafloor is more nuanced than that of a single crystal or grains in suspension, and the concept of control is treated differently (Boudreau and Guinasso, 1982). Whereas the dissolution reaction still occurs at solid surfaces, transport must move reactants within sediment pores and also across a DBL that exists on the water side of the disk or above the sediment-water interface (SWI). The dissolution reaction generates a concentration gradient that drives a flux of solute products through both the pores and across the DBL. The question of control shifts from consideration of kinetics of reaction at grain surfaces versus transport of solutes to/away from a crystal/grain to a comparison of rates of processes in the sediment versus transport on the water side of the SWI.

When dissolution of a disk or at seafloor is controlled by rates of the combined reaction and transport within the sediment, then "deep" solute gradients develop within the sediment, on a scale far greater than the thickness on the DBL; the DBL is typically about a millimeter thick for deep-sea conditions, but can be thinner (or thicker) in a reactor. Conversely, under this geometry, transport control refers not to the rate of diffusion (or perhaps advection) of solutes within the sediments, but to the rate of transfer across the DBL (Boudreau and Guinasso, 1982). This particular dichotomy is adopted because control by DBL transport will cause the reaction rate to be affected by benthic currents, whereas control by processes within the sediments will be impervious to such effects, baring resuspension or flow penetration. In this study, we will refer to transport and surface reaction limitations that take place within the sediment as "sediment-side control" and to diffusion limitation through the DBL above the bed as "water-side control". Note that dissolution controlled by water-side processes (DBL transport) are inherently linear, which would stand in contrast to past assertions of high-order nonlinearity for calcite dissolution.

Previous laboratory-based $CaCO_3$ dissolution studies have removed the role of water-side processes by re-suspending the sediment in seawater, in order to expose all the mineral surfaces

and minimize the boundary layer around each grain (Gehlen et al., 2005; Keir, 1980; Morse, 1978; Walter and Morse, 1985). Although these studies provide good insights on calcite dissolution kinetics in the water column (after normalization to the exposed surface area), they are not representative of benthic dissolution conditions (Boudreau, 2013). Whereas several research groups have demonstrated that calcite dissolution rates become (classically) transport-controlled for pH < 4 and low saturation states, i.e., $\Omega_c < 0.4$ (Berner and Morse, 1974; Morse and Arvidson, 2002; Sjöberg and Rickard, 1984), these conditions diverge widely from those encountered at the seafloor. In this study, we investigated the dissolution kinetics of a simulated, organic-free, and carbonate-rich sediment in natural seawater, held in a thermostated, stirred-flow reactor and subject to a range of undersaturations and shear stresses, all to simulate conditions more representative of the seafloor.

2.2 Materials and methods

2.2.1 Stirred-flow reactor

The experimental design depicted in ***Fig. 2.1*** is based on the principle of the stirred-flow reactor (Denbigh, 1944; Keir, 1980, 1983). Dissolution experiments were carried out in a water-jacketed reaction vessel held at 25.0 (± 0.1) °C and in which a synthetic sediment, including its low-density polyethylene (LDPE) mold, was immersed. Between 104 and 872 mL of the treated natural seawater (depending on the volume of the reactor and thickness of the sediment disk) were added to the reactor without disturbing the sediment surface.

The natural seawater used for our experiments was collected between 2013 and 2016 at 300 to 400 meters depth in the Gulf of St. Lawrence and stored in high-density polyethylene (HDPE) carboys. These waters originate from the northwestern Atlantic Ocean (Koutitonsky and Bugden, 1991). The practical salinities (S_P) of the seawater were between 34.55 and 34.79 at the time of sampling, as determined with a Seabird SBE-911 conductivity probe mounted on the sampling rosette. Aliquots stored in glass bottles revealed that the soluble reactive phosphate (SRP) concentrations at the time of sampling were between 1.94 and 2.24 µM, whereas dissolved organic carbon (DOC) concentrations were between 53 and 67 µM (Y. Gélinas, pers. comm.). Prior to use, the seawater was pre-equilibrated for several days in the presence of calcite powder (solid:solution ratio of 15g:1L) to scavenge SRP and DOC, both strong calcite dissolution and

precipitation inhibitors (Berner and Morse, 1974; Sjöberg, 1978), by adsorption onto the mineral surface. The slurry was then vacuum-filtered through a 0.45 μm Millipore polycarbonate filter and the seawater stored in Nalgene (LDPE or HDPE) bottles for several months. After that period, the SRP concentrations were between 1.48 and 1.67 μM.

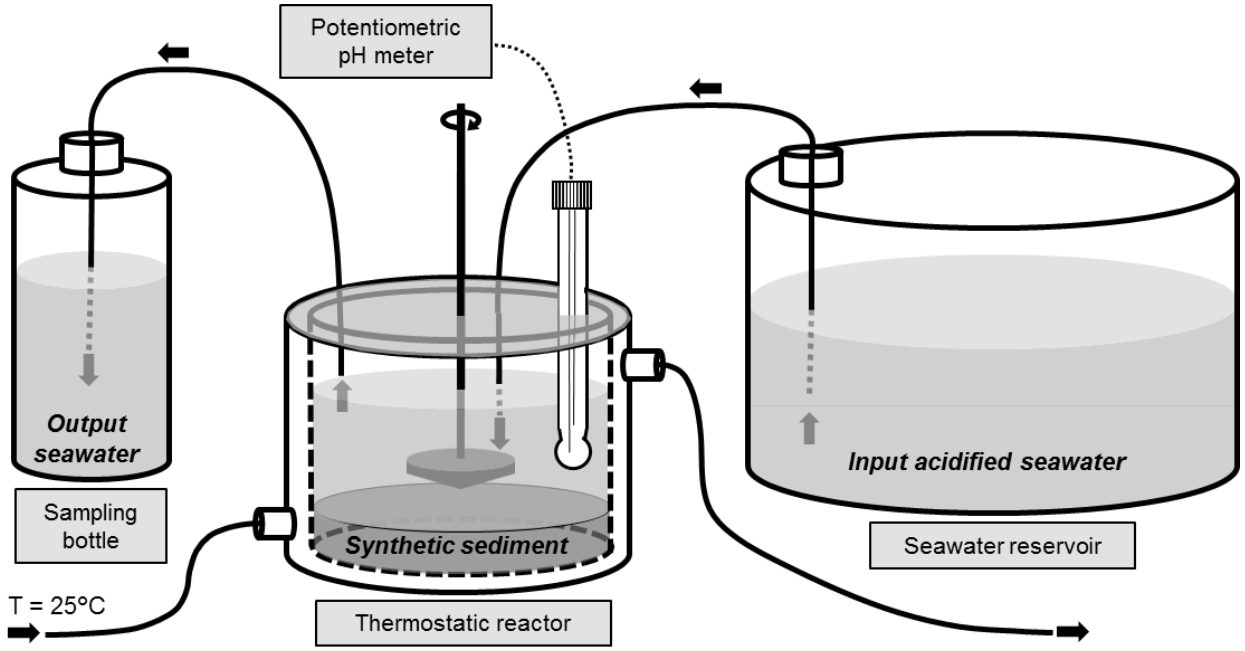

Fig. 2.1 | *Schematic representation of the experimental design.*

The calcite contained in the synthetic sediment, if exposed to a solution undersaturated with respect to calcite ($\Omega_c < 1$), should dissolve. In order to obtain an undersaturated solution, a fraction of the treated seawater was acidified by adding dilute hydrochloric acid (~1N) to reduce the total alkalinity (TA) from ~2300 μmol kg^{-1} to ~400 μmol kg^{-1} ("TA in" in ***Tables 2.1*** and ***2.2***) and Ω_c from ~4 to ~0.15. This treatment did not modify the original salinity of the seawater by more than 0.2% (relative). The acidified seawater was equilibrated with the ambient atmosphere (pCO_2 ~ 400 ppm) by bubbling laboratory air with an aquaria pump at a constant flow rate of ~1 mL s^{-1}. The air was pre-humidified, by bubbling it through a distilled water-filled, glass-washing bottle equipped with a fritted disk, to avoid evaporation and salinity variations of the seawater solutions. At room temperature (23 ± 1°C), it took approximately 24 hours to equilibrate the

solutions with the atmosphere, as determined from measurements of the pH_T (pH on the total hydrogen ion scale) and TA of the solution. This acidified seawater served as the input solution and was injected into the reactor, initially filled with calcite-equilibrated seawater ($\Omega_c = 1$), at a constant rate through a 0.51 mm inner diameter (ID) Tygon polyvinylchloride (PVC) tube, using a multi-channel peristaltic pump (Gilson's Minipuls^{TM} 3 Peristaltic Pump). The pumping rate was determined for each setting in each experiment by weighing the amount of solution pumped out of the reactor over a fixed period of time. To keep a constant volume of solution in the reactor, the solution was withdrawn from the reactor by the same pump through a 0.76 mm ID tube fixed at the surface of the solution. The batch reactor was capped by a PVC cover equipped with multiple openings for insertion of the stirrer, the solution input and output tubes, and a combination glass-reference pH electrode. The outer shell of the reactors was wrapped in opaque paper to avoid the proliferation of bacteria that otherwise developed at the surface of the sediment disk within a few weeks. A stirrer, whose design was inspired by the shear stress inducer described by Javadi and Khalili (2009), was used and driven by an overhead, variable-speed motor. In theory, the stirrer is designed to generate a uniform, bottom shear stress and consists of a rotating 3.5 cm diameter PVC cone held at the tip of a 13 cm long PVC shaft (***Fig. 2.1***). The diameter of the stirrer (3.5 cm) was, depending on the diameter of the reactor (between 6.5 and 8.5 cm), between 54 and 41% of the latter, respectively.

The evolution of the dissolution reaction was assessed by monitoring the pH_T of the experimental solution inside the reactor at a fixed acidified seawater pumping rate. Once a steady-state pH_T was achieved, an aliquot of the output solution was collected and analyzed to determine the steady-state TA, S_P and SRP concentration. The pumping rate was then increased and, consequently, the residence time of the solution in the reactor as well as the saturation state of the reactor solution decreased, triggering an increase of the calcite dissolution rate. Residence times of the input solution in the reactors varied between 8.2 and 603.1 hours, corresponding to input flow rates between 72.2 and 0.4 g hr^{-1}, respectively. The experiments were carried out over several weeks or months depending on the injection rate and the range of saturation states investigated. The sediment disks were replaced after no more than two months. Note that, in our experimental design, the saturation state of the bulk solution was not fixed and reached a steady state upon balancing the pumping rate of acidified seawater and the calcite dissolution rate.

2.2.2 Sediment preparation

The montmorillonite-calcite mixture was prepared by mixing 35 g of montmorillonite and 40 g of calcite powder (53 wt% calcite) into 100 mL of calcite-equilibrated seawater ($\Omega_c = 1$) under constant stirring and the homogeneous mixture laid out in the cut-out bottom of LDPE bottles to form uniform disks of various thicknesses and diameters. Disks containing 10, 30, 90 and 100 wt% calcite on a dry weight basis were also prepared following the same procedure.

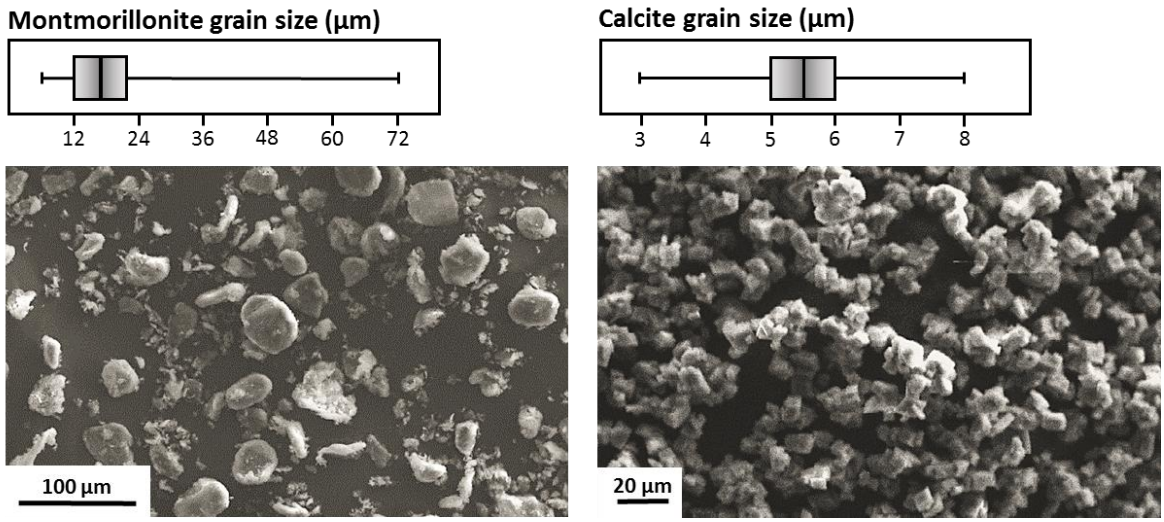

Fig. 2.2 | *Scanning electron microscope image of (left) montmorillonite and (right) calcite powder. Boxplots represent the distribution of grain size (diameter expressed in µm) of the montmorillonite powder for a sample of 100 grains, and of calcite powder for a sample of 150 grains. Each boxplot depicts the minimum and maximum measured grain sizes, the median value, and the first and third quartiles.*

ACS reagent-grade $CaCO_3$ powder was purchased from Baker® and an XRD analysis confirmed that it was pure calcite, although trace amounts of other polymorphs would have gone undetected if present at less than a few weight percent. The average length of the grains was estimated at 5.65 ± 0.92 µm from a sample of 150 grains examined in a scanning electron microscope (SEM). Based on the latter, and assuming that the shape of the grains is cubic, the geometric specific surface area of the calcite was estimated at 0.39 ± 0.23 $m^2\ g^{-1}$. The calcite powder and the rhombohedral shape of the grains can be seen in ***Fig. 2.2***. A highly purified montmorillonite clay (Mineral Colloid® BP) with specific gravity of 2.6 g cm^{-3}, purchased from Southern Clay Products Inc. USA, was used to make the simulated carbonate-rich sediment. The

main criteria used to assess the suitability of the synthetic sediment was the cohesion and stability of the mixture, especially at the sediment-seawater interface when the beaker was jiggled. The fresh disks were stored in calcite-equilibrated seawater and kept in the dark to avoid the proliferation of bacteria until used within a few days. Porosity was measured from weight loss upon drying at low temperature (~ 50°C). Sediment disks were placed in an oven for several weeks at a temperature ~ 50°C until porewater was completely evaporated. Based on the measured salinity of the seawater, the weight of salts precipitated during evaporation was computed and subtracted from the total weight of solids, to obtain the weight of dry sediments. Given an average solid density of 2.65, the volume of dry sediment was calculated. Dividing the volume of dry sediment by the volume of bulk (wet) sediment gave the porosity (Φ). For the simulated 53 wt% calcite sediment, Φ was estimated at 0.79 ± 0.01 (n = 5). Given the similar specific gravity of the calcite and montmorillonite powders (respectively 2.71 and 2.6 g cm^{-3}), the sediment disks porosity was, within the uncertainty of our determinations, independent of the calcite content. Freeze-drying of the wet 53 wt% calcite sediment yielded a similar primary porosity of 0.801 ± 0.002 (n = 4).

Dissolution experiments were also performed on cylindrical cores (4.9 to 7.2 cm in diameter, 3.5 to 6.5 cm thick) of Indiana limestone (see ILI (2007)) inserted tightly into the cut-out bottom of LDPE bottles so that only the flat surface of the disk was exposed to the solution. The limestone porosity was estimated at 0.144 using the Mercury Intrusion Porosimetry (MIP) technique (P. Selvadurai, pers. comm.). The grain size of Indiana limestone is usually quite variable, ranging from < 5 µm to > 300 µm and its macropores (i.e., features with diameter > 33 µm) are not interconnected (i.e., isolated; Ji et al. (2012)). Assuming that only the surface of the Indiana limestone is dissolving, it is possible to observe the dependence of the measured alkalinity flux on the stirring rate due to the diffusion through the DBL, regardless of potential variations of the diffusion depth, i.e., the maximum sediment depth over which the reactants and reaction products diffuse within the sediment.

2.2.3 Analytical methods

pH_T was measured inside the reactor with a Radiometer Analytical® GK2401C combination glass electrode connected to a Radiometer Analytical® PHM84 pH/millivolt-meter.

Prior to each measurement, the electrode was calibrated against three NIST-traceable buffer solutions: pH-4.00, pH-7.00 and pH-10.00 at 25°C. The pH values of these low ionic strength buffers are assigned under the infinite-dilution convention. The electrode response to these buffers was then least-squares fitted to obtain the Nernstian slope and measurements converted to the "total" hydrogen ion concentration scale (pH_T), defined under the constant ionic medium convention (Dickson, 1984), using a TRIS buffer solution with an assigned pH_T of 8.089 at S_P = 35 and 25°C.

TA was determined by potentiometric titration of the initial reservoir and steady-state solutions with a dilute hydrochloric acid solution (0.01N), using an automated Radiometer (TitraLab865®) titrator and a Red Rod® combination pH electrode (pHC2001). The dilute HCl titrant was calibrated prior, during, and after each titration session, using certified reference materials (CRM Batch #131 and #140) provided by Andrew Dickson (Scripps Institute of Oceanography) and a laboratory sub-standard of Lower St. Lawrence Estuary seawater (S_P = 34.41; TA = 2283 ± 3 μmol kg^{-1}). The reproducibility of the method was better than 0.5%. The uncertainties presented in this study for total alkalinity, as well as steady-state pH_T, were estimated based on multiple replicate measurements of each sample.

The change in calcium concentration brought by the dissolution of calcite was computed from the difference in TA between the input ("TA in") and the output ("TA out") solutions.

$$\Delta[\mathbf{Ca^{2+}}] = \frac{\Delta \mathbf{TA}}{\mathbf{2}} \qquad \textbf{(2.4)}$$

The salinity of the experimental solution was monitored regularly by potentiometric titration of an aliquot of the output solution with a $AgNO_3$ solution calibrated with IAPSO standard seawater. The measurements were performed with an automated Radiometer (TTT80) titrator, a silver electrode, and a mercuric sulfate reference electrode. The reproducibility was better than 0.2%.

The SRP concentration of the initial reservoir and steady-state solutions was determined spectrophotometrically using the technique developed by Murphy and Riley (1962) and described in Grasshoff et al. (1999). The absorbance of the phosphomolybdate reaction product was measured manually at 880 nm on a Hewlett-Packard Agilent 8453 UV-visible spectrophotometer using a 10-cm cell. The detection limit was 0.01 μM and the reproducibility was better than 0.5%.

Calibration curves were constructed by 4 successive dilutions of a 10 mM standard phosphate stock solution in a 0.7M NaCl solution to prevent salt effects and the corresponding R^2 values were always better than 0.999.

2.2.4 Analytical methods

At a given temperature, salinity and pressure, only two of the following four measurable carbonate-system parameters, i.e., TA, pH, pCO_2 and DIC, and the appropriate carbonic acid and boric acid dissociation constants are sufficient to estimate the speciation of dissolved inorganic carbon in solution. The Microsoft Excel version of CO2SYS (Pierrot et al., 2006), based on the original algorithm of Lewis and Wallace (1998), was used to calculate the initial reservoir and steady-state solution pCO_2, carbonate ion concentration and saturation state with respect to calcite (Ω_c) from the steady-state pH_T and TA. The uncertainties on Ω_c values reported in ***Tables 2.1*** and ***2.2*** were computed separately and included errors on the solubility constant. All calculations were carried out on the total hydrogen ion concentration scale, using the stoichiometric carbonic acid dissociation constants determined by Lueker et al. (2000), as recommended by Dickson et al. (2007) (see Orr et al. (2015)), the total boron concentration $[B]_T$ value from Uppström (1974), and the standard acidity constant of the HSO_4^- ion ($K(HSO_4)$) from Dickson (1990). The SRP, S_P, T, TA and pH_T were used as input parameters in CO2SYS.

2.2.5 Dissolution rate estimates

The dissolution rate r (mol m^{-2} yr^{-1}) was determined from the difference in the composition of the input and output solutions (ΔTA/2 or Δ[Ca]), according to:

$$\boldsymbol{r = \frac{m_{SW}\,\Delta TA}{2\,S\,\Delta t}} \qquad \textbf{(2.5)}$$

where m_{SW} is the mass of seawater present in the reactor, Δt is the residence time of the solution in the reactor (yr), as given by the volume of solution in the reactor divided by the pumping rate, and S is the surface area of the simulated sediment disk (interface surface area; ISA).

As shown in ***Tables 2.1*** and ***2.2***, although the steady-state experimental solutions have significantly lower total alkalinities than modern-day seawater at an equivalent salinity, dissolution

experiments were carried out over a range of undersaturations representative of deep-sea conditions, i.e., Ω_c between 1.0 and 0.6 (Dunne et al., 2012), and a few data points were obtained at higher degrees of undersaturation ($\Omega_c \sim 0.4$). The data were fitted to the logarithmic form of ***Eq. 2.3***, i.e., log(r) vs log(1-Ω_c), to estimate the dissolution rate constant (intercept) and the reaction order (slope). Given the nearly invariant calcium concentration in the deep ocean, and in our reactors, the degree of undersaturation, (1-Ω_c), can also be expressed as a difference between the carbonate ion concentration at equilibrium with $CaCO_3$, C_S, and the carbonate concentration in the overlying water, C_0 (Boudreau, 2013; Boudreau and Guinasso, 1982). Under this formalism, the dissolution rate, r, is related to the product of a concentration difference, ($C_S - C_0$), and an overall (or apparent) mass-transfer coefficient for the dissolved CO_3^{2-}, here referred to as k^*. As explained in Boudreau and Guinasso (1982), for linear dissolution kinetics, k^* has units of length per unit time and is a non-linear combination of both the sediment-side mass transfer coefficient (k_S) and the water-side mass transfer coefficient, β, calculated as the CO_3^{2-} diffusion coefficient divided by the thickness of the DBL (Boudreau, 2013), i.e.,

$$\boldsymbol{k^* = \frac{k_S \beta}{(k_S + \beta)}} \qquad \textbf{(2.6)}$$

We chose to use the Williamson-York bivariate, iterative, fitting method described in Cantrell (2008), based on the work of Williamson (1968) and York (1969), to fit our data to Eqn. (2.3). This method accounts for uncertainties in both the dissolution rate (r) and undersaturation state (1-Ω_c) (or in both k^* and ($C_S - C_0$), as discussed above), and minimizes the deviation between data points and the fitted line along both axes, rather than a standard least-squares fit that simply considers variations in the y-direction. For each fit, we report both the determination coefficient (R^2) and the goodness of the bivariate fit as defined in York et al. (2004) and Cantrell (2008), with its expected value being unity.

2.2.6 Shear-stress generation

Hydrodynamic conditions at the reactive surface of a non-porous media are commonly represented in the framework of the diffusive boundary-layer model (Boudreau and Jørgensen, 2001; Levich, 1962; Santschi et al., 1983; Schink and Guinasso, 1977). As noted above, the thickness of the DBL is influenced by hydrodynamic conditions or shear stress at the solid-solution

interface (Schlichting, 1979). Higher stirring speeds, generating high current velocities, such as those encountered on shallow carbonate platforms or near-shore environments and that usually exceed tens of centimeters per second, thin the DBL and increase the rate at which a solute (i.e., carbonate ions) can diffuse to the overlying waters, i.e., its mass transfer coefficient. Conversely, lower stirring speeds are representative of areas of the seafloor where the current velocities are slow, i.e., a few centimeters per second or less, such as abyssal plains, and generate a thick DBL.

Experimental reactor designs that yield a uniform bottom shear stress have been the subject of numerous studies, but have not been entirely satisfactory (Buchholtz-ten Brink et al., 1989; Khalili et al., 2008). Our shear-stress inducer device presumably generates a quasi-uniform bottom shear stress and consists of a right circular cone (cone radius of 1.75 cm, cone angle of 5°), rotating (stirring speed between 0 and 416 rpm) in a fixed cylindrical container, with a vertical gap between the SWI and the apex of the cone of approximatively 1.5 cm (Javadi and Khalili, 2009; Khalili et al., 2008). The bottom surface shear stress (τ), neglecting the vertical side wall, can be computed from the cone parameters and the equations of Javadi and Khalili (2009). Nevertheless, qualitative observations of the water flow in the reactor using a dye with a density similar to seawater reveal that the shear stress estimates derived from the equations of Javadi and Khalili (2009) underestimate the fluid velocity by at least one order of magnitude under our experimental conditions.

Sediment disk descriptions, experimental conditions, and dissolution rate measurement results, along with all their relative uncertainties, are reported in ***Table 2.1*** (sediment disks with 53 wt% calcite at various stirring speeds) and ***Table 2.2*** (sediment disks of various calcite content in both stirred and unstirred reactors). Salinity measurements of aliquots of the steady-state output solutions (S_P varied between 34.45 ± 0.04 and 36.88 ± 0.04) reveal that even after two months, evaporation was minimal and all calculations were carried out at the *in situ* salinity. During each phase of the experimental protocol, seawater was nearly in equilibrium with the atmosphere. pCO_2 values computed using CO2SYS from the steady-state S_P, TA, pH_T and [SRP] values of samples varied between 333 and 557 ppm.

Table 2.1 | *Description of dissolution experiments for synthetic sediments with 53 wt% of calcite, with the computed steady-state saturation states with respect to calcite and dissolution rates normalized to the interface surface area (ISA).*

stirring speed (rpm)	total sed. mass (g) (± 0.1)	sed. thickness (cm) (± 0.1)	ISA (cm^2) (± 5%)	res. time (hr) (± 0.1)	pH_T (± 0.003)	TA in ($\mu mol\ kg^{-1}$)	TA out ($\mu mol\ kg^{-1}$)	Ω_c	ISA-norm. dissolution rate ($mol\ m^{-2}\ yr^{-1}$)	[SRP] (µM) (± 0.5%)
0	108.3	2.0	39.6	71.7	7.569	454.6 *± 4.4*	758.3 *± 3.9*	0.64 *± 0.03*	1.4 *± 0.1*	4.3
0	71.9	1.3	39.6	38.5	7.583	520.1 *± 2.5*	696.8 *± 1.9*	0.61 *± 0.02*	1.5 *± 0.1*	0.8
0	62.3	1.6	28.3	22.3	7.506	520.1 *± 2.5*	629.5 *± 0.2*	0.46 *± 0.02*	1.3 *± 0.1*	1.3
0	62.3	1.6	28.3	18.1	7.494	555.0 *± 1.8*	644.6 *± 5.0*	0.47 *± 0.02*	1.3 *± 0.1*	-
0	278.2	5.1	39.6	28.6	7.502	357.2 *± 0.7*	529.6 *± 5.6*	0.38 *± 0.02*	1.1 *± 0.1*	0.8
0	132.8	2.5	38.3	27.9	7.510	575.3 *± 0.2*	810.2 *± 3.0*	0.61 *± 0.03*	1.7 *± 0.1*	0.6
0	132.8	2.5	38.3	27.9	7.555	575.3 *± 0.2*	773.7 *± 3.0*	0.64 *± 0.03*	1.5 *± 0.1*	0.6
0	132.8	2.5	38.3	27.9	7.540	575.3 *± 0.2*	739.2 *± 3.0*	0.59 *± 0.03*	1.2 *± 0.1*	0.6
0	132.8	2.5	38.3	17.3	7.522	585.0 *± 0.8*	660.3 *± 3.0*	0.50 *± 0.02*	0.9 *± 0.1*	0.9
0	132.8	2.5	38.3	17.3	7.522	585.0 *± 0.8*	673.3 *± 3.0*	0.51 *± 0.02*	1.1 *± 0.1*	0.9
0	132.8	2.5	38.3	13.2	7.548	585.0 *± 0.8*	669.6 *± 3.0*	0.54 *± 0.03*	1.3 *± 0.1*	1.1
0	132.8	2.4	38.5	603.1	7.655	581.6 *± 1.5*	913.0 *± 3.0*	0.93 *± 0.04*	0.1 *± 0.0*	2.3
0	132.8	2.4	38.5	384.5	7.644	574.7 *± 2.0*	827.0 *± 3.0*	0.82 *± 0.04*	0.1 *± 0.0*	1.9
0	132.8	2.4	38.5	233.3	7.642	574.7 *± 2.0*	792.0 *± 3.0*	0.78 *± 0.04*	0.2 *± 0.0*	1.4
39	132.4	2.4	39.6	464.9	7.661	581.6 *± 1.5*	943.1 *± 4.7*	0.97 *± 0.05*	0.2 *± 0.0*	2.7
39	132.4	2.4	39.6	296.4	7.647	574.7 *± 2.0*	854.1 *± 4.3*	0.85 *± 0.04*	0.3 *± 0.0*	1.9
39	132.4	2.4	39.6	179.8	7.644	574.7 *± 2.0*	832.8 *± 4.2*	0.82 *± 0.04*	0.4 *± 0.0*	1.4
39	132.4	2.4	39.6	75.5	7.641	574.7 *± 2.0*	982.4 *± 4.9*	0.97 *± 0.05*	1.6 *± 0.1*	1.2
50	132.4	2.4	39.6	66.7	7.636	1045.0 *± 4.2*	1062.4 *± 0.8*	1.05 *± 0.05*	0.1 *± 0.0*	-
74	112.1	2.0	39.6	131.0	7.588	454.6 *± 4.4*	873.0 *± 1.0*	0.77 *± 0.04*	1.0 *± 0.1*	2.3
74	112.1	2.0	39.6	103.1	7.569	454.6 *± 4.4*	874.0 *± 3.0*	0.75 *± 0.04*	1.3 *± 0.1*	2.2
74	115.6	2.1	39.6	74.9	7.592	454.6 *± 4.4*	866.6 *± 8.1*	0.78 *± 0.04*	1.7 *± 0.1*	-
74	115.6	2.1	39.6	66.1	7.593	454.6 *± 4.4*	788.6 *± 4.4*	0.71 *± 0.03*	1.6 *± 0.1*	3.7
74	108.3	2.0	39.6	193.3	7.617	454.6 *± 4.4*	903.1 *± 1.0*	0.85 *± 0.04*	0.7 *± 0.0*	2.6
74	108.3	2.0	39.6	145.3	7.598	454.6 *± 4.4*	866.7 *± 0.5*	0.79 *± 0.04*	0.9 *± 0.1*	-
74	108.2	1.1	72.4	278.7	7.640	454.6 *± 4.4*	933.5 *± 6.9*	0.92 *± 0.04*	0.9 *± 0.0*	2.0
74	108.2	1.1	72.4	196.0	7.623	454.6 *± 4.4*	837.9 *± 3.4*	0.80 *± 0.04*	1.0 *± 0.0*	1.1
74	98.2	1.0	72.4	166.6	7.605	454.6 *± 4.4*	815.3 *± 5.1*	0.74 *± 0.04*	1.1 *± 0.0*	1.4
74	120.7	2.2	39.6	26.3	7.613	520.1 *± 2.5*	730.8 *± 5.4*	0.67 *± 0.03*	2.4 *± 0.1*	0.8
74	98.2	1.0	72.4	79.2	7.666	520.1 *± 2.5*	729.0 *± 0.2*	0.74 *± 0.03*	1.4 *± 0.0*	0.9
74	206.8	3.8	39.6	21.2	7.532	520.1 *± 2.5*	758.3 *± 5.2*	0.59 *± 0.03*	2.7 *± 0.2*	1.6
74	120.7	2.2	39.6	23.4	7.576	555.0 *± 1.8*	746.8 *± 0.9*	0.64 *± 0.03*	2.5 *± 0.1*	-
74	627.9	11.4	39.6	41.6	7.626	357.2 *± 0.7*	736.7 *± 1.2*	0.70 *± 0.03*	3.6 *± 0.2*	2.2
96	108.3	2.0	39.6	89.0	7.577	454.6 *± 4.4*	845.0 *± 4.5*	0.73 *± 0.03*	1.4 *± 0.1*	1.8
96	278.2	5.1	39.6	29.2	7.579	357.2 *± 0.7*	832.9 *± 1.4*	0.72 *± 0.03*	3.0 *± 0.2*	0.8
96	205.8	3.7	39.6	22.6	7.617	357.2 *± 0.7*	690.7 *± 0.3*	0.64 *± 0.03*	3.3 *± 0.2*	0.8
96	205.8	3.7	39.6	22.7	7.585	357.2 *± 0.7*	699.7 *± 2.6*	0.61 *± 0.03*	3.4 *± 0.2*	0.8
96	480.7	8.8	39.6	29.7	7.614	357.2 *± 0.7*	651.1 *± 3.6*	0.60 *± 0.03*	3.2 *± 0.2*	2.0
96	104.9	1.9	39.6	8.8	7.517	397.4 *± 0.5*	553.4 *± 3.5*	0.42 *± 0.02*	6.0 *± 0.3*	6.3
96	97.5	1.8	39.6	10.0	7.532	397.4 *± 0.5*	555.1 *± 2.6*	0.43 *± 0.02*	5.6 *± 0.3*	6.8
96	92.8	1.7	39.6	8.2	7.507	397.4 *± 0.5*	513.6 *± 1.0*	0.37 *± 0.02*	9.3 *± 0.5*	4.7
229	132.4	2.4	39.6	75.8	7.646	989.9 *± 5.5*	1041.3 *± 5.2*	1.04 *± 0.05*	0.2 *± 0.0*	1.2
416	132.4	2.4	39.6	75.8	7.651	982.1 *± 1.1*	1025.7 *± 5.1*	1.04 *± 0.05*	0.2 *± 0.0*	1.2

Table 2.2 | *Description of dissolution experiments for synthetic sediments with various calcite contents, with the computed steady-state saturation states with respect to calcite and dissolution rates normalized to the interface surface area (ISA).*

calcite dry content (wt%)	total sed. mass (g) (± 0.1)	sed. thickness (cm) (± 0.1)	ISA (cm^2) (± 5%)	res. time (hr) (± 0.1)	pH_T (± 0.003)	TA in (µmol kg^{-1})	TA out (µmol kg^{-1})	Ω_c	ISA-norm. dissolution rate (mol m^{-2} yr^{-1})	[SRP] (µM) (± 0.5%)
Dissolution experiments carried out in unstirred reactors										
10	99.7	2.1	39.6	50.0	7.497	367.5 *± 0.3*	567.5 *± 0.2*	0.41 *± 0.02*	0.5 *± 0.0*	10.7
10	99.7	2.1	39.6	106.6	7.520	367.5 *± 0.3*	662.1 *± 1.0*	0.50 *± 0.01*	0.3 *± 0.0*	13.4
10	99.7	2.1	39.6	502.1	7.652	367.5 *± 0.3*	823.4 *± 2.9*	0.81 *± 0.04*	0.1 *± 0.0*	12.8
30	106.2	2.3	37.4	35.9	7.501	367.5 *± 0.3*	636.2 *± 2.5*	0.46 *± 0.02*	0.9 *± 0.1*	12.7
30	106.2	2.3	37.4	119.3	7.567	367.5 *± 0.3*	722.1 *± 2.1*	0.60 *± 0.03*	0.4 *± 0.0*	13.3
30	106.2	2.3	37.4	465.3	7.648	367.5 *± 0.3*	855.6 *± 3.5*	0.84 *± 0.04*	0.1 *± 0.0*	13.1
90	111.3	1.7	52.8	52.1	7.604	367.5 *± 0.3*	763.5 *± 0.7*	0.69 *± 0.03*	0.7 *± 0.0*	6.8
90	111.3	1.7	52.8	105.5	7.653	367.5 *± 0.3*	793.2 *± 2.6*	0.80 *± 0.04*	0.3 *± 0.0*	7.9
90	111.3	1.7	52.8	410.0	7.665	367.5 *± 0.3*	891.2 *± 3.9*	0.92 *± 0.04*	0.1 *± 0.0*	5.9
100	40.0	0.7	44.2	51.5	7.570	572.3 *± 0.2*	774.1 *± 1.0*	0.66 *± 0.03*	1.0 *± 0.1*	0.4
100	40.0	0.7	44.2	23.8	7.468	572.3 *± 0.2*	676.1 *± 3.0*	0.46 *± 0.02*	1.1 *± 0.1*	0.4
100	40.0	0.7	44.2	23.8	7.525	572.3 *± 0.2*	687.5 *± 0.9*	0.53 *± 0.03*	1.3 *± 0.1*	0.4
100	40.0	0.7	44.2	23.8	7.589	572.3 *± 0.2*	698.9 *± 0.9*	0.61 *± 0.03*	1.4 *± 0.1*	0.7
100	40.0	0.7	44.2	14.7	7.540	585.0 *± 0.8*	649.7 *± 1.9*	0.51 *± 0.02*	1.1 *± 0.1*	0.7
100	40.0	0.7	44.2	14.7	7.522	585.0 *± 0.8*	640.4 *± 1.5*	0.49 *± 0.02*	1.0 *± 0.0*	0.9
100	40.0	0.7	44.2	11.7	7.550	585.0 *± 0.8*	656.9 *± 1.1*	0.53 *± 0.03*	1.6 *± 0.1*	0.9
100	96.4	1.5	52.8	512.3	7.671	367.5 *± 0.3*	902.1 *± 2.4*	0.94 *± 0.04*	0.1 *± 0.0*	1.0
Dissolution experiments carried out in reactors stirred at a constant rate of 74 rpm										
10	99.0	2.1	39.6	212.3	7.683	319.0 *± 1.4*	861.0 *± 3.6*	0.91 *± 0.04*	0.8 *± 0.0*	12.4
10	99.0	2.1	39.6	164.1	7.631	319.0 *± 1.4*	803.9 *± 3.1*	0.76 *± 0.04*	0.9 *± 0.1*	13.6
10	98.7	2.1	39.6	54.0	7.584	486.7 *± 3.1*	790.1 *± 2.2*	0.68 *± 0.03*	1.8 *± 0.1*	15.1
10	98.7	2.1	39.6	26.4	7.591	486.7 *± 3.1*	690.9 *± 3.5*	0.59 *± 0.03*	2.4 *± 0.1*	16.4
30	106.5	2.3	37.4	164.6	7.659	319.0 *± 1.4*	855.4 *± 3.2*	0.86 *± 0.04*	1.0 *± 0.1*	10.8
30	106.5	2.3	37.4	143.3	7.647	319.0 *± 1.4*	804.5 *± 0.9*	0.79 *± 0.04*	1.1 *± 0.1*	11.2
30	109.1	2.3	37.4	50.4	7.584	486.7 *± 3.1*	786.2 *± 4.1*	0.68 *± 0.03*	1.9 *± 0.1*	11.6
30	109.1	2.3	37.4	22.3	7.580	486.7 *± 3.1*	685.0 *± 2.3*	0.58 *± 0.03*	2.8 *± 0.2*	12.4
90	140.6	2.2	52.8	260.5	7.677	319.0 *± 1.4*	853.1 *± 0.7*	0.90 *± 0.04*	0.7 *± 0.0*	3.2
90	140.6	2.2	52.8	147.4	7.659	319.0 *± 1.4*	833.4 *± 1.4*	0.85 *± 0.04*	1.2 *± 0.1*	3.6
90	147.8	2.2	52.8	49.9	7.631	486.7 *± 3.1*	785.1 *± 1.7*	0.75 *± 0.04*	2.1 *± 0.1*	5.2
90	147.8	2.2	52.8	22.9	7.648	486.7 *± 3.1*	713.3 *± 0.8*	0.70 *± 0.03*	3.5 *± 0.2*	4.8

2.3 Results

2.3.1 Quiescent conditions

We performed a number of experiments without stirring (rotation). If these are controlled by diffusion in the water column, then the rate should be linear. A bivariate linear fit to the data, without forcing the intercept through origin (red line in ***Fig. 2.3***), yields

$$r_0 = (3.5 \pm 1.0 \text{ mol m}^{-2} \text{ yr}^{-1})\,(1 - \Omega_c) - 0.4 \pm 0.4 \text{ mol m}^{-2} \text{ yr}^{-1} \quad \textbf{(2.7a)}$$

$$r_0 = (102.4 \pm 28.6 \text{ m yr}^{-1})\,(C_S - C_0) - 0.7 \pm 0.5 \text{ mol m}^{-2} \text{ yr}^{-1} \quad \textbf{(2.7b)}$$

where r_0 is the ISA-normalized dissolution rate under water-side control, where the limiting step is diffusion in the water column. ***Eq. 2.7a*** reports the dissolution rate law in terms of undersaturation state with respect to calcite and ***Eq. 2.7b*** is the fit with respect to the deviation of $[CO_3^{2-}]$ from equilibrium ($C_S - C_0$), as explained in ***section 2.5***. The goodness of the linear fit (Cantrell, 2008; York et al., 2004) was 0.44 for ***Eq. 2.7a*** and 0.50 for ***2.7b***, whereas the R^2 value was estimated to be 0.47 for ***Eq. 2.7a*** and 0.48 for ***2.7b***, which reflect the limited data at our disposal.

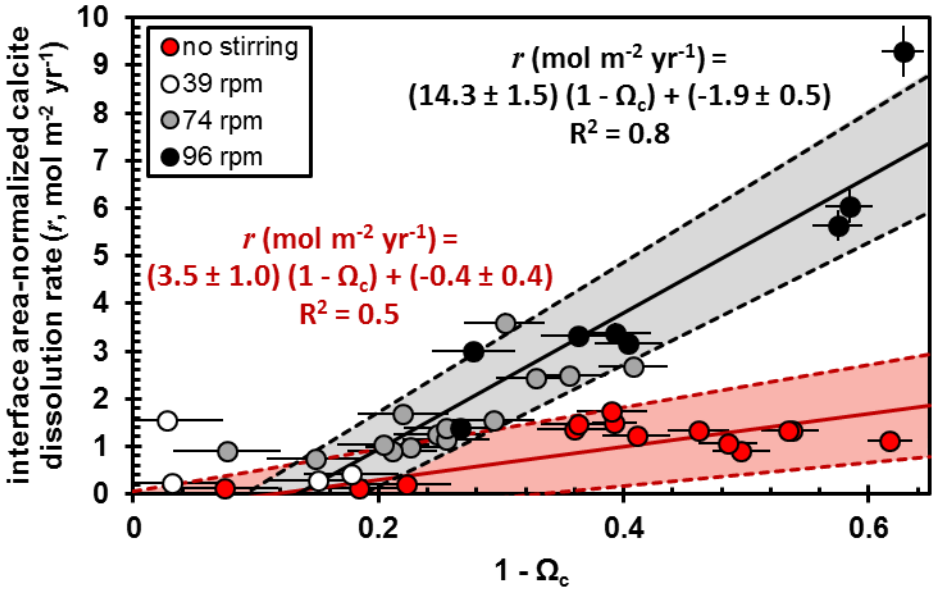

Fig. 2.3 | *Steady-state ISA-normalized calcite dissolution rate as a function of the steady-state undersaturation state ($1 - \Omega_c$). The color of each point represents the stirring speed used during the dissolution experiments. Uncertainties are represented by error bars on both the saturation state and the dissolution rate. The red and the black solid lines are, respectively, the linear bivariate fit to the experimental dissolution data obtained in unstirred (**Eq. 2.7a**) and stirred reactors (**Eq. 2.8b**), and the dashed lines describe the standard errors for each model.*

Figure 2.4 displays sediment dissolution rates as a function of the undersaturation state of seawater with respect to calcite, in unstirred and stirred (74 rpm) reactors, for different relative calcite contents. Linear regressions to the rate data for each calcite content were applied to estimate their rate constants as a function of the undersaturation. As indicated in ***Fig. 2.5***, the ISA-normalized dissolution rate constant determined under quiescent conditions increases slowly with the calcite content and reaches a plateau for the highest calcite contents (90 and 100 wt%). A

standard least-squares regression of the calcite dissolution rate constant (k) to the calcite weight fraction in a dry sediment (B) yields a square-root dependence of 0.54 ± 0.17, with a correlation coefficient $R^2 = 0.78$. This relationship is in excellent agreement with the prediction of Boudreau and Guinasso (1982), Boudreau (2013) and Keir (1982) that, when calcite is the single calcium carbonate mineral present in a sediment, the dissolution rate is proportional to the square root of the reactive surface area, assuming that the reactive surface area of calcite increases linearly with the calcite content.

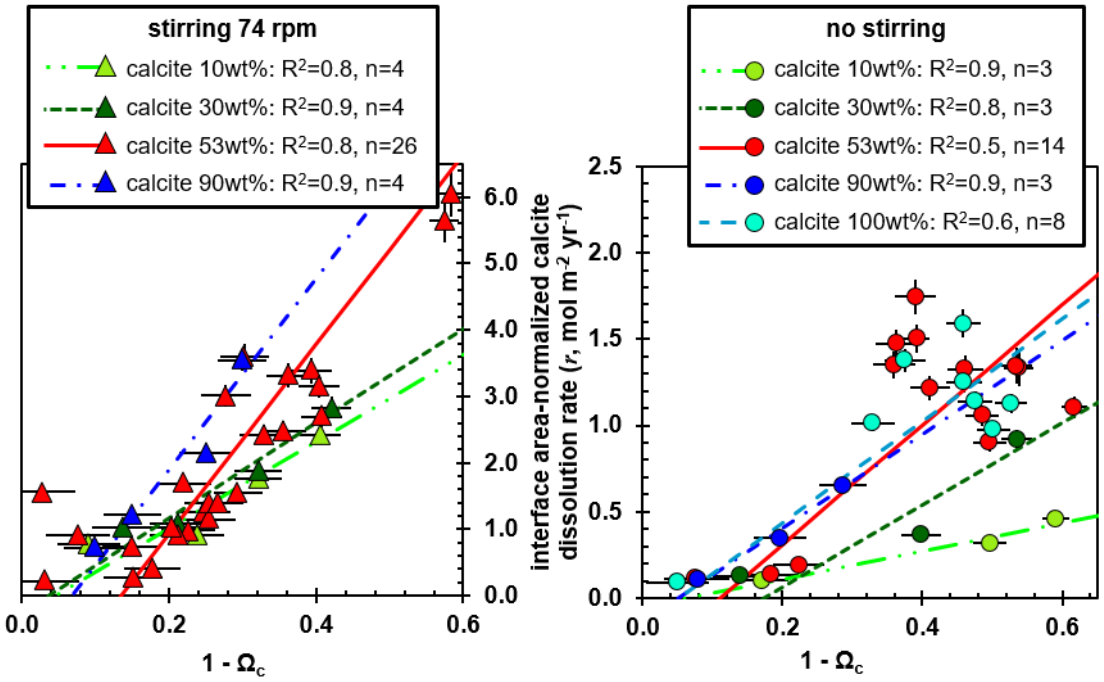

Fig. 2.4 | *ISA-normalized calcite dissolution rates as a function of the undersaturation state. The color of the data points represents the calcite content and the lines are the linear bivariate fits for each of the calcite contents. The diagram on the left represents the dissolution rates for experiments in a reactor stirred at a constant rate of 74 rpm (i.e., sediment-side controlled), whereas the diagram on the right displays the results obtained for sediment disks under quiescent conditions (i.e., water-side transport-controlled). The slopes of the lines represent the dissolution rate constant (k) for each calcite content, and are displayed, along with their uncertainties, in* ***Fig. 2.5****.*

2.3.2 Stirred conditions

In the discussion that follows, we neglect irregularities at the surface of our synthetic sediment disks (millimetre-scale and smaller), assume that a continuous and uniform DBL is present above the SWI (which varied in thickness with rotation), all which we recognize as potentially inaccurate, and that fluid movement within the pores (< 15 µm) of sediment is through molecular diffusion. In defense of these assumptions, surface irregularities on a scale smaller than the viscous sublayer (about 1 cm in the deep-sea) will not seriously affect mass transfer. In addition, the synthetic sediment made with montmorillonite should have permeabilities that are so low as to prevent any appreciable water flow (Boudreau, 1997), and what remains is molecular diffusion.

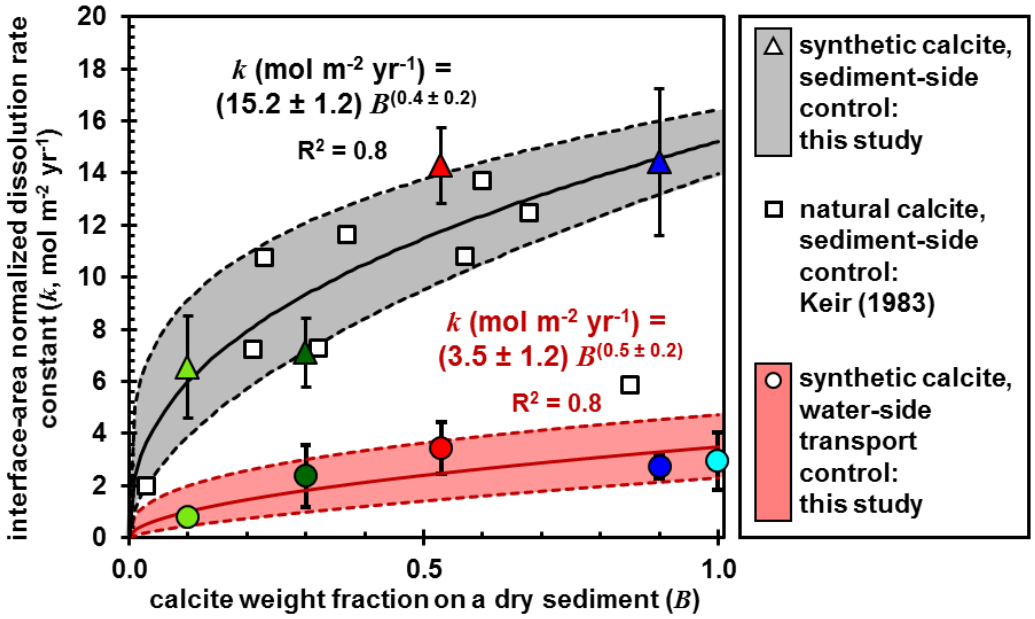

Fig. 2.5 | *The apparent ISA-normalized rate constants (k, with error bars) as a function of the calcite content (B) of the sediment disks. The circles are rate constants from experiments carried out under quiescent conditions and the triangles are rate constants from experiments in stirred (74 rpm) reactors. The solid lines are standard power regression models and their equations are displayed above each data group with uncertainties, represented by the dashed lines, on both the slope and the order of dependence on the calcite weight fraction. The white squares are dissolution rate constants derived from experiments carried out by Keir (1983) on natural deep-sea calcitic sediments.*

Figure 2.6 shows the dependence of the dissolution rates of Indiana limestone on the stirring rate. Interface area-normalized (ISA-normalized) calcite dissolution rates of Indiana limestone disks increased from 1.1 ± 0.1 to 5.4 ± 0.6 mol m^{-2} yr^{-1} as the stirring rate was increased from 0 and 53 rpm and as Ω_c rose from 0.23 ± 0.04 to 0.38 ± 0.03. At higher stirring rates (> 53 rpm), the ISA-normalized rates did not vary significantly, nor did the saturation state of the bulk solution. Thus, we conclude that the Indiana limestone dissolution rate is controlled by mass transport through the DBL above the bed for stirring speeds ≤ 53 rpm. Above this value, the dissolution regime shifts from a water-side transport control to a sediment-side control, when the DBL above the sediment bed has been thinned enough that k_S, the sediment-side control term, becomes smaller than β (see De Baere et al. (2016)), as determined by ***equation 2.6***.

Results of the calcite dissolution kinetic experiments with sediment disks containing 53 wt% calcite can be regrouped into 4 distinct sets based on the stirring rates investigated: 0, 39, 74 and 96 rpm. Like the Indiana limestone experiments, the ISA-normalized calcite dissolution rate from the sediment disks increased as the stirring rate was increased from 0 and 74 rpm, but, as shown in ***Fig. 2.3***, became invariant between 74 and 96 rpm. Assuming those results that exhibited stirring-rate dependence were sediment-side (transport) controlled, then the dissolution rate should be linearly proportional to the undersaturation state of seawater with respect to calcite, as implied by Fick's first law of diffusion.

A total of 43 dissolution experiments on sediment disks containing 53 wt% calcite were carried out at 25°C and ambient atmospheric pressure. The dissolution kinetics were investigated over a large range of saturation states with respect to calcite, from highly undersaturated (Ω_c = 0.37 ± 0.02) to slightly supersaturated (Ω_c = 1.05 ± 0.05) solutions. The best fits (black line on ***Fig. 2.3***) to the experimental dissolution measurements carried out under stirred conditions (39, 74 and 96 rpm) yield:

$$\boldsymbol{r = (10.8 \pm 1.4\ mol\ m^{-2}\ yr^{-1})\ (1 - \Omega_c)^{1.27 \pm 0.22}} \quad \textbf{(2.8a)}$$

$$\boldsymbol{r = (14.3 \pm 1.5\ mol\ m^{-2}\ yr^{-1})\ (1 - \Omega_c) - 1.9 \pm 0.5\ mol\ m^{-2}\ yr^{-1}} \quad \textbf{(2.8b)}$$

$$\boldsymbol{r = (326.9 \pm 39.5\ m\ yr^{-1})\ (C_S - C_0) - 1.7 \pm 0.5\ mol\ m^{-2}\ yr^{-1}} \quad \textbf{(2.8c)}$$

The goodness of the fit was 1.01 for ***Eq. 2.8a***, 1.16 for ***Eq. 2.8b*** and 1.15 for ***Eq. 2.8c***, whereas the R^2 values were, respectively, 0.51, 0.76 and 0.77; hence, a linear model properly

describes the data, and the dissolution kinetics, under our experimental conditions, are well represented by a law that does not go through origin.

The ISA-normalized rate dependence on $(1 - \Omega_c)$ is nearly linear, as reported in ***Eq. 2.8a***. As explained in Boudreau (2013), setting an intercept through the origin introduces a statistically biased restriction, as this intercept is part of the overall experimental uncertainty. As discussed later in this paper, deviations of the intercept from the origin can be explained by the contribution of parallel reactions. The rate constant (k) in ***Eq. 2.8b*** is about 4 times larger than the water-side transport-controlled rate constant from ***Eq. 2.7a*** determined under quiescent conditions (unstirred reactors). As noted previously, there is no significant variation of the measured dissolution rates at stirring rates between 74 and 96 rpm; consequently, the dissolution rate is believed to be controlled by processes at and below the SWI, i.e., sediment-side control (Boudreau, 2013; Boudreau and Guinasso, 1982) at these stirring rates.

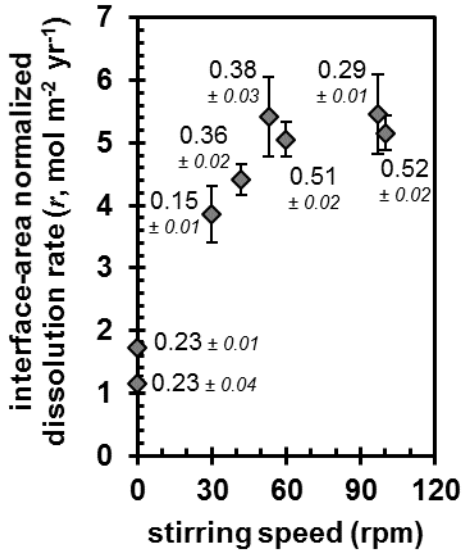

Fig. 2.6 | *Indiana limestone calcite dissolution rates as a function of the stirring speed. The labels indicate the measured steady-state saturation state with respect to calcite (Ωc) in the bulk seawater for each experiment.*

Finally, the dissolution rate constants derived from sediment disks of various calcite contents under the sediment-side control regime, overlain by seawater stirred at 74 rpm, display an order of dependence on the calcite weight fraction that is not statistically different than 0.5, in accordance with the theoretical value derived by Boudreau and Guinasso (1982), Keir (1982), and Boudreau (2013). A comparison of our results with those of Keir (1983), obtained from the dissolution of natural sediments (mostly foraminifera) in stirred reactors, as reanalyzed by

Boudreau (2013), reveals that these two datasets are in excellent agreement (***Fig. 2.5***). Thus, although we plan to investigate it experimentally in the near future, the comparison implies that synthetic and natural calcite sediments display similar dissolution kinetic behaviours.

2.4 Discussion

2.4.1 Linear dissolution kinetics

Most laboratory-derived calcite dissolution rate data published to date (Cubillas et al., 2005; Gehlen et al., 2005; Keir, 1980, 1983; Morse, 1978; Subhas et al., 2015; Teng, 2004; Walter and Morse, 1985; Xu et al., 2012) display a non-linear dependence on the saturation state of the solution, regardless of their experimental design or measurement techniques. Conversely, several researchers have attempted to demonstrate a linear relationship between calcite dissolution rate and saturation state in seawater (Boudreau, 2013; Emerson and Bender, 1981; Hales and Emerson, 1997b). Hales and Emerson (1997b) re-evaluated Keir (1980)'s original experimental data for suspended sediment and found evidence that calcite dissolution rates may be linearly correlated to the saturation state of the seawater solution. They reached this conclusion after assuming that the saturation states of the experimental solutions were underestimated, more specifically that the calcite stoichiometric solubility product used to calculate the saturation state was erroneous and overestimated. Likewise, after a re-examination of Keir (1983)'s original experimental data with natural carbonate sediments, Boudreau (2013) concluded that linear $CaCO_3$ dissolution kinetics were inherent to the data, even without having to call upon a revised solubility constant.

Previous studies have advanced that the calcite dissolution reaction is reaction-controlled near equilibrium, $\Omega \rightarrow 1$, and tends to be transport-controlled far from equilibrium, $\Omega << 1$ (e.g., Morse and Arvidson, 2002; Sjöberg and Rickard, 1984). We have found that calcite dissolution rates (***Figs 2.3*** and ***2.4***) are linear, regardless of the controlling regime (water-side versus sediment-side), which contradicts the conclusions of these past studies. Furthermore, the observed dependence of the rate on stirring below 74 rpm indicates water-side control by hydrodynamic conditions below this stirring limit, regardless of the degree of undersaturation, a point that also contradicts past conclusions. Whereas it is difficult to translate our stirring rates to oceanic conditions, we firmly believe that the fits that we report, based on linear relationships between the dissolution rate and the undersaturation state, are more representative of the processes occurring

at the seafloor. Simple dye tracer experiments in our experimental vessels (not shown) reveal that water velocities are faster at all our non-null stirring rates than velocities estimated for the deep-sea, i.e., typically 4 cm s^{-1} (Armi, 1977).

All our linear fits contain a positive intercept on the x-axis, i.e., over-estimated undersaturation, and thus a negative y-axis intercept, i.e., a lower than expected rate error (see ***Figs 2.3*** and ***2.4***). Two explanations for lower apparent solubility on the time scales of our experiment come to mind. One could be elevated pore-water SRP concentrations. SRP is released by desorption from the montmorillonite. SRP is known to be a strong inhibitor of both calcite dissolution and precipitation (Berner and Morse, 1974; Burton and Walter, 1990; Morse, 1974a; Mucci, 1986; Sjöberg, 1978) due to its adsorption at high-energy sites on the calcite mineral surface (Alkattan et al., 2002; Millero et al., 2001; Svensson and Dreybrodt, 1992). These past studies have attributed this effect to a lower rate constant for the dissolution reaction, but a lower rate can also be affected by a smaller apparent solubility (on the experimental time scale). Another possibility are effects from the concurrent precipitation from seawater of a slightly less soluble form of $CaCO_3$ containing up to 4 mole% $MgCO_3$ (Bischoff et al., 1987), during dissolution.

In situ pore-waters microelectrode profiles of conductivity, oxygen and pH have shown calcite dissolution to occur over the first cm in deep-sea sediments overlain by undersaturated seawater (Archer et al., 1989a; Archer et al., 1989b; Oxburgh and Broecker, 1993), which suggests that dissolution does not occur primarily at the sediment-seawater interface, as implied by our results. Two factors may, however, account for these observations. The first is that real deep-sea sediments contain labile organic matter that is subject to microbial oxidation, which produces CO_2. The metabolic CO_2 can lower the saturation state of porewaters and trigger $CaCO_3$ dissolution (Emerson and Bender, 1981). In the interpretation of his results, Keir (1983) proposed that his observation of carbonate dissolution in the presence of calcite-supersaturated overlying waters could only be due to metabolic forcing or the presence and dissolution of adventitious aragonite, for which the overlying waters would have been undersaturated.

The other possibility is that the observed deeper dissolution is partly an artifact of early micro-electrode measurements. Glud et al. (1994) showed that early micro-electrodes, inserted into sediments from the water-side of the SWI, measured deeper O_2 penetration in sediments than electrodes inserted from below and moved upward. The micro-electrodes inserted from the water-

side caused overlying water to penetrate the sediment to some extent; if this afflicted the Archer et al. (1989a, 1989b) study, then undersaturated overlying waters may have been introduced into the sediment, leading to dissolution at depths where no dissolution was occurring previous to electrode insertion. Our experiments show that $CaCO_3$ dissolution responds rapidly to changes in saturation state, so that this artifact is a possibility.

Finally, to investigate if a gradient in the calcite content developed within the sediment disks following the dissolution experiments, the inorganic carbon content of our un-reacted and reacted synthetic sediment disks was determined coulometrically (reproducibility of 0.5%, detection limit of 0.15%) at ~2 mm resolution (following freezing of the disks and shaving with a scalpel). Whereas the calcite content within the un-reacted simulated sediment varied slightly (5.9 ± 0.1% C or 49.2 ± 0.8% $CaCO_3$), no discernable gradient developed within the reacted sediments. This observation is not surprising because one would not expect a detectable concentration gradient to develop, even if restricted to the top first cm, unless dissolution had been carried out for several months at the lowest undersaturation ($\Omega_C \sim 0.4$) investigated.

2.4.2 Sediment-side dissolution rate constants

Calcite dissolution rate constants determined in the laboratory in seawater can be several orders of magnitude higher than results of *in situ* measurements (Green and Aller, 2001; Hales and Emerson, 1997a). Calcite in deep-sea sediments is mostly biogenic (Honjo et al., 1982; Sun and Turchyn, 2014) and may be less reactive than the reagent-grade calcite used in laboratory studies, although natural calcitic sediments dissolved in laboratory experiments yielded rate constants similar to those of synthetic calcite (Keir, 1980, 1983; Walter and Morse, 1985). It is interesting to note that lower rate constants are consistently determined for biogenic carbonates than for synthetic calcite. This discrepancy has been ascribed to the different approaches used to determine the surface area of the solids and the normalization of the rates (Lüttge, 2005; Lüttge et al., 2013). As noted by Colombani (2016), there is no consensus about the magnitude of the calcite dissolution rate constant due to the extremely diverse conditions under which dissolution experiments have been carried out and the various surface area normalizations that have been applied.

The (apparent) sediment-side ISA-normalized rate constant derived from this study (k = 14.3 ± 1.5 mol m^{-2} yr^{-1}) is slightly higher than that obtained from a fit to the Keir (1983) calcite-dissolution experimental results (k_{Keir} = 10.5 ± 1.5 mol m^{-2} yr^{-1}), obtained with pure reagent grade calcite, which was laid down uniformly (~ 0.6 cm thick) at the bottom of a stirred reactor filled with artificial seawater at 20 ± 1°C and atmospheric pressure (***Fig. 2.7***). The latter study is, by far, the closest analog to our experiments. Keir (1983) normalized his dissolution rates to the surface area of the reactor bottom, which we denoted as ISA in this study, and gave little information about the hydrodynamic conditions in the reactor. Nevertheless, he noted that the stirring rate was high enough to generate "moderate mixing", but not fast enough to induce resuspension. Based on our results, we believe that his stirring rate was high enough to render the reaction sediment-side controlled, i.e., k_S is the smaller term in the expression of the overall mass transfer coefficient k^*, see ***Eq. 2.6***.

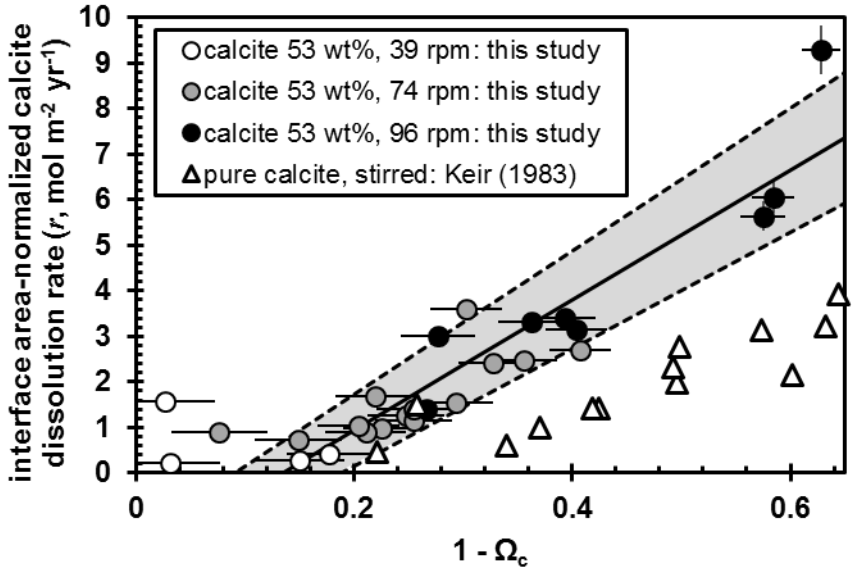

Fig. 2.7 | *Comparison of the dissolution rates measured by Keir (1983) in a stirred reactor on pure synthetic calcite with our experimental data on the dissolution rates of synthetic sediments (53 wt% of calcite at various stirring rates) as a function of the steady-state undersaturation state.*

Our ISA-normalized calcite dissolution rates and those obtained by Keir (1983) with synthetic calcite display notably similar dissolution kinetics (***Fig. 2.7***). Boudreau (2013) refitted Keir's data as a function of (C_S – C_0) and reported two sediment-side mass transfer coefficients, one for each of the seawater batches used during the dissolution experiments, i.e., 263.1 ± 24.1

and 490.5 ± 89.2 m yr^{-1} for the data Keir (1983) obtained on disks of pure synthetic calcite. These values bracket the sediment-side mass transfer coefficient, i.e., k_S = 326.9 ± 39.5 m yr^{-1} (see ***Eq. 2.8c***) that we obtained under similar experimental conditions. The latter observation is interpreted as transport limitation within the sediment, i.e., reaction products accumulate in pore waters and escape the sediment by diffusion through the sediment, thus constraining the apparent dissolution rate measured at the SWI, in accordance to the square-root dependence of the calcite dissolution rates on the calcite contents of the sediment (Boudreau and Guinasso, 1982) as reproduced in ***Fig. 2.5***. Our results are also consistent with Keir's observations that the calcite dissolution rate constant in a sediment increases with its calcite content between 0 and about 60%, whereas it becomes statistically invariant at higher calcite contents (> 60%). The strong similarity in ***Fig. 2.5*** between dissolution rates measured with our synthetic sediments and the natural deep-sea sediments of Keir (1983) suggests that the hydrodynamic conditions under which these experiments were performed, and the design of these experiments, exert a stronger control on the dissolution kinetics than the type of calcitic material that is being dissolved (e.g., synthetic powder or foraminifera). Nevertheless, in order to accurately extrapolate these results to the seafloor, an extended investigation of physical parameters that could influence mass transfer across the DBL is required. The experiments presented in this study were performed at a temperature of 25°C, a value that is more representative of shallow environments than the deep-sea, where the temperature is usually below 4°C (Waelbroeck et al., 2002). Previous investigators reported a systematic increase in the calcite dissolution rates with increasing temperature (Gutjahr et al., 1996; Pokrovsky et al., 2009; Sjöberg and Rickard, 1983). On the other hand, the water-side control term of the calcite dissolution kinetic equation (i.e., β in ***Eq. 2.6***) is also affected by variations in temperature, mainly because the carbonate ion diffusion coefficient decreases with decreasing temperature (Zeebe, 2011). Similarly, the effects of elevated pressure in the deep ocean could also alter the calcite dissolution kinetics, although over the range encountered in the ocean, the pressure effect on the viscosity of seawater and on the diffusion coefficients of ions in seawater is thought to be relatively small (i.e., < 8%, Boudreau, 1997; Li and Gregory, 1974; Stanley and Batten, 1969). Furthermore, our synthetic sediment does not reproduce the high permeabilities observed in shallow sediments that can support advection of overlying waters and porewaters across the sediment-water interface (Cyronak et al., 2013). Permeable sediments, like sands, allow for the percolation of overlying and porewaters through the sediment-water interface as a results of

pressure gradients generated by seafloor topography (e.g., ripples) and waves. An investigation of the influence of sediment porosity and grain size would extend the relevance of these results to a broad range of sedimentary environments and are, along with the influence of temperature and pressure, among the variables we plan to investigate in our ongoing study.

We should note that, on occasion, we measured net $CaCO_3$ dissolution rates (although very weak, see ***Table 2.1***) at low apparent supersaturations ($\Omega_c \leq 1.05$), as has been reported by Subhas et al. (2015). This may reflect the dissolution of a more soluble $CaCO_3$ polymorph (e.g., XRD- and SEM-undetectable aragonite or vaterite contamination of the reagent grade calcite) or a short-lived surface phase that develops upon the introduction of the pure calcite to the seawater solution, e.g. a magnesian calcite. Mucci and Morse (1983) and Mucci et al. (1985) determined that a 8 mole% magnesian calcite precipitates on pure calcite powders at 25°C from seawater under controlled-laboratory conditions. As this phase is more soluble than pure calcite and the most stable phase in seawater, i.e., minimum solubility at 4 mole% magnesian calcite (Bischoff et al., 1987; Busenberg and Plummer, 1989; Mucci and Morse, 1983), it may lead to an apparent supersaturation. Alternately, the slow dissolution rates (0.1 - 0.2 mol m^{-2} yr^{-1}, see ***Table 2.1***) at these apparent supersaturations (calculated from measured pH, TA and $[Ca^{2+}]/S$) could be explained by bacterial respiration in the synthetic sediment or in the seawater, although its effect is most likely negligible compared to the dissolution rates measured in undersaturated seawater (up to 9.3 mol m^{-2} yr^{-1}). In addition, uncertainties inherent to our saturation state calculations (alkalinity, pH determinations, carbonic and boric acid dissociation constants) also contribute to the apparent supersaturation.

2.4.3 Calcite compensation depth

Whereas calcite dissolves in the oceanic water column below its saturation depth, i.e., the R_0 level or saturation depth where $\Omega_c = 1$ (Ben-Yaakov et al., 1974), it still accumulates in deep-sea sediments down to the calcite compensation depth (CCD). The position of the CCD is determined by the balance between the flux of particulate CaCO3 from the overlying water and the ambient calcite dissolution rate (Berner et al., 1976; Boudreau et al., 2010b; Edmond, 1974; Edmond and Gieskes, 1970; Morse and Berner, 1972). In other words, the CCD is the depth below which seawater undersaturation is sufficient to generate a seafloor dissolution rate that is

equivalent or faster than the CaCO3 particulate flux (Edmond, 1974), thus preventing accumulation. Additional calcite dissolution caused by anthropogenic acidification will occur over the area of the seafloor located between the rising CCD and calcite saturation depth. As these two latter horizons shallow with acidification, a greater surface area of calcitic sediments is exposed to undersaturated waters and undergoes dissolution. Calcite-bearing sediment deposited when the CCD was deeper, but now found below the rising CCD, will also undergo dissolution, as the $CaCO_3$ particles are returned to the sediment-water interface by bioturbation.

Assuming an exponential dependence of the calcite solubility on the hydrostatic pressure and linear kinetics, Boudreau et al. (2010b) derived a simple expression to estimate the position of the CCD, which can be written as:

$$z_{cc} = \frac{p_c}{\rho\, g} \ln\left(\frac{[Ca^{2+}]\, F_B}{K_{sp}^{*}\, A_D\, k^{*}} + \frac{[Ca^{2+}]\,[CO_3^{2-}]_D}{K_{sp}^{*}}\right) \quad \textbf{(2.9)}$$

where z_{cc} represents the CCD, p_c is a characteristic pressure set as 511 atm (Boudreau et al., 2010b), ρ is the mean density of seawater, g is the mean gravitational acceleration on Earth, F_B is the flux of solid calcite from the surface ocean (rain rate), A_D is the seafloor surface below 200 m, and $[CO_3^{2-}]_D$ is the carbonate ion concentration in the deep ocean.

In order to test this model with our dissolution rate, we must first estimate the overall dissolution mass transfer coefficient (k^*) under the hydrodynamic conditions encountered at the seafloor. Dissolution cannot occur faster than the limit placed by transport across the benthic DBL; this transfer limit is embodied by the mass transfer coefficient β. Following the arguments presented in Boudreau (2013), typically β = 12.7 m yr^{-1}, which implies a benthic DBL of about 1.2 mm, the overall mass transfer coefficient computed using ***Eq. 2.6***, resulting of the benthic estimated β value and the k_S value reported in ***Eq. 2.8c***, is k^* = 12.2 ± 1.5 m yr^{-1}. Thus, given that our dissolution mass transfer coefficient under sediment-side control is more than 25 times larger than the mass transfer coefficient through the benthic DBL, calcite dissolution at the seafloor is largely controlled by diffusion through the benthic DBL. A similar hypothesis of (at least partial) water-side control on calcite dissolution has previously been considered by several other authors (Broecker, 2009; Oxburgh, 1998; Schink and Guinasso, 1977; Takahashi and Broecker, 1977).

Next, assuming a constant $[CO_3^{2-}]_D$ of 0.09 mM for the average deep ocean (Boudreau et al., 2010b; Broecker and Clark, 2003; Key et al., 2004) and a calcite rain rate (F_B) of 40 x10^3 Gmol yr^{-1} (Archer, 1996; Berelson et al., 2007; Sarmiento and Gruber, 2006), we estimate, using ***Eq. 2.9***, the average calcite compensation depth at 4.4 ± 0.2 km. For a larger calcite export rate (i.e., 60 x10^3 Gmol yr^{-1}), the CCD deepens to 4.6 ± 0.2 km, as compared to a worldwide average of 4.75 km estimated by Boudreau et al. (2010b). Note that all our attempts to model the CCD based on non-linear kinetics, using a fit to our data with an order of reaction greater than unity, fail to reproduce the observed world-average CCD. Given a predicted, mean deep ocean $[CO_3^{2-}]$ of 0.045 mM by the end of this millennia (Ridgwell and Hargreaves, 2007), the CCD would rise to a depth of 1.3 ± 0.2 km for a calcite rain rate of 40 x10^3 Gmol yr^{-1}, regardless of any feedback mechanism in the biological production of calcium carbonate minerals, the climate or the heat content of the ocean (Archer et al., 2009; Ries et al., 2016; Tanhua et al., 2013).

2.5 Conclusion

We have measured the dissolution rate of calcite in a synthetic, inorganic sediment when exposed to undersaturated natural seawater and simulated hydrodynamic conditions at the seafloor. Under our experimental conditions, calcite dissolution rates, normalized to the interface area of the sediment surface, vary linearly with the degree of undersaturation of the solution, i.e., $(1 - \Omega_c)$. The dissolution rates of Indiana limestone and the synthetic sediment increase with the stirring rate up to a point where the measured flux of alkalinity becomes independent of the hydrodynamic conditions at the sediment-water interface. The transition corresponds to a shift from a system controlled by water-side transport (across the diffusive boundary layer) to a system controlled by sediment-side processes (reactions within the sediment and diffusion of pore-water solutes), or by surface reactions in the case of low porosity Indiana limestone. Furthermore, we observed that the calcite sediment dissolution rates are square-root dependent on the calcite content, consistent with the interpretation that rates are controlled by diffusion and reaction within the sediments at high stirring rates.

Unlike the dissolution kinetic studies carried out during the past decades on carbonate mineral suspensions, our study fills an important knowledge gap by taking into account transport limitations through both the diffusive boundary layer above the sediment bed and the sediment

pore waters, and is thus more representative of dissolution occurring at the seafloor. Results of this study are quantitatively compatible with those of Keir (1983), who used a similar experimental design (sediment disks). A reinterpretation of Keir (1983) by Boudreau (2013) showed that those earlier results also exhibited first-order kinetics and a square-root dependence of the dissolution rate with the calcite content of the sediment. Our sediment-side mass-transfer coefficient (k_S = 326.5 ± 35.9 m yr^{-1}) is more than 25 times larger than the estimated mean water-side mass-transfer coefficient at the seafloor (β = 12.7 m yr^{-1}), and supports a shift of the current paradigm to transport-controlled of carbonate dissolution at the seafloor. Our linear dissolution rate kinetics provide a good prediction of the world-average CCD. Finally, our findings are an important step toward reconciling results of calcite reaction kinetic studies published to date and provide a simplified description of the calcite dissolution kinetics at the sediment-water interface at the seafloor.

References

Alkattan, M., Oelkers, E.H., Dandurand, J.-L. and Schott, J. (2002) An experimental study of calcite dissolution rates at acidic conditions and 25°C in the presence of $NaPO_3$ and $MgCl_2$. *Chemical Geology*, 190(1-4), 291-302.

Archer, D. (1996) A data-driven model of the global calcite lysocline. *Global Biogeochemical Cycles*, 10, 511-526, https://doi.org/10.1029/96GB01521.

Archer, D. (2005) Fate of fossil fuel CO_2 in geologic time. *Journal of Geophysical Research*, 110(C09S05).

Archer, D., Emerson, S. and Reimers, C. (1989a) Dissolution of calcite in deep-sea sediments: pH and O_2 microelectrode results. *Geochimica et Cosmochimica Acta*, 53(11), 2831-2845.

Archer, D., Emerson, S. and Smith, C.R. (1989b) Direct measurement of the diffusive sublayer at the deep sea floor using oxygen microelectrodes. *Nature*, 340, 623-626.

Archer, D., Kheshgi, H. and Maier-Reimer, E. (1998) Dynamics of fossil fuel CO_2 neutralization by marine $CaCO_3$. *Global Biogeochemical Cycles*, 12, 259-276, https://doi.org/10.1029/98GB00744

Archer, D., Eby, M., Brovkin, V., Ridgwell, A., Cao, L., Mikolajewicz, U., Caldeira, K., Matsumoto, K., Munhoven, G., Montenegro, A. and Tokos, K. (2009) Atmospheric Lifetime of Fossil Fuel Carbon Dioxide. *Annual Review of Earth and Planetary Sciences*, 37, 117-134, https://doi.org/10.1146/annurev.earth.031208.100206

Armi, L. (1977) The Dynamics of the Bottom Boundary Layer of the Deep Ocean. In: C.J.J. Nihoul (Eds), Bottom turbulence. 8th International Liege Colloquium on Ocean Hydrodynamics. Elsevier, Amsterdam, pp. 153-164.

Ben-Yaakov, S., Ruth, E. and Kaplan, I.R. (1974) Carbonate compensation depth: relation to carbonate solubility in ocean waters. *Science*, 184(4140), 982-984.

Berelson, W.M., Balch, W.M., Najjar, R., Feely, R.A., Sabine, C. and Lee, K. (2007) Relating estimates of $CaCO_3$ production, export, and dissolution in the water column to measurements of $CaCO_3$ rain into sediment traps and dissolution on the sea floor: A revised global carbonate budget. *Global Biogeochemical Cycles* 21(1), https://doi.org/10.1029/2006GB002803

Berner, R.A. and Morse, J.W. (1974) Dissolution kinetics of calcium carbonate in sea water: IV. Theory of calcite dissolution. *American Journal of Science*, 274(2), 108-134.

Berner, R.A., Berner, E.K. and Keir, R.S. (1976) Aragonite dissolution on the Bermuda Pedestal: its depth and geochemical significance. *Earth and Planetary Science Letters*, 30(2), 169-178.

Bischoff, W.D., Mackenzie, F.T. and Bishop, F.C. (1987) Stabilities of synthetic magnesian calcites in aqueous solution: Comparison with biogenic materials. *Geochimica et Cosmochimica Acta*, 51(6): 1413-1423.

Boudreau, B.P. (1997) Diagenetic Models and Their Implementation. Springer-Verlag, Berlin.

Boudreau, B.P. (2013) Carbonate dissolution rates at the deep ocean floor. *Geophysical Research Letters* 40, 744-748, https://doi.org/10.1029/2012GL054231

Boudreau, B.P. and Guinasso Jr., N.L. (1982) The influence of a diffusive boundary layer on accretion, dissolution, and diagenesis at the sea floor. In: Fanning, K.A., Manheim, F.T. [Eds.]. *The Dynamic Environment of the Ocean Floor*. Lexington Books, Lexington, pp. 115-145.

Boudreau, B.P. and Jørgensen, B.B. (2001) The Benthic Boundary Layer: Transport Processes and Biogeochemistry. Oxford University Press, Oxford.

Boudreau, B.P., Middelburg, J.J. and Meysman, F.J.R. (2010b) Carbonate compensation dynamics. *Geophysical Research Letters*, 37, https://doi.org/10.1029/2009GL041847

Broecker, W.S. (2009) Wally's quest to understand the ocean's $CaCO_3$ cycle. *Annual Review of Marine Science*, 1, 1-18.

Broecker, W.S. and Clark, E. (2003) Pseudo dissolution of marine calcite. *Earth and Planetary Science Letters*, 208(3-4), 291-296.

Buchholtz-ten Brink, M.R., Gust, G. and Chavis, D. (1989) Calibration and performance of a stirred benthic chamber. *Deep Sea Research Part A. Oceanographic Research Papers*, 36(7): 1083-1101.

Burton, E.A. and Walter, L.M. (1990) The role of pH in phosphate inhibition of calcite and aragonite precipitation rates in seawater. *Geochimica et Cosmochimica Acta*, 54(3), 797-808.

Busenberg, E. and Plummer, L. (1989) Thermodynamics of magnesian calcite solid-solutions at 25°C and 1 atm total pressure. *Geochimica et Cosmochimica Acta*, 53(6), 1189-1208.

Caldeira, K. and Wickett, M.E. (2003) Anthropogenic carbon and ocean pH. *Nature* 425, 365-365, https://doi.org/10.1038/425365a

Cantrell, C.A. (2008) Technical Note: Review of methods for linear least-squares fitting of data and application to atmospheric chemistry problems. *Atmospheric Chemistry and Physics* 8(17), 5477-5487.

Ciais, P., Sabine, C., Bala, G., Bopp, L., Brovkin, V., Canadell, J., Chhabra, A., DeFries, R., Galloway, J., Heimann, M., Jones, C., Le Quéré, C., Myneni, R.B., Piao, S. and Thornton, P. (2013) Carbon and Other Biogeochemical Cycles. In: Stocker, T.F., D. Qin, G.-K. Plattner, M. Tignor, S.K. Allen, J. Boschung, A. Nauels, Y. Xia, V. Bex and P.M. Midgley [Eds.] Climate Change 2013: The Physical Science Basis. Contribution of Working Group I to the Fifth Assessment Report of the Intergovernmental Panel on Climate Change. Cambridge University Press, Cambridge, United Kingdom and New York, NY, USA.

Colombani, J. (2016) The alkaline dissolution rate of calcite. *The Journal of Physical Chemistry Letters* 7(13), 2376-2380.

Cubillas, P., Köhler, S., Prieto, M., Chaïrat, C. and Oelkers, E.H. (2005). Experimental determination of the dissolution rates of calcite, aragonite, and bivalves. *Chemical Geology* 216(1-2), 59-77.

Cyronak, T., Santos, I.R. and Eyre, B.D. (2013) Permeable coral reef sediment dissolution driven by elevated pCO_2 and pore water advection. *Geophysical Research Letters* 40(18), 4876-4881.

Dade, W.B. (1993) Near-bed turbulence and hydrodynamic control of diffusional mass transfer at the sea floor. *Limnology and Oceanography* 38, 52-69, https://doi.org/10.4319/lo.1993.38.1.0052

De Baere, B., Molins, S., Mayer, K.U. and François, R. (2016) Determination of mineral dissolution regimes using flow-through time-resolved analysis (FT-TRA) and numerical simulation. *Chemical Geology* 430, 1-12.

Delille, B., Harlay, J., Zondervan, I., Jacquet, S., Chou, L., Wollast, R., Bellerby, R.G.J., Frankignoulle, M., Borges, A.V., Riebesell, U. and Gattuso, J.-P. (2005) Response of primary production and calcification to changes of pCO_2 during experimental blooms of the coccolithophorid Emiliania huxleyi. *Global Biogeochemical Cycles* 19(GB2023).

Denbigh, K.G. (1944) Velocity and yield in continuous reaction systems. *Transactions of the Faraday Society* 40, 352-373.

Dickson, A.G. (1984) pH scales and proton-transfer reactions in saline media such as sea water. *Geochimica et Cosmochimica Acta* 48(11), 2299-2308.

Dickson, A.G. (1990) Standard potential of the reaction: $AgCl(s)+1/2H_2(g) = Ag(s)+HCl(aq)$, and the standard acidity constant of the ion HSO_4^- in synthetic sea water from 273.15 to 318.15 K. *The Journal of Chemical Thermodynamics* 22, 113-127, https://doi.org/10.1016/0021-9614(90)90074-Z

Dickson, A.G., Sabine, C.L. and Christian, J.R. (2007) Guide to best practices for ocean CO_2 measurements. *PICES Special Publication* 3, 191 pp.

Dunne, J.P., Hales, B. and Toggweiler, J.R. (2012) Global calcite cycling constrained by sediment preservation controls. *Global Biogeochemical Cycles* 26(3), https://doi.org/10.1029/2010GB003935.

Edmond, J.M. (1974) On the dissolution of carbonate and silicate in the deep ocean. *Deep Sea Research* 21, 455-480, https://doi.org/10.1016/0011-7471(74)90094-1

Edmond, J.M., Gieskes, J.M.T.M. (1970) On the calculation of the degree of saturation of sea water with respect to calcium carbonate under in situ conditions. *Deep-Sea Research* 34, 1261–1291.

Feely, R.A., Sabine, C.L., Lee, K., Berelson, W., Kleypas, J., Fabry, V.J. and Millero, F.J. (2004) Impact of Anthropogenic CO_2 on the $CaCO_3$ System in the Oceans. *Science* 305(5682), 362-366.

Gattuso, J.-P. and Hansson, L. (2011) Ocean Acidification. Oxford University Press, Oxford.

Gehlen, M., Bassinot, F.C., Chou, L. and McCorkle, D. (2005) Reassessing the dissolution of marine carbonates: II. Reaction kinetics. *Deep Sea Research Part I: Oceanographic Research Papers* 52(8), 1461-1476.

Gehlen, M., Gangstø, R., Schneider, B., Bopp, L., Aumont, O. and Ethe, C. (2007) The fate of pelagic $CaCO_3$ production in a high CO_2 ocean: a model study. *Biogeosciences* 4(4), 505-519.

Glud, R.N., Gundersen, J.K., Revsbech, N.P. and Jørgensen, B.B. (1994) Effects on the benthic diffusive boundary layer imposed by microelectrodes. *Limnology and Oceanography* 39, 462-467.

Grasshoff, K., Kremling, K. and Ehrhardt, M. (1999) Methods of Seawater Analysis. Wiley.

Green, M.A. and Aller, R.C. (2001) Early diagenesis of calcium carbonate in Long Island Sound sediments: Benthic fluxes of Ca^{2+} and minor elements during seasonal periods of net dissolution. *Journal of Marine Research* 59(5), 769-794.

Gutjahr, A., Dabringhaus, H. and Lacmann, R. (1996) Studies of the growth and dissolution kinetics of the $CaCO_3$ polymorphs calcite and aragonite I. Growth and dissolution rates in water. *Journal of Crystal Growth* 158(3), 296-309.

Hales, B. and Emerson, S. (1996) Calcite dissolution in sediments of the Ontong-Java Plateau: In situ measurements of pore water O_2 and pH. *Global Biogeochemical Cycles* 10(3), 527-541.

Hales, B. and Emerson, S. (1997a) Calcite dissolution in sediments of the Ceara Rise: In situ measurements of porewater O_2, pH, and $CO_{2\,(aq)}$. *Geochimica et Cosmochimica Acta* 61(3), 501-514.

Hales, B. and Emerson, S. (1997b) Evidence in support of first-order dissolution kinetics of calcite in seawater. *Earth and Planetary Science Letters* 148(1), 317-327.

Hönisch, B., Ridgwell, A., Schmidt, D.N., Thomas, E., Gibbs, S.J., Sluijs, A., Zeebe, R., Kump, L., Martindale, R.C., Greene, S.E., Kiessling, W., Ries, J., Zachos, J.C., Royer, D.L., Barker, S., Marchitto, T.M., Jr., Moyer, R., Pelejero, C., Ziveri, P., Foster, G.L. and Williams, B. (2012) The geological record of ocean acidification. *Science* 335(6072), 1058-1063.

Honjo, S., Manganini, S.J. and Cole, J.J. (1982) Sedimentation of biogenic matter in the deep ocean. *Deep Sea Research Part A. Oceanographic Research Papers* 29(5): 609-625.

ILI (2007) Indiana Limestone Handbook, Indiana Limestone Institute of America, Inc., Belford, IN.

Javadi, K. and Khalili, A. (2009) On generating uniform bottom shear stress. Part II: Shear stress inducing devices. *Recent Patents on Chemical Engineering 2*, 223-229.

Ji, Y., Baud, P., Vajdova, V. and Wong, T.-F. (2012) Characterization of pore geometry of Indiana Limestone in relation to mechanical compaction. *Oil & Gas Science and Technology – Revue d'IFP Energies nouvelles* 67(5), 753-775.

Jørgensen, B.B. and Revsbech, N.P. (1985) Diffusive boundary layers and the oxygen uptake of sediments and detritus. *Limnology and Oceanography* 30, 111-122.

Keir, R.S. (1980) The dissolution kinetics of biogenic calcium carbonates in seawater. *Geochimica et Cosmochimica Acta* 44(2), 241-252.

Keir, R.S. (1982) Dissolution of calcite in the deep-sea: theoretical prediction for the case of uniform size particles settling into a well-mixed sediment. *American Journal of Science* 282(3), 193-236.

Keir, R.S. (1983) Variation in the carbonate reactivity of deep-sea sediments: determination from flux experiments. *Deep-Sea Research* 30, 279-296.

Key, R.M., Kozyr, A., Sabine, C.L., Lee, K., Wanninkhof, R., Bullister, J.L., Feely, R.A., Millero, F.J., Mordy, C. and Peng, T.H. (2004) A global ocean carbon climatology: Results from Global Data Analysis Project (GLODAP). *Global Biogeochemical Cycles*, 18(GB4031).

Khalili, A., Javadi, K., Saidi, A., Goharzadeh, A., Huettel, M. and Jorgensen, B.B. (2008) On generating uniform bottom shear stress. Part I: A quantitative study of microcosm chambers. *Recent Patents on Chemical Engineering* 1(3), 174-191.

Koutitonsky, V.G. and Bugden, G.L. (1991) The physical oceanography of the Gulf of St. Lawrence: a review with emphasis on the synoptic variability of the motion. In Therriault, J.-C. [Ed.] The Gulf of St. Lawrence: Small ocean or big estuary? Canadian special publication of fisheries and aquatic sciences, pp. 57-90.

Le Quéré, C., Raupach, M.R., Canadell, J.G., Marland, G., Bopp, L., Ciais, P., Conway, T.J., Doney, S.C., Feely, R.A., Foster, P., Friedlingstein, P., Gurney, K., Houghton, R.A., House, J.I., Huntingford, C., Levy, P.E., Lomas, M.R., Majkut, J., Metzl, N., Ometto, J.P., Peters, G.P., Prentice, I.C., Randerson, J.T., Running, S.W., Sarmiento, J.L., Schuster, U., Sitch, S., Takahashi, T., Viovy, N., van der Werf, G.R. and

Woodward, F.I. (2009) Trends in the sources and sinks of carbon dioxide. *Nature Geoscience* 2(12), 831-836.

Le Quéré, C., Peters, G. P., Andres, R. J., Andrew, R. M., Boden, T. A., Ciais, P., Friedlingstein, P., Houghton, R. A., Marland, G., Moriarty, R., Sitch, S., Tans, P., Arneth, A., Arvanitis, A., Bakker, D. C. E., Bopp, L., Canadell, J. G., Chini, L. P., Doney, S. C., Harper, A., Harris, I., House, J. I., Jain, A. K., Jones, S. D., Kato, E., Keeling, R. F., Klein Goldewijk, K., Körtzinger, A., Koven, C., Lefèvre, N., Maignan, F., Omar, A., Ono, T., Park, G.-H., Pfeil, B., Poulter, B., Raupach, M. R., Regnier, P., Rödenbeck, C., Saito, S., Schwinger, J., Segschneider, J., Stocker, B. D., Takahashi, T., Tilbrook, B., van Heuven, S., Viovy, N., Wanninkhof, R., Wiltshire, A., and Zaehle, S. (2014). Global carbon budget 2013. *Earth System Science Data* 6(1), 235-263.

Levich, V. G. (1962) *Physicochemical Hydrodynamics*, Prentice-Hall.

Lewis, E. and Wallace, D.W.R. (1998) Program Developed for CO_2 System Calculations. ORNL/CDIAC-105. Carbon Dioxide Information Analysis Center, Oak Ridge National Laboratory, U.S. Department of Energy, Oak Ridge, Tennessee.

Li, Y.-H. and Gregory, S. (1974) Diffusion of ions in sea water and in deep-sea sediments. *Geochimica et Cosmochimica Acta* 38(5), 703-714.

Lueker, T.J., Dickson, A.G. and Keeling, C.D. (2000) Ocean pCO_2 calculated from dissolved inorganic carbon, alkalinity, and equations for K_1 and K_2: validation based on laboratory measurements of CO_2 in gas and seawater at equilibrium. *Marine Chemistry* 70, 105-119, https://doi.org/10.1016/S0304-4203(00)00022-0

Lüthi, D., Le Floch, M., Bereiter, B., Blunier, T., Barnola, J.M., Siegenthaler, U., Raynaud, D., Jouzel, J., Fischer, H., Kawamura, K. and Stocker, T.F. (2008) High-resolution carbon dioxide concentration record 650,000-800,000 years before present. *Nature* 453(7193): 379-82.

Lüttge, A. (2005) Etch pit coalescence, surface area, and overall mineral dissolution rates. *American Mineralogist* 90(11-12), 1776-1783.

Lüttge, A., Arvidson, R.S. and Fischer, C. (2013). A stochastic treatment of crystal dissolution kinetics. *Elements* 9(3), 183-188.

Millero, F.J. (1979) The thermodynamics of the carbonic acid system in seawater. *Geochimica et Cosmochimica Acta* 43(10), 1651-1661.

Millero, F., Huang, F., Zhu, X., Liu, X. and Zhang, J.-Z. (2001) Adsorption and desorption of phosphate on calcite and aragonite in seawater. *Aquatic Geochemistry* 7(1), 33-56.

Morse, J.W. (1974a) Dissolution kinetics of calcium carbonate in seawater: V. Effects of natural inhibitors and the position of the chemical lysocline. *American Journal of Science* 274, 638-647.

Morse, J.W. (1978) Dissolution kinetics of calcium carbonate in sea water: VI. The near-equilibrium dissolution kinetics of calcium carbonate-rich deep sea sediments. *American Journal of Science* 278(3): 344-353.

Morse, J.W. and Berner, R.A. (1972) Dissolution kinetics of calcium carbonate in sea water: I, A kinetic origin for the lysocline. *American Journal of Science* 272(9), 840-851.

Morse, J.W. and Mackenzie, F.T. (1990) Geochemistry of Sedimentary Carbonates. Elsevier, Amsterdam.

Morse, J.W. and Arvidson, R.S. (2002) The dissolution kinetics of major sedimentary carbonate minerals. *Earth-Science Reviews* 58, 51-84, https://doi.org/10.1016/S0012-8252(01)00083-6

Mucci, A. (1983) The solubility of calcite and aragonite in seawater at various salinities, temperatures and one atmosphere total pressure. *American Journal of Science* 283, 780-799, http://doi.org/10.2475/ajs.283.7.780

Mucci, A. (1986) Growth kinetics and composition of magnesian calcite overgrowths precipitated from seawater: Quantitative influence of orthophosphate ions. *Geochimica et Cosmochimica Acta* 50(10): 2255-2265.

Mucci, A. and Morse, J.W. (1983) The incorporation of Mg^{2+} and Sr^{2+} into calcite overgrowths: influences of growth rate and solution composition. *Geochimica et Cosmochimica Acta* 47(2), 217-233.

Mucci, A., Morse, J.W. and Kaminsky, M.S. (1985) Auger spectroscopy analysis of magnesian calcite overgroths precipitated from seawater and solutions of similar composition. *American Journal of Science* 285(4): 289-305.

Murphy, J. and Riley, J. P. (1962). A modified single solution method for the determination of phosphate in natural waters. *Analytica Chimica Acta* 27, 31-36.

Orr, J.C., Epitalon, J.M. and Gattuso, J.P. (2015) Comparison of ten packages that compute ocean carbonate chemistry. *Biogeosciences* 12(5), 1483-1510.

Oxburgh, R. (1998) The Holocene preservation history of equatorial Pacific sediments. *Paleoceanography* 13(1), 50-62.

Oxburgh, R. and Broecker, W.S. (1993) Pacific carbonate dissolution revisited. *Palaeogeography, Palaeoclimatology, Palaeoecology* 103: 31-39.

Passow, U. and Carlson, C.A. (2012) The biological pump in a high CO_2 world. *Marine Ecology Progress Series* 470, 249-271.

Pierrot, D., Lewis, E. and Wallace, D. (2006) *MS Excel Program Developed for CO_2 System Calculations*. ORNL/CDIAC-105a, Carbon Dioxide Information Analysis Center, Oak Ridge National Laboratory, U.S. Department of Energy, Oak Ridge, Tennessee.

Pokrovsky, O.S., Golubev, S.V., Schott, J. and Castillo, A. (2009) Calcite, dolomite and magnesite dissolution kinetics in aqueous solutions at acid to circumneutral pH, 25 to 150 °C and 1 to 55 atm pCO_2: New constraints on CO_2 sequestration in sedimentary basins. *Chemical Geology* 265(1-2), 20-32.

Ridgwell, A. and Hargreaves, J.C. (2007) Regulation of atmospheric CO_2 by deep-sea sediments in an Earth system model. *Global Biogeochemical Cycles* 21, https://doi.org/10.1029/2006GB002764

Ries, J.B., Ghazaleh, M.N., Connolly, B., Westfield, I. and Castillo, K.D. (2016) Impacts of seawater saturation state (Ω_A = 0.4–4.6) and temperature (10, 25°C) on the dissolution kinetics of whole-shell biogenic carbonates. *Geochimica et Cosmochimica Acta* 192, 318-337.

Sabine, C.L. and Feely, R.A. (2007) The oceanic sink for carbon dioxide. In: D. Reay, N. Hewitt, J. Grace and K. Smith (Eds.), Greenhouse Gas Sinks. CABI Publishing, Oxfordshire, UK, pp. 31-49.

Santschi, P. H., Bower, P., Nyffeler, U. P., Azevedo, A. and Broecker, W. S. (1983) Estimates of the resistance to chemical transport posed by the deep-sea boundary layer. *Limnology and Oceanography* 28: 899-912, https://doi.org/10.4319/lo.1983.28.5.0899.

Sarmiento, J.L. and Gruber, N. (2006) Ocean Biogeochemical Dynamics. Princeton University Press, Princeton, NJ.

Schink, D. R., and Guinasso, N. L. (1977) Modelling the influence of bioturbation and other processes on calcium carbonate dissolution at the sea floor. In N. R. Andersen and A. Malahoff [Eds.]. The Fate of Fossil Fuel CO_2 in the Oceans. Plenum Press. p. 375-400.

Schlichting, H. (1979) Boundary Layer Theory. McGraw-Hill, New York.

Sjöberg, E.L. (1978) Kinetics and mechanism of calcite dissolution in aqueous solutions at low temperatures, Stockholm University, Stockholm, 92 pp.

Sjöberg, E.L. and Rickard, D.T. (1983) Temperature dependence of calcite dissolution kinetics between 1 and 62°C at pH 2.7 to 8.4 in aqueous solutions. *Geochimica et Cosmochimica Acta* 48(3), 485-493.

Sjöberg, E.L. and Rickard, D.T. (1984) Calcite dissolution kinetics: Surface speciation and the origin of the variable pH dependence. *Chemical Geology* 42(1-4), 119-136.

Stanley, E.M. and Batten, R.C. (1969) Viscosity of sea water at moderate temperatures and pressures. *Journal of Geophysical Research*, 74: 3415-3420.

Steinberger, N. and Hondzo, M. (1999) Diffusional mass transfer at sediment-water interface. *Journal of Environmental Engineering* 125, 192-200, https://doi.org/10.1061/(ASCE)0733-9372(1999)125:2(192)

Subhas, A.V., Rollins, N.E., Berelson, W.M., Dong, S., Erez, J. and Adkins, J.F. (2015) A novel determination of calcite dissolution kinetics in seawater. *Geochimica et Cosmochimica Acta* 170, 51-68.

Sun, X. and Turchyn, A.V. (2014) Significant contribution of authigenic carbonate to marine carbon burial. *Nature Geoscience* 7(3), 201-204.

Svensson, U. and Dreybrodt, W. (1992) Dissolution kinetics of natural calcite minerals in CO_2-water systems approaching calcite equilibrium. *Chemical Geology* 100, 129-145.

Takahashi, T. and Broecker, W.S. (1977) Mechanisms for calcite dissolution on the sea floor. In: N.R. Anderson and A. Malahoff [Eds.], The Fate of Fossil Fuel CO_2 in the Oceans, Plenum, New York, pp. 455-477.

Tanhua, T., Bates, N.R. and Körtzinger, A. (2013) The Marine Carbon Cycle and Ocean Carbon Inventories. In: G. Siedler, J. Gould and C. J. [Eds.], Ocean Circulation and Climate: A 21st Century Perspective. 2nd Ed. International Geophysics, 103. Academic Press, Oxford, GB, pp. 787-815.

Tans, P.P. and Keeling, R. (2016) Dr. Pieter Tans, NOAA/ESRL (www.esrl.noaa.gov/gmd/ccgg/trends/) and Dr. Ralph Keeling, Scripps Institution of Oceanography (scrippsco2.ucsd.edu/).

Teng, H.H. (2004) Controls by saturation state on etch pit formation during calcite dissolution. *Geochimica et Cosmochimica Acta* 68(2), 253-262.

Tyrrell, T. (2011) Anthropogenic modification of the oceans. *Philosophical Transactions Of The Royal Society*, 369(1938), 887-908.

Uppström, L. R. (1974) The boron/chlorinity ratio of deep-sea water from the Pacific Ocean. *Deep-Sea Research* 21, 161-162.

Waelbroeck, C., Labeyrie, L., Michel, E., Duplessy, J.C., McManus, J.F., Lambeck, K., Balbon, E. and Labracherie, M. (2002) Sea-level and deep water temperature changes derived from benthic foraminifera isotopic records. *Quaternary Science Reviews* 21(1-3), 295-305.

Walter, L.M. and Morse, J.W. (1985) The dissolution kinetics of shallow marine carbonates in seawater: A laboratory study. *Geochimica et Cosmochimica Acta* 49(7): 1503-1513.

Williamson, J.H. (1968) Least-squares fitting of a straight line. *Canadian Journal of Physics* 46, 1845-1847.

Xu, J., Fan, C. and Teng, H.H. (2012) Calcite dissolution kinetics in view of Gibbs free energy, dislocation density, and pCO_2. *Chemical Geology*, 322-323, 11-18.

York, D. (1969) Least squares fitting of a straight line with correlated errors. *Earth and Planetary Science Letters* 5, 320-324.

York, D., Evensen, N.M., Martínez, M.L. and De Basabe Delgado, J. (2004) Unified equations for the slope, intercept, and standard errors of the best straight line. *American Journal of Physics* 72(3), 367.

Zeebe, R.E. (2011) On the molecular diffusion coefficients of dissolved CO_2, HCO_3^-, and CO_3^{2-} and their dependence on isotopic mass. *Geochimica et Cosmochimica Acta* 75, 2483-2498, https://doi.org/10.1016/j.gca.2011.02.010

Preface to Chapter 3

The diffusive boundary layer (DBL) is a thin layer of fluid at the interface with a solid surface in which frictional forces cause molecular diffusion to become the dominant mode of solute transport. The thickness of the DBL is a function of the nature and roughness of sediment substrate, as well as the turbulence of the overlying fluid or bottom-current speed. In low-energy natural aquatic environments, such as abyssal plains or lakes, the thickness of the DBL can reach several millimetres and significantly impede the diffusive rate of solutes through the sediment-water interface (SWI). Thus, precisely reproducing the DBL in the laboratory is required to simulate benthic diffusive fluxes similar to those encountered on the seafloor. Yet, an experimental apparatus allowing precise control of the DBL thickness at the SWI in the laboratory has not been described in the literature.

Here, we present a simple temperature-controlled rotating-disk system, that is suitable for use with natural sediments and is capable of generating thick DBLs. Water overlying the rotating sediment disk can be sampled discretely or continuously to monitor the chemical reaction progress. We tested the validity of the reactor by dissolving a foraminiferal sand bed in natural seawater. We found that (1) measured dissolution fluxes agree with those predicted by theory and (2) the dissolution of calcite in these seafloor-like hydrodynamic conditions is controlled by mass transfer across the DBL above the sediment bed. Guidelines for best practices under various experimental conditions, possible future developments, and the theoretical equations to compute the DBL thickness and diffusive fluxes in this reactor are described.

Chapter 3

Controlling the diffusive boundary layer thickness above the sediment-water interface in a thermostated, rotating-disk reactor*

Olivier Sulpis[1], Alfonso Mucci, Bernard P. Boudreau[2], Mark A. Barry[3] and Bruce D. Johnson[2,3]

[1]GEOTOP and Department of Earth and Planetary Sciences, McGill University, Montreal QC, Canada

[2]Department of Oceanography, Dalhousie University, Halifax NS, Canada

[3]Pro-Oceanus Systems Inc., Bridgewater NS, Canada

**Published in Limnology and Oceanography: Methods,* doi:10.1002/lom3.10309

Abstract

The diffusive boundary layer (DBL) is a thin layer of fluid at the interface with a solid surface in which frictional forces cause molecular diffusion to become the dominant mode of solute transport. The thickness of the DBL is a function of the nature and roughness of sediment substrates, as well as the bottom-current speed. In low-energy natural aquatic environments, such as abyssal plains or lakes, the thickness of the DBL can reach several millimeters and significantly impede the diffusive rate of solutes through the sediment–water interface (SWI). Thus, precisely reproducing the DBL in the laboratory is required to simulate benthic diffusive fluxes similar to those encountered in situ. Yet, an experimental apparatus allowing precise control of the DBL thickness at the SWI in the laboratory has not been described in the literature. Here, we present a simple temperature-controlled rotating-disk system, which is suitable for the use with natural sediments and that is capable of generating thick DBLs. Water overlying the rotating sediment can be sampled discretely or continuously to monitor the chemical reaction progress. We tested the validity of the reactor by dissolving a foraminiferal sand bed in natural seawater. We find that (1) measured dissolution fluxes agree with those predicted by theory and (2) the dissolution of calcite in these seafloor-like hydrodynamic conditions is controlled by mass transfer across the DBL above the bed. Guidelines for best practices under various experimental conditions, possible future

developments, and the theoretical equations to compute the DBL thickness and diffusive fluxes in this reactor are described.

3.1 Introduction

In many situations, boundary conditions are critical in defining the hydrodynamics of natural environments. In limnology and oceanography, the bottom (or benthic) boundary layer is the part of the water column that is directly affected by the drag of currents on the sediment bed; its thickness is typically on the order of meters to tens of meters (Trowbridge and Lentz 2018). Within this bottom boundary layer, current velocities decrease towards the sediment bed, until ultimately reaching zero velocity relative to the solid boundary at the sediment-water interface (SWI) of low-permeability sediments, a concept commonly termed the no-slip condition (Day 1990). A few centimetres above the SWI, internal friction within water causes viscous transport of momentum to dominate over turbulent dispersion, in a region termed the viscous sublayer (Boudreau and Jørgensen 2001). Closer to the SWI, in a thin film of water with a thickness typically on the order of a few tens of microns (e.g., in rivers or coastal areas) to millimetres (e.g., in lakes or abyssal environments), molecular diffusion becomes the dominant mode of solute transport, rather than much faster turbulent diffusion, which dominates solute transport further away from the interface. This layer is termed the diffusive boundary layer (DBL).

Numerous investigators have reported the presence of a DBL at the SWI (Archer et al. 1989; Glud et al. 1994; Gundersen and Jørgensen, 1990; Santschi et al., 1991), as well as at algal or coralline surfaces (Larkum et al. 2003; Hendriks et al. 2017; Lichtenberg et al. 2017). The thickness of this DBL depends on the nature and roughness of the substrate (Chriss and Caldwell 1982; Dade 1993; Boudreau and Jørgensen 2001; Røy et al. 2002; Han et al. 2018), as well as on the current speed of the overlying water. Slow currents generate thick DBLs, whereas fast currents cause the DBL to thin, as predicted by theory (Boudreau and Guinasso 1982; Higashino and Stefan 2004; Levich 1962) and confirmed by observations (Larkum et al. 2003; Lorke et al. 2003; Santschi et al. 1983; Santschi et al. 1991).

Across the DBL, solute transport occurs by molecular diffusion driven by a total concentration difference (gradient), $\Delta[i]$ (mol). The (steady state) flux of solute i across the DBL, J_i (mol m^{-2} a^{-1}), is then given by (Boudreau 2013; Frank-Kamenetskii 2015):

$$J_i = - k^* \Delta[i] \quad (3.1)$$

where k^* is the overall mass transfer coefficient for solute i (m a^{-1}), i.e.,

$$k^* = \frac{k_S \beta}{(k_S + \beta)} \quad (3.2)$$

where k_s is the sediment-side mass transfer coefficient (m a^{-1}) and β is the water-side (DBL) mass-transfer coefficient (m a^{-1}). β is simply the (free solution) diffusion coefficient for solute i, D_i (m^2 a^{-1}), divided by the thickness of the DBL, δ_i (m), for that solute, i.e.,

$$\beta = D_i (\delta_i)^{-1} \quad (3.3)$$

The sediment-side mass-transfer coefficient, k_s, for a solid surface without porosity is the heterogeneous rate constant for reaction within that sediment. For a porous sediment, the functionality of k_s can be complex, depending on the exact form of the kinetics and the nature of transport within the pores. Nevertheless, for a linear dissolution reaction of a solid and molecular/ionic transport within the pores, such as we will consider here, k_s has the form (Boudreau and Guinasso 1982; Boudreau 2013):

$$k_s = [\varphi (1- \varphi) k_c D_c B]^{1/2} \quad (3.4)$$

where φ is the porosity of the sediment, k_c is the apparent first-order rate constant for dissolution in the sediment (a^{-1}), D_c is the tortuosity-corrected diffusion coefficient of the solute of interest (m^2 a^{-1}), and B is the fraction of dissolvable solid in the sediment; this k_s can be determined experimentally.

If $k_S << \beta$, the diffusive flux is termed *internal* or *sediment side-controlled*, and the overall mass-transfer coefficient (k^*) tends towards k_S. Reactions under the sediment-side controlled regime include the dissolution of biogenic silica at the seafloor (Fanning and Pilson 1971; Schink and Guinasso 1975) or the release of soluble reactive phosphate from lacustrine sediments (Schauser et al. 2006; Ding et al. 2016;). Conversely, if $\beta << k_S$, virtually the totality of the gradient in solute i is comprised within the DBL above the sediment-water interface (SWI), and the

chemical flux across the DBL is termed *external* or *water-side transport-controlled*. Examples of water-side transport-controlled reaction are the dissolution of calcium carbonate at the deep-seafloor (Schink and Guinasso 1977; Santschi et al. 1991; Sulpis et al. 2017) and the accretion of manganese at the surface of deep-sea nodules (Boudreau and Scott 1978). Commonly, the diffusion through the DBL of most solutes is ruled by a combination of both regimes, termed *mixed-control*, e.g., dissolved oxygen (Jørgensen and Revsbech 1985; Hondzo 1998; Lorenzen et al. 1998; Rassmann et al., 2016) or radon (Homoky et al. 2016; Cook et al. 2018), that display concentration gradients extending on both sides of the SWI. For more details on the theoretical framework of solute exchange across the SWI, we refer the reader to the comprehensive review published by Boudreau and Guinasso (1982).

The present study describes a newly developed experimental system that reproduces the DBL above the SWI over a range of thicknesses representative of various aqueous environments and, therefore, applicable to studies of external or mixed-controlled chemical exchanges through the DBL.

Reproducing natural scale DBLs at the SWI in laboratory experiments has been a long-term challenge for experimentalists. Attempts to simulate chemical boundary layers in laboratory flumes (Steinberger and Hondzo 1999; Røy et al. 2004) or stirred reactors (Keir 1983; Javadi and Khalili 2009) and benthic chambers (Santschi et al., 1983) have been less than satisfactory for several reasons. (1) In a classical linear flume (***Fig. 3.1a***), there is inevitably a leading edge of the reactive sediment on the flume floor. The chemical boundary layer does not exist until that edge is reached by the flow, and it grows downstream for a considerable length (roughly proportional to the square-root of the distance); this means that a dissolution reaction, as we consider, is subject to internal control at the leading edge and can only shift to transport control somewhere downstream, where the DBL has become thick enough to exert its control. No such edge exists on the seafloor, and the water-side control always occurs for an appropriately fast reaction. Measurements in such laboratory flumes are thus compromised. (2) While stirred reactors (***Fig. 3.1b***) have been designed as an alternative to flumes, they suffer from exactly the same problem. The main flow may appear to be simply a circular flow over the bed surface, but that belies a pressure gradient created by the rotating bar or disk, which engenders a secondary flow that sweeps down the sides of the chamber and then across the sediment. The secondary flow encounters the

sediment at the floor-wall intersection, where a chemical boundary layer will initiate and grow downstream across the sediment, as the flow crosses the floor. Thus, stirred reactors only hide the growing boundary layer problem; they do not eliminate it. Efforts have been made to replace rotating disks with a cone to counteract the pressure gradient (e.g., Javadi and Khalili 2009), but that has enjoyed questionable success, from a physicochemical point of view, as the angle of the cone then needs to be matched exactly to the rotation speed and that is exceedingly difficult to implement. Race-track-shaped flumes also suffer from this exact problem. (3) All these experimental systems typically fail to reproduce the slow flows encountered in low energy environments, such as abyssal plains or lakes, where the bottom currents are on the order of a few millimeters per second and the DBLs of several mm thick (Frenzel et al. 1990; Dade 1993; Sulpis et al. 2018). (4) Finally, measurements of fluxes from benthic chambers cannot be compared with any expected theoretical values, as no theory of mass transfer for such chambers currently exists. The solution for the flux with a growing laminar boundary layer in a flume does exist (e.g., Apelblat 1980) but it is not in closed form, making it inconvenient to use; unfortunately, flows under deep-sea environmental conditions are usually turbulent in such flumes, making that solution approximate.

As a viable alternative, we build upon the development of rotating-disk reactors (***Fig. 3.1c***) that have been used extensively to study single crystal dissolution and precipitation kinetics (Tomlan and Hudson 1971; Sjöberg and Rickard 1983; Alkattan et al. 1998; Fredd and Fogler 1998; Gautelier et al. 1999; Chang and Abbad 2011) and which have a well-defined hydrodynamic (Schlichting 1968, pp. 93-99, 232-235, 508-509, 606-610) and mass transfer theory (Levich 1962, pp. 157-159). We adapt this approach for use with a (non-cohesive) sediment, where the sediment disk is mounted at the bottom of the reactor, rather than suspended upside down in the reactor.

3.2 Materials and procedures

3.2.1 Experimental design

The design and technical description of the rotating disk reactor are presented in ***Fig. 3.2***. This reactor was designed to simulate slow flow in a reaction chamber containing a rotating-sediment disk, where the entire water velocity gradient is reproduced, from zero velocity at the sediment-water interface (no-slip condition), to constant full velocity at the top of the water level.

The reactor can be thermally controlled, and the overlying water can be sampled without disturbing the flow.

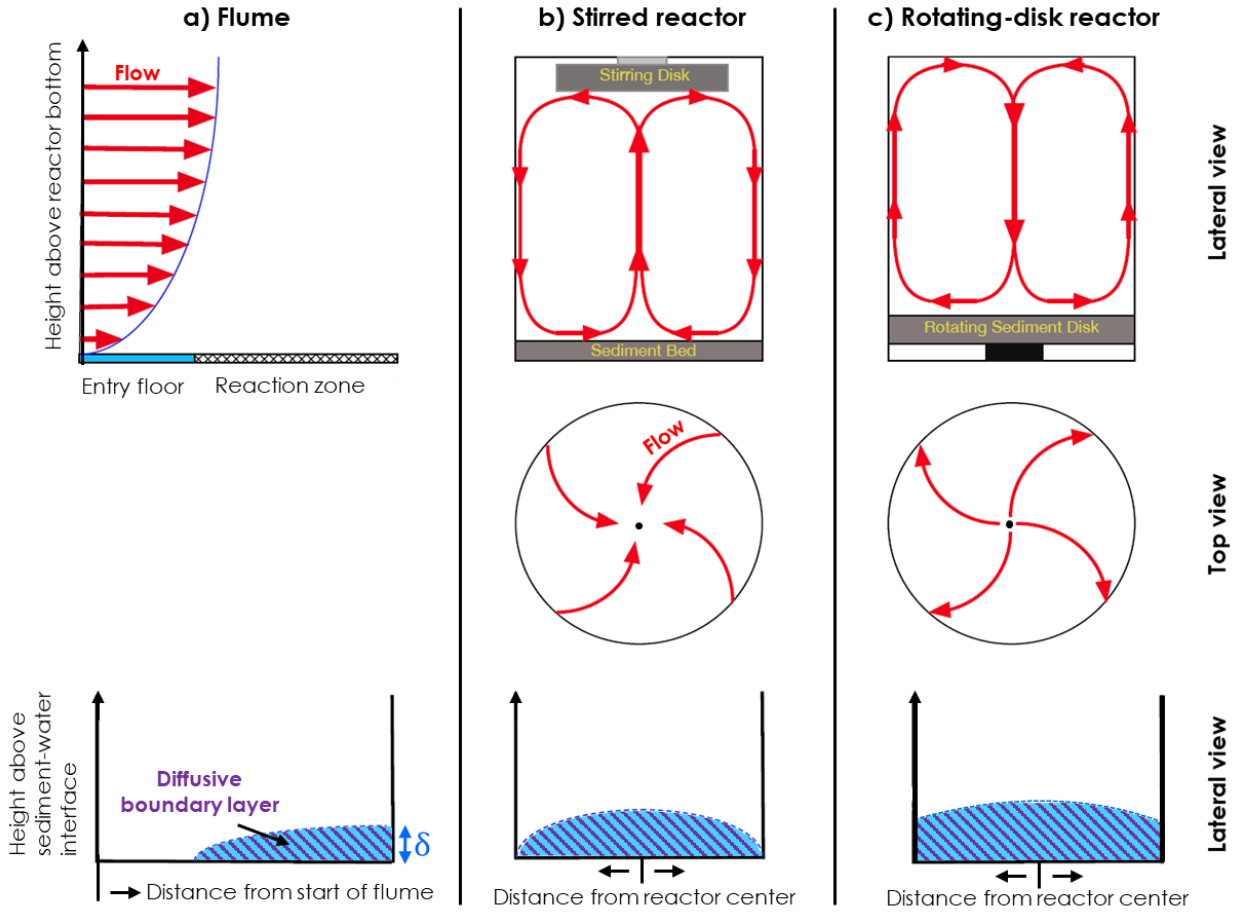

Fig. 3.1 | *Comparison of the flow and assumed diffusive boundary layer spatial patterns in three different experimental apparati.*

A cylindrical polyvinyl chloride (PVC) disk support - the sediment container, ***Fig. 3.2f,g*** - is screwed atop a stainless-steel shaft (***Fig. 3.2l***) driven by a high-torque motor (***Fig. 3.2p***) through a belt-and-pulley system (***Fig. 3.2m,o***). The shaft is maintained in its vertical axis by two ball bearings (***Fig. 3.2j***), located on either side of the height-adjustable belt drive (***Fig. 3.2m***). A nitrile seal (***Fig. 3.2h***) was placed around the shaft at the base of the reactor chamber, which holds the experimental solution and contains the rotating sediment disk, to prevent fluid leaks. The shaft height-adjustable pulley was connected to a motor with a rubber belt to mitigate the propagation of motor vibrations to the reactor chamber and prevent disruption of the DBL or flow. The motor

was fixed vertically and powered by 12V power supply through a variable potentiometer with digital power display (not shown), to precisely control the rotation speed. The reactor chamber is jacketed by a ~1 cm inner diameter wall through which water can be pumped from a thermostated water-recirculating bath to control the temperature of the experimental solution and sediment disk. PVC pieces a–d and i (in ***Fig. 3.2***) were glued together with methylene chloride under a fume hood. Finally, the reactor was wrapped in an opaque and thermally-insulating material, e.g., aluminium foil paper, to maintain a temperature-controlled environment and prevent light penetration; the latter is needed to curb the proliferation of photosynthetic organisms during week- to month-long experiments.

During the experiment, the water in the reactor can be continuously or discretely analysed to follow the evolution of the reaction. In the present study, we tested the reactor by measuring the dissolution kinetics of a $CaCO_3$-rich sediment. In this flow-through experiment, an undersaturated solution is introduced in the reactor, driving the solution to a new steady state controlled by the rate of introduction of the inlet solution and the rate of dissolution of the $CaCO_3$ in the sediment. The input solution was injected into the reactor chamber at a constant rate through a 0.51 mm inner diameter (ID) Tygon polyvinylchloride (PVC) tube, using a multi-channel peristaltic pump (Gilson's Minipuls™ 3 Peristaltic Pump). The pumping rate was determined for each setting in each experiment by weighing the amount of solution pumped out of the reactor over a fixed period of time. To keep a constant volume of solution in the reactor, the solution was withdrawn from the reactor by the same pump through a 0.76 mm ID tube fixed at the surface of the solution, as shown in ***Fig. 3.3***. For users carrying out experiments on water containing suspended particles, a filter should be mounted at the mouth of the output tube to avoid clogging or modifying the solid:solution ratio. Sensors (e.g., pH electrode) should not be inserted directly within the reactor chamber, to avoid disrupting the DBL. Alternatively, discrete measurements should be performed in a separate vial where the outlet solution is collected or using sensors mounted within the inner wall to the reactor without altering its geometry or surface roughness. The former method could be adapted to monitor sediment diffusive fluxes by continuous flow analysis of dissolved elements or isotopic ratios (Brenna et al. 1997; Stoll et al. 2001; St-Jean 2003).

Thermostated rotating-disk reactor

Pos.	Nb.	Description	Material
a	1	reactor top wall	polyvinyl chloride
b	1	thermostated bath connector	polyvinyl chloride
c	1	reactor external wall	polyvinyl chloride
d	1	reactor internal wall	polyvinyl chloride
e	1	Screw	stainless steel
f	1	disk wall	polyvinyl chloride
g	1	disk support	polyvinyl chloride
h	1	rotary shaft seal	nitrile rubber / acrylic
i	1	reactor bottom wall	polyvinyl chloride
j	2	ball bearing	Steel
k	1	ball bearing support	stainless steel
l	1	rotary shaft	stainless steel
m	2	height adjustable pulley	stainless steel
n	1	reactor support cylinder	stainless steel
o	1	pulley belt	polyurethane rubber
p	1	high torque motor	-

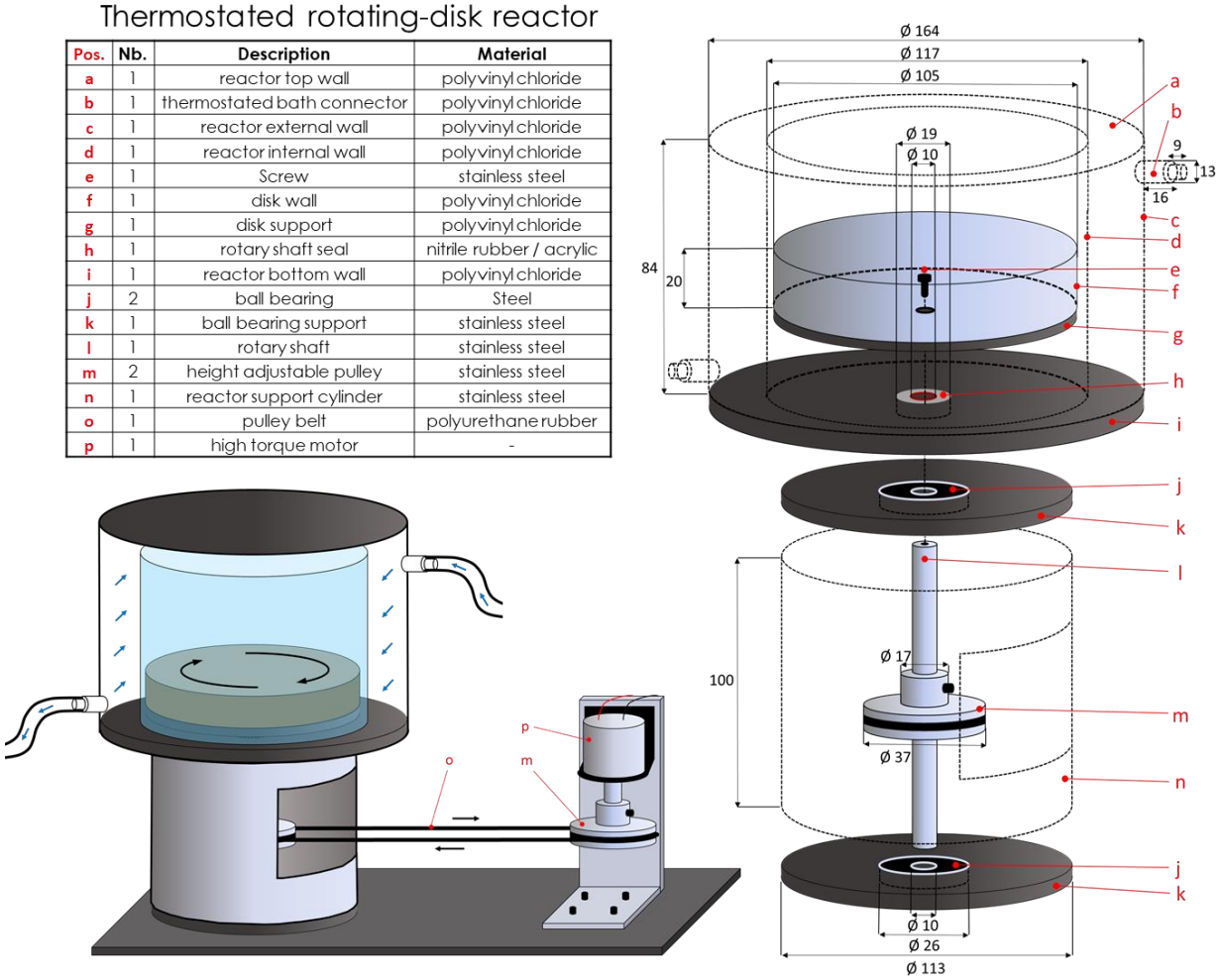

Fig. 3.2 | *Technical drawing of the thermostated, rotating-disk reactor.*

After each experiment, the upper section of the reactor (***Fig. 3.2a-i***) can be removed from its base (***Fig. 3.2j-n***) for cleaning. Under the experimental conditions tested to date, i.e., temperatures between 6 and 25 ºC, rotation speeds between 1 and 10 rpm, seawater salinities between 0 and 35, the shaft can rotate for several weeks without interruption or leakage. If the seal deteriorates with time or usage, it can easily be replaced, as it is not glued to the reactor bottom wall, but simply pressure fitted. It is also preferable that the sediment disk holder rotate counter-clockwise, so that it does not unscrew from the driving shaft.

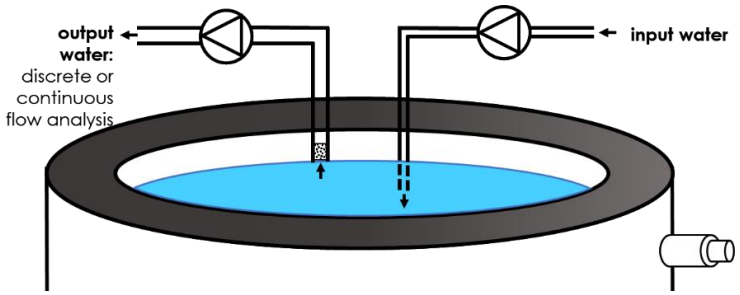

Fig. 3.3 | *Schematic representation of the flow-through system of the rotating-disk reactor.*

3.2.2 Rotating disk theory

The motion of the seawater in the reactor chamber is driven by the spinning action of the immersed sediment disk, acting as a pump drawing in fluid axially and driving it away towards the outer edge of the disk in an outward spiral (von Karman 1921; Escudier 1984; Hyun and Kim 1987). Levich (1962) modelled the rotating-disk flow system in a cylindrical coordinate system where the continuity and Navier-Stokes equations are decomposed into a radial, azimuthal and axial component. Far above the SWI, the axial fluid velocity component is constant and downward while the other velocity components are nearly zero. In a thin layer of fluid adjacent to the SWI, the water is dragged by the rotating disk with an azimuthal velocity that increases as the surface of the disk is approached, until the azimuthal velocity of the disk is attained just above the SWI (Bircumshaw and Riddiford 1952; Levich 1962). Solutions to the equations that describe the velocity distribution throughout the body of the viscous fluid are reported in Schlichting (1968), and solutes concentration profiles, DBL thicknesses and molecular diffusion fluxes above a rotating disk were derived and reported in the pioneering work of Levich (1962). It is not our intent here to review this theory; instead we refer the reader to the numerous, previous studies in which mathematical descriptions and solutions to the rotating-disk hydrodynamics are provided (Levich 1962; Brady and Durlofsky 1987; Chang and Abbad 2011; Imayama 2012).

As noted by Levich (1962), the DBL thickness for a given species i, δ_i, on a rotating disk is largely not a function of the distance from the axis of rotation, but is constant over the entire disk surface (except very close to the external edge, potentially subject to eddies), i.e., the DBL thickness can be considered as radially uniform. Assuming that the disk is sufficiently large, edge effects become negligible and, regardless of the distance from the rotation axis, the disk reactive surface is uniformly accessible from the standpoint of diffusion (Levich 1962; Frank-Kamenetskii

2015). Under this assumption, assuming laminar flow and steady state, δ_i is a function of the (free solution) diffusion coefficient of the species, the kinematic viscosity of the fluid (ν, in $m^2\ s^{-1}$), and the angular velocity of the disk (ω, in rad s^{-1}):

$$\boldsymbol{\delta_i = 1.61 \left(\frac{D_i}{\nu}\right)^{\frac{1}{3}} \sqrt{\frac{\nu}{\omega}}} \qquad \textbf{(3.5)}$$

This equation has been extensively and successfully applied by many experimentalists (Gregory and Riddiford 1956; Ellison and Cornet 1971; Lund et al. 1973; Sjöberg and Rickard 1983; Compton and Daly 1987), supporting the uniformity assumption of negligible DBL radial-dependency.

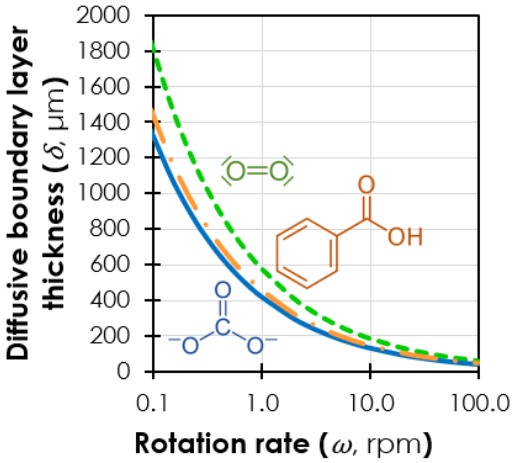

Fig. 3.4 | *Predicted DBL thicknesses (δ) as a function of the disk rotation speed (ω) in water at 10 °C for the carbonate ion (CO_3^{2-}, solid blue line), dissolved oxygen (O_2, dashed green line) and benzoic acid ($C_7H_6O_2$, dotted dashed orange line) computed using* ***Eq. 3.5****.*

The microtopography of the sediment bed can lead to small-scale horizontal variations of the DBL thickness, as documented by Gundersen and Jørgensen (1990): the DBL being thinner over the "peaks" and thicker over the "troughs". In this study, we treat the DBL above our sediment disk as a single, mean value, as we assume that the DBL negative anomalies on the micro-"peaks" approximately compensate for the positive anomalies on the micro-"troughs". We acknowledge, however, that this treatment may oversimplify the 3-dimensional structure of the DBL over rough, natural sediment bed surfaces, which is not the case of the sediment used in this study, described below. To illustrate to the reader the range of DBLs achievable by the rotating-disk reactor, we report, in ***Fig. 3.4***, the theoretical DBL thicknesses for O_2 (D_{O_2} = 1.33 x 10^{-9} $m^2\ s^{-1}$ (Han and Bartels 1996)), CO_3^{2-} ($D_{CO_3^{2-}}$ = 5.21 x 10^{-10} $m^2\ s^{-1}$ (Zeebe 2011)) and benzoic acid

($C_7H_6O_2$, $D_{C_7H_6O_2}$ = 6.7 x 10^{-10} m^2 s^{-1} (Delgado 2007)) as a function of the rotating speed of the disk (ω), for a temperature of 10 ºC in freshwater (ν = 1.31 x 10^{-6} m^2 s^{-1}).

By adopting ***Eq. 3.5*** and substituting it into ***Eqs. 3.1*** and ***3.2***, the expression for the diffusive flux of the species i (J_i) across the DBL above the rotating sediment disk becomes:

$$\boldsymbol{J_i = \frac{k_{s,i} \times 0.62\left(\frac{D_i^{\frac{2}{3}}\omega^{\frac{1}{2}}}{\nu^{\frac{1}{6}}}\right)}{k_{s,i} + 0.62\left(\frac{D_i^{\frac{2}{3}}\omega^{\frac{1}{2}}}{\nu^{\frac{1}{6}}}\right)}([i]_s - [i]_0)} \quad \textbf{(3.6)}$$

where $[i]_s$ is the concentration of i at or below the SWI, at the lower limit of the concentration gradient, i.e., at saturation, and $[i]_0$ is the concentration of i in the bulk water, i.e., at the top of the water height in the reactor chamber. Note that, in our experimental apparatus, the sediment disk is placed at the bottom of the reactor chamber; thus, the diffusive flux J_i is upward.

3.2.3 Methods validation

We assessed the validity of the rotating-disk reactor by measuring alkalinity fluxes resulting from $CaCO_3$ dissolution in a sediment disk containing natural calcitic grains (foraminifera) immersed in natural seawater and then comparing these measurements with the predicted diffusive fluxes (J_i) and DBL thicknesses (δ_i) from the theory described above.

Calcite dissolution in an aqueous solution can be described by the reaction:

$$\mathbf{CaCO_{3\,(s)} \leftrightarrow Ca^{2+}_{(aq)} + CO_3^{2-}{}_{(aq)}} \quad \textbf{(3.7)}$$

In seawater, at a salinity of 35, $[Ca^{2+}]$ is about two orders of magnitude larger than $[CO_3^{2-}]$. Given the nearly invariant $[Ca^{2+}]$ in the deep ocean, and in our reactors, the saturation state of seawater with respect to calcite, i.e., $\Omega_C = [Ca^{2+}][CO_3^{2-}]/K^*_{sp}$, where K^*_{sp} is the stoichiometric solubility constant of calcite at *in situ* T, P and S, as given in Mucci (1983) and Millero (1995), can simply be represented by the ratio of the carbonate ion concentration in the overlying water, $[CO_3^{2-}]_{SW}$, to the carbonate ion concentration at equilibrium with calcite, $[CO_3^{2-}]_{eq}$. The quantity ($[CO_3^{2-}]_{eq} - [CO_3^{2-}]_{SW}$) is a measure of the disequilibrium and the driving force that controls the rate (r) of the

calcite dissolution reaction at the sediment-water interface. Here, we consider the calcite dissolution rate at the sediment-water interface as a diffusive flux (J_{CO3}) in response to a CO_3^{2-} concentration gradient ($\Delta[CO_3^{2-}]$), following ***Eq. 3.1***.

We used a natural foraminiferal sand from the top 10 cm of a sediment gravity core sampled in the Southern Central Pacific Ocean (26° 5.07' S; 146° 45.01' W) at 1916 m-depth in April 2010. This sediment was composed at ~98% of *Globigerinoides ruber* (T. de Garidel-Thoron, pers. comm.). These foraminifera were rinsed with deionized water and dried at room temperature before the experiments. The foraminiferal sediment was then mixed with natural seawater collected at ~400 m depth in the Gulf of St. Lawrence in May 2017. The seawater was aged for several months in polypropylene carboys before being filtered and calcite-equilibrated following the protocols described in Sulpis et al. (2017). The main criteria used to assess the suitability of the sediment was the cohesion and stability of the mixture, especially at the sediment-seawater interface when the beaker was moved. The fresh disks were stored in calcite-equilibrated seawater and kept in the dark to avoid the proliferation of bacteria until used within a few days. Based on weight loss upon drying at low temperature (<50°C), a solid density of 2.71, and the salinity of the seawater, the primary porosity (φ) of the foraminiferal sand sediment was estimated at 0.84 ± 0.03 (n = 3).

The calcite contained in the simulated sediment, if exposed to a solution undersaturated with respect to calcite, should dissolve. In order to obtain an undersaturated solution, a fraction of the treated seawater was acidified by adding dilute hydrochloric acid (~1N) to reduce the total alkalinity (*TA*) from ~2300 μmol kg^{-1} to ~400 μmol kg^{-1} and Ω_C from ~4 to ~0.15. Seawater acidification was performed following the protocols described in Sulpis et al. (2017). This acidified seawater served as the input solution and was pumped into the reactor, initially filled with calcite-equilibrated seawater (Ω_C = 1).

The evolution of the dissolution reaction was assessed by monitoring the pH_T of the experimental solution by collecting the output seawater in a separate, flow-through and sealed vial at a fixed acidified seawater pumping rate. Once a steady-state pH_T was achieved, an aliquot of the output solution was collected and analysed to determine the steady-state *TA*, *S* and soluble reactive phosphorus (*SRP*) concentration. The pumping rate was then increased and, consequently, the residence time of the solution in the reactor, as well as the saturation state of the reactor solution

decreased, triggering an increase in the calcite dissolution rate. Residence times of the input solution in the reactor varied between 28 and 303 hours, corresponding to input flow rates between 7 and 2 g hr^{-1}.

Following Sulpis et al. (2017), the dissolution rate r (mol m^{-2} a^{-1}) was determined from the difference in the composition of the input and output solutions, according to:

$$\boldsymbol{r = \frac{m_{sw}(TA_{output} - TA_{input})}{2\,A\,\Delta t}} \qquad \textbf{(3.8)}$$

where m_{SW} is the mass of seawater in the reactor chamber, TA_{output} is the steady-state TA of the output solution (see ***Fig. 3.3***), TA_{input} is the TA of the input solution, A is the sediment surface area and Δt is the residence time of seawater in the reactor chamber.

3.2.4 Analytical procedures

The pH_T of the output solution was measured in a flow-through, sealed vial with a Radiometer Analytical® GK2401C combination glass electrode, connected to a Radiometer Analytical® PHM84 pH/millivolt-meter. Prior to each measurement, the electrode response (in mV) was calibrated against three NIST-traceable buffer solutions: pH-4.00, pH-7.00 and pH-10.00 at 25°C, and a TRIS buffer solution with an assigned pH_T of 8.100 at S_P = 35 and 25°C to convert these measurements to the "total" hydrogen ion concentration scale (pH_T).

TA was determined by potentiometric titration of both the initial reservoir solution and subsequent steady-state solutions with a dilute hydrochloric acid solution (0.005N < [HCl] < 0.010N, according to the TA of the sample), using an automated Radiometer (TitraLab865®) titrator and a Red Rod® combination pH electrode (pHC2001). The dilute HCl titrant was calibrated prior to, during, and after each titration session, using certified reference materials (CRM Batch #140 and #154) provided by Andrew Dickson (Scripps Institute of Oceanography). The reproducibility of the method was better than 0.5%. The uncertainties presented in this study for total alkalinity, as well as steady-state pH_T, were estimated based on multiple replicate measurements of each sample.

The salinity of the experimental solution was monitored regularly by potentiometric titration of an aliquot of the output solution with a $AgNO_3$ solution calibrated with IAPSO standard

seawater. The measurements were performed with an automated Radiometer (TTT80) titrator, a silver electrode, and a mercuric sulphate reference electrode. The reproducibility was better than 0.2%.

The *SRP* concentration of the initial reservoir and steady-state solutions was determined spectrophotometrically using the technique developed by Murphy and Riley (1962) and described in Grasshoff et al. (1999). The absorbance of the phosphomolybdate reaction product was measured manually at 880 nm with a Hewlett-Packard Agilent 8453 UV-visible spectrophotometer using a 10-cm cell. The detection limit was 0.01 µM and the reproducibility was better than 0.5%. Calibration curves were constructed by 4 successive dilutions of a 10 mM standard phosphate stock solution prepared in a 0.7M NaCl solution to prevent salt effects and the corresponding R^2 values were always better than 0.999.

The Microsoft Excel version of CO2SYS (Pierrot et al. 2006), based on the original algorithm of Lewis and Wallace (1998), was used to calculate the initial reservoir and steady-state solution pCO_2, $[CO_3^{2-}]_{eq}$ and $[CO_3^{2-}]_{SW}$ from the steady-state pH_T and *TA*, at *in situ T*, *S* and [*SRP*]. The uncertainties on $[CO_3^{2-}]_{eq}$ values reported here were computed separately and included errors of the solubility constant estimate. All calculations were carried out on the total hydrogen ion concentration scale, using the stoichiometric carbonic acid dissociation constants determined by Lueker et al. (2000), the total boron concentration $[B]_T$ value from Uppström (1974), and the standard acidity constant of the HSO_4^- ion from Dickson (1990).

3.3 Results

We ran 16 distinct, week-long dissolution experiments at 3 different disk-rotation speeds, over a range of ($[CO_3^{2-}]_{eq} - [CO_3^{2-}]_{SW}$) values from near equilibrium ($[CO_3^{2-}]_{eq} - [CO_3^{2-}]_{SW}$ = 3.4 µmol kg^{-1}) to highly undersaturated ($[CO_3^{2-}]_{eq} - [CO_3^{2-}]_{SW}$ = 28.2 µmol kg^{-1}). The corresponding saturation states with respect to calcite (Ω_C) are 0.94 and 0.33, respectively. Calculated pCO_2 in steady-state aliquots varied between 382 and 790 µatm, measured salinities ranged from 34.82 to 35.90 and [*SRP*] was between 0.9 and 3.1 µmol kg^{-1}. We report the data obtained from each experiment in ***Table 2.1***.

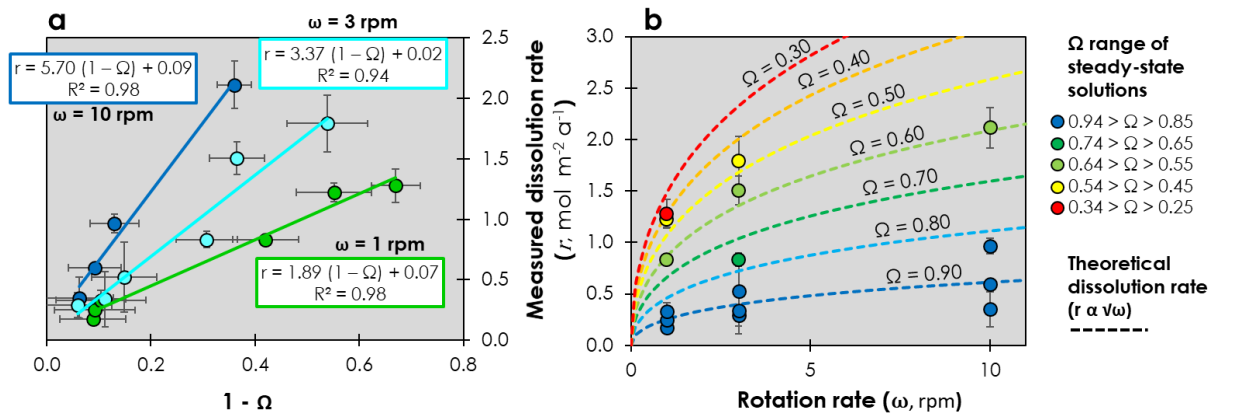

Fig. 3.5 | *(a) Measured calcite dissolution rates (r) as a function of the steady-state undersaturation state of seawater with respect to calcite (1 - Ω_C), for three different rotation rates (ω = 1, 3 and 10 rpm, shown in green, turquoise and blue, respectively). Solid lines are linear regression fits to the data for each rotation-rate group, shown along with their equations and coefficients of determination (R^2). (b) Measured r as a function of ω for different groups of steady-state Ω_C. Dashed lines indicate the theoretical r values computed using* ***Eq. 3.6*** *as a function of ω for a range of Ω_C, for comparison with our data. Each data point is shown with an error bar that represents one standard deviation.*

Figure 3.5 presents the measured calcite dissolution rates normalized by the sediment-water interfacial surface area, as a function of (a) calcite undersaturation state with respect to calcite (1 -Ω_C) and (b) disk rotation rate. The measured dissolution rates follow a square-root dependency on the disk-rotation rate predicted by ***Eq. 3.6*** and are linearly dependent on (1 – Ω_C) over the range of undersaturation rates investigated. A comparison of the observed dissolution rates, estimated from the alkalinity fluxes, using ***Eq. 3.8***, with theoretical dissolution fluxes, computed as a function of the disk rotation rate and ($[CO_3^{2-}]_{eq} - [CO_3^{2-}]_{SW}$) from ***Eq. 3.6***, is presented in ***Fig. 3.6a***. Our measured dissolution rates (vertical axis in ***Fig. 3.6a***) are linearly correlated with the theoretical dissolution rates (horizontal axis in ***Fig. 3.6a***) with a coefficient of determination (R^2) of 0.96. In ***Fig. 3.6b***, we compare the diffusive boundary layer thicknesses computed from the measured dissolution rates, using ***Eqs. 3.1-3.3***, with the theoretical diffusive boundary layer thicknesses derived using ***Eq. 3.5***. Note that we did not measure directly the thickness of the diffusive boundary layer. Instead, the values on the vertical axis of ***Fig. 3.6b*** are the diffusive boundary layer thicknesses that are required to explain our measured dissolution fluxes, as computed using ***Eqs. 3.1-3.3***; thus, ***Fig. 3.6b*** compares values inferred from measurements with values from the Levich (1962) theory. A statistical analysis reveals that the

inferred values are linearly correlated to the predicted values with a R^2 of 0.80. These results show that diffusive fluxes in the rotating-disk reactor can be successfully predicted by the Levich (1962) theory.

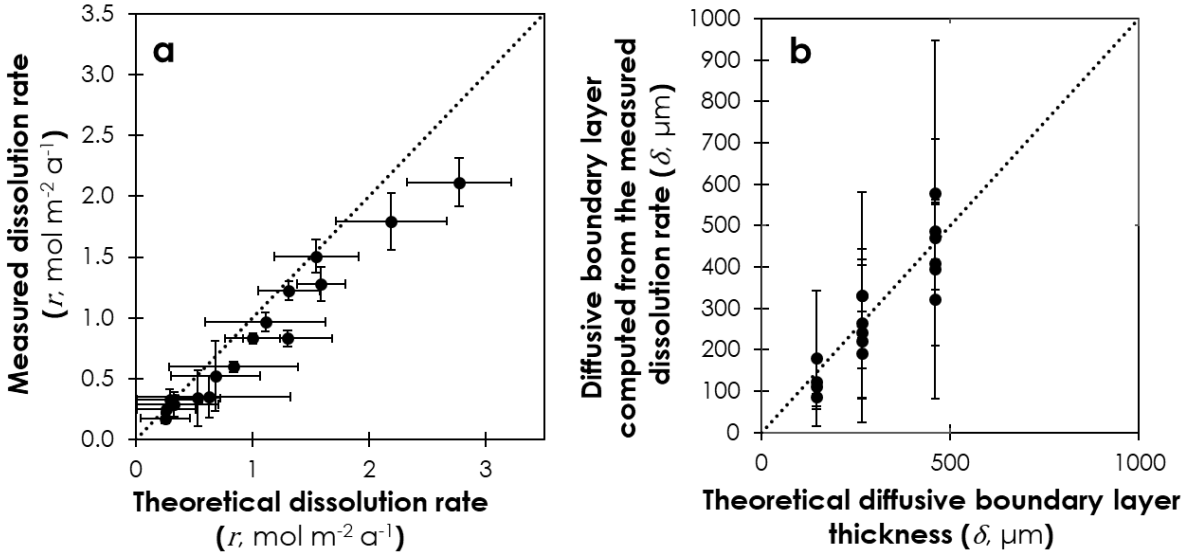

Fig. 3.6 | *Scatter plots of measured compared to theoretical values for (a) the calcite dissolution rate at the sediment-water interface and (b) the diffusive boundary layer thickness. The stippled black line stands for a perfect agreement between measured and predicted values. Each data point is shown with an error bar that represents one standard deviation.*

To interpret these results in terms of controlling mechanism for calcite dissolution at the sediment-water interface, we compared our results with theoretical sediment-side, water-side and overall mass-transfer coefficients as a function of the disk-rotating speed. To obtain the mass-transfer coefficient for each of the data points, we divided the measured dissolution rate by the disequilibrium CO_3^{2-} concentration $([CO_3^{2-}]_{eq} - [CO_3^{2-}]_{SW})$; these experimental mass-transfer coefficients are the black circles in ***Fig. 3.7***. The sediment-side mass-transfer coefficient for calcite dissolution in sediment beds (k_S, the dashed blue line in ***Fig. 3.7***) is from Sulpis et al. (2017), set as k_S = 326.9 ± 39.5 m a^{-1}, which is similar to the value calculated by Boudreau (2013) from the Keir (1983) data. The water-side mass-transfer coefficient (β, the dashed green line in ***Fig. 3.7***) is obtained by dividing the diffusion coefficient of CO_3^{2-} at 25°*C* by the diffusive boundary layer thickness in our reactor, obtained from the Levich (1962) theory through ***Eq. 3.5***. Finally,

the overall mass-transfer coefficient (k*, the solid red line in ***Fig. 3.5***) was derived from ***Eq. 3.2***. As can be seen in ***Fig. 3.7***, our data fall on the predicted overall mass-transfer coefficients and follow a square-root dependency on the disk-rotation speed, as it should be observed for a water-side transport-controlled reaction. In addition, $\beta << k_S$ for the entire range of hydrodynamic conditions investigated in this study. These experimental results constitute further evidence that, in these deep-seafloor-like experimental conditions, and in the absence of respiration-driven dissolution, calcite dissolution is controlled by diffusion through the diffusive boundary layer above the sediment bed.

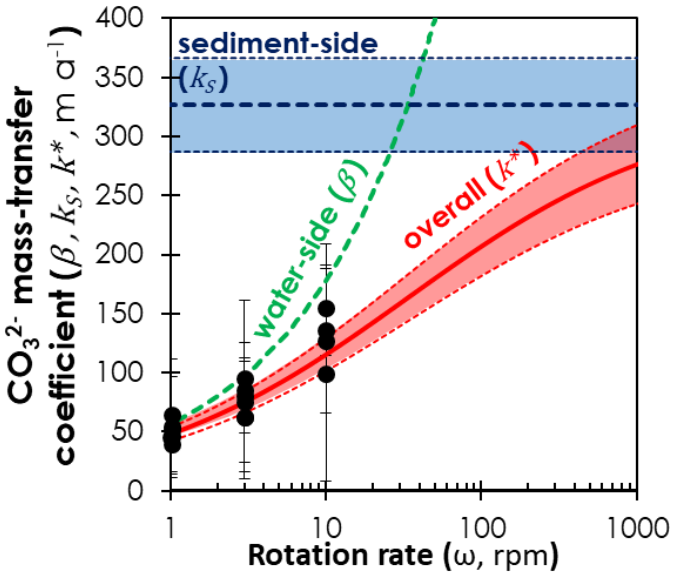

Fig. 3.7 | *A comparison of the experimental mass-transfer coefficients (black dots) with the predicted overall mass-transfer coefficient (k*, solid red line, as calculated from **Eq. 3.2**), its sediment-side limit (k_S, blue dashed line, obtained from Sulpis et al. (2017)), and the purely water-side transport limit (β, the green dashed line, calculated by dividing the CO_3^{2-} diffusion coefficient by the DBL thickness from **Eq. 3.5**), all as a function of the disk-rotation rate (ω). Each data point is shown with an error bar that represents one standard deviation.*

3.4 Discussion

We initially designed this rotating-disk reactor to reproduce well-defined hydrodynamics (flow) above a sediment bed in the laboratory, generating diffusive boundary layers with thicknesses representative of most natural sedimentary aquatic environments, including very low-

energy environments such as deep lakes or abyssal plains. Although experimental systems have been developed in the past to simulate benthic hydrodynamics (Keir 1983; Javadi and Khalili 2009), these systems often generate uncharacterized turbulence (Sulpis et al. 2017), spawning DBLs of unknown thicknesses. Whereas flumes (Steinberger and Hondzo 1999; Røy et al. 2004;) seemingly offer a potential solution to this issue, as noted above, the resulting DBLs are again difficult to calculate, compromising the interpretation of experimental results.

We have adapted the rotating-disk reactors traditionally used for the study of single crystal dissolution/precipitation kinetics (Tomlan and Hudson 1971; Sjöberg and Rickard 1983; Alkattan et al. 1998; Fredd and Fogler 1998; Gautelier et al. 1999; Chang and Abbad 2011) to a (non-cohesive) sediment, placing the disk at the bottom of the reactor and inducing a rotation of the sediment through a pulley system in order to attenuate motor vibrations. Based on our experimental results, we believe that the reactor fulfils all of our initial requirements. It produces a well-defined flow of water over a sediment disk, unaffected by stirrer/motor vibrations or turbulence or by the presence of sensors, and generates diffusive fluxes and diffusive boundary layer thicknesses that are well predicted by theory. The latter are similar in thickness to deep lake and ocean environments.

We note that during one experiment carried out using sediment disks of pure synthetic calcite and quartz sand, i.e., with a non-cohesive texture and with grains readily movable, we observed mm-scaled spiralling sediment ripple marks developing at the surface of the sediment after a few weeks. These sedimentary structures are usually observed on sediment beds under low flow regimes (Boggs Jr., 2012). Thus, our system is also able to reproduce, in the laboratory, natural sedimentary structures.

In addition to its ability to successfully reproduce DBLs encountered in benthic environments, we wish to highlight a few practical benefits of this reactor. First, this reactor can be assembled at a relatively low cost. All components and materials can be purchased from traditional suppliers. With the exception of applications involving trace metals or requiring peculiar properties, engineering the different components out of PVC and stainless steel, as shown in ***Fig. 3.2***, should suffice. Second, the reactor is portable and, thus, can be brought to the field to perform experiments on freshly sampled sediments, but a mobile thermostatic system and

peristaltic pump may be required. Third, the reactor can be entirely disassembled for maintenance and cleaning.

Table 3.1 | *Description of dissolution experiments, steady-state seawater chemistry and experimental results for sediment disks containing foraminifera in natural seawater. ω is the disk rotation rate, Δt is the residence time of water in the reactor, A is the surface area of the sediment disk, m_{SW} is the mass of water in the reactor, pH_T is the steady-state seawater pH on the total proton concentration scale, TA_{out} is the steady-state total alkalinity, $[CO_3^{2-}]_{SW}$ is the steady-state CO_3^{2-} concentration, [SRP] is the steady-state soluble reactive phosphate concentration, S is the steady-state salinity, r is the measured calcite dissolution rate, δ is the diffusive boundary layer thickness computed from the measured r and k* is the overall CO_3^{2-} mass-transfer coefficient computed from the measured r.*

Experiments characteristics			Steady-state seawater chemistry						Results		
Δt (h) (±0.1)	A (cm^2) (±5%)	m_{SW} (g) (± 0.1)	pH_T (±0.003)	TA_{out} (µmol kg^{-1})	$[CO_3^{2-}]_{SW}$ (µmol kg^{-1})	Ω_C	[SRP] (µmol l^{-1})	S	r (mol m^{-2} a^{-1})	δ (µm)	k^* (m a^{-1})
Disk-rotation rate (ω) of 1 rpm											
27.6	35.3	212.7	7.423	523.1 ± *1.8*	13.4 ± *1.8*	0.33 ± *0.05*	0.9	35.12	1.3 ± *0.1*	486 ± *69*	45 ± *6*
52.9	35.3	212.7	7.471	634.4 ± *2.8*	18.2 ± *2.9*	0.45 ± *0.07*	1.1	35.22	1.2 ± *0.1*	409 ± *65*	52 ± *8*
80.2	35.3	212.7	7.529	1077.1 ± *2.6*	36.1 ± *2.7*	0.91 ± *0.08*	1.0	35.90	0.2 ± *0.1*	395 ± *314*	54 ± *43*
95.5	35.3	212.7	7.529	1110.5 ± *3.1*	36.6 ± *3.2*	0.90 ± *0.09*	1.0	34.99	0.3 ± *0.1*	322 ± *240*	64 ± *48*
105.4	35.3	212.7	7.523	721.2 ± *2.3*	23.3 ± *2.4*	0.58 ± *0.06*	0.9	35.54	0.8 ± *0.1*	470 ± *82*	47 ± *8*
198.3	35.3	212.7	7.509	1132.2 ± *1.9*	36.4 ± *1.9*	0.91 ± *0.06*	1.0	35.78	0.2 ± *0.1*	579 ± *369*	39 ± *25*
Disk-rotation rate (ω) of 3 rpm											
39.1	72.4	537.4	7.498	605.1 ± *3.0*	18.4 ± *3.1*	0.46 ± *0.08*	2.3	35.75	1.8 ± *0.2*	242 ± *50*	80 ± *16*
64.9	72.4	537.4	7.506	1095.0 ± *2.0*	34.5 ± *2.0*	0.85 ± *0.06*	1.1	35.21	0.5 ± *0.3*	264 ± *179*	75 ± *51*
75.8	72.4	537.4	7.568	740.0 ± *1.8*	25.9 ± *1.8*	0.64 ± *0.05*	2.0	35.00	1.5 ± *0.1*	191 ± *36*	95 ± *18*
82.7	72.4	537.4	7.524	1087.8 ± *1.3*	35.8 ± *1.3*	0.89 ± *0.04*	1.0	35.46	0.3 ± *0.2*	331 ± *249*	62 ± *47*
167.8	72.4	537.4	7.548	819.1 ± *2.0*	28.0 ± *2.1*	0.69 ± *0.06*	1.0	35.41	0.8 ± *0.1*	331 ± *73*	62 ± *14*
192.6	72.4	537.4	7.523	1172.3 ± *2.0*	38.3 ± *2.1*	0.94 ± *0.07*	1.4	35.09	0.3 ± *0.1*	221 ± *196*	85 ± *76*
Disk-rotation rate (ω) of 10 rpm											
52.4	72.4	548.5	7.578	723.2 ± *0.6*	25.9 ± *0.6*	0.64 ± *0.03*	1.7	35.22	2.1 ± *0.2*	110 ± *17*	136 ± *21*
115.5	72.4	548.5	7.549	1123.5 ± *2.0*	39.3 ± *2.1*	0.94 ± *0.06*	1.2	35.82	0.4 ± *0.2*	179 ± *164*	99 ± *91*
151.3	72.4	548.5	7.664	829.9 ± *1.0*	35.5 ± *1.0*	0.87 ± *0.05*	3.1	35.07	1.0 ± *0.1*	87 ± *31*	154 ± *54*
302.7	72.4	548.5	7.623	934.6 ± *1.2*	37.1 ± *1.2*	0.91 ± *0.05*	2.2	35.02	0.6 ± *0.1*	123 ± *59*	127 ± *61*

One limitation of this system is that it is difficult to place sensors into the sediment disk to follow the reaction progress (e.g., O_2 or pH microelectrodes) because these would likely disrupt the flow and the diffusive boundary layer above the sediment disk. To remedy this issue, sensors (e.g., microelectrodes) could be inserted from below the sediment disk, instead of penetrating the

sediment on the water side, or inserted in the wall of the reactor. Future work should focus on quantifying the spatial distribution of the DBL, rather than assuming its uniformity over the entire disk surface, as we did here following Levich (1962). This could be achieved with multiple microelectrode measurements or using optical methods such as particle image velocimetry. It should be noted that, whereas the dimensions presented in ***Fig. 3.2*** are suitable for the study of water-side transport-controlled reactions, such as the dissolution of calcite, they may not be ideal to characterize sediment-side controlled fluxes. The sediment disk in ***Fig. 3.2*** is only 2 cm-thick and likely too thin to reproduce realistic solute concentration gradients that would develop during early diagenesis.

3.5 Conclusion

The thermostated, rotating-disk reactor, as described in this paper, can reproduce diffusive boundary layer (DBL) thicknesses that are typically encountered at a sediment-water interface (SWI). Calcite-rich sediment dissolution experiments reveal that the DBL thickness and diffusive fluxes through the SWI can be accurately predicted using the equations also described in this communication. In particular, this reactor can reach slow flow rates and thick DBLs, representative of low-energy aquatic natural environments, such as lakes or abyssal plains. The present rotating-disk reactor is a practical and suitable alternative to other traditional experimental reactors, e.g., flumes or stirred reactors, that may be more adapted to high-energy benthic conditions.

References

Alkattan, M., Oelkers, E. H., Dandurand, J.-L., and Schott, J. (1998) An experimental study of calcite and limestone dissolution rates as a function of pH from −1 to 3 and temperature from 25 to 80°C. *Chemical Geolology,* 151, 199–214, https://doi.org/10.1016/S0009-2541(98)00080-1

Apelblat, A. (1980) Mass transfer with a chemical reaction of the first order: Analytical solution. *Chemical Engineering Journal* 19, 19–37, https://doi.org/10.1016/0300-9467(80)85074-X

Archer, D., Emerson, S., and Smith, C. R. (1989) Direct measurement of the diffusive sublayer at the deep sea floor using oxygen microelectrodes. *Nature,* 340, 623–626 https://doi.org/10.1038/340623a0

Bircumshaw, L. L., and Riddiford, A. C. (1952) Transport control in heterogeneous reactions. *Quaternary Review, Chemical Society,* 157–185, https://doi.org/doi:10.1039/QR9520600157

Boggs, S. (2012) Principles of sedimentology and stratigraphy, 5th Edition. Pearson Prentice Hall.

Boudreau, B. P. (2013) Carbonate dissolution rates at the deep ocean floor. *Geophysical Research Letters*, 40, 744–748, https://doi.org/10.1029/2012GL054231

Boudreau, B. P., and Scott, M. R. (1978) A model for the diffusion-controlled growth of deep-sea manganese nodules. *American Journal of Science*, 278, 903–929, https://doi.org/doi:10.2475/ajs.278.7.903

Boudreau, B. P., and Guinasso, N. L. (1982) The influence of a diffusive boundary layer on accretion, dissolution, and diagenesis at the sea floor, p. 115– 145. In K. A. Fanning and F. T. Manheim [eds.], The Dynamic Environment of the Ocean Floor. Lexington Books.

Boudreau, B. P., and Jørgensen, B. B. (2001) The Benthic Boundary Layer: Transport Processes and Biogeochemistry. Oxford University Press.

Brady, J. F., and Durlofsky, L. (1987). On rotating disk flow. *Journal of Fluid Mechanics*, 175, 363–394, https://doi.org/10.1017/S0022112087000430

Brenna, J. T., Corso, T. N., Tobias, H. J., and Caimi, R. J. (1997) High-precision continuous-flow isotope ratio mass spectrometry. *Mass Spectrometry Review*, 16, 227–258, https://doi.org/10.1002/(SICI)1098-2787(1997)16:5<227::AID-MAS1>3.0.CO;2-J

Chang, F., and Abbad, M. (2011) Moddeling mass transfer in a rotating disk reaction vessel. King Abdullah Univ. of Science and Technology, Study Group Report, 1st KSG. Accessible on [http://www.maths-in-industry.org/miis/349/1/SLB-disk.pdf]

Chriss, T. M., and Caldwell, D. R. (1982) Evidence for the influence of form drag on bottom boundary layer flow. *Journal of Geophysical Research*, 87, 4148–4154, https://doi.org/10.1029/JC087iC06p04148

Compton, R. G., and Daly, P. J. (1987) The dissolution/precipitation kinetics of calcium carbonate: An assessment of various kinetic equations using a rotating disk method. *Journal of Colloid and Interface Science*, 115, 493– 498

Cook, P. G., Rodellas, V., Andrisoa, A., and Stieglitz, T. C. (2018) Exchange across the sediment-water interface quantified from porewater radon profiles. *Journal of Hydrology*, 559, 873–883, https://doi.org/10.1016/j.jhydrol.2018.02.070

Dade, W. B. (1993) Near-bed turbulence and hydrodynamic control of diffusional mass transfer at the sea floor. *Limnology and Oceanography*, 38, 52–69, https://doi.org/10.4319/lo.1993.38.1.0052

Day, M. A. (1990) The no-slip condition of fluid dynamics. *Erkenntnis*, 33, 285–296, https://doi.org/10.1007/BF00717588

Delgado, J. M. P. Q. (2007) Molecular diffusion coefficients of organic compounds in water at different temperatures. *Journal of Phase Equilibria and Diffusion*, 28, 427–432, https://doi.org/10.1007/s11669-007-9160-4

Dickson, A. G. (1990) Standard potential of the reaction: $AgCl(s)+1/2H_2(g) = Ag(s)+HCl(aq)$, and the standard acidity constant of the ion HSO_4^- in synthetic sea water from 273.15 to 318.15 K. *The Journal of Chemical Thermodynamics*, 22, 113– 127, https://doi.org/10.1016/0021-9614(90)90074-z

Ding, S., Wang, Y., Wang, D., Li, Y. Y., Gong, M., and Zhang, C. (2016) In situ, high-resolution evidence for iron-coupled mobilization of phosphorus in sediments. *Scientific Reports* 6(24341), https://doi.org/10.1038/srep24341

Ellison, B. T., and Cornet, I. (1971) Mass transfer to a rotating disk. *Journal of the Electrochemical Society* 118, 68-72, https://doi.org/10.1149/1.2407954

Escudier, M. P. (1984) Observations of the flow produced in a cylindrical container by a rotating endwall. *Experiments in Fluids* 2(4), 189-196, https://doi.org/10.1007/BF00571864

Fanning, K. A., and Pilson, M. E. Q. (1971) Interstitial silica and pH in marine sediments: Some effects of sampling procedures. *Science*, 173, 1228–1231, https://doi.org/10.1126/science.173.4003.1228

Frank-Kamenetskii, D. A. 2015. Diffusion and heat exchange in chemical kinetics. Princeton Univ. Press.

Fredd, C.N. and Fogler, H.S. (1998) The kinetics of calcite dissolution in acetic acid solutions. *Chemical Engineering Science* 53, 3863-3874, https://doi.org/10.1016/S0009-2509(98)00192-4

Frenzel, P., Thebrath, B., and Conrad, R. (1990) Oxidation of methane in the oxic surface layer of a deep lake sediment (Lake Constance). *FEMS Microbiol. Ecol.* 73, 149-158, https://doi.org/10.1016/0378-1097(90)90661-9

Gautelier, M., Oelkers, E.H. and Schott, J. (1999) An experimental study of dolomite dissolution rates as a function of pH from −0.5 to 5 and temperature from 25 to 80°C. *Chemical Geology* 157, 13-26, https://doi.org/10.1016/S0009-2541(98)00193-4

Glud, R.N., Gundersen, J.K., Revsbech, N.P. and Jørgensen, B.B. (1994) Effects on the benthic diffusive boundary layer imposed by microelectrodes. *Limnology and Oceanography* 39, 462-467, https://doi.org/10.4319/lo.1994.39.2.0462

Grasshoff, K., Kremling, K., and Ehrhardt, M.. 1999. Methods of seawater analysis. Wiley.

Gregory, D.P. and Riddiford, A.C. (1956) Transport to the surface of a rotating disk. Journal of the Chemical Society, 3756-3764, https://doi.org/10.1039/JR9560003756

Gundersen, J.K. and Jørgensen, B.B. (1990) Microstructure of diffusive boundary layers and the oxygen uptake of the sea floor. *Nature* 345, 604-607, https://doi.org/10.1038/345604a0

Han, P. and Bartels, D.M. (1996) Temperature Dependence of Oxygen Diffusion in H_2O and D_2O. *The Journal of Physical Chemistry* 100(13), 5597-5602, https://doi.org/10.1021/jp952903y

Han, X., Fang, H., He, G. and Reible, D. (2018) Effects of roughness and permeability on solute transfer at the sediment water interface. Water Research 129: 39-50, https://doi.org/10.1016/j.watres.2017.10.049

Hendriks, I.E., Duarte, C.M., Marbà, N. and Krause-Jensen, D. (2017) pH gradients in the diffusive boundary layer of subarctic macrophytes. *Polar Biology* 40: 2343-2348, https://doi.org/10.1007/s00300-017-2143-y

Higashino, M., and Stefan, H. G. (2004) Diffusive boundary layer development above a sediment-water interface. *Water Environment Research* 76: 292-300, https://doi.org/10.2175/106143004X141870.

Homoky, W.B., Weber, T., Berelson, W.M., Conway, T.M., Henderson, G.M., van Hulten, M., Jeandel, C., Severmann, S. and Tagliabue, A. (2016) Quantifying trace element and isotope fluxes at the ocean–sediment boundary: a review. *Philosophical Transactions of the Royal Society A* 374(2081), https://doi.org/10.1098/rsta.2016.0246

Hondzo, M. (1998) Dissolved oxygen transfer at the sediment-water interface in a turbulent flow. *Water Resources Research* 34, 3525-3533, https://doi.org/10.1029/1998WR900009

Hyun, J.M. and Kim, J.W. (1987) Flow driven by a shrouded spinning disk with axial suction and radial inflow. Fluid Dynamics Research 2, 175-182, https://doi.org/10.1016/0169-5983(87)90027-X

Imayama, S. (2012) Experimental study of the rotating-disk boundary-layer flow. Royal Institutte of Technology. Stockholm, Sweden.

Javadi, K. and Khalili, A. (2009) On generating uniform bottom shear stress. Part II: Shear stress inducing devices. *Recent Patents on Chemical Engineering 2*, 223-229, https://doi.org/10.2174/1874478810902030223

Jørgensen, B.B. and Revsbech, N.P. (1985) Diffusive boundary layers and the oxygen uptake of sediments and detritus. *Limnology and Oceanography* 30, 111-122, https://doi.org/10.4319/lo.1985.30.1.0111

Keir, R.S. (1983) Variation in the carbonate reactivity of deep-sea sediments: determination from flux experiments. *Deep-Sea Research* 30, 279-296, https://doi.org/10.1016/0198-0149(83)90011-0

Larkum, A.W.D., Koch, E.M.W., and Kühl, M. (2003) Diffusive boundary layers and photosynthesis of the epilithic algal community of coral reefs. *Marine Biology* 142: 1073-1082, https://doi.org/10.1007/s00227-003-1022-y.

Levich, V. G. (1962) Physicochemical hydrodynamics. Prentice-Hall.

Lewis, E. and Wallace, D.W.R. (1998) Program Developed for CO_2 System Calculations. ORNL/CDIAC-105. Carbon Dioxide Information Analysis Center, Oak Ridge National Laboratory, U.S. Department of Energy, Oak Ridge, Tennessee.

Lichtenberg, M., Norregaard, R. D., and Kuhl, M. (2017) Diffusion or advection? Mass transfer and complex boundary layer landscapes of the brown alga Fucus vesiculosus. *Journal of the Royal Society Interface* 14(128), https://doi.org/10.1098/rsif.2016.1015

Lorenzen, J., Larsen, L. H., Kjær, T., and Revsbech, N.-P. (1998) Biosensor determination of the microscale distribution of nitrate, nitrate assimilation, nitrification, and denitrification in a diatom-inhabited freshwater sediment. *Applied and Environmental Microbiology* 84, 3264-3269.

Lorke, A., Müller, B., Maerki, M. and Wüest, A. (2003) Breathing sediments: The control of diffusive transport across the 530 sediment-water interface by periodic boundary-layer turbulence. *Limnology and Oceanography* 48: 2077-2085, https://doi.org/10.4319/lo.2003.48.6.2077.

Lueker, T.J., Dickson, A.G. and Keeling, C.D. (2000) Ocean pCO_2 calculated from dissolved inorganic carbon, alkalinity, and equations for K_1 and K_2: validation based on laboratory measurements of CO_2 in gas and seawater at equilibrium. *Marine Chemistry* 70, 105-119, https://doi.org/10.1016/S0304-4203(00)00022-0

Lund, K., Fogler, H. S. and McCune, C. C. (1973) Acidization-I. The dissolution of dolomite in hydrochloric acid. *Chemical Engineering Science* 28: 691-700, https://doi.org/10.1016/0009-2509(77)80003-1

Millero, F.J. (1995) Thermodynamics of the carbon dioxide system in the oceans. *Geochimica et Cosmochimica Acta* 59, 661-677, https://doi.org/10.1016/0016-7037(94)00354-O

Mucci, A. (1983) The solubility of calcite and aragonite in seawater at various salinities, temperatures and one atmosphere total pressure. *American Journal of Science* 283, 780-799, http://doi.org/10.2475/ajs.283.7.780

Murphy, J. and Riley, J. P. (1962). A modified single solution method for the determination of phosphate in natural waters. *Analytica Chimica Acta* 27, 31-36, https://doi.org/10.1016/S0003-2670(00)88444-5

Pierrot, D., Lewis, E. and Wallace, D. (2006) *MS Excel Program Developed for CO_2 System Calculations*. ORNL/CDIAC-105a, Carbon Dioxide Information Analysis Center, Oak Ridge National Laboratory, U.S. Department of Energy, Oak Ridge, Tennessee.

Rassmann, J., Lansard, B., Pozzato, L., and Rabouille, C. (2016) Carbonate chemistry in sediment porewaters of the Rhône River delta driven by early diagenesis (northwestern Mediterranean). *Biogeosciences* 13, 5379-5394, https://doi.org/10.5194/bg-13-5379-2016

Røy, H., Huettel, M. and Jørgensen, B. B. (2004) Transmission of oxygen concentration fluctuations through the diffusive boundary layer overlying aquatic sediments. *Limnology and Oceanography* 49, 686-692, https://doi.org/10.4319/lo.2004.49.3.0686

Røy, H., Hüttel, M. and Jørgensen, B. B. (2002) The role of small-scale sediment topography for oxygen flux across the diffusive boundary layer. *Limnology and Oceanography* 47, 837-847, https://doi.org/10.4319/lo.2002.47.3.0837

Santschi, P. H., Bower, P., Nyffeler, U. P., Azevedo, A. and Broecker, W. S. (1983) Estimates of the resistance to chemical transport posed by the deep-sea boundary layer. *Limnology and Oceanography* 28: 899-912, https://doi.org/10.4319/lo.1983.28.5.0899.

Santschi, P.H., Anderson, R.F., Fleisher, M.Q. and Bowles, W. (1991) Measurements of diffusive sublayer thicknesses in the ocean by alabaster dissolution, and their implications for the measurements of benthic fluxes. *Journal of Geophysical Research: Oceans* 96, 10641-10657, https://doi.org/10.1029/91JC00488

Schauser, I., Chorus, I., and Lewandowski, J. (2006) Effects of nitrate on phosphorus release: comparison of two Berlin lakes. *Clean Soil Air Water* 34(4), 325-332, https://doi.org/10.1002/aheh.200500632

Schink, D. R., and Guinasso, N. L. (1977) Modelling the influence of bioturbation and other processes on calcium carbonate dissolution at the sea floor. In N. R. Andersen and A. Malahoff [Eds.]. The Fate of Fossil Fuel CO_2 in the Oceans. Plenum Press. p. 375-400.

Schink, D. R., Guinasso, N. L. and Fanning, K. A. (1975) Processes affecting the concentration of silica at the sediment-water interface of the Atlantic Ocean. *Journal of Geophysical Research* 80(21), 3013-3031, https://doi.org/10.1029/JC080i021p03013

Schlichting, H. (1968) Boundary Layer Theory. McGraw-Hill, New York.

Sjöberg, E. L. and Rickard, D. (1983) The influence of experimental design on the rate of calcite dissolution. *Geochimica Cosmochimica Acta* 47, 2281-2285, https://doi.org/10.1016/0016-7037(83)90051-0

St-Jean, G. (2003) Automated quantitative and isotopic (^{13}C) analysis of dissolved inorganic carbon and dissolved organic carbon in continuous-flow using a total organic carbon analyser. *Rapid Communications in Mass Spectrometry* 17: 419-428, https://doi.org/10.1002/rcm.926

Steinberger, N. and Hondzo, M. (1999) Diffusional mass transfer at sediment-water interface. *Journal of Environmental Engineering* 125, 192-200, https://doi.org/10.1061/(ASCE)0733-9372(1999)125:2(192)

Stoll, M. H. C., Bakker, K., Nobbe, G. H. and Haese, R. R. (2001) Continuous-flow analysis of dissolved inorganic carbon content in seawater. *Analytical Chemistry* 73, 4111-4116, https://doi.org/10.1021/ac010303r

Sulpis, O., Boudreau, B.P., Mucci, A., Jenkins, C.J., Trossman, D.S., Arbic, B.K. and Key, R.M. (2018) Current $CaCO_3$ dissolution at the seafloor caused by anthropogenic CO_2. *Proceedings of the National Academy of Sciences of the United States of America* 115, 11700-11705, https://doi.org/10.1073/pnas.1804250115

Sulpis, O., Lix, C., Mucci, A. and Boudreau, B.P. (2017) Calcite dissolution kinetics at the sediment-water interface in natural seawater. *Marine Chemistry* 195, 70-83, https://doi.org/10.1016/j.marchem.2017.06.005

Tomlan, P. F., and Hudson, J. L. (1971) Flow near an enclosed rotating disk: Analysis. *Chemical Engineering Science* 26, 1591-1600, https://doi.org/10.1016/0009-2509(71)86049-9

Trowbridge, J. H., and Lentz, S. J. (2018) The bottom boundary layer. *Annual Review of Marine Sciences* 10, 397-420, https://doi.org/10.1146/annurev-marine-121916-063351

Uppström, L. R. (1974) The boron/chlorinity ratio of deep-sea water from the Pacific Ocean. *Deep-Sea Research* 21, 161-162, https://doi.org/10.1016/0011-7471(74)90074-6

von Kármán, T. (1921) Uber laminare and turbulente Reibung. *Journal of Applied Mathematics and Mechanics* 1(4), 233-252.

Zeebe, R.E. (2011) On the molecular diffusion coefficients of dissolved CO_2, HCO_3^-, and CO_3^{2-} and their dependence on isotopic mass. *Geochimica et Cosmochimica Acta* 75, 2483-2498, https://doi.org/10.1016/j.gca.2011.02.010

Preface to Chapter 4

In ***Chapter 1***, we used a stirred, flow-through reactor to study the dissolution kinetics of calcite contained in a synthetic sediment disk immersed in natural seawater. We were, however, unable to generate slow laminar flows such as those encountered in deep-sea environments because stirred reactors easily generate turbulent flow that disrupt the diffusive boundary layer. The rotating-disk reactor presented in ***Chapter 3*** solved that issue as it generates diffusive boundary layers with a thickness representative of deep-sea benthic environments.

In this Chapter, we use this newly designed flow-through rotating-disk reactor and study the effects of a set of environmental variables to estimate the calcite dissolution rate under deep-sea like conditions, and an associated uncertainty. Among all the investigated oceanographic variables that may potentially influence the dissolution rate, i.e., sediment porosity, permeability, grain size and specific surface area, biogenic or synthetic particles, seawater temperature, current speed and carbonate ion concentration [CO_3^{2-}], results show that only seawater [CO_3^{2-}] and the current speed have a statistically significant influence on calcite dissolution rates. Based on these observations, it is argued that geologically long- or medium-term changes in bottom-current velocities, such as those that may be induced by changes in continental positions or evolving climate, should be considered along with variations of calcite deposition fluxes and seawater acidification when interpreting calcite preservation data through time.

Chapter 4

Impact of environmental conditions and sediment properties on the dissolution kinetics of natural and synthetic calcites*

Olivier Sulpis[1], Alfonso Mucci[1], Pascale Daoust[1], Deneyn White[1] and Bernard P. Boudreau[2]

[1]GEOTOP and Department of Earth and Planetary Sciences, McGill University, Montreal QC, Canada

[2]Department of Oceanography, Dalhousie University, Halifax NS, Canada

**In preparation for submission*

4.1 Introduction

Calcium carbonate ($CaCO_3$) minerals and dolomite represent approximately a third of the sedimentary rock mass of the Phanerozoic eon (Berner and Mackenzie, 2011). Whereas calcite and aragonite, two $CaCO_3$ polymorphs, can be commonly found in the modern surface ocean, low-magnesian calcite (>99% of $CaCO_3$) predominates in the deep sea (Morse and Mackenzie, 1990). In the modern ocean, coccolithophores - an order of unicellular phytoplanktonic organisms covered by several calcitic plates called *coccoliths* - and foraminifera - unicellular planktonic or benthic organisms with a shell made of $CaCO_3$ or agglutinated sediment particles – account for the vast majority of $CaCO_3$ deposits in the deep-ocean (Erez, 2003).

Of the ~133 Tmol of planktonic $CaCO_3$ produced at the surface ocean each year, less than 10% accumulates in pelagic sediments (Smith and Mackenzie, 2016), implying that 90% of falling calcitic particles escape burial by dissolution. About 20% of this dissolution is thought to occur at the sediment-water interface (Berelson et al., 2007; Sulpis et al., 2018), and the remainder in the water-column or after burial through metabolic dissolution or later diagenesis. Whether in the water column or in sediments, calcite should dissolve if ambient seawater is undersaturated with respect to calcite, i.e., if the saturation state of seawater with respect to calcite (Ω_C) is lower than 1. The latter is defined as:

$$\Omega = \frac{[Ca^{2+}][CO_3^{2-}]}{K_{sp}^*} \quad \textbf{(4.1)}$$

where the square brackets indicate total concentrations in mol kg^{-1} of seawater and K_{sp}* is the stoichiometric solubility constant of the mineral of interest (calcite, aragonite, mol^2 kg^{-2} seawater) at ambient temperature, pressure and salinity (Millero, 1979; Mucci, 1983). In the water column, Ω_C usually decreases with water depth (***Fig. 4.1a***), because calcite is more soluble at low temperatures (Mucci, 1983) and high pressures (Millero, 1995), and due to CO_2 produced by the microbial respiration of organic matter settling from the surface, acidifying bottom waters (Sarmiento and Gruber, 2006). The depth below which seawater becomes undersaturated with respect to calcite (Ω_C < 1) is called the Calcite Saturation Depth (CSD). With the addition of anthropogenic CO_2 in the ocean, the CSD is rising (Feely et al., 2004), and a greater surface area of calcitic sediments is exposed to corrosive water and undergoes dissolution (Gehlen et al., 2008; Sulpis et al., 2018).

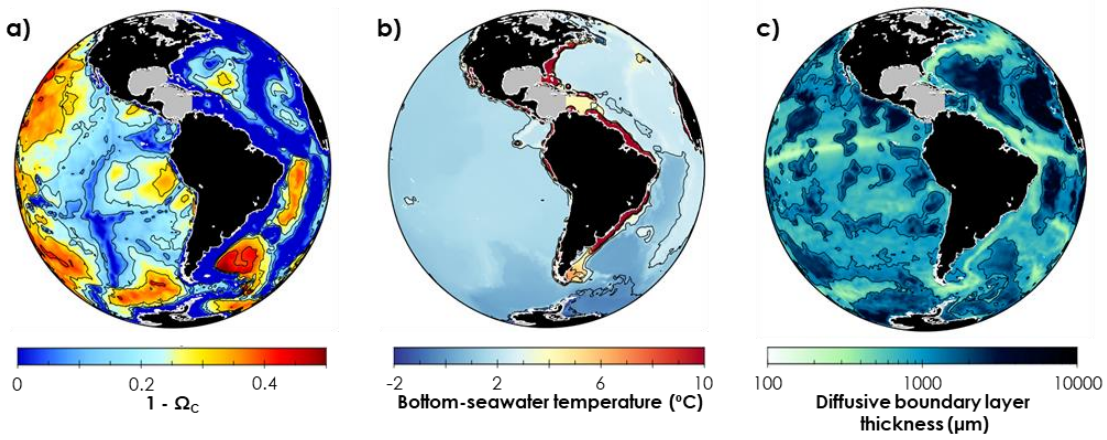

Fig. 4.1 | *Overview of the range of (a) calcite undersaturation state (1 - Ω_C), (b) temperature and (c) current velocity encountered in the bottom waters of the eastern Pacific and western Atlantic Oceans. The data used to plot these maps are from GLODAPv2 (Key et al., 2015; Lauvset et al., 2016; Olsen et al., 2016) and the DBL thickness is computed from HYCOM bottom-current speed (Trossman et al., 2016) following the methods presented in Sulpis et al. (2018).*

Numerous scientists studying the kinetics of calcite dissolution, i.e., the rate, in seawater, have reported increasing dissolution rates as the undersaturation state of seawater with respect to

calcite ($1 - \Omega_C$) increases (Cubillas et al., 2005; Dong et al., 2018; Gehlen et al., 2005; Keir, 1980, 1983; Morse, 1978; Naviaux et al., 2019; Subhas et al., 2017; Subhas et al., 2015; Subhas et al., 2018; Sulpis et al., 2017; Sulpis et al., 2019; Walter and Morse, 1985). Although avoiding any mechanistic understanding, the most common way to express the dissolution rate (r, in mol m^{-2} a^{-1}) of calcite as a function of ($1 - \Omega_C$) is though the following empirical equation:

$$\boldsymbol{r = k\,(1 - \Omega_C)^n} \qquad \textbf{(4.2)}$$

where *k* is termed a rate constant (in mol m^{-2} a^{-1}) and *n* referred to as the reaction order (unitless). Throughout the scientific literature, reported values for *n* vary widely. Whereas studies have reported data-fitted *n* values higher than 4, e.g., Keir (1980) for synthetic calcite, others have reported *n* values closer to 2, e.g., Gehlen et al. (2005) for natural sediments, or linear kinetics, i.e., a reaction order of 1, e.g., Sulpis et al. (2017) for synthetic sediment beds, Hales and Emerson (1997) for suspended particles, and Rickard and Sjoberg (1983) for a solid calcite disk. The implications for our understanding of the marine calcite cycle are critical considering that, for a similar rate constant, increasing the value of *n* implies dramatically lowering the dissolution rate close to equilibrium. Disparities are even larger with respect to the value of *k*, as literature values range from ~3 $x10^{-4}$ mol m^{-2} a^{-1} for a natural calcitic sediment from the Sierra Leone Rise in artificial seawater (Gehlen et al., 2005) to ~36 mol m^{-2} a^{-1}, for coarse synthetic calcite grains in artificial seawater (Subhas et al., 2015).

Despite these apparent inconsistencies, which may emanate from the diversity of experimental conditions and protocols or from surface area estimation methods (Colombani, 2016), an interesting pattern emerges when the reactivity of natural and synthetic materials is compared. It appears that coccoliths and foraminifera consistently dissolve slower than synthetic materials, when the dissolution rate is normalized by the surface area of the grains, despite the fact that biogenic calcites have larger reactive surface areas (when expressed in m^2 per gram of material) than synthetic calcites (Keir, 1980; Subhas et al., 2018; Walter and Morse, 1985). It has been proposed that organic coatings inhibit the dissolution of coccoliths (Honjo and Erez, 1978; Keir, 1980). In contrast, Subhas et al. (2018), based on the results of Gal et al. (2016), suggested that organic macromolecules bound to the coccoliths could catalyze calcite nucleation and, hence, its precipitation, even in slightly undersaturated seawater, reducing the apparent net dissolution.

In sediments, the link between organic matter and calcite dissolution is more complex than for individual coccoliths. While organic matter may hinder calcite dissolution for reasons mentioned above, metabolic CO_2 production due to bacterial organic matter degradation could acidify porewaters, accelerating dissolution (Emerson and Bender, 1981; Jansen et al., 2002). In addition, burrowing organisms can strongly alter the distribution of solids and solutes in sediment, and their dependency on organic matter is known to be complex (Boudreau, 1996; Meysman et al., 2005; Teal et al., 2010). Before attempting to fully understand the organic carbon – calcite sedimentary system, much remains to be learned about abiotic calcite dissolution.

It is becoming more and more conspicuous that calcite dissolution in seawater does not proceed by a single mechanism but, instead, a sequence of mechanisms predicated to a given region of the $(1 - \Omega_C)$ spectrum (Arvidson et al., 2015; Dong et al., 2018; Naviaux et al., 2019; Subhas et al., 2017; Subhas et al., 2015). Recently, Naviaux et al. (2019), based on laboratory dissolution experiments with ^{13}C-enriched calcites, asserted that close to equilibrium ($\Omega_C > 0.9$), dissolution is limited to the retreat of pre-existing steps, kinks and adatoms on the calcite surface. Further away from equilibrium ($0.9 > \Omega_C > \sim 0.75$), defect-assisted dissolution would dominate, while below $\Omega_C \sim 0.75$, the measured rates show a sharp increase, as undersaturation is high enough to allow dissolution to occur homogeneously across the mineral surface. This apparent criticality in the mineral-solution system might explain the nonlinear dissolution behaviors observed by researchers who studied the dissolution behavior of calcite grains kept in suspension in seawater. In this framework, Naviaux et al. (2019) observed that temperature increases both the rate constant and the reaction order, especially far from equilibrium. Such a complex kinetic behavior is problematic for – although it does not preclude – the development of a simple equation describing the dissolution rate of individual calcite grains as a function of environmental variables.

Boudreau (2013) argued that, at the sediment-water interface (SWI) and under deep-sea-like hydrodynamic conditions, calcite dissolution is almost entirely controlled by the diffusion of reactants and reaction products through the diffusive boundary layer (DBL) above the SWI; typically, 0.5-1 mm-thick in the deep sea (Sulpis et al., 2018). In this case, the reaction is termed (water-side) transport-controlled, and DBL-diffusion acts as the rate limiting-step. The alternative dissolution regime for calcite at the SWI would be sediment-side control, a regime in which porewater diffusion combined with chemical reactions at the surface of the grains are the rate

limiting steps. In reality, calcite dissolution at the SWI always follows a mixed regime, tilting more strongly towards water-side transport control when bottom currents are slow (a few cm s^{-1}) and the DBL is thick (a few mm), and towards sediment-side control, when sediments are calcite-poor, or when much microbial respiration-driven dissolution occurs within sediments (Boudreau and Guinasso, 1982; Sulpis et al., 2018; Sulpis et al., 2019).

The idea of a diffusive transport-control of calcite dissolution at the SWI was raised by earlier investigators (Broecker and Peng, 1982; Santschi et al., 1991; Schink and Guinasso, 1977) and is supported by recent experimental studies (Sulpis et al., 2017; Sulpis et al., 2019). On one hand, a strong diffusive transport-control should, in theory, reduce the effects of temperature or the nature (biogenic or synthetic) of the calcite on the dissolution rates, as discussed above, although temperature also affects the viscosity of seawater (Sharqawy et al., 2010) and could influence the rate of diffusion. On the other hand, rheological variables specific to the sediment, e.g., porosity or permeability, could also affect dissolution.

The dynamics of the flow above the SWI and the structure of the bottom boundary layer have been reviewed by Boudreau and Guinasso (1982), Boudreau and Jørgensen (2001) and Trowbridge and Lentz (2018). One assumption of most DBL models, including ours (Sulpis et al., 2018), is that the flow velocities decrease toward the sediment bed until reaching zero velocity at the SWI, a concept referred to as the no-slip condition, a standard boundary condition used by almost all, if not all, investigations of fluid dynamics. Nevertheless, near the surface of sufficiently porous sediments, a pressure-induced flow can exist, coupled with the overlying bottom-water flow (Dade et al., 2001). According to Darcy's law (Whitaker, 1986), laminar flow in a porous medium is related to a pressure gradient by the *permeability*, which is proper to the nature and rheology of the sediment, and correlated with grain size (Shepherd, 1989). Nevertheless, it is generally accepted that because of the presence of clay particles in marine sediments, which dramatically reduces their permeability, no appreciable flow is encountered below the SWI, unlike for sands or coarse-grain sediments (Boudreau and Jørgensen, 2001).

The objective of the present study is to test, experimentally, the effect of a set of oceanographic variables (temperature, DBL thickness, Ω_C) and sediment properties (sediment composition, nature of calcite, porosity, permeability) on the dissolution rate of calcite at the SWI. For this purpose, we exposed sediment disks containing synthetic calcite mixed with quartz sand

and clay, natural foraminifera or coccoliths, to undersaturated, natural seawater in a newly developed rotating disk reactor which reproduces hydrodynamic conditions encountered at the seafloor (Sulpis et al., 2019). We use these experiments to derive an equation that can readily estimate the calcite dissolution rate at the SWI, neglecting any metabolic dissolution. Finally, we compare our results with those of previous work and show that patterns can be drawn regarding the link between reaction order, dissolution rate constant and hydrodynamics.

4.2 Materials and methods

4.2.1 Computing the dissolution rates at the sediment-water interface

For every mole of calcite dissolved, two equivalents of total alkalinity (*TA*) and one mole of dissolved inorganic carbon are released to solution. Here, we will derive the dissolution rate of calcite at the SWI by measuring the *TA* flux from a set of dissolving calcitic sediments exposed to undersaturated seawater. The methodology that we use is the same as described in Sulpis et al. (2017) and we refer the reader to this publication for a more detailed description of the procedure and analyses.

Briefly, a calcitic sediment disk is placed at the bottom of a reactor and immersed in natural seawater initially in equilibrium with calcite ($\Omega_C = 1$). The natural seawater was aged, filtered and acidified, so that its *TA* is reduced from ~2300 μmol kg^{-1} to values comprised between 380-1000 μmol kg^{-1} and, thus various degrees of undersaturation ($\Omega_C < 1$). After equilibration with the ambient, laboratory pCO_2, this acidified seawater is injected in the reactor at a constant and known rate using a peristaltic pump, after which it mixes with seawater in the reactor chamber, in contact with the sediment disk. The pH of the overlying seawater, monitored daily with a combination glass pH electrode, is drawn down due to the injection of acidified seawater, until a steady state is reached after a few days or weeks. At steady state, the pH decrease due to the injection of the acidified seawater is exactly compensated by the pH increase due to calcite dissolution. An aliquot of the steady-state (output) solution is sampled and its *TA* determined potentiometrically. Because the *TA* of the input seawater and the residence time of seawater within the reactor are known, the calcite dissolution rate of the disk surface can be derived according to:

$$r = m_{SW} \times \Delta TA / (2 \times A \times \Delta t) \quad (4.3)$$

where r is the interface area-normalized calcite dissolution rate (mol m^{-2} a^{-1}), m_{SW} is the mass of seawater in the reactor (kg), ΔTA is the difference in total alkalinity between the (steady-state) output and the input seawater (mol kg^{-1}), A is the surface area of the sediment disk (m^2) and Δt is the residence time of seawater in the reactor (a).

At the seafloor, hydrodynamics control the shape and thickness of the DBL above the sediment bed. This can, by extension, determine the magnitude of the calcite dissolution flux out of a sediment and, thus, particular attention should be given to using experimental systems that reproduce the hydrodynamic conditions encountered at the seafloor. In this study, two different reactors are used to simulate high and low energy benthic environments. Most experiments were carried out in a rotating-disk reactor, that has been comprehensively described elsewhere (Sulpis et al., 2019). In this reactor, a sediment disk (***Fig. 4.2a***) spins within a thermally-controlled reactor chamber. The DBL thickness above this disk can be computed from the angular velocity of the spinning disk, at any temperature, and for any diffusing ion. Under our experimental conditions, this reactor can generate DBLs as thick as 500 μm, at the thinner end of the DBL thicknesses of the deep sea (Boudreau and Jørgensen, 2001; Santschi et al., 1991; Sulpis et al., 2018; see ***Fig. 4.1c*)**. Thus, experiments carried out in the rotating-disk reactor are presumably representative of deep-sea, low-energy, benthic hydrodynamics. Alternatively, a few experiments were carried out in a stirred reactor, described by Sulpis et al. (2017). In this reactor, a conical stirrer driven by an overhead motor creates a rotating flow in water overlaying the sediment disk, generating a uniform shear stress on the sediment surface and thinning the DBL. This type of design is suited for very thin or inexistent DBL generation, rather than the thick DBLs found in deep sea environments, as we suspect that turbulence and small-scale eddies are inevitably formed by the jerky motion of the stirrer, and by the presence of an electrode within the reactor chamber for regular pH measurements (Sulpis et al., 2017). At high stirring rates (>50 rpm, rotations per minute), such as what we use here, the influence of a DBL is negligible on the measured dissolution rate, and calcite dissolution rates can be considered as sediment-side controlled (Sulpis et al., 2017). The types of natural benthic environments that this stirred-flow reactor can simulate are high energy marine environments, such as those encountered on shallow-water carbonate platforms (Pomar, 2001; Vital et al., 2008).

Once a steady-state is reached and a dissolution rate estimated using ***Eq. 4.3***, the steady-state solution is analyzed spectrophotometrically for its soluble reactive phosphate (*SRP*) concentration (Grasshoff et al., 1999; Murphy and Riley, 1962) and its practical salinity (S_P), following an argentometric potentiometric titration. These variables are used, along with the steady-state *TA*, pH on the total scale (pH_T, Dickson (1984)) and temperature (*T*), to determine the steady-state Ω_C of the experimental solution using CO2SYS (Lewis and Wallace, 1998; Pierrot et al., 2006). All calculations are carried out on the total hydrogen ion concentration scale, using the stoichiometric carbonic acid dissociation constants from Lueker et al. (2000), as recommended by Dickson et al. (2007) and Orr et al. (2015), the total boron concentration from Uppström (1974) and the standard acidity constant of the HSO_4^- ion from Dickson (1990). Overall uncertainties on estimates of Ω_C were computed from the algorithm developed by Orr et al. (2018), taking into account the measurement uncertainties for each variable, as reported in ***Tables 4.1-4.3***, and the uncertainties on the various stoichiometric constants proposed by Orr et al. (2018). Uncertainties for the dissolution rates (r) were computed from the measurement uncertainties of m_{SW}, *TA*, *S* and Δt (see SI), following standard error propagation rules.

4.2.2 Sediment properties and preparation

The experiments described in this study fall into three categories. The first category of experiments explores the effects of *T*, sediment porosity and permeability, seawater Ω_C and the DBL thickness on sediment calcite dissolution rates. One can choose to quantify the role of these variables individually, but that would be very time consuming and would ignore potential synergistic interactions among variables. On the other hand, changing several variables at the same time reduces the number of experiments to be carried and can reveal potential synergistic interactions among variables, but results of these experiments are more difficult to unravel.

Sediment disks were prepared by mixing various amount of montmorillonite, quartz sand, and synthetic calcite with calcite-saturated natural seawater saturated (***Fig. 4.2b***). ACS reagent grade synthetic calcite with a specific gravity of 2.71 g cm^{-3} was purchased from Baker®. Based on the averaged length of the grains (5.65 ± 0.92 μm, n=150), the geometric specific surface area of the synthetic calcite was estimated at 0.39 ± 0.23 m^2 g^{-1} (Sulpis et al., 2017). A five-point BET-

N_2 surface area analysis (Brunauer et al., 1938) yielded a specific surface area of 0.245 ± 0.014 m^2 g^{-1}, within the uncertainties of the geometric specific surface area estimate. Highly purified montmorillonite clay with an average grain size of 18.1 ± 9.1 μm (n=99) and a specific gravity of 2.6 g cm^{-3} was purchased from Southern Clay Products Inc. USA. Pure quartz sand washed several times with deionized water and dried prior to use had an average grain size of 0.83 ± 0.31 mm (n=30). This material served as a coarser fill in an attempt to increase the permeability of the simulated sediments. In the simulated-sediment disks, the calcite weight fraction was always 50% of the dry solid weight but the relative dry weight percentage of montmorillonite was either 50%, 25% or 0%, with the quartz sand making up the difference. This resulted in the production of three possible sediment compositions: calcite-clay, calcite-clay-quartz or calcite-quartz (see ***Fig. 4.3***). Porosity was measured by weight loss upon drying at low temperature (< 50 °C) for a week, for 3 replicates for each sample, assuming an average solid density of 2.65 g cm^{-3} and subtracting the weight of precipitated seawater salts. The resulting porosities were 0.79 ± 0.02, 0.78 ± 0.03 and 0.73 ± 0.03, respectively. Permeability of pure quartz sand and synthetic calcite sediment disks was estimated from the porosity of the sediment and the mean diameter of the grains, assuming spherical solid particles, using the Kozeny-Carman equation as presented in Xu and Yu (2008). For montmorillonite, because the assumption of spherical particles does not hold, the permeability was taken from Amarasinghe et al. (2012) at 25 ºC. Then, it was assumed that the permeability of the sediment mixtures can be linearly interpolated from the permeabilities of the three poles of composition (i.e., synthetic calcite, quartz sand and montmorillonite clay), see ***Fig. 4.3***. The resulting permeabilities were 6.2 ± 2.7 x 10^{-9} cm^2 for the calcite-clay sediment, 7.6 ± 5.6 x 10^{-5} cm^2 for the calcite-clay-quartz sediment and 1.5 ± 1.1 x 10^{-4} cm^2 for the calcite-quartz sediment (***Fig. 4.3***). Experiments were carried out either at a controlled temperature of 25.0 ºC, or in a cold room at a temperature of 7 ± 1.5 ºC (***Fig. 4.1b***). The rotating disk reactor, which can readily simulate seafloor-like DBLs, was used for this set of experiments. The disks were rotated at between 1 and 6 rpm which, depending on the viscosity (which is dependent on temperature), generates DBLs between 170 and 470 μm (Levich, 1962).

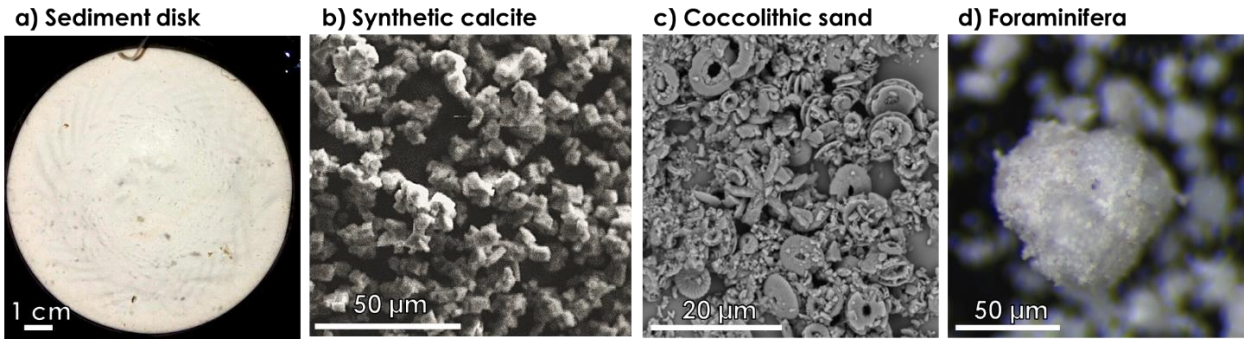

Fig. 4.2 | *Picture of (a) a sediment-disk filled with pure synthetic calcite in the rotating-disk reactor and scanning electron micrographs of (b) synthetic calcite powder, (c) coccolithic sediment and (d) foraminifera (binocular microscope).*

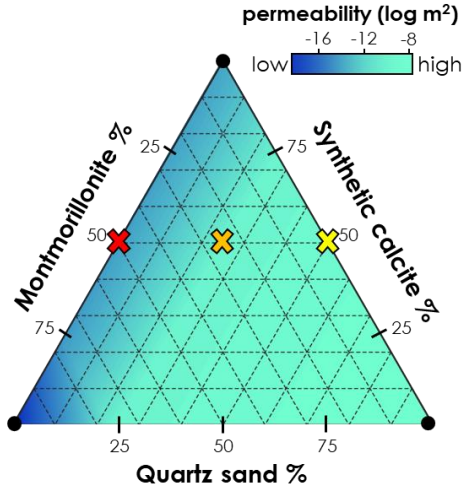

Fig. 4.3 | *Ternary diagram representing the composition of the three sediments containing synthetic calcite (red cross is for calcite-clay, orange cross is for calcite-clay-quartz and yellow cross is for calcite-quartz) as well as other sediments prepared specifically for porosity measurements. From grain sizes and porosities, permeabilities were computed using the Kozeny-Carman equation as presented in Xu and Yu (2008) except for montmorillonite, for which permeability was taken from Amarasinghe et al. (2012). Permeabilities were subsequently linearly interpolated and are shown on this diagram in blue color.*

In a second category of experiments, again in rotating-disk reactors, natural calcites were dissolved in order to compare their dissolution kinetics (rate constants and reaction orders) with those of experiments carried out with synthetic calcite sediments. One batch of sediment was prepared using sediment recovered with a piston core during North Atlantic IODP expedition 303 in November 2004, at site U1308 lying between the eastern side of the mid-oceanic ridge and the

Isengard Ridge, at a water-depth of ~ 3900 m (Channell et al., 2006). The sediment was taken at ~350 m below the core top, which corresponds to ages of between 5.6 and 6.5 Ma, in the late Miocene (Channell et al., 2006). About 90% of the sample was composed of $CaCO_3$ nannofossils (***Fig. 4.2c***), and less than 0.1 % was organic carbon (Channell et al., 2006). About a third of the nannofossils, counted on a smear slide using a scanning electron microscope (n ~ 2000), were represented by the species *Reticulofenestra pseudoumbilicus* (Gartner, 1967) and another third by *Gephyrocapsa spp*. (Flores et al., 2000). About 2% of the nannofossils belonged to the species *Discoaster brouweri*, an extinct 6-legged star shaped marine algae (Bukry, 1971) visible in ***Fig. 4.2c***. We also noted the presence of rare foraminifera and palynomorphs in the sediment, and the absence of radiolarian (Channell et al., 2006). This sediment was rinsed with deionized water several times and dried at room temperature before being mixed with calcite-equilibrated natural seawater. The porosity was 0.88 ± 0.02 (n = 3). The BET-surface area of this coccolithic sediment was measured at 8.15 ± 0.20 $m^2\ g^{-1}$ (n = 2).

Another batch of sediment was composed of foraminiferal sand, previously described in Sulpis et al. (2019). This foraminiferal sand was made up of ~98% of *Globigerinoides ruber* (***Fig. 4.2d***), a shallow-water planktonic foraminifera species (Hayward et al., 2018). This sediment was retrieved from the top 10 cm of a gravity core sampled at 1916 m-depth in the Southern Central Pacific Ocean, in April 2010. This sediment was rinsed several times with deionized water, dried at room temperature, and mixed with calcite-equilibrated natural seawater. The porosity of this foraminiferal sediment was 0.84 ± 0.03 (n = 3). The BET-surface area of the foraminifera was 4.07 ± 0.01 $m^2\ g^{-1}$ (n = 2), which is about half that of the coccoliths, consistent with results of similar studies (Keir, 1980; Subhas et al., 2018). The spinning rates of the sediment disks were between 1 and 10 rpm, and the temperature always 25 ºC. The resulting DBL thicknesses ranged between 145 and 459 μm. In these experiments, to prevent any bacterial respiration of organic matter, the seawater was poisoned with ~100 mg of $HgCl_2$ per liter, as recommended by Kattner (1999) for long-term storage measurements of dissolved inorganic nutrients in seawater.

Finally, to obtain insights on the dissolution of calcite grains under high shear stress conditions, and to determine whether the presence of $HgCl_2$ in seawater affects the dissolution rates, three sets of experiments were carried out in a stirred-flow reactor (Sulpis et al., 2017). In one set of experiments, synthetic calcite grains were spread out at the bottom of a reactor in which

a conical stirrer, driven by an overhead motor, creating a rotating flow (see Sulpis et al. (2017)) so that the grains were mobile and were moved around by the overlying water, but without being in being resuspended, i.e., still under the form of a sediment bed. The stirring rate was ~300 rpm. $HgCl_2$ was added to the seawater at a concentration of ~100 mg per liter. A second set of experiments was run under the same conditions, with synthetic calcite, but without any $HgCl_2$. Finally, a third set of experiments was performed at the same stirring rate, with ~100 mg of $HgCl_2$ per liter of seawater, using the foraminiferal sand described above.

4.3 Results

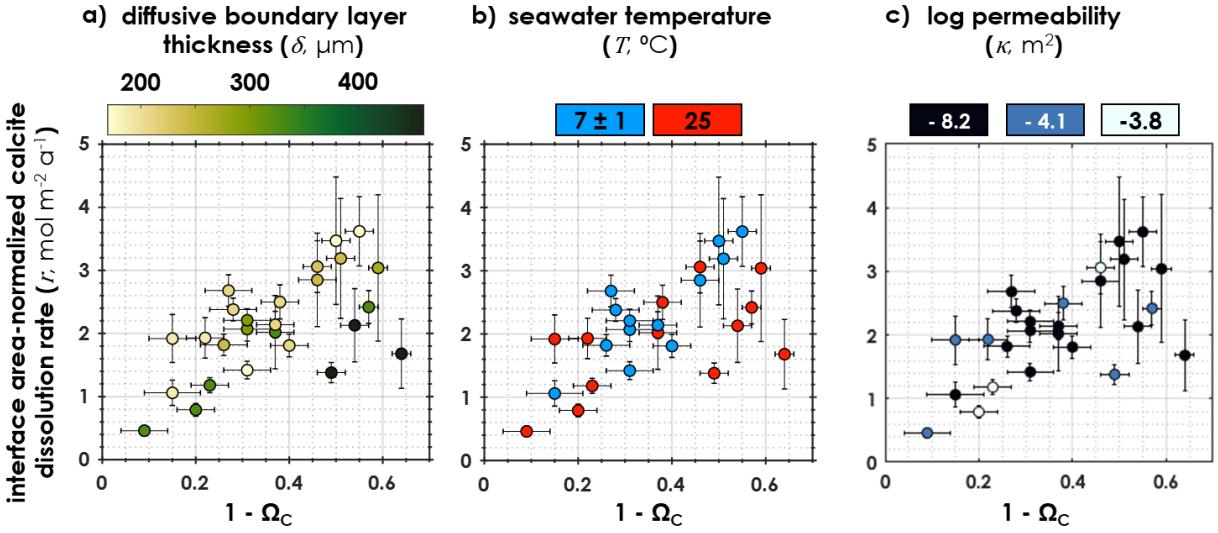

Fig. 4.4 | *Interface area-normalized dissolution rates as a function of steady-state undersaturation state ($1 - \Omega_C$) and a) diffusive boundary layer thickness (δ), b) seawater temperature (T) and c) permeability on a log scale (κ) for sediment with various proportions of montmorillonite clay, quartz sand and synthetic calcite.*

The data reported here originates from 70 different week-long dissolution experiments. All data obtained in this study are shown in ***Tables 4.1-4.3***. Practical salinities of the steady-state aliquots range between 34.82 ± 0.04 and 35.98 ± 0.04, suggesting that minimal evaporation has occurred between the sampling of natural seawater in the Gulf of Saint Lawrence (S_P = 34.72 ± 0.04) and the end of the experiments several months later. Saturation states (Ω_C) range from slightly supersaturated (Ω_C = 1.05) to highly undersaturated (Ω_C = 0.32), essentially covering the

range depicted in ***Fig. 4.1a***. Steady-state pCO_2 values, computed with CO2SYS, range from 275.6 ± 5.6 µatm to 798.6 ± 15.7 µatm, the latter being more representative of typical indoor pCO_2. This wide pCO_2 variability is due to a combination of factors including seasonal variations or changing human presence, the assumption being that seawater in our reactors is in equilibrium with the room air. Although this is certainly the case at the beginning of experiments, because we equilibrate acidified seawater with room air, this might not be always true at the end of the dissolution experiments, as we note a weak (R^2 = 0.23) negative linear dependency between the computed pCO_2 values and the dissolution rates, suggesting that calcite dissolution effectively neutralizes dissolved CO_2.

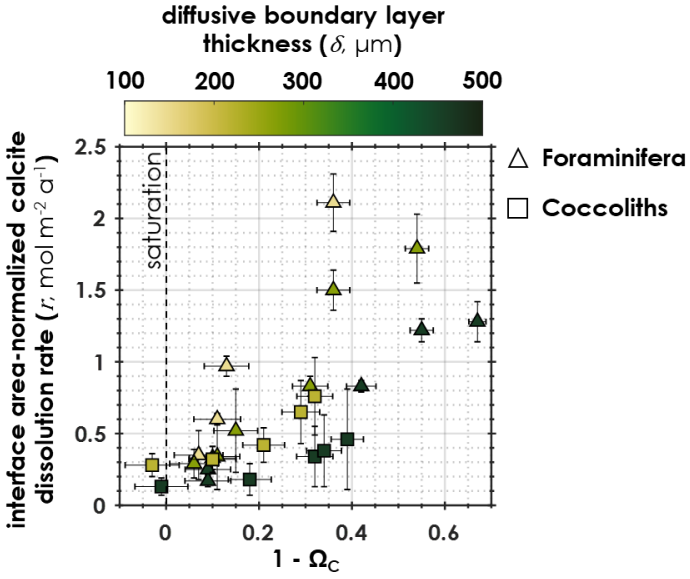

Fig. 4.5 | *Interface area-normalized dissolution rates as a function of steady-state undersaturation state (1 – Ω_C) and diffusive boundary layer thickness (δ) for coccolithic and foraminiferal sediments.*

Twenty six dissolution experiments were performed with synthetic calcite sediments over a range of DBL thicknesses (δ) and undersaturation states, at two different temperatures (25 ºC or 7 ± 1.5 ºC) and three different permeabilities (6.2 ± 2.7 x 10^{-9} cm^2, 7.6 ± 5.6 x 10^{-5} cm^2 and 1.5 ± 1.1 x 10^{-4} cm^2), depending on the proportion of montmorillonite clay and quartz sand in the sediment disks. Results for these experiments are presented in ***Fig. 4.4*** and reported in ***Table 4.1***. Uncertainties on the dissolution rate value increase at high undersaturation, as the gap between the TA of the input solution and the TA of the steady-state output seawater narrows. Despite these

uncertainties, it is clear that under our experimental conditions, for a similar Ω_C value, dissolution rates increase with a decreasing DBL thickness (***Fig. 4.4a***). The effects of temperature or permeability are less obvious, and no explicit pattern can be identified (***Fig. 4.4b,c***).

Dissolution experiments carried out on natural coccolithic and foraminiferal sediments are shown in ***Fig. 4.5*** and reported in ***Table 4.2***. For coccoliths, two steady-state samples obtained in slightly supersaturated waters (Ω_C = 1.01 ± 0.06 and Ω_C = 1.03 ± 0.06) showed significantly positive dissolution rates (r = 0.13 ± 0.06 and 0.28 ± 0.08 mol m^{-2} a^{-1}, respectively). These could be explained by the presence of more soluble calcite phases in the coccolithic sediment, such as aragonite or high-Mg calcite, or uncertainty in estimated Ω_C values. For both sediments, dissolution rates increase with decreasing DBL thickness. As in Subhas et al. (2018), coccoliths appear to dissolve slower than foraminifera, despite their specific surface area that is about twice larger.

No apparent effect of $HgCl_2$ was observed on the dissolution kinetics of synthetic calcite in stirred reactor (***Fig. 4.6***). The dissolution rates of foraminifera sediment grains, when normalized to the SWI-surface area, are slightly slower than that of synthetic calcite. For synthetic calcite and foraminifera, samples obtained in supersaturated waters showed no dissolution rate values statistically different than zero, as shown in ***Fig. 4.6*** and reported in ***Table 4.3***.

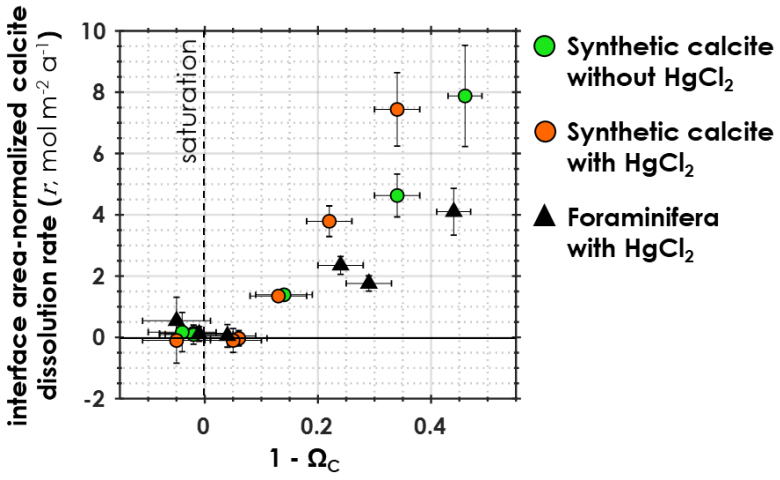

Fig. 4.6 | *Interface area-normalized dissolution rates as a function of steady-state undersaturation state (1 – Ω_C) for synthetic calcite (with or without $HgCl_2$) and foraminifera, in stirred reactors.*

Soluble reactive phosphate (SRP) concentrations were measured from steady-state seawater samples for all dissolution experiments. SRP concentration differs depending on the nature of the sediment. In sediments containing synthetic calcite (***Fig. 4.3***), SRP concentration in the overlying water at steady state was 1.9 ± 1.1 μmol kg^{-1} and showed a weak, positive linear correlation ($R^2 = 0.32$) with the dissolution rate and with the clay content ($R^2 = 0.25$). To identify the source of SRP in our experiments, we carried out SRP desorption experiments from pure calcite powder and montmorillonite in seawater. Four grams of the two solids were transferred separately into closed glass bottles filled with 200 mL of natural seawater with an initial SRP concentration of 0.85 μM. The solutions were allowed to equilibrate for one week under constant stirring before being filtered through a 0.45 μm Millipore HA filter and the final SRP concentration determined spectrophotometrically within 24h. Results of these experiments revealed that the montmorillonite released 1.15 μM phosphate per gram of montmorillonite in a week whereas the $CaCO_3$ powder adsorbed 0.17 μM of phosphate per gram of calcite onto its surface. The latter observation is consistent with results found in the literature (de Kanel and Morse, 1978; House and Donaldson, 1986; Millero et al., 2001; Sø et al., 2011), i.e., that SRP has a strong affinity for calcite surfaces. Following the SRP evolution with time for a calcite – montmorillonite sediment (porosity = 0.79, 53 weight % of calcite) immersed in natural seawater, see ***Fig. 4.7***, we measured a net decrease in [SRP] (SRP adsorption on calcite) during the first 5 days, followed by a net increase (SRP desorption by montmorillonite) between 5 and 20 days. The average rate of net desorption between 4 and 14 days after immersion of the disks was 2.0 ± 0.74 μmol per gram of dry sediment per day (μmol g^{-1} d^{-1}). After 40 days, SRP desorption was not statistically different than zero (0.10 ± 0.21 μmol g^{-1} d^{-1}). Our interpretation of the data is that montmorillonite SRP desorption and calcite SRP adsorption reactions occur concurrently but with different kinetics and adsorption capacities. Whereas calcite SRP adsorption is initially faster than SRP desorption from montmorillonite, the calcite adsorption capacity or kinetics ultimately is overwhelmed by SRP desorption from the montmorillonite. The link between SRP release and dissolution rate is evident for experiments with coccolithic sediments ($R^2 = 0.74$), in which the measured steady-state SRP concentration was as high as 10.21 ± 0.05 μmol kg^{-1}. For sediment beds of pure synthetic calcite and foraminifera in stirred-flow reactors, under high shear stress, no correlation was observed between dissolution and SRP release ($R^2 = 0.04$), and the SRP concentration was smaller, at 1.7 ± 0.4 μmol kg^{-1}.

4.4 Discussion

Dissolution of $CaCO_3$ at the SWI is influenced by a complex network of variables that are changing synergistically. Here, we use the data from the first category of experiments, carried out in the rotating disk reactor with simulated sediments containing synthetic calcite, to study the role of each of the variables on the calcite dissolution rate.

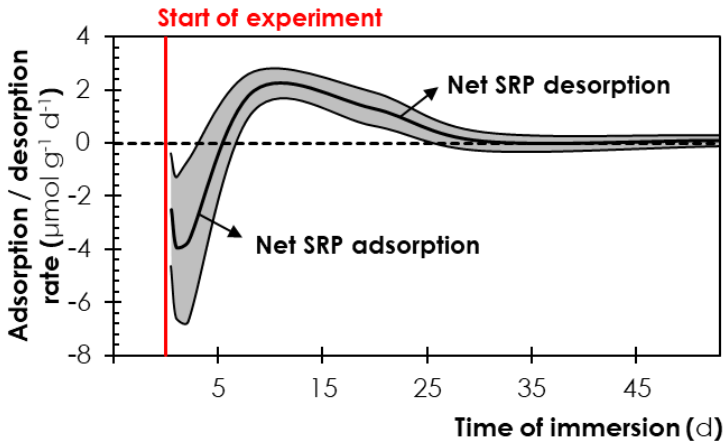

Fig. 4.7 | *Soluble reactive phosphate (SRP) adsorption on or desorption from a synthetic calcite-montmorillonite sediment as a function of the time of immersion in natural seawater. The black dashed line represents no net SRP adsorption or desorption, as a reference, and the shaded area represents plus or minus one standard deviation from the measurement.*

Linear regression models are commonly used to study dependencies between variables. In such models, the first step is to identify which variables in a given dataset are independent, i.e., are not influenced by any other variable, and which variables are dependent, i.e., a direct or indirect consequence of the independent variables. In the present study, the DBL thickness (δ), sediment permeability (κ), seawater temperature (T) and salinity (S_P) are all independent variables, as they are set by the experimenter. Here, we will treat [SRP] as an independent variable. Although one could consider Ω_C as both an independent and a dependent variable, as low Ω_C favours dissolution, but the latter reaction releases CO_3^{2-} ions, increasing Ω_C, we will also treat Ω_C as an independent variable. The dissolution rate, r, is a dependent variable, affected by a combination of all the variables previously mentioned. Using the Paleontological Statistics Software Package for Education and Data Analysis described in Hammer et al. (2001), we performed a multiple regression of *r* on a linear combination of our 6 independent variables, by minimizing the sum of

the squared residuals between the predicted and measured *r*. We find that, statistically, *r* can be expressed as a linear combination of all defined independent variables ($F = 10.3$, $p = 4 \times 10^{-5}$, degrees of freedom = 6 and 19), and 77 % of the variability in the measured *r* values can be explained by a linear combination of our 6 independent variables (multiple linear regression coefficient $R^2 = 0.77$), the rest being due to other undetermined factors or to the analytical uncertainty. Among the 6 independent variables, only Ω_C and δ exert a statistically significant control over *r* (i.e., the fitting coefficients for these variables are significantly different than zero, with p values of 4×10^{-5} and 2×10^{-3}, respectively), while the contributions of T, κ, S_P and [SRP] to the overall dissolution rate are insignificant (i.e., the fitting coefficients for these variables are not significantly different than zero, with p values of 0.94, 0.76, 0.94, 0.36, respectively).

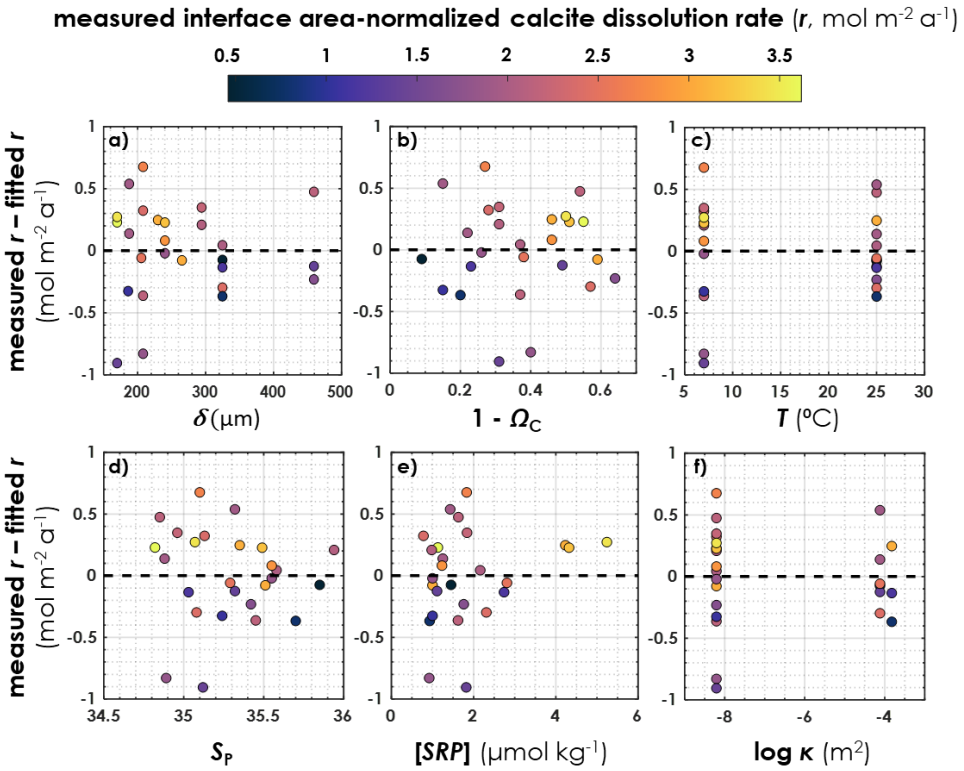

Fig. 4.8 | *Dissolution rate residuals (fitted r – measured r) as a function of a) the diffusive boundary layer thickness (δ), b) steady-state undersaturation state of seawater with respect to calcite ($1 - \Omega_C$)c) temperature (T), d) practical salinity (S_P), e) soluble reactive phosphate concentration ([SRP]) and f) permeability on a log scale (κ). Color indicates the measured dissolution rate.*

Since only two variables have a statistically significant influence on the dissolution rates, i.e., δ and Ω_C, we can go further in the fitting of our dissolution rates and, using a Levenberg-Marquardt algorithm (Pujol, 2007), fit our experimental data to a three-dimensional second-order polynomial regression model (26 iterations, degrees of freedom = 20, R^2 = 0.78):

$$r = -8.5 \times 10^{-6}\,\delta^2 - 3.2 \times 10^{-3}\,\delta\,(1 - \Omega_c) + 1.2 \times 10^{-3}\,\delta - 3\,(1 - \Omega_c)^2 + 7.6\,(1 - \Omega_c) + 0.48 \qquad (4.4)$$

Note that this expression has no mechanistic significance, as it deviates from the first order kinetics ruling calcite dissolution kinetics at the SWI. The fit residuals, i.e., differences between measured dissolution rates and values computed with ***Eq. 4.4***, are shown as a function of each of the 6 independent variables in ***Fig. 4.8***. In ***Fig. 4.9a***, we represent r for the 26 experiments run on sediments with synthetic calcite as a function of δ and Ω_C. ***Fig. 4.9b*** shows the data from the same experiments, but for theoretical dissolution rates, i.e., fitted from ***Eq. 4.4*** instead of being measured from ***Eq. 4.3***. In ***Fig. 4.9c***, we show the theoretical dissolution rate, computed with ***Eq. 4.4***, extrapolated to cover a δ range between 100 and 500 μm, and a $(1 - \Omega_C)$ range between 0 and 0.6.

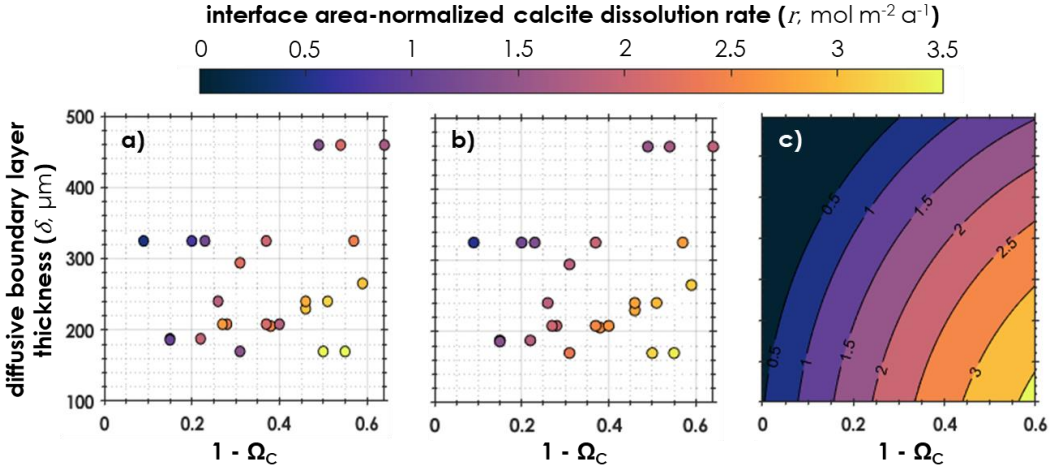

Fig. 4.9 | *a) Measured, b) fitted and c) extrapolated calcite dissolution rate (r) as a function of the diffusive boundary layer thickness (δ) and the steady-state undersaturation state of seawater with respect to calcite ($1 - \Omega_C$).*

The diffusive boundary layer thickness, δ, which is comprised roughly between 200 μm and 1 mm at the deep seafloor (Sulpis et al., 2018), thickens as bottom currents decelerate, and

thins as they accelerate (Boudreau and Guinasso, 1982; Higashino and Stefan, 2004; Larkum et al., 2003; Levich, 1962; Lorke et al., 2003; Santschi et al., 1991; Santschi et al., 1983). Thus, since δ is, as Ω_C, controlling the dissolution rate of calcite at the SWI, both the variations in bottom current speed and in bottom-water chemistry (i.e., Ω_C) should be taken into account when interpreting calcite dissolution / preservation data through time.

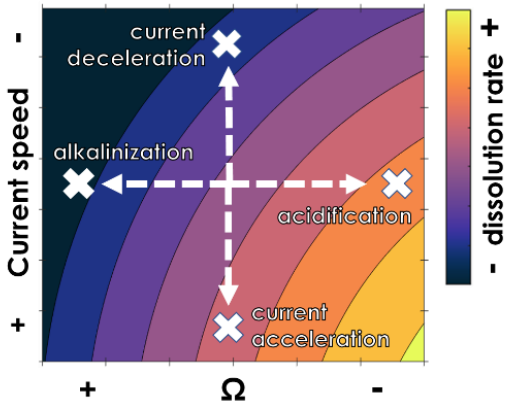

Fig. 4.10 | *Conceptual diagram representing the calcite dissolution rate at the SWI as a function of the bottom-current speed and the bottom-water undersaturation state with respect to calcite ($1 - \Omega_C$). White arrows represent the theoretical paths of the dissolution rate, starting at the center of the diagram, in response to four events, current deceleration, current acceleration, seawater acidification and seawater alkalinization.*

It is well known that seawater Ω_C can fluctuate through time, whether it is at a diel timescale (e.g., Cyronak et al., 2013), centennial timescale (e.g., Orr et al., 2005), or on the scale of million of years (e.g., Boudreau et al., 2019). The role that this varying Ω_C plays on the dissolution of calcite in seawater is well understood. Here, we wish to point out that the direction and speed of bottom currents also changes with time, even deep in the ocean, and that according to the results presented here, this should be taken into account along with Ω_C changes. For instance, using current-meter measurements, Thomson and Davis (2017) showed that at 4300 m-depth, in the Middle America Trench off Costa Rica, 21 m above the bottom, the current speed fluctuates from less than 1 to 27 cm s^{-1} within a single day. Assuming $S_p = 35$ and $T = 2$ ºC and using the equations presented in Sulpis et al. (2018), that would represent a DBL thickness oscillating between 5.2 mm and 331 μm, respectively. Likewise, bottom currents can weaken or strengthen due to climate changes, as it is currently the case in the North Atlantic due to a weakening of the Atlantic meridional overturning circulation (Caesar et al., 2018; Thornalley et al., 2018). Finally, in the geological past, examples of abrupt (Garcia-

Castellanos and Villasenor, 2011) or gradual (Ramsay et al., 1998) changes in the ocean circulation patterns have been documented in the literature. In this context, and as summarized in ***Fig. 4.10***, both current deceleration and a Ω_C increase will lead to slower calcite dissolution at the SWI, while both current acceleration and seawater acidification tend to enhance the dissolution rate.

4.5 Conclusion

The dissolution of calcite at the seafloor will be the ultimate sink for anthropogenic CO_2. Hence, an accurate kinetic description of the dissolution reaction is required to estimate the timescales at which the ocean may return to its pre-acidification state. Yet, an experimental study attempting to accurately quantify and identify the controlling factors of the kinetics of dissolution of calcite under deep-sea like conditions is absent from the literature. Here, we have run 70 dissolution experiments over a range of temperature, sediment porosity and permeability, grain size and specific surface area, seawater saturation state with respect to calcite (Ω_C) and diffusive boundary layer thicknesses δ that is representative of deep-sea conditions, for biogenic and synthetic calcite particles. Our results show, at the sediment-water interface (SWI) and under our experimental conditions, only Ω_C and δ have a statistically significant influence on calcite dissolution rate. This confirms the water-side control of the dissolution reaction at the SWI. Based on these observations, we argue that geologically long- or medium-term changes in bottom-current velocities, such as those that may be induced by changes in continental positions or evolving climate, should be considered along with variations of calcite deposition fluxes or seawater acidification when interpreting calcite preservation data through time.

References

Amarasinghe, P.M., Katti, K.S. and Katti, D.R. (2012) Insight into role of clay-fluid molecular interactions on permeability and consolidation behavior of Na-montmorillonite swelling clay. *Journal of Geotechnical and Geoenvironmental Engineering*, 138, 138-146.

Arvidson, R.S., Fischer, C. and Luttge, A. (2015) Calcite Dissolution Kinetics. *Aquatic Geochemistry* 21, 415-422.

Berelson, W.M., Balch, W.M., Najjar, R., Feely, R.A., Sabine, C. and Lee, K. (2007) Relating estimates of $CaCO_3$ production, export, and dissolution in the water column to measurements of $CaCO_3$ rain into sediment traps and dissolution on the sea floor: A revised global carbonate budget. *Global Biogeochemical Cycles* 21(1), https://doi.org/10.1029/2006GB002803

Berner, R.A. and Mackenzie, F.T. (2011) Burial and Preservation of Carbonate Rocks Over Phanerozoic Time. *Aquatic Geochemistry* 17, 727-733.

Boudreau, B.P. (1996) A method-of-lines code for carbon and nutrient diagenesis in aquatic sediments. *Computers & Geosciences* 22, 479-496.

Boudreau, B.P. (2013) Carbonate dissolution rates at the deep ocean floor. *Geophysical Research Letters* 40, 744-748.

Boudreau, B.P. and Guinasso Jr., N.L. (1982) The influence of a diffusive boundary layer on accretion, dissolution, and diagenesis at the sea floor. In: Fanning, K.A., Manheim, F.T. [Eds.]. *The Dynamic Environment of the Ocean Floor*. Lexington Books, Lexington, pp. 115-145.

Boudreau, B.P. and Jørgensen, B.B. (2001) The Benthic Boundary Layer: Transport Processes and Biogeochemistry. Oxford University Press, Oxford.

Boudreau, B.P., Middelburg, J.J., Sluijs, A. and van der Ploeg, R. (2019) Secular variations in the carbonate chemistry of the oceans over the Cenozoic. *Earth and Planetary Science Letters* 512, 194-206.

Broecker, W.S. and Peng, T.H. (1982) Tracers in the Sea. Lamont-Doherty Geological Observatory, Columbia University, Palisades, New York.

Brunauer, S., Emmett, P.H. and Teller, E. (1938) Adsorption of gases in multimolecular layers. *Journal of the American Chemical Society*, 60, 309-319.

Bukry, D. (1971) Discoaster evolutionary trends. *Micropaleontology*, 17, 43-52.

Caesar, L., Rahmstorf, S., Robinson, A., Feulner, G. and Saba, V. (2018) Observed fingerprint of a weakening Atlantic Ocean overturning circulation. *Nature* 556, 191-196, https://doi.org/10.1038/s41586-018-0006-5

Channell, J., Sato, T., Kanamatsu, T., Stein, R., Alvarez Zarikian, C. and Scientists, t.E. (2006) Expedition 303/306 synthesis: North Atlantic climate. Proc. IODP, vol. 303/306, IODP Management International, College Station, TX.

Colombani, J. (2016) The alkaline dissolution rate of calcite. *The Journal of Physical Chemistry Letters* 7(13), 2376-2380.

Cubillas, P., Köhler, S., Prieto, M., Chaïrat, C. and Oelkers, E.H. (2005). Experimental determination of the dissolution rates of calcite, aragonite, and bivalves. *Chemical Geology* 216(1-2), 59-77.

Cyronak, T., Santos, I.R., McMahon, A. and Eyre, B.D. (2013) Carbon cycling hysteresis in permeable carbonate sands over a diel cycle: Implications for ocean acidification. *Limnology and Oceanography* 58, 131-143.

Dade, W.B., Hogg, A.J. and Boudreau, B.P. (2001) Physics of flow above the sediment-water interface. In Boudreau, B.P., Jørgensen, B.B. (Eds.), The Benthic Boundary Layer. Oxford University Press, New York.

de Kanel, J. and Morse, J.W. (1978) The chemistry of orthophosphate uptake from seawater on to calcite and aragonite. *Geochimica et Cosmochimica Acta* 42, 1335-1340.

Dickson, A.G. (1984) pH scales and proton-transfer reactions in saline media such as sea water. *Geochimica et Cosmochimica Acta* 48(11), 2299-2308.

Dickson, A.G. (1990) Standard potential of the reaction: $AgCl(s)+1/2H_2(g) = Ag(s)+HCl(aq)$, and the standard acidity constant of the ion HSO_4^- in synthetic sea water from 273.15 to 318.15 K. *The Journal of Chemical Thermodynamics* 22, 113-127, https://doi.org/10.1016/0021-9614(90)90074-Z

Dickson, A.G., Sabine, C.L. and Christian, J.R. (2007) Guide to best practices for ocean CO_2 measurements. *PICES Special Publication* 3, 191 pp.

Dong, S., Subhas, A.V., Rollins, N.E., Naviaux, J.D., Adkins, J.F. and Berelson, W.M. (2018) A kinetic pressure effect on calcite dissolution in seawater. *Geochimica et Cosmochimica Acta* 238, 411-423.

Emerson, S. and Bender, M. (1981) Carbon fluxes at the sediment-water interface of the deep-sea: calcium carbonate preservation. *Journal of Marine Research* 39, 139-162.

Erez, J. (2003) The source of ions for biomineralization in foraminifera and their implications for paleoceanographic proxies. *Reviews in Mineralogy & Geochemistry* 54, 115-149.

Feely, R.A., Sabine, C.L., Lee, K., Berelson, W., Kleypas, J., Fabry, V.J. and Millero, F.J. (2004) Impact of Anthropogenic CO_2 on the $CaCO_3$ System in the Oceans. *Science* 305(5682), 362-366.

Flores, J.-A., Gersonde, R., Sierro, F.J. and Niebler, H.-S. (2000) Southern Ocean Pleistocene calcareous nannofossil events: calibration with isotope and geomagnetic stratigraphies. *Marine Micropaleontology* 40, 377-402.

Gal, A., Wirth, R., Kopka, J., Fratzl, P., Faivre, D. and Scheffel, A. (2016) Macromolecular recognition directs calcium ions to coccolith mineralization sites. *Science* 353, 590-593.

Garcia-Castellanos, D. and Villasenor, A. (2011) Messinian salinity crisis regulated by competing tectonics and erosion at the Gibraltar arc. *Nature* 480, 359-363.

Gartner, S., Jr. (1967) Calcareous nannofossils from Neogene of Trinidad, Jamaica, and Gulf of Mexico. Paleontological Contributions. *University of Kansas* 29, 1-7.

Gehlen, M., Bassinot, F.C., Chou, L. and McCorkle, D. (2005) Reassessing the dissolution of marine carbonates: II. Reaction kinetics. *Deep Sea Research Part I: Oceanographic Research Papers* 52(8), 1461-1476.

Gehlen, M., Bopp, L. and Aumont, O. (2008) Short-term dissolution response of pelagic carbonate sediments to the invasion of anthropogenic CO_2: A model study. *Geochemistry, Geophysics, Geosystems*, 9(2), https://doi.org/10.1029/2007gc001756

Grasshoff, K., Kremling, K. and Ehrhardt, M. (1999) Methods of Seawater Analysis. Wiley.

Hales, B. and Emerson, S. (1997) Evidence in support of first-order dissolution kinetics of calcite in seawater. *Earth and Planetary Science Letters* 148(1), 317-327.

Hammer, Ø., Harper, D.A.T., and Ryan, P.D. (2001) PAST: Paleontological statistics software package for education and data analysis. *Palaeontologia Electronica* 4(1): 9pp.

Hayward, B.W., Le Coze, F. and Gross, O. (2018) World Foraminifera Database. Globigerinoides ruber (d'Orbigny, 1839). Accessed at: http://www.marinespecies.org/foraminifera/aphia.php?p=taxdetails&id=113444 on 2019-02-25,

Higashino, M., and Stefan, H. G. (2004) Diffusive boundary layer development above a sediment-water interface. *Water Environment Research* 76: 292-300, https://doi.org/10.2175/106143004X141870.

Honjo, S. and Erez, J. (1978) Dissolution rates of calcium carbonate in the deep ocean; an in-situ experiment in the North Atlantic Ocean. *Earth and Planetary Science Letters* 40, 287-300.

House, W.A. and Donaldson, L. (1986) Adsorption and coprecipitation of phosphate on calcite. *Journal of Colloid and Interface Science* 112, 309-324.

Jansen, H., Zeebe, R.E. and Wolf-Gladrow, D.A. (2002) Modeling the dissolution of settling $CaCO_3$ in the ocean. *Global Biogeochemical Cycles* 16, 11-11-11-16.

Kattner, G. (1999) Storage of dissolved inorganic nutrients in seawater: poisoning with mercuric chloride. *Marine Chemistry* 67, 61-66.

Keir, R.S. (1980) The dissolution kinetics of biogenic calcium carbonates in seawater. *Geochimica et Cosmochimica Acta* 44(2), 241-252.

Keir, R.S. (1983) Variation in the carbonate reactivity of deep-sea sediments: determination from flux experiments. *Deep-Sea Research* 30, 279-296.

Key, R.M., Olsen, A., van Heuven, S., Lauvset, S.K., Velo, A., Lin, X., Schirnick, C., Kozyr, A., Tanhua, T., Hoppema, M., Jutterström, S., Steinfeldt, R., Jeansson, E., Ishi, M., Perez, F.F. and Suzuki, T. (2015) Global Ocean Data Analysis Project, Version 2 (GLODAPv2), ORNL/CDIAC-162, NDP-P093. Carbon Dioxide Information Analysis Center, Oak Ridge National Laboratory, US Department of Energy, Oak Ridge, Tennessee.

Larkum, A.W.D., Koch, E.M.W., and Kühl, M. (2003) Diffusive boundary layers and photosynthesis of the epilithic algal community of coral reefs. *Marine Biology* 142: 1073-1082, https://doi.org/10.1007/s00227-003-1022-y.

Lauvset, S.K., Key, R.M., Olsen, A., Heuven, S.v., Velo, A., Lin, X., Schirnick, C., Kozyr, A., Tanhua, T., Hoppema, M., Jutterström, S., Steinfeldt, R., Jeansson, E., Ishii, M., Perez, F.F., Suzuki, T. and Watelet, S. (2016) A new global interior ocean mapped climatology: the 1° × 1° GLODAP version 2. *Earth System Science Data* 8, 325-340, https://doi.org/10.5194/essd-8-325-2016

Levich, V. G. (1962) *Physicochemical Hydrodynamics*, Prentice-Hall.

Lewis, E. and Wallace, D.W.R. (1998) Program Developed for CO_2 System Calculations. ORNL/CDIAC-105. Carbon Dioxide Information Analysis Center, Oak Ridge National Laboratory, U.S. Department of Energy, Oak Ridge, Tennessee.

Lorke, A., Müller, B., Maerki, M. and Wüest, A. (2003) Breathing sediments: The control of diffusive transport across the 530 sediment-water interface by periodic boundary-layer turbulence. *Limnology and Oceanography* 48: 2077-2085, https://doi.org/10.4319/lo.2003.48.6.2077.

Lueker, T.J., Dickson, A.G. and Keeling, C.D. (2000) Ocean pCO_2 calculated from dissolved inorganic carbon, alkalinity, and equations for K_1 and K_2: validation based on laboratory measurements of CO_2 in gas and seawater at equilibrium. *Marine Chemistry* 70, 105-119, https://doi.org/10.1016/S0304-4203(00)00022-0

Meysman, F.J.R., Boudreau, B.P. and Middelburg, J.J. (2005) Modeling reactive transport in sediments subject to bioturbation and compaction. *Geochimica et Cosmochimica Acta* 69, 3601-3617.

Millero, F., Huang, F., Zhu, X., Liu, X. and Zhang, J.-Z. (2001) Adsorption and desorption of phosphate on calcite and aragonite in seawater. *Aquatic Geochemistry* 7(1), 33-56.

Millero, F.J. (1995) Thermodynamics of the carbon dioxide system in the oceans. *Geochimica et Cosmochimica Acta* 59, 661-677, https://doi.org/10.1016/0016-7037(94)00354-O

Morse, J.W. (1978) Dissolution kinetics of calcium carbonate in sea water: VI. The near-equilibrium dissolution kinetics of calcium carbonate-rich deep sea sediments. *American Journal of Science* 278(3): 344-353.

Morse, J.W. and Mackenzie, F.T. (1990) Geochemistry of Sedimentary Carbonates. Elsevier, Amsterdam.

Mucci, A. (1983) The solubility of calcite and aragonite in seawater at various salinities, temperatures and one atmosphere total pressure. *American Journal of Science* 283, 780-799, http://doi.org/10.2475/ajs.283.7.780

Murphy, J. and Riley, J. P. (1962). A modified single solution method for the determination of phosphate in natural waters. *Analytica Chimica Acta* 27, 31-36.

Naviaux, J.D., Subhas, A.V., Rollins, N.E., Dong, S., Berelson, W.B. and Adkins, J.F. (2019). Temperature dependence of calcite dissolution kinetics in seawater. *Geochimica et Cosmochimica Acta* 246: 363-384, https://doi.org/10.1016/j.gca.2018.11.037

Olsen, A., Key, R. M., van Heuven, S., Lauvset, S. K., Velo, A., Lin, X., Schirnick, C., Kozyr, A., Tanhua, T., Hoppema, M., Jutterström, S., Steinfeldt, R., Jeansson, E., Ishii, M., Pérez, F. F., and Suzuki, T. (2016) The Global Ocean Data Analysis Project version 2 (GLODAPv2) – an internally consistent data product for the world ocean, *Earth System Science Data*, 8, 297-323, https://doi.org/10.5194/essd-8-297-2016.

Orr, J.C., Epitalon, J.-M., Dickson, A.G. and Gattuso, J.-P. (2018) Routine uncertainty propagation for the marine carbon dioxide system. *Marine Chemistry* 207: 84-107, https://doi.org/10.1016/j.marchem.2018.10.006

Orr, J.C., Epitalon, J.M. and Gattuso, J.P. (2015) Comparison of ten packages that compute ocean carbonate chemistry. *Biogeosciences* 12(5), 1483-1510.

Orr, J.C., Fabry, V.J., Aumont, O., Bopp, L., Doney, S.C., Feely, R.A., Gnanadesikan, A., Gruber, N., Ishida, A., Joos, F., Key, R.M., Lindsay, K., Maier-Reimer, E., Matear, R., Monfray, P., Mouchet, A., Najjar, R.G., Plattner, G.K., Rodgers, K.B., Sabine, C.L., Sarmiento, J.L., Schlitzer, R., Slater, R.D., Totterdell, I.J., Weirig, M.F., Yamanaka, Y. and Yool, A. (2005) Anthropogenic ocean acidification over the twenty-first century and its impact on calcifying organisms. *Nature* 437, 681-686, https://doi.org/10.1038/nature04095

Pierrot, D., Lewis, E. and Wallace, D. (2006) *MS Excel Program Developed for CO_2 System Calculations*. ORNL/CDIAC-105a, Carbon Dioxide Information Analysis Center, Oak Ridge National Laboratory, U.S. Department of Energy, Oak Ridge, Tennessee.

Pomar, L. (2001) Types of carbonate platforms: a genetic approach. *Basin Research* 13, 313-334.

Pujol, J. (2007) The solution of nonlinear inverse problems and the Levenberg-Marquardt method. *Geophysics* 72, W1-W16.

Ramsay, A.T.S., Smart, C.W. and Zachos, J.C. (1998) A Model of early to middle Miocene Deep Ocean circulation for the Atlantic and Indian Oceans. *Geological Society, London, Special Publications* 131, 55-70.

Santschi, P. H., Bower, P., Nyffeler, U. P., Azevedo, A. and Broecker, W. S. (1983) Estimates of the resistance to chemical transport posed by the deep-sea boundary layer. *Limnology and Oceanography* 28: 899-912, https://doi.org/10.4319/lo.1983.28.5.0899.

Santschi, P.H., Anderson, R.F., Fleisher, M.Q. and Bowles, W. (1991) Measurements of diffusive sublayer thicknesses in the ocean by alabaster dissolution, and their implications for the measurements of benthic fluxes. *Journal of Geophysical Research: Oceans* 96, 10641-10657, https://doi.org/10.1029/91JC00488

Sarmiento, J.L. and Gruber, N. (2006) Ocean Biogeochemical Dynamics. Princeton University Press, Princeton, NJ.

Schink, D. R., and Guinasso, N. L. (1977) Modelling the influence of bioturbation and other processes on calcium carbonate dissolution at the sea floor. In N. R. Andersen and A. Malahoff [Eds.]. The Fate of Fossil Fuel CO_2 in the Oceans. Plenum Press. p. 375-400.

Sharqawy, M.H., Lienhard, J.H. and Zubair, S.M. (2010) Thermophysical properties of seawater: a review of existing correlations and data. *Desalination and Water Treatment* 16, 354-380.

Shepherd, R.G. (1989) Correlations of Permeability and Grain Size. *Groundwater* 27, 633-638.

Sjöberg, E. L. and Rickard, D. (1983) The influence of experimental design on the rate of calcite dissolution. *Geochimica Cosmochimica Acta* 47, 2281-2285, https://doi.org/10.1016/0016-7037(83)90051-0

Smith, S.V., Mackenzie, F.T. (2016) The role of $CaCO_3$ reactions in the contemporary oceanic CO_2 cycle. *Aquatic Geochemistry* 22, 153-175.

Sø, H.U., Postma, D., Jakobsen, R. and Larsen, F. (2011) Sorption of phosphate onto calcite; results from batch experiments and surface complexation modeling. *Geochimica et Cosmochimica Acta* 75, 2911-2923.

Subhas, A.V., Rollins, N.E., Berelson, W.M., Dong, S., Erez, J. and Adkins, J.F. (2015) A novel determination of calcite dissolution kinetics in seawater. *Geochimica et Cosmochimica Acta* 170, 51-68.

Subhas, A.V., Adkins, J.F., Rollins, N.E., Naviaux, J., Erez, J. and Berelson, W.M. (2017) Catalysis and chemical mechanisms of calcite dissolution in seawater. *Proceedings of the National Academy of Sciences of the U.S.A* 114(31), 8175-8180.

Subhas, A.V., Rollins, N.E., Berelson, W.M., Erez, J., Ziveri, P., Langer, G. and Adkins, J.F. (2018) The dissolution behavior of biogenic calcites in seawater and a possible role for magnesium and organic carbon. *Marine Chemistry* 205, 100-112.

Sulpis, O., Boudreau, B.P., Mucci, A., Jenkins, C.J., Trossman, D.S., Arbic, B.K. and Key, R.M. (2018) Current $CaCO_3$ dissolution at the seafloor caused by anthropogenic CO_2. *Proceedings of the National Academy of Sciences of the United States of America* 115, 11700-11705, https://doi.org/10.1073/pnas.1804250115

Sulpis, O., Lix, C., Mucci, A. and Boudreau, B.P. (2017) Calcite dissolution kinetics at the sediment-water interface in natural seawater. *Marine Chemistry* 195, 70-83, https://doi.org/10.1016/j.marchem.2017.06.005

Sulpis, O., Mucci A., Boudreau, B.P., Barry M. and Johnson B. (2019) Controlling the diffusive boundary layer thickness above the sediment-water interface in a thermostated, rotating-disk reactor. *Limnology and Oceanography: Methods*.

Teal, L.R., Bulling, M.T., Parker, E.R. and Solan, M. (2008) Global patterns of bioturbation intensity and mixed depth of marine soft sediments. *Aquatic Biology* 2: 207-218, https://doi.org/10.3354/ab00052.

Thomson, R.E. and Davis, E.E. (2017) Equatorial Kelvin waves generated in the western tropical Pacific Ocean trigger mass and heat transport within the Middle America Trench off Costa Rica. *Journal of Geophysical Research: Oceans* 122, 5850-5869.

Thornalley, D.J.R., Oppo, D.W., Ortega, P., Robson, J.I., Brierley, C.M., Davis, R., Hall, I.R., Moffa-Sanchez, P., Rose, N.L., Spooner, P.T., Yashayaev, I. and Keigwin, L.D. (2018) Anomalously weak Labrador Sea convection and Atlantic overturning during the past 150 years. *Nature* 556, 227-230, https://doi.org/10.1038/s41586-018-0007-4

Trossman, D.S., Arbic, B.K., Richman, J.G., Garner, S.T., Jayne, S.R. and Wallcraft, A.J. (2016) Impact of topographic internal lee wave drag on an eddying global ocean model. *Ocean Modelling* 97, 109-128.

Trowbridge, J. H., and Lentz, S. J. (2018) The bottom boundary layer. *Annual Review of Marine Sciences* 10, 397-420.

Uppström, L. R. (1974) The boron/chlorinity ratio of deep-sea water from the Pacific Ocean. *Deep-Sea Research* 21, 161-162.

Vital, H., Stattegger, K., Amaro, V.E., Schwarzer, K., FrazÃO, E.P., Tabosa, W.F. and Silveira, I.M. (2008) A Modern High-Energy Siliciclastic–Carbonate Platform: Continental Shelf Adjacent to Northern Rio Grande Do Norte State, Northeastern Brazil. *Recent Advances in Models of Siliciclastic Shallow-Marine Stratigraphy*, 177-190.

Walter, L.M. and Morse, J.W. (1985) The dissolution kinetics of shallow marine carbonates in seawater: A laboratory study. *Geochimica et Cosmochimica Acta* 49(7): 1503-1513.

Whitaker, S. (1986) Flow in porous media I: A theoretical derivation of Darcy's Law. *Transport in Porous Media* 1, 3-25.

Xu, P. and Yu, B. (2008) Developing a new form of permeability and Kozeny–Carman constant for homogeneous porous media by means of fractal geometry. *Advances in Water Resources* 31, 74-81.

Table 4.1 | *Description of dissolution experiments for sediments containing synthetic calcite in rotating-disk reactors. We report the sediment porosity (**φ**), permeability (κ), relative dry weight percentage of quartz sand, montmorillonite clay and calcite, temperature (T), diffusive boundary layer thickness (δ), soluble reactive phosphate concentration ([SRP]), practical salinity (S_P), steady-state seawater pCO_2 and saturation state with respect to calcite (Ω_C) and interface surface-area normalized calcite dissolution rate.*

φ	κ	Quartz sand	Clay	Calcite	T	δ	[SRP] ±5%	S_P ±0.04	pCO_2	Ω_C	r
(%)	(m^2)	(wt %)	(wt %)	(wt %)	(ºC)	(µm)	(µmol kg^{-1})		(µatm)		(mol m^{-2} a^{-1})
79 ± 2	6.2 x10^{-9} ± 2.7 x10^{-9}	0	50	50	25	265	2.94	35.51	442.3 ± 10.6	0.41 ± 0.02	3.04 ± 1.16
79 ± 2	6.2 x10^{-9} ± 2.7 x10^{-9}	0	50	50	25	459	1.63	34.85	506.8 ± 10.9	0.46 ± 0.03	2.13 ± 0.58
79 ± 2	6.2 x10^{-9} ± 2.7 x10^{-9}	0	50	50	25	325	2.16	35.58	317.5 ± 6.7	0.63 ± 0.04	2.02 ± 0.58
79 ± 2	6.2 x10^{-9} ± 2.7 x10^{-9}	0	50	50	25	459	1.76	35.42	570.7 ± 11.5	0.36 ± 0.02	1.68 ± 0.55
78 ± 2	7.6 x10^{-5} ± 5.6 x10^{-5}	25	25	50	25	325	1.45	35.85	356.9 ± 7.6	0.91 ± 0.05	0.46 ± 0.08
78 ± 2	7.6 x10^{-5} ± 5.6 x10^{-5}	25	25	50	25	188	1.25	34.88	608.3 ± 12.1	0.78 ± 0.04	1.93 ± 0.32
78 ± 2	7.6 x10^{-5} ± 5.6 x10^{-5}	25	25	50	25	188	1.43	35.32	406.3 ± 8.5	0.85 ± 0.05	1.92 ± 0.38
79 ± 2	6.2 x10^{-9} ± 2.7 x10^{-9}	0	50	50	7 ± 1.5	208	1.73	35.13	445.7 ± 9.0	0.72 ± 0.05	2.38 ± 0.18
79 ± 2	6.2 x10^{-9} ± 2.7 x10^{-9}	0	50	50	7 ± 1.5	170	1.13	34.82	332.7 ± 6.8	0.45 ± 0.03	3.62 ± 0.55
79 ± 2	6.2 x10^{-9} ± 2.7 x10^{-9}	0	50	50	7 ± 1.5	294	1.98	35.94	338.6 ± 6.8	0.69 ± 0.05	2.07 ± 0.19
79 ± 2	6.2 x10^{-9} ± 2.7 x10^{-9}	0	50	50	7 ± 1.5	240	2.00	35.55	311.8 ± 6.3	0.74 ± 0.05	1.82 ± 0.17
79 ± 2	6.2 x10^{-9} ± 2.7 x10^{-9}	0	50	50	7 ± 1.5	208	2.83	35.10	314.2 ± 6.3	0.73 ± 0.05	2.68 ± 0.25
78 ± 2	7.6 x10^{-5} ± 5.6 x10^{-5}	25	25	50	25	325	2.31	35.08	684.0 ± 13.5	0.43 ± 0.02	2.42 ± 0.26
78 ± 2	7.6 x10^{-5} ± 5.6 x10^{-5}	25	25	50	25	459	1.11	35.32	592.3 ± 11.8	0.51 ± 0.03	1.38 ± 0.16
78 ± 2	7.6 x10^{-5} ± 5.6 x10^{-5}	25	25	50	25	205	2.81	35.29	516.6 ± 10.6	0.62 ± 0.04	2.50 ± 0.27
73 ± 2	1.5 x10^{-4} ± 1.1 x10^{-4}	50	0	50	25	230	1.24	35.35	495.0 ± 10.1	0.54 ± 0.03	3.06 ± 0.41
73 ± 2	1.5 x10^{-4} ± 1.1 x10^{-4}	50	0	50	25	325	0.62	35.70	309.2 ± 6.3	0.80 ± 0.04	0.79 ± 0.10
73 ± 2	1.5 x10^{-4} ± 1.1 x10^{-4}	50	0	50	25	325	0.93	35.03	441.7 ± 9.1	0.77 ± 0.04	1.18 ± 0.12
79 ± 2	6.2 x10^{-9} ± 2.7 x10^{-9}	0	50	50	7 ± 1.5	294	2.84	34.96	439.7 ± 8.9	0.69 ± 0.05	2.21 ± 0.18
79 ± 2	6.2 x10^{-9} ± 2.7 x10^{-9}	0	50	50	7 ± 1.5	208	1.92	34.89	359.1 ± 7.4	0.60 ± 0.04	1.81 ± 0.18
79 ± 2	6.2 x10^{-9} ± 2.7 x10^{-9}	0	50	50	7 ± 1.5	208	2.62	35.45	352.0 ± 7.1	0.63 ± 0.04	2.14 ± 0.21
79 ± 2	6.2 x10^{-9} ± 2.7 x10^{-9}	0	50	50	7 ± 1.5	170	2.82	35.12	307.4 ± 6.2	0.69 ± 0.05	1.42 ± 0.14
79 ± 2	6.2 x10^{-9} ± 2.7 x10^{-9}	0	50	50	7 ± 1.5	240	2.23	35.55	314.0 ± 6.3	0.54 ± 0.04	2.85 ± 0.74
79 ± 2	6.2 x10^{-9} ± 2.7 x10^{-9}	0	50	50	7 ± 1.5	186	1.21	35.24	275.6 ± 5.6	0.85 ± 0.06	1.06 ± 0.20
79 ± 2	6.2 x10^{-9} ± 2.7 x10^{-9}	0	50	50	7 ± 1.5	240	4.32	35.49	301.9 ± 6.2	0.49 ± 0.03	3.19 ± 0.95
79 ± 2	6.2 x10^{-9} ± 2.7 x10^{-9}	0	50	50	7 ± 1.5	170	5.24	35.07	303.9 ± 6.2	0.50 ± 0.03	3.47 ± 1.01

Table 4.2 | *Description of dissolution experiments for coccolithic and foraminiferal sand in rotating-disk reactors. We report the sediment porosity (**φ**), diffusive boundary layer thickness (δ), soluble reactive phosphate concentration ([SRP]), practical salinity (S_P), steady-state seawater pCO_2 and saturation state with respect to calcite (Ω_C) and interface surface-area normalized normalised calcite dissolution rate. All experiments were carried out at a temperature of 25ºC.*

Material	φ (%)	δ (μm)	[SRP] ±5% (μmol kg^{-1})	S_P ±0.04	pCO_2 (μatm)	Ω_C	r (mol m^{-2} a^{-1})
Coccoliths	88 ± 2	217	3.21	35.78	515.7 ± 10.2	1.03 ± 0.06	0.28 ± 0.08
Coccoliths	88 ± 2	217	4.09	35.86	607.2 ± 12.0	0.90 ± 0.05	0.32 ± 0.09
Coccoliths	88 ± 2	217	3.65	35.68	706.4 ± 14.0	0.79 ± 0.04	0.42 ± 0.12
Coccoliths	88 ± 2	217	6.32	35.65	745.9 ± 14.7	0.71 ± 0.04	0.65 ± 0.22
Coccoliths	88 ± 2	217	10.21	35.20	768.9 ± 15.0	0.68 ± 0.04	0.76 ± 0.27
Coccoliths	88 ± 2	459	2.43	35.56	477.6 ± 9.8	1.01 ± 0.06	0.13 ± 0.06
Coccoliths	88 ± 2	459	-	34.90	595.3 ± 11.8	0.82 ± 0.05	0.18 ± 0.11
Coccoliths	88 ± 2	459	5.32	34.88	718.1 ± 14.4	0.68 ± 0.04	0.34 ± 0.21
Coccoliths	88 ± 2	459	4.97	35.91	754.2 ± 15.0	0.66 ± 0.04	0.38 ± 0.25
Coccoliths	88 ± 2	459	8.21	35.61	798.6 ± 15.7	0.61 ± 0.03	0.46 ± 0.35
Foraminifera	84 ± 3	145	1.25	34.82	708.9 ± 14.0	0.93 ± 0.05	0.35 ± 0.17
Foraminifera	84 ± 3	145	2.18	35.02	482.9 ± 9.6	0.89 ± 0.05	0.60 ± 0.04
Foraminifera	84 ± 3	145	3.07	35.07	382.1 ± 7.6	0.85 ± 0.05	0.97 ± 0.07
Foraminifera	84 ± 3	145	1.69	35.22	413.9 ± 8.2	0.62 ± 0.04	2.11 ± 0.20
Foraminifera	84 ± 3	265	1.36	35.09	789.7 ± 15.5	0.92 ± 0.05	0.29 ± 0.10
Foraminifera	84 ± 3	265	1.00	35.46	728.0 ± 14.3	0.86 ± 0.05	0.34 ± 0.23
Foraminifera	84 ± 3	265	1.06	35.21	768.0 ± 15.1	0.83 ± 0.05	0.52 ± 0.29
Foraminifera	84 ± 3	265	0.96	35.41	509.9 ± 10.1	0.67 ± 0.04	0.83 ± 0.07
Foraminifera	84 ± 3	265	2.05	35.00	435.6 ± 18.7	0.62 ± 0.04	1.50 ± 0.14
Foraminifera	84 ± 3	265	2.27	35.75	419.5 ± 8.5	0.44 ± 0.03	1.79 ± 0.24
Foraminifera	84 ± 3	455	0.95	35.78	786.7 ± 15.5	0.87 ± 0.05	0.17 ± 0.16
Foraminifera	84 ± 3	455	0.98	35.90	709.8 ± 14.0	0.86 ± 0.05	0.25 ± 0.39
Foraminifera	84 ± 3	455	1.04	34.99	736.2 ± 14.6	0.88 ± 0.05	0.33 ± 0.33
Foraminifera	84 ± 3	455	0.94	35.54	475.2 ± 9.5	0.56 ± 0.03	0.83 ± 0.16
Foraminifera	84 ± 3	455	1.08	35.22	475.2 ± 9.6	0.44 ± 0.02	1.22 ± 0.29
Foraminifera	84 ± 3	455	0.85	35.12	438.6 ± 8.7	0.32 ± 0.02	1.28 ± 0.50

Table 4.3 | *Description of dissolution experiments in stirred reactors. We the mercuric chloride concentration in seawater ([$HgCl_2$]), soluble reactive phosphate concentration ([SRP]), practical salinity (S_P), steady-state seawater pCO_2 and saturation state with respect to calcite (Ω_C) and interface surface-area normalized normalised calcite dissolution rate. All experiments were carried out at a temperature of 25ºC.*

Material	[$HgCl_2$] (mg l^{-1})	[SRP] ±5% (µmol kg^{-1})	S_P ±0.04	pCO_2 (µatm)	Ω_C	r (mol m^{-2} a^{-1})
Synthetic calcite	0	1.23	35.60	454.8 ± 9.1	1.02 ± 0.06	0.13 ± 0.21
Synthetic calcite	0	1.08	35.42	426.1 ± 8.8	1.02 ± 0.06	0.09 ± 0.31
Synthetic calcite	0	1.11	35.83	481.4 ± 9.7	1.04 ± 0.06	0.17 ± 0.64
Synthetic calcite	0	1.24	35.75	417.0 ± 8.4	0.86 ± 0.05	1.39 ± 0.16
Synthetic calcite	0	1.73	35.98	369.1 ± 7.3	0.66 ± 0.04	4.63 ± 0.70
Synthetic calcite	0	1.14	35.13	321.7 ± 6.4	0.54 ± 0.03	7.88 ± 1.65
Synthetic calcite	100	1.23	35.78	434.0 ± 8.9	0.94 ± 0.05	-0.03 ± 0.25
Synthetic calcite	100	1.36	35.35	415.9 ± 8.3	0.95 ± 0.05	-0.10 ± 0.39
Synthetic calcite	100	1.39	35.24	437.6 ± 8.7	1.05 ± 0.06	-0.10 ± 0.74
Synthetic calcite	100	1.25	35.03	457.0 ± 9.1	0.87 ± 0.05	1.35 ± 0.15
Synthetic calcite	100	1.01	35.33	378.8 ± 7.6	0.78 ± 0.04	3.79 ± 0.50
Synthetic calcite	100	0.94	35.16	341.4 ± 6.9	0.66 ± 0.04	7.44 ± 1.20
Foraminifera	100	1.29	35.57	448.9 ± 9.1	1.01 ± 0.06	0.11 ± 0.24
Foraminifera	100	1.42	35.41	443.4 ± 8.8	0.96 ± 0.05	0.05 ± 0.37
Foraminifera	100	1.21	35.71	525.2 ± 10.8	1.05 ± 0.06	0.54 ± 0.77
Foraminifera	100	1.01	35.06	386.9 ± 7.7	0.71 ± 0.04	1.76 ± 0.25
Foraminifera	100	1.34	35.25	431.7 ± 8.8	0.76 ± 0.04	2.35 ± 0.29
Foraminifera	100	1.64	34.90	343.0 ± 6.9	0.56 ± 0.03	4.10 ± 0.76

Preface to Chapter 5

The geological record contains numerous examples of "greenhouse periods" and ocean acidification episodes, where the spreading of corrosive (CO_2-enriched) bottom waters enhances the dissolution of $CaCO_3$ minerals delivered to the seafloor or contained within deep-sea sediments. The dissolution of sedimentary $CaCO_3$ neutralizes excess CO_2, thus preventing runaway acidification, and acts as a negative feedback mechanism in regulating atmospheric CO_2 levels over time scales of centuries to millennia. Yet, there has been no concerted assessment of the current extent of anthropogenic $CaCO_3$ dissolution at the deep seafloor. In the following chapter, recent databases of bottom-water chemistry, benthic currents, and $CaCO_3$ content of deep-sea sediments are combined with a new rate model to derive the global distribution of benthic calcite dissolution rates and obtain primary confirmation of an anthropogenic component. By comparing pre-industrial with present-day rates, we determine that significant anthropogenic dissolution now occurs in the western North Atlantic, amounting to 40-100% of the total seafloor dissolution at its most intense locations. At these locations, the calcite compensation depth has risen ~300 m. Increased benthic dissolution was also revealed at various hot spots in the southern extent of the Atlantic, Indian and Pacific Oceans. Our findings place constraints on future predictions of ocean acidification, are consequential to the fate of benthic calcifiers, and indicate that a by-product of human activities is currently altering the geological record of the deep sea.

Chapter 5

Current $CaCO_3$ dissolution at the seafloor caused by anthropogenic CO_2*

Olivier Sulpis[1], Bernard P. Boudreau[2], Alfonso Mucci[1], Chris Jenkins[3], David S. Trossman[4], Brian K. Arbic[5] and Robert M. Key[6]

[1]GEOTOP and Department of Earth and Planetary Sciences, McGill University, Montreal QC, Canada

[2]Department of Oceanography, Dalhousie University, Halifax NS, Canada

[3]INSTAAR, University of Colorado at Boulder, Boulder CO, USA

[4]Institute of Computational Engineering and Sciences, University of Texas-Austin, Austin TX, USA

[5]Department of Earth and Environmental Sciences, University of Michigan, Ann Arbor MI, USA

[6]Atmospheric and Oceanic Sciences, Princeton University, Princeton NJ, USA

**Published in Proceedings of the National Academy of Sciences of the USA,*
doi:10.1073/pnas.1804250115

Abstract

Oceanic uptake of anthropogenic CO_2 leads to decreased pH, carbonate ion concentration, and saturation state with respect to $CaCO_3$ minerals, causing increased dissolution of these minerals at the deep seafloor. This additional dissolution will figure prominently in the neutralization of man-made CO_2. However, there has been no concerted assessment of the current extent of anthropogenic $CaCO_3$ dissolution at the deep seafloor. Here, recent databases of bottom-water chemistry, benthic currents, and $CaCO_3$ content of deep-sea sediments are combined with a rate model to derive the global distribution of benthic calcite dissolution rates and obtain primary confirmation of an anthropogenic component. By comparing preindustrial with present-day rates, we determine that significant anthropogenic dissolution now occurs in the western North Atlantic, amounting to 40–100% of the total seafloor dissolution at its most intense locations. At these locations, the calcite compensation depth has risen ~300 m. Increased benthic dissolution was also revealed at various hot spots in the southern extent of the Atlantic, Indian, and Pacific Oceans. Our findings place constraints on future predictions of ocean acidification, are consequential to the fate

of benthic calcifiers, and indicate that a by-product of human activities is currently altering the geological record of the deep sea.

5.1 Introduction

Seafloor dissolution of $CaCO_3$ minerals will constitute a primary feedback to ocean acidification over time scales of centuries to tens of millennia (Montenegro et al., 2007). The overall dissolution reaction is

$$\mathbf{CaCO_3 + CO_2 + H_2O \rightarrow Ca^{2+} + 2\,HCO_3^-} \qquad \mathbf{(5.1)}$$

where $CaCO_3$ denotes solid carbonate in bottom sediments, mainly as calcite. This process is termed (geo)chemical carbonate compensation. Consequently, CO_2 entering the ocean, including that of anthropogenic origin, can be neutralized permanently by conversion to dissolved bicarbonate ion (HCO_3^-).

The upper oceans are wholly supersaturated with respect to calcite, despite the current acidification. Largely because of the increasing solubility of calcite with pressure, the deeper oceans become undersaturated, and the rate of ***reaction 1*** increases with oceanographic depth. The depth where undersaturation first occurs is the calcite saturation depth (CSD) (Boudreau et al., 2010b). The pre-industrial oceans contained CO_2 acquired from the atmosphere, from marine volcanism, and from oxic organic matter decay. At the same time, calcifying organisms precipitated $CaCO_3$ shells that settled to the seafloor upon their death. Combined, these processes and ***reaction 1*** lead to decreasing $CaCO_3$ content in sediments below the CSD. The depth where the deposition rate of $CaCO_3$ is exactly balanced by ***reaction 1*** is called the calcite compensation depth (CCD) (Boudreau et al., 2010b), although operationally it is commonly defined as the depth where the sediment $CaCO_3$ content falls below 10%. The snowline (Boudreau et al., 2010b) denotes the depth below which no $CaCO_3$ is found in the sediment; the snowline and CCD coincide at steady state (Boudreau et al., 2010b).

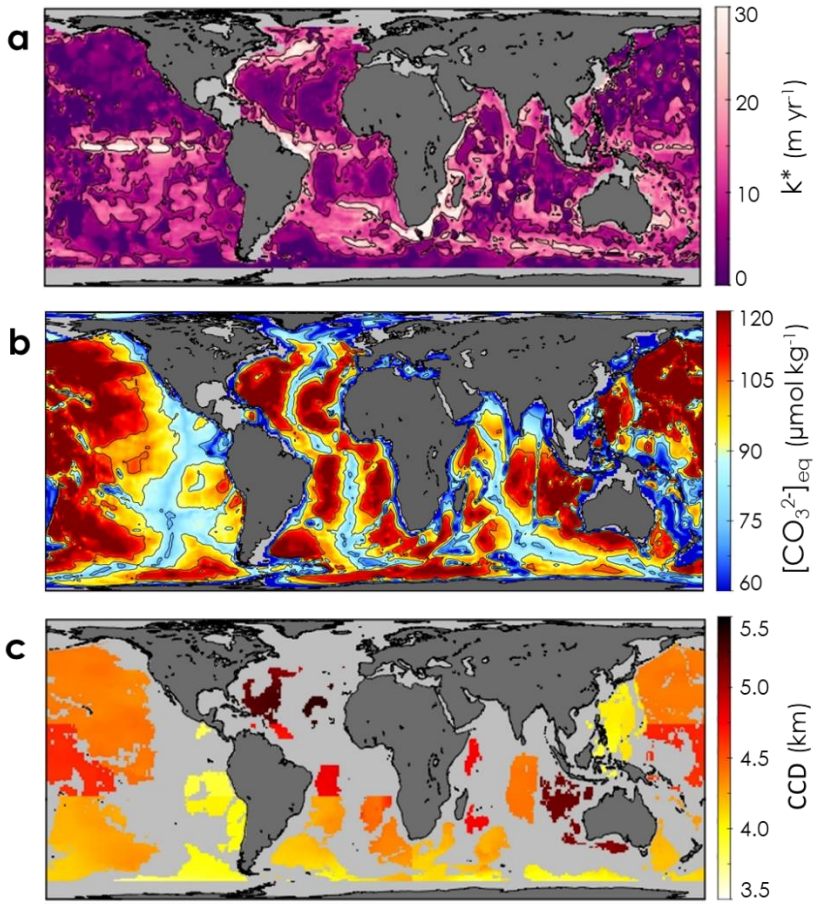

Fig. 5.1 | *Chemical and physical parameters for calcite dissolution. (**a**) Overall mass-transfer coefficient k* for $CaCO_3$ dissolution, (**b**) current bottom-water saturation concentration $[CO_3^{2-}]_{eq}$ at in situ temperature, salinity and pressure and (**c**) present-day calcite compensation depth (CCD), regionally averaged as described in the methods section, where the light grey identifies areas where the CCD is deeper than the depth of the seafloor, i.e., where calcite can undergo net sediment accumulation. The CCD is not computed in the Arctic and Southern Oceans (south of 60°S).*

The geological record contains numerous examples of deep-sea $CaCO_3$ dissolution events driven by natural acidification, e.g., at ~56 Myr BP, known as the Paleocene-Eocene Thermal Maximum (Zachos et al., 2005; Zeebe et al., 2009; Cuy et al., 2011). During these events, $CaCO_3$ disappeared from deep-sea sediments, where it had previously accumulated, burial rates dropped, and the snowline shoaled. The same scenario has been predicted for the Anthropocene oceans (Archer, 2005; Boudreau et al., 2010a), but no estimates of increased deep-sea sediment $CaCO_3$ dissolution has been published. This lack of documentation might be attributed to the restricted penetration of anthropogenic CO_2 to shallow depths, but this premise is contradicted by observed

changes in the carbonate chemistry of the deeper oceans (Feely et al., 2004; Ríos et al., 2015; Perez et al., 2018) and as reported here. Both numerical ocean models and the presence in abyssal waters of transient tracers produced almost entirely after the end of the 1940s, i.e., CFCs and PCBs, strongly imply the presence of anthropogenic CO_2 in the deep oceans. Anthropogenic CO_2 in deep and bottom waters is simply very difficult to measure because it is a small signal superimposed on a large natural background concentration. Early changes in $CaCO_3$ content of sediments caused by anthropogenic acidification are also extremely difficult to detect through changes in either solid mass or dissolution indices.

Given that sediment monitoring is unlikely to yield immediate evidence of anthropogenic calcite dissolution at the seafloor, we employ a different approach and compare the rate of dissolution at the seafloor under pre-industrial (ca. 1800 AD) and modern (2002 AD) benthic conditions. In accord with recent work (Boudreau, 2013; Sulpis et al., 2017) on the dissolution kinetics of calcite beds, the dissolution rate (r) at any depth between the CSD and the CCD is given by (Boudreau, 2013):

$$r = k^* ([CO_3^{2-}]_{eq} - [CO_3^{2-}]_{SW}) \quad (5.2)$$

where $[CO_3^{2-}]_{eq}$ is the calcite-equilibrium carbonate-ion concentration (***Fig. 5.1b***), $[CO_3^{2-}]_{SW}$ is the carbonate-ion concentration in bottom waters, and k^* is the overall CO_3^{2-} mass-transfer coefficient (Boudreau, 2013),

$$k^* = k_s \beta (k_s + \beta)^{-1} \quad (5.3)$$

where k_s is the sediment-side mass-transfer coefficient, which characterizes dissolution and transport (diffusion) of the carbonate ion within the sediment, and β is the water-side mass-transfer coefficient (Boudreau and Jørgensen, 2001). In this formulation, k^* tends towards the value of the smallest rate-limiting mass transfer coefficient, β or k_S, without ever reaching it, as predicted by theory and validated by observations.

With any Anthropocene (Waters et al., 2016) rise in the CCD, r is supplemented by dissolution of previously deposited $CaCO_3$ between the new and old CCD positions (see M*aterials and Methods*). Hence, the difference between the calculated r over the deep seafloor for pre-industrial and current conditions reflects the impacts of anthropogenic acidification. To perform this calculation globally, we require the spatial distributions of k^*, $[CO_3^{2-}]_{eq}$, $[CO_3^{2-}]_{SW}$, and the

$CaCO_3$ contents of surface sediments, whose distribution is available from a new database (Jenkins, 1997; Goff et al., 2008) and displayed in ***Fig. 5.6a***.

The distribution of k^* at the seafloor is shown in ***Fig. 5.1a***. The water-side mass-transfer coefficient, β, appears in ***Eq. 5.3*** because the seafloor is covered by a water layer through which solute transport occurs via molecular diffusion (Boudreau and Jørgensen, 2001), termed the diffusive boundary layer (DBL). The existence of the DBL has been amply illustrated by previous research (Archer, 1989b; Gundersen and Jørgensen, 1990, Santschi, 1991). β is calculated as the ratio of the diffusion coefficient of CO_3^{2-} ($D_{CO_3^{2-}}$), at *in situ* temperature (T) and salinity (S_P), to the thickness of the DBL (Z_{DBL}), as β is effectively independent of pressure (see *Materials and Methods*). Whereas $D_{CO_3^{2-}}$ does not vary widely, Z_{DBL} depends on the flow velocities at the seafloor (Boudreau and Jørgensen, 2001), but an ocean-wide distribution of Z_{DBL} has never been reported in the literature. Herein, we use a global bottom-current-velocity (U) model to derive *in situ* β values (see *Materials and Methods*). ***Fig. 5.7c*** provides an ocean-wide distribution of β and shows that this parameter is high on the east side of continents, beneath the Equator, and on the northern fringe of the Southern Ocean, all areas with enhanced bottom currents. Conversely, β is very small over much of the abyssal ocean due to relatively sluggish flow. The magnitude of k_s is derived from available experiments and calculated as a function of the $CaCO_3$ content in surface sediments (see *Materials and Methods*). The distribution of k_s at the seafloor is shown in ***Fig. 5.6b***. Overall, the rate of deep-sea $CaCO_3$ dissolution, k^*, is largely controlled by β, rather than k_s (Boudreau, 2013; Sulpis et al., 2017), except in regions of high bottom currents or where sediments are $CaCO_3$-poor, such as the North Pacific or the Southern Ocean (see ***Fig 5.9***).

The benthic distribution of $[CO_3^{2-}]_{eq}$ in ***Eq. 5.2*** is calculated by dividing the stoichiometric solubility constant of calcite, K^*_{sp} at *in situ* conditions, by the Ca^{2+} concentration of the oceans. ***Figure 5.1b*** illustrates the resulting map of $[CO_3^{2-}]_{eq}$. $[CO_3^{2-}]_{eq}$ is commonly near 75 µmol kg^{-1} on top of oceanic ridges (~2500m), but increases to values as high as ~140 µmol kg^{-1} on the abyssal plains (~6000m).

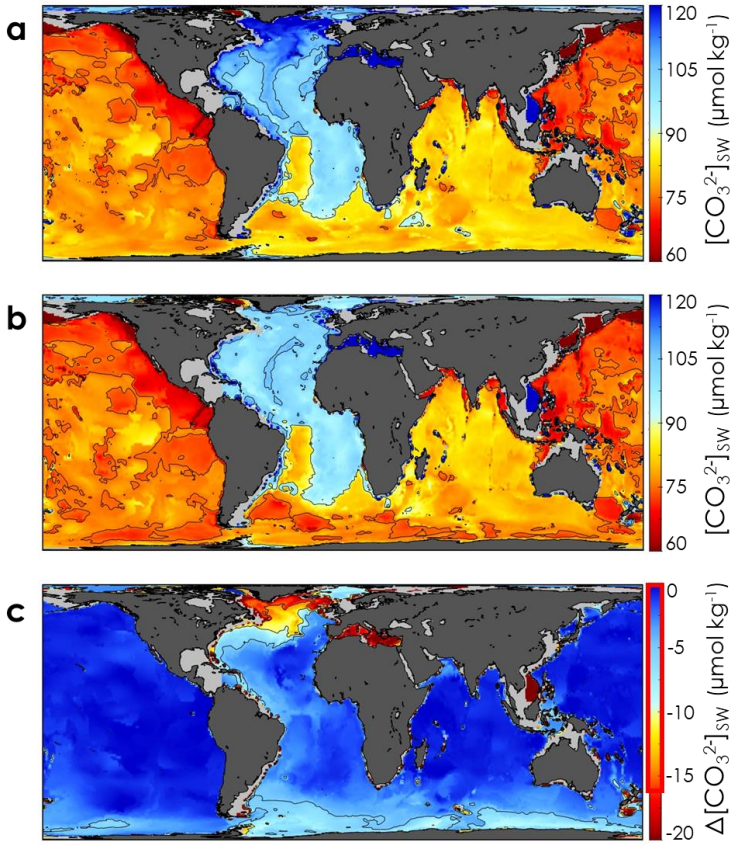

Fig. 5.2 | *Ocean acidification and bottom-water $[CO_3^{2-}]_{SW}$ decrease. (**a**) Pre-industrial bottom-water $[CO_3^{2-}]_{SW}$, (**b**) current bottom-water $[CO_3^{2-}]_{SW}$, and (**c**) difference between pre-industrial and current bottom-water $[CO_3^{2-}]_{SW}$ ($\Delta[CO_3^{2-}]_{SW}$ = current bottom-water $[CO_3^{2-}]_{SW}$ – pre-industrial bottom-water $[CO_3^{2-}]_{SW}$), below 300 m. Uncertainties are indicated by the red outline on the color bar, corresponding to one standard deviation of 16.9 µmol kg^{-1} for $\Delta[CO_3^{2-}]_{SW}$.*

Next, we need to estimate the position of the pre-industrial CCD to calculate the amount of dissolution below this depth. As stated earlier, the CCD and snowline are coincident at oceanic steady state. In addition, there is no evidence that the calcite snowline has, as yet, migrated measurably due to anthropogenic dissolution (Boudreau et al., 2010a; Boudreau et al., 2015). Therefore, we set the pre-industrial CCD to the current snowline depth that we estimate from the $CaCO_3$ contents of sediments for each basin (see *Materials and Methods*). With these local pre-industrial CCD values, the flux (F) of $CaCO_3$ at that depth, and corresponding grid point, can be estimated (Boudreau et al., 2010b) and the dissolution rate below the CCD, set to the value of F, mapped.

We note that calcifying organisms exhibit various responses to elevated pCO_2 conditions, due to the influence of other climate-change related effects, such as the warming of waters that counteracts acidification (Fukuda et al., 2014; Maugendre et al., 2017; Pinsonneault et al., 2012; Wootton et al., 2008). In the absence of unequivocal evidence of an immediate increase or decrease in the total calcification rate in the pelagic oceans, we assume that the flux of calcitic particles reaching the CCD (F) has remained invariant since the pre-industrial era. This is supported by what took place in similar acidification events in the geological record, such as the Paleocene-Eocene Thermal Maximum, where no obvious plankton carbonate productivity reduction is readily detectable (Gibbs et al., 2010). Thus, the "current" CCD was computed from the fixed (known) F and the present-day $[CO_3^{2-}]_{SW}$, and is represented in ***Fig. 5.1c***.

Finally, the pre-industrial distribution of bottom-water $[CO_3^{2-}]_{SW}$ (***Fig. 5.2a***) is computed using estimated pre-industrial, deep-ocean dissolved inorganic carbon (DIC) concentrations (Lauvset et al., 2016) and the present-day total alkalinity (TA), that is assumed to have remained invariant over the Anthropocene (see *Materials and Methods*). The current bottom-water $[CO_3^{2-}]_{SW}$ is estimated from the DIC, normalized to the calendar year 2002 (Lauvset et al., 2016) – see ***Fig. 5.2b***. The anthropogenic decrease of bottom-water $[CO_3^{2-}]_{SW}$ is currently limited mostly to the northern Atlantic Ocean and the Southern Ocean, where surface waters enter the deep-ocean reservoir (Khatiwala et al., 2009). Accordingly, North Atlantic $[CO_3^{2-}]_{SW}$ has decreased from ~110 µmol kg^{-1} to ~95 µmol kg^{-1}, whereas the North Pacific $[CO_3^{2-}]_{SW}$ has remained approximately constant at ~70 µmol kg^{-1}. The difference between the pre-industrial and current bottom-water $[CO_3^{2-}]_{SW}$ is illustrated in ***Fig. 5.2c***, which highlights areas of deep acidification in the northwestern North Atlantic and Southern Ocean.

5.2 Results

With the above information, we calculated the distribution of both pre-industrial (***Fig. 5.3a***) and current (***Fig. 5.3b***) calcite dissolution rates at the seafloor. In both figures, areas with low k* values (***Fig. 5.1a***), such as the abyssal plains on each side of the North Atlantic mid-ocean ridge or in the North Pacific are typified by low calcite dissolution rates, whereas sediments subject to faster currents (larger β values) or rich in $CaCO_3$ (larger k_S values) exhibit greater rates. The difference between current and pre-industrial calcite dissolution rates, as plotted in ***Fig. 5.3c***,

corresponds to the rate of anthropogenic calcite dissolution at the seafloor. The anthropogenic dissolution is most pronounced and widespread in the northwestern Atlantic Ocean. There are also areas of significant dissolution in the southern Atlantic and Indian Oceans, resulting from the presence of tangible anthropogenic CO_2 in these deep waters (Ríos et al., 2015; Lauvset et al., 2016), and a consequent rise in the CSD. These prominent dissolution areas reflect the loci of anthropogenic CO_2 introduction into the deep oceans (North Atlantic and the Antarctic margins) and/or the presence of faster bottom currents (larger β values). In the "hot" area of the northwest Atlantic, the anthropogenic component now accounts for 40-100% of the total dissolution rate.

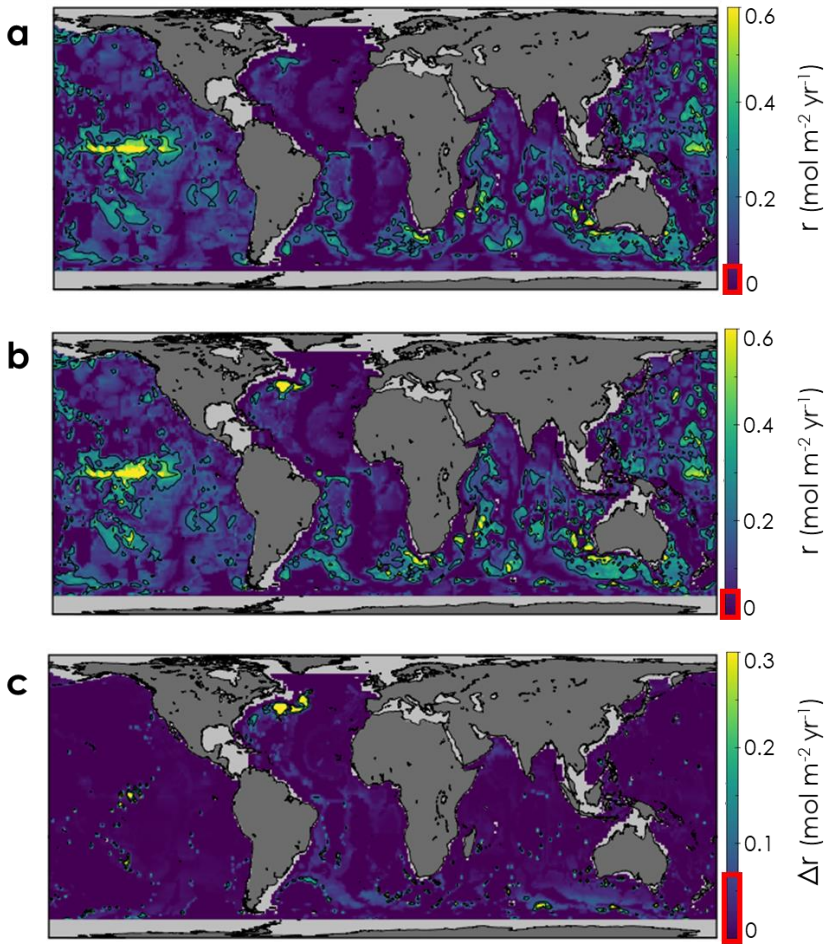

Fig. 5.3 | *Geographic calcite dissolution rate distribution and anthropogenic impact. (**a**) Pre-industrial and (**b**) current calcite dissolution rate (r) at the sediment-water interface, and (**c**) the difference between pre-industrial and current calcite dissolution rate below 300 m (Δr = current r – pre-industrial r), i.e., the anthropogenic CO_2-driven calcite dissolution rate. Hence, this excludes possible calcite dissolution on the continental shelves, particularly in the North Pacific where the CCD shoals to less than 300 m. Uncertainties are indicated by the red outline on the color bars, corresponding to the standard deviation, equal to 0.05 mol m yr^{-1} for r and to 0.07 mol m yr^{-1} for Δr.*

The seafloor area between the current and the pre-industrial CCD contains the calcitic sediments subjected to the greatest increase in their dissolution rate. In this fringe of high-end anthropogenic dissolution, the $CaCO_3$ budget at the sediment-water interface switches from gain (net accumulation) to deficit (net depletion) when the rising CCD becomes shallower than the seafloor, causing the dissolution of falling calcitic particles before their burial in the sediment. ***Figure 5.3c*** also suggests the existence of numerous small "hot spots" of dissolution in the Indian and Pacific Oceans, corresponding to topographic highs or islands, e.g., Guam and Pitcairn Islands, where the CCD has risen above the seafloor.

Because of anthropogenic CO_2 uptake by the oceans, both the saturation (CSD) and compensation (CCD) depths should shoal, leading to dissolution of previously deposited carbonate minerals (Archer et al., 1998), also known as chemical burndown. ***Figure 5.4*** presents our estimates of the upward displacements of the CSD and CCD to date for the Atlantic, plotted with the regionally-averaged surface-sediment calcite content water-depth profiles (see ***Table 5.1*** for other basins). These results constitute strong signs of anthropogenic dissolution just below the current (risen) CSD, illustrating dissolution of previously deposited calcite, in particular in the North Atlantic where shoaling of the CSD and CCD is greatest.

5.3 Discussion

On average, we find that *F*, the flux of $CaCO_3$ that must reach the CCD in order to explain the observed $CaCO_3$ contents in surficial sediments (see Materials and Methods) is 0.17 ± 0.07 mol m^{-2} yr^{-1}. This value is equivalent to $CaCO_3$ fluxes to the deep-ocean derived from previous studies based on excess total alkalinity (TA^*) budgets (Berelson et al., 2007; Battaglia et al., 2016). Integrating over the surface of the seafloor, we find a global calcite downward flux at the CCD of 54 ± 17 $x10^{12}$ mol yr^{-1} (i.e., 0.7 ± 0.2 Gt C yr^{-1}), and a current global seafloor $CaCO_3$ dissolution flux of 32 ± 12 $x10^{12}$ moles yr^{-1} of $CaCO_3$ (i.e., 0.4 ± 0.1 Gt C yr^{-1}). Both of these values are similar to and more precise than the observation-based estimates presented in Berelson et al. (2007). Our global dissolution estimate represents only 22 ± 8 % of the total estimated $CaCO_3$ dissolution in the marine environment each year, i.e., 144 $x10^{12}$ mol yr^{-1}, or 1.7 Gt C yr^{-1} (Smith and Mackenzie, 2016). The remainder of the dissolution occurs primarily in the water column

and, possibly, after burial through metabolic dissolution or later diagenesis at shallow to mid depths.

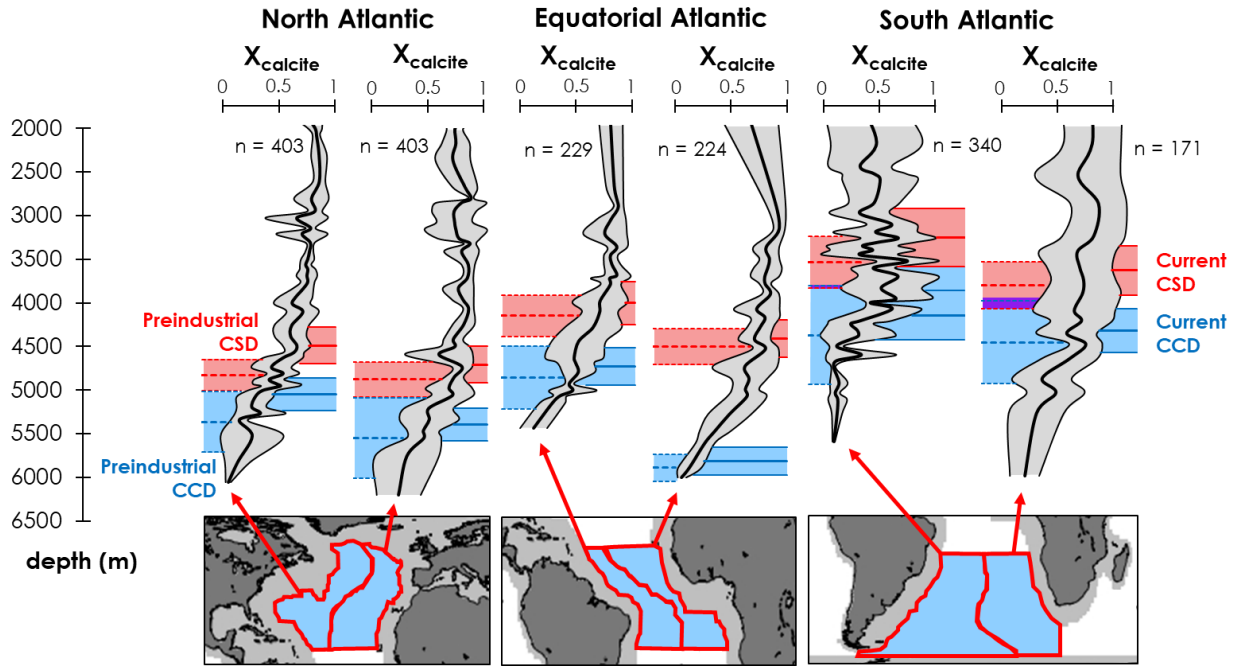

Fig. 5.4 | *Atlantic Ocean sediment calcite content profiles and calcite marker horizons. Calcite fraction in dry sediments ($X_{calcite}$), plus or minus one standard deviation, for the basins defined by the maps below the plots. The number of measurements (n) comprised within each basin is also reported. The pre-industrial Calcite Compensation Depth (CCD) and Saturation Depth (CSD) are represented with dashed horizontal lines (on the left of each profile), whereas solid horizontal lines correspond to current values (on the right of each profile). Both the CCD and CSD are reported along with their uncertainties.*

As stated and justified earlier, we assumed that the calcite rain rate has remained invariant since pre-industrial times. Although a decrease in the precipitation rate of calcite might be expected under more acidic conditions (Doney et al., 2009), thus reducing the calcite export from the surface ocean and the rain rate to deep-sea sediments, no such trend is clearly observed today (Riebesell et al., 2009). Testing the sensitivity of the computed sediment dissolution rates (r) to a reduction in the calcite downward flux (F), we find that when F is decreased by 10%, the global dissolution rate increases by 2.5%. Likewise, when F is decreased by 20%, the global dissolution rate increases by 3.1%. Thus, counterintuitively, if less calcite is currently delivered to the seafloor than during the pre-industrial era, more calcite is being dissolved at the sediment-water interface because a weaker F causes the CCD to fluctuate faster in response to changes in $[CO_3^{2-}]_{SW}$, as

explained in Boudreau et al. (2010b), and in the case of the present acidification, to rise faster. Sediments that were above the pre-industrial CCD and are now below the current CCD are subject to the greatest dissolution rate increase, as can be seen when comparing ***Eqs. 5.12-5.14*** in the Materials and Methods section. In other words, if *F* has remained constant, ~ 2% of the seafloor is currently comprised between the pre-industrial and current CCD, but this fraction increases to 9.3% when *F* is reduced by 20% relative to its pre-industrial value.

Our results provide the first tangible indication that significant anthropogenic calcite dissolution is currently occurring at the seafloor. This dissolution will eventually change the $CaCO_3$ accumulation patterns and rates in the oceans, while mitigating runaway ocean acidification. Any future model of oceanic acidification needs to reproduce our observations to assure its validity. The consequences of this anthropogenic dissolution to the ecology of benthic calcifiers has not been determined with certainty, but could be as substantial as it is for pelagic calcifiers (Smith et al., 2012). Chemical burndown of previously deposited carbonate-rich sediments has already begun and will intensify and spread over vast areas of the seafloor during the next decades and centuries, thus altering the geological record of the deep sea. The deep-sea benthic environment, which covers ~60% of our planet, has indeed entered the Anthropocene.

5.4 Materials and methods

5.4.1 Bottom-water chemistry

$[CO_3^{2-}]_{SW}$ were computed using the Matlab version of the CO2SYS program (Lewis and Wallace, 1998; van Heuven et al., 2011), based on GLODAPv2.2016b 1°x1° global mapped climatologies (Lauvset et al., 2016; Key et al., 2015) at the deepest resolved layers of the GLODAPv2.2016b model (***Fig. 5.5***), assumed to be near the seafloor. The GLODAPv2.2016b variables used for our computation are represented in ***Fig. 5.5*** and include *in situ* bottom-water *TA*, *DIC*, *T*, S_P, as well as soluble reactive phosphate ([*SRP*]) and dissolved inorganic silica ([*DSi*]) concentrations. Current $[CO_3^{2-}]_{SW}$ were derived using GLODAPv2.2016b bottom-water *DIC* data normalized to the year 2002 (***Fig. 5.5g***), whereas pre-industrial $[CO_3^{2-}]_{SW}$ were computed using the GLODAPv2.2016b bottom-water pre-industrial *DIC* data (Lauvset et al., 2016) (***Fig. 5.5h***). For computational purposes, we assume that bottom-water *TA* has not changed since the end of the pre-industrial period (ca. 1800 AD), in accordance with recent studies that predict an

insignificant global mean deep-water *TA* anomaly (ΔTA ~ 2.5 µmol kg^{-1} relative to the mean concentration from 1950 to 1959) before ca. 2060 AD, although some changes might already be detectable (during the 2010-2020 decade) in the deep North Atlantic (Carter et al., 2014). We computed the *TA* flux generated by anthropogenic dissolution of $CaCO_3$ sediments since the pre-industrial times. Assuming that this *TA* mixes in the water column up to the permanent thermocline, we found that it has resulted in a world-averaged *TA* increase of less than 0.1 µmol kg^{-1}, and of ~3 µmol kg^{-1} above the hotspot of anthropogenic dissolution in the North-West Atlantic; both values are at or below the current analytical uncertainty. $[CO_3^{2-}]_{eq}$ was estimated from the equations presented in Boudreau et al., (2010b) using $[Ca^{2+}]$ computed from S_p following Riley and Tongudai (1967), the stoichiometric solubility product of calcite (K_{sp}^*) (Mucci, 1983) at *in situ T* and S_p and the pressure (*P*) derived from GEBCO bathymetry (Weatherall, 2015).

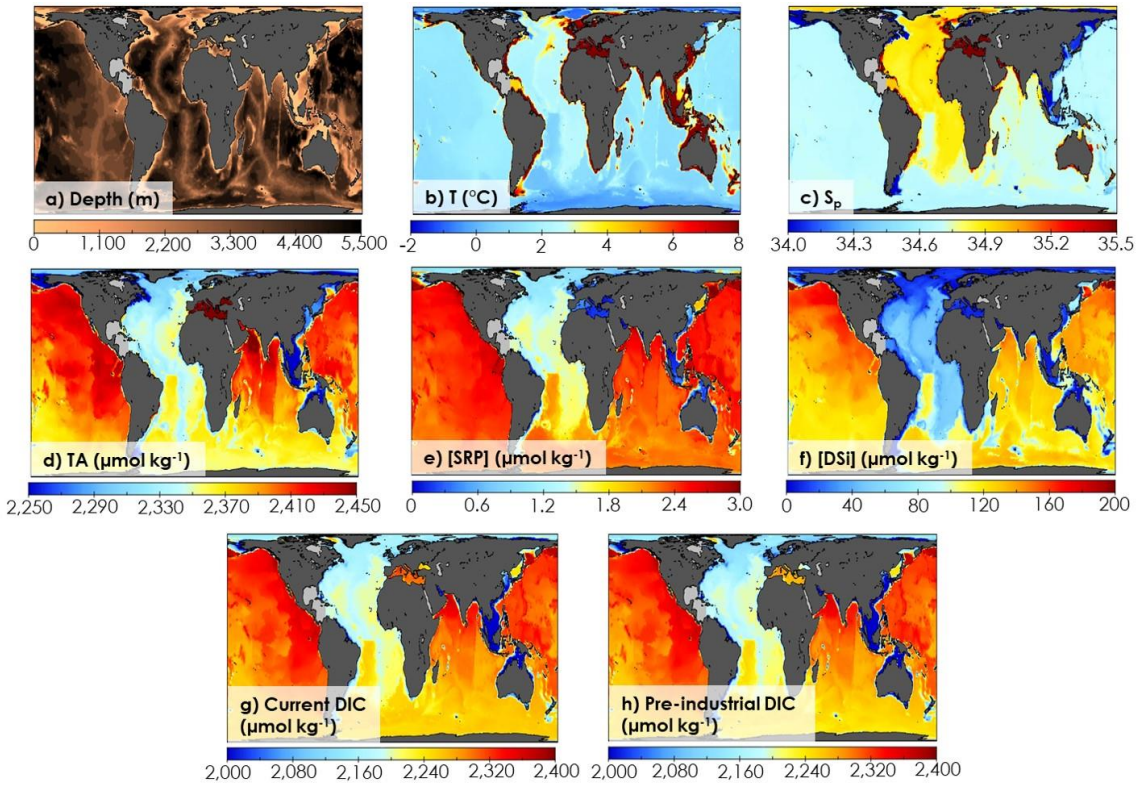

Fig. 5.5 | *Bottom-water distribution of the GLODAPv2.2016b variables used in the computation of $[CO_3^{2-}]_{SW}$. (**a**) depth of the deepest resolved layer of GLODAPv2.2016b considered to be bottom waters, (**b**) temperature (T), (**c**) practical salinity (S_p) , (**d**) total alkalinity (TA), (**e**) soluble reactive phosphate (SRP) concentration, (**f**) dissolved inorganic silica (DSi) concentration, (**g**) current and (**h**) pre-industrial dissolved inorganic carbon (DIC) concentrations.*

5.4.2 $CaCO_3$ distribution in deep-sea sediments

The data (***Fig. 5.6a***) on carbonate mineral sediment contents are comprised of 1.7 million sites throughout the world's ocean, extracted from the comprehensive database of seabed sediment properties, dbSEABED (Jenkins, 1997). The original data are quality controlled and harmonized (Goff et al., 2008) so that analytical results and descriptions can be combined into a statistically homogeneous set of values. The sites are located geographically and by water depth. The surficial 0-10cm (occasionally 0-30cm) average values were used to compile the maps, a depth that takes account of scales of seafloor-seawater contact, including the effects of erosion and bioturbation.

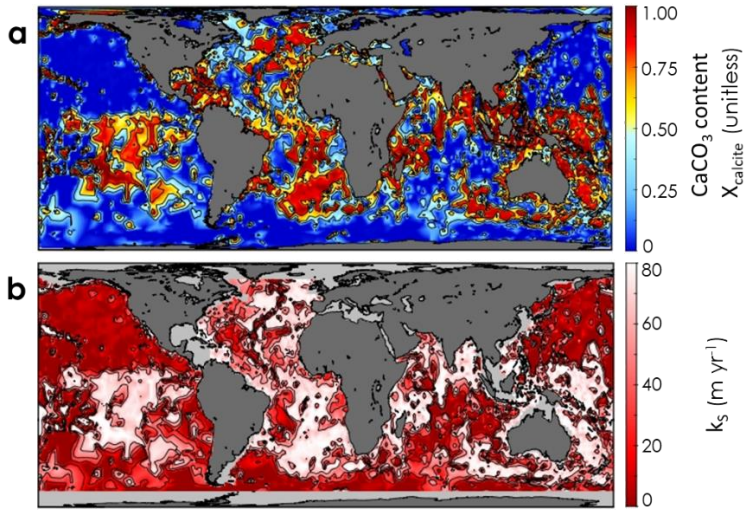

Fig. 5.6 | ***(a)*** *Global-scale $CaCO_3$ content of surficial sediments and* ***(b)*** *sediment-side CO_3^{2-} mass-transfer coefficient computed using* ***Eq. 5.10****.*

5.4.3 Water-side CO_3^{2-} mass transfer coefficient (β)

The diffusive boundary layer (DBL) thickness (Z_{DBL}) at the air-sea interface is commonly derived from wind-speed (Takahashi et al., 2002). In analogy, we describe a set of equations to estimate the benthic Z_{DBL} and the CO_3^{2-} water-side mass transfer coefficient (β) at *in situ T* and S_P, using the horizontal current speed (U) near the seafloor. In this study, we consider β to be independent of pressure, as the pressure effect on the viscosity of seawater and on the diffusion coefficients of ions in seawater is thought to be relatively small, i.e., at most 8% (Li and Gregory, 1974). We use an interpolated version of horizontal bottom-water current speeds at 1° x 1° resolution from a higher resolution model (***Fig. 5.7a***). The bottom currents were inferred from an inline computation of the annually averaged kinetic energy field of a nominally 1/25th degree

global configuration of the HYbrid Coordinate Ocean Model (HYCOM). It accounts for topographic internal lee wave drag, forced by air-sea fluxes and winds from reanalysis, but does not include tides (Trossman et al., 2016). Neglecting tides is a source of uncertainty in this study, and this should be examined in future research. Nevertheless, abyssal tidal velocities (typically about 1 cm s^{-1}) (Timko et al., 2013) are very likely to be smaller than non-tidal velocities over most areas studied in this paper (***Fig. 5.7a***). For a discussion of the sensitivity of our dissolution rate model to various initial kinetic energy distribution models, we refer the reader to the supplementary information. Herein, for the sake of brevity, we refer to the current "speed" (a scalar) as current "velocity" (a vector), although our model does not use or require any information about the direction of the current. We assume: (a) that these current velocities, averaged over the bottom 500 meters, are representative of the current velocities just above the bottom boundary layer, i.e., portions of sediment and water column affected directly in the distribution of their properties and processes by the presence of the sediment-water interface (SWI) (Boudreau and Jørgensen, 2001), comprising, among others, the DBL, (b) that the seafloor is hydrodynamically smooth, and (c) that there is no vertical density gradient, i.e., the bottom boundary layer is unstratified.

Using the universal logarithmic velocity distribution, we then have:

$$\frac{u(z)}{u^*} = \frac{1}{\kappa} ln\left(\frac{zu^*}{\nu}\right) + C \qquad \textbf{(5.4)}$$

where z is the height above the bottom, κ is the dimensionless von Karman constant (0.40) from Monin and Yaglom (1971), ν is the molecular kinematic viscosity of seawater at S_P = 35 and *in situ T*, and C is an empirical dimensionless constant with a value of 5.1, taken from Monin and Yaglom (1971).

The current velocity U at the upper edge of the bottom boundary layer is assumed to be equal to the current velocity averaged over the bottom 500 meters and is then given by

$$U = \frac{u^*}{\kappa} ln\left(\frac{\delta u^*}{\nu}\right) + Cu^* \qquad \textbf{(5.5)}$$

where δ is the bottom boundary layer thickness.

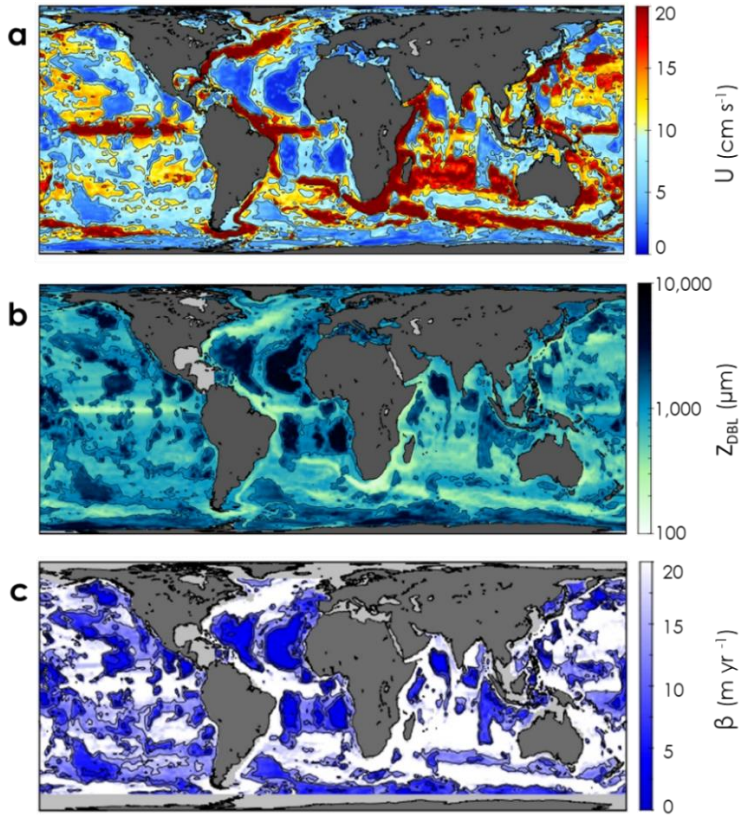

Fig. 5.7 | *Diffusive boundary layer thickness as a function of the bottom-current velocity. (**a**) Current speed resolved by the 1/25th degree HYCOM simulation, averaged over the final year of its run and over the bottom 500 meters, (**b**) diffusive boundary layer thicknesses at the sediment-water interface and (**c**) water-side CO_3^{2-} mass-transfer coefficient.*

We further assume that δ corresponds to the so-called Ekman scale height (Boudreau and Jørgensen, 2001), reflecting classical Ekman dynamics, in which the height of the bottom boundary layer is limited by the Earth's rotation:

$$\boldsymbol{\delta = \frac{\kappa u^*}{f}} \qquad \textbf{(5.6)}$$

where f is the Coriolis parameter (set to 1×10^{-4} s^{-1}). We consider a constant S_P of 35, due to the small variations of this variable in oceanic bottom waters, as shown in ***Fig. 5.5c***.

Combining ***equations 5*** and ***6***, we obtain:

$$\boldsymbol{U = \frac{u^*}{\kappa} ln\left(\frac{\kappa u^{*2}}{f\nu}\right) + Cu^*} \qquad \textbf{(5.7)}$$

Fitting a power function that relates u^* to U, for T = 2 °C, with $R^2 > 0.999$, we have that:

$$\boldsymbol{u^* = 0.023U^{0.84}} \qquad \textbf{(5.8)}$$

This equation gives u^* values that are notably similar to previously published empirical relationships (Armi, 1997; Csanady, 1967), e.g., $u^* = U / 30$, as shown in ***Fig. 5.8a***.

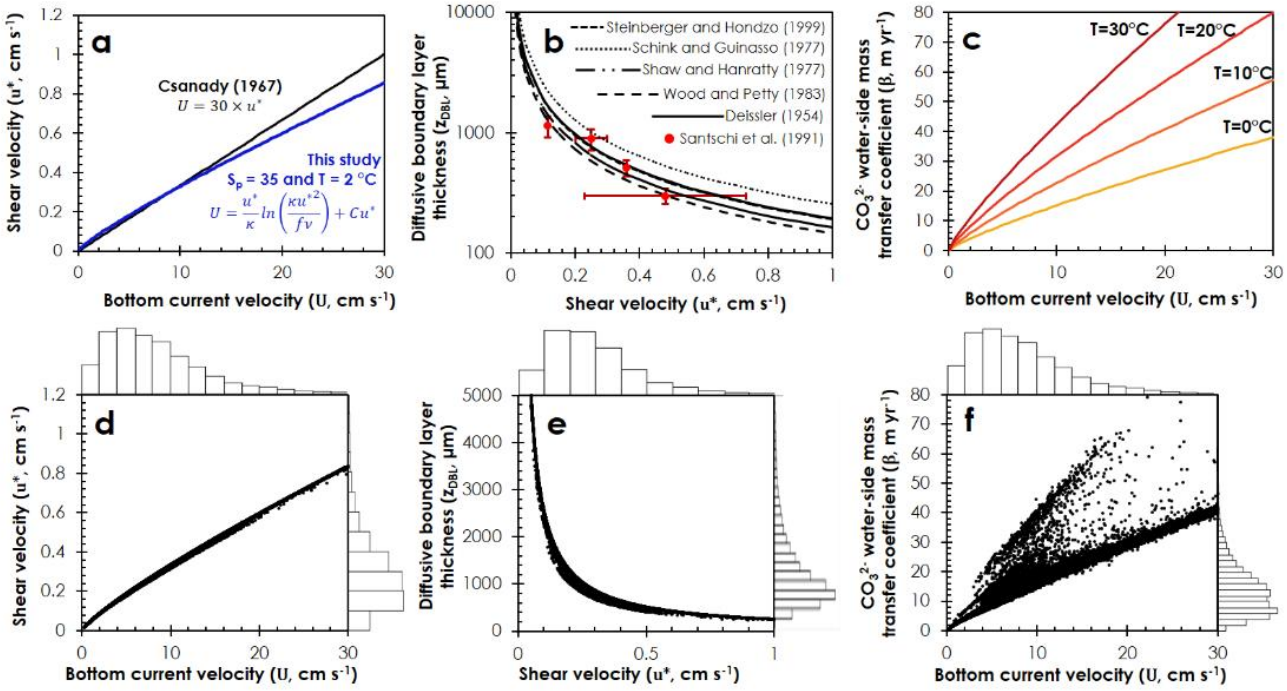

Fig. 5.8 | *Impact of temperature and current velocity on the water-side CO_3^{2-} mass-transfer coefficient and the DBL thickness. (**a**) Shear velocity (u*) as a function of the current velocity (U) at the outer edge of the bottom boundary layer, according to the equation derived in this study (in blue) and to the empirical equation from Csanady (1967). (**b**) DBL thickness (z_{DBL}) as a function of the shear velocity(u*) for 5 different empirical models (Schink and Guinasso, 1977; Steinberger, 1999; Deissler, 1954; Shaw and Hanratty, 1977; Wood and Petty, 1983) and comparison with observation-based DBL thicknesses from Santschi et al. (1991). (**c**) Water-side CO_3^{2-} mass-transfer coefficient (β) as a function of the current velocity (U) at various temperatures. (**d-f**) Plots representing the entirety of the data on the seafloor, where each black point represents one 1°x1° value. Each plot is associated with a histogram on each of its axes showing the relative distribution of the data over the range observed at the seafloor.*

The mass transfer coefficient, β, can be found for the carbonate ion (CO_3^{2-}) following Schink and Guinasso (1977) and u^* from ***Eq. 5.8***:

$$\boldsymbol{\beta = 0.0417 u^{*} Sc^{-2/3}} \qquad \textbf{(5.9)}$$

where *Sc* is the Schmidt coefficient for CO_3^{2-}, i.e., $Sc = \nu / D_{CO_3^{2-}}$ at S_p = 35 and *in situ T*, $D_{CO_3^{2-}}$ is the CO_3^{2-} diffusion coefficient from Zeebe (2011). The geographical distribution of β is provided in ***Fig. 5.7c***. It should be noted that β is dependent on the temperature (***Fig. 5.8c***) and, in contrast to the deep sea where the temperature is relatively constant (***Fig. 5.5b***), significant variations can be encountered in warmer environments such as on carbonate platforms. Although studies such as Purkey and Johnson (2013) have shown that there might have been a measurable change in bottom-water temperatures over the hydrographic period (late 1970's to today), accounting for it would have a very small impact on our results, given that these changes are currently limited to a few tenths of °C (Purkey and Johnson, 2013).

Finally, we provide a 1° x 1° global model of the DBL thicknesses (Z_{DBL}) at the SWI, obtained by dividing $D_{CO_3^{2-}}$ (at S_P = 35 and *in situ T*) by β, in ***Fig. 5.7b***. This model can be used to estimate solute exchange at the SWI and is available upon request.

Note that other empirical laws estimating β as function of *Sc* and *u**, similarly to ***Eq. 5.9***, can be found in the literature (Schink and Guinasso, 1977; Steinberger, 1999; Deissler, 1954; Shaw and Hanratty, 1977; Wood and Petty, 1983). In ***Fig. 5.8b***, we provide a comparison of the DBL thickness as a function of the shear velocity (*u**) for *T* = 2°C and S_p = 35 from various studies. ***Fig. 5.7d-f*** shows the range of bottom-current velocities, shear velocities, DBL thicknesses and CO_3^{2-} mass transfer coefficients encountered at the seafloor. In addition, we represent in ***Fig. 5.8b*** the DBL thicknesses observed in Santschi et al. (1991) based on the dissolution of Alabaster plates deployed at the seafloor, as a function of the shear velocities from current-meter measurements or skin friction probes - see Santschi et al. (1991).

5.4.4 Sediment-side CO_3^{2-} mass transfer coefficient (k_S)

Values for k_s have been obtained from experiments on the dissolution of $CaCO_3$ beds, as reported in Sulpis et al. (2017) and Keir (1983). Based on Sulpis et al. (2017), whose results are statistically similar to those from Keir (1983),

$$k_s \approx (326.9 \pm 39.5 \text{ m a}^{-1})\, X_{calcite}^{\ 0.5} \qquad (5.10)$$

at 25 °C, where $X_{calcite}$ is the calcite content in surficial sediments from the 1° x 1° distribution model in ***Fig. 5.6a***. The sediment-side mass-transfer coefficients were subsequently adjusted from the laboratory temperature to the deep-seafloor temperature (T = 2°C) by assuming an activation energy for calcite dissolution in seawater of 50 kJ mol^{-1}, following the arguments presented in Boudreau (2013). The distribution of k_S is shown in ***Fig. 5.6b***.

We provide a comparison of *in situ* k_S and β in ***Fig. 5.9***, where the blue end of the colorbar represents a strongly water-side transport-controlled calcite dissolution reaction while the red end stands for a strongly sediment-side controlled reaction. As it can be seen in ***Fig. 5.9***, calcite dissolution over most (72%) of the seafloor is water-side transport-controlled, except for areas covered by calcite depleted sediments, where the reaction rate is limited by internal processes such as porewater diffusion or processes occurring at the surface of the calcite grains, thus independent of bottom-water hydrodynamics.

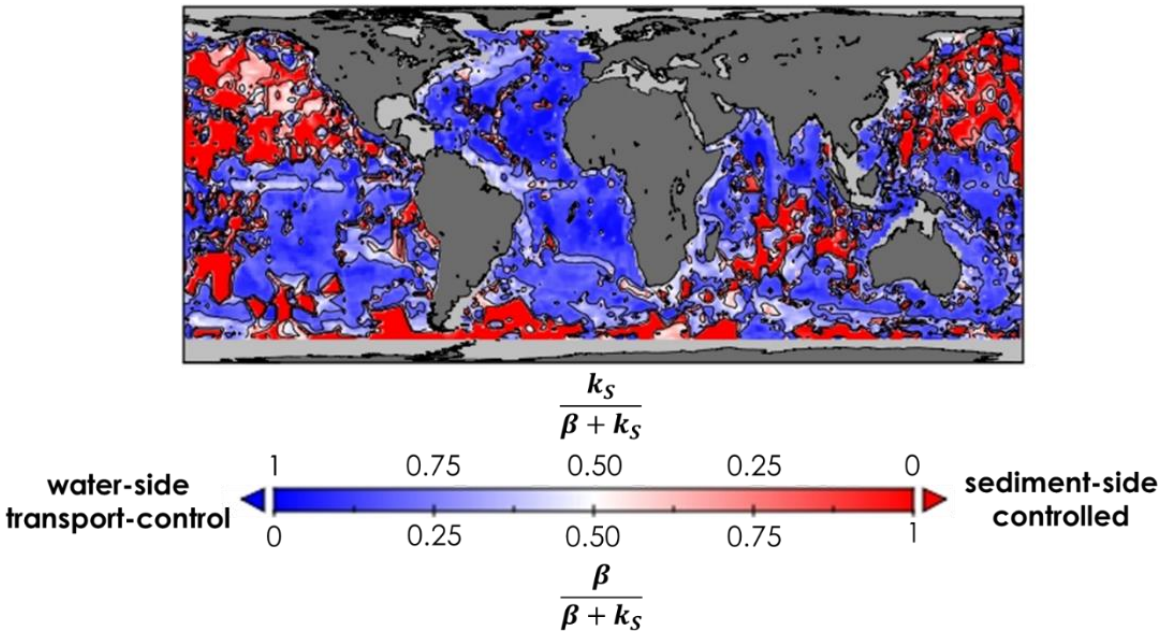

Fig. 5.9 | *Relative control from the sediment-side (k_S) or water-side (β) mass-transfer coefficients on the overall CO_3^{2-} mass transfer coefficient (k^*).*

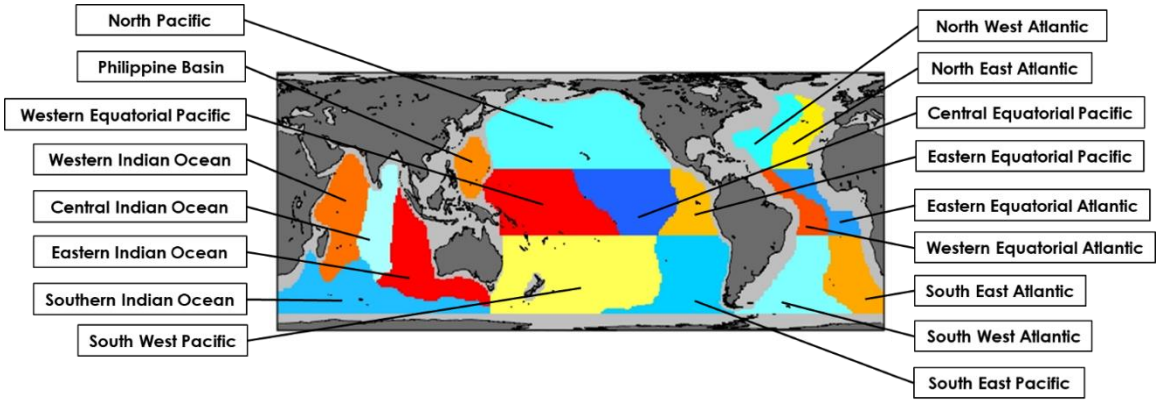

Fig. 5.10 | *Geographical boundaries of the 11 regions used to estimate the CCD from the calcite contents of sediments ($X_{calcite}$). The Southern Ocean, the Arctic Ocean, and all depths shallower than 300 m are not included in our CCD estimates.*

5.4.5 Calcite compensation depth (CCD) and calcite rain rate at the CCD (F)

The calcite content data in surficial sediments ($X_{calcite}$) from the dbSEABED database were used to estimate the CCD in each basin, as defined in ***Fig. 5.10***, excluding the Arctic and Southern Oceans (below 60 °S) as well as continental shelves and near-shore areas. As mentioned in the introduction, the CCD is operationally defined as the depth where the $CaCO_3$ content falls below 10%. Thus, for each basin, we selected the data points for which $X_{calcite}$ is equal to 0.10 ± 0.03 (or 10 ± 3%) and computed the arithmetic average of the seafloor depths associated with these measurements. These depths constitute our CCD estimates for each basin and are assumed to be representative of pre-industrial conditions. The CCD for each basin is reported along with the associated uncertainty and number of measurement used in ***Table 5.1***.

At the CCD, by definition, the calcite sinking rate is equal to its dissolution rate. Thus, the calcite downward flux at the CCD level (F) was computed from the estimated pre-industrial CCD and GLODAPv2.2016b data, per:

$$\boldsymbol{F = \frac{K_{sp}{}^{*} k^{*}}{[Ca^{2+}]} exp\left(CCD \frac{\rho g}{p_c}\right) - k^{*}\left[CO_3{}^{2-}\right]_{SW}^{p-i}} \qquad \textbf{(5.11)}$$

where p_c is a characteristic pressure (Boudreau et al., 2010b) set to 511 atm, ρ is the mean density of seawater, g is the mean gravitational acceleration on Earth and $\left[CO_3{}^{2-}\right]_{SW}^{p-i}$ is the pre-industrial bottom-water CO_3^{2-} concentration.

5.4.6 Calcite dissolution rate calculation

For pre-industrial conditions, the dissolution rate at the seafloor between the CSD and the CCD is given by

$$\boldsymbol{r = k^{*}\left([CO_3^{2-}]_{eq} - [CO_3^{2-}]_{SW}\right)} \quad \textbf{(5.12)}$$

which is ***Eq. 5.2*** of the text. For the seafloor located below the CCD, all $CaCO_3$ arriving at the seafloor (F) dissolves, i.e.,

$$\boldsymbol{r = F} \quad \textbf{(5.13)}$$

and these two latter equations account for all the benthic dissolution.

With added anthropogenic dissolution, ***Eq. 5.12*** still accounts for dissolution between the CSD and the CCD, both of which may now have been migrated upward, and ***Eq. 5.13*** still accounts for dissolution below the snowline, which remained in place. To account for dissolution between the snowline and the CCD, which have now separated as a result of anthropogenic CO_2 intrusion in the deep ocean, all $CaCO_3$ settling between these depths now dissolves at the seafloor (and in the water column). In addition, previously deposited $CaCO_3$ will dissolve as well. We account for these two sources by setting

$$\boldsymbol{r = F + k^{*}\left([CO_3^{2-}]_{eq} - [CO_3^{2-}]_{SW}\right)} \quad \textbf{(5.14)}$$

This assumes that dissolution has not been sufficient to deplete $CaCO_3$ in the sediment.

5.4.7 Statistical treatment

Standard deviations for GLODAPv2 variables (***Fig. 5.5***) were computed as the sum of the observational errors reported in Olsen et al. (2016) and the mapping interpolation errors from Lauvset et al. (2016). The standard deviation on the average CCD values are reported along with the number of measurements used for each estimate. Standard deviations for $[CO_3^{2-}]_{SW}$, $\Delta[CO_3^{2-}]_{SW}$, r, Δr and F were computed following the standard rules of error propagation, as described in ***Table 5.2***. Because r was computed using either ***Eq. 5.12***, ***Eq. 5.13*** or ***Eq. 5.14***, depending on the position of the sediment relative to the pre-industrial and current CCDs, σ_r was computed using three different equations, reported in ***Table 5.2***. No uncertainty was considered for r (i.e., σ_r was

set to zero) at locations where calcite dissolution is thermodynamically impossible, i.e., when $([CO_3^{2-}]_{SW} + \sigma_{[CO_3{}^{2-}]_{SW}}) > [CO_3^{2-}]_{eq}$.

Table 5.1 | *Regional averages of pre-industrial and current calcite marker horizons and dissolution rates. Pre-industrial CCD (calcite compensation depth) estimated from carbonate content of surficial sediments, current CCD, pre-industrial and current CSD (calcite saturation depth) computed from GLODAPv2.2016b data, regional averages of the calcite dissolution rate (mol m^{-2} yr^{-1}) and global rates (x10^{12} mol yr^{-1}). Also reported are the standard deviations associated with each horizon and the number (n) of data points from the dbSEABED database used to derive pre-industrial CCD from the calcite contents of the sediments.*

	Pre-industrial values (ca. 1800 AD)				Current values (2002 AD)			
	CCD (m)	**CSD** (m)	***r*** (mol m^{-2} yr^{-1})	**global *r*** (x10^{12} mol yr^{-1})	**CCD** (m)	**CSD** (m)	***r*** (mol m^{-2} yr^{-1})	**global *r*** (x10^{12} mol yr^{-1})
North West Atlantic	**5402** ± 346 (n=26)	**4866** ± 180	**0.02** ± 0.03	**0.1** ± 0.2	**5086** ± 185	**4524** ± 206	**0.05** ± 0.03	**0.3** ± 0.2
North East Atlantic	**5402** ± 441 *(n=7)*	**4756** ± 174	**0.02** ± 0.02	**0.1** ± 0.1	**5253** ± 178	**4592** ± 203	**0.02** ± 0.02	**0.1** ± 0.1
Western Equatorial Atlantic	**4896** ± 363 (*n=5)*	**4187** ± 234	**0.06** ± 0.03	**0.3** ± 0.2	**4767** ± 215	**4040** ± 248	**0.07** ± 0.03	**0.3** ± 0.2
Eastern Equatorial Atlantic	**5926** ± 155 (*n=8)*	**4542** ± 205	**0.03** ± 0.03	**0.2** ± 0.2	**5853** ± 161	**4446** ± 212	**0.03** ± 0.03	**0.2** ± 0.2
South West Atlantic	**4407** ± 569 (*n=15)*	**3573** ± 299	**0.05** ± 0.02	**0.7** ± 0.3	**4180** ± 280	**3288** ± 334	**0.07** ± 0.02	**1.0** ± 0.3
South East Atlantic	**4491** ± 475 (*n=5)*	**3834** ± 269	**0.08** ± 0.05	**0.9** ± 0.6	**4358** ± 251	**3667** ± 287	**0.10** ± 0.05	**1.1** ± 0.6
North Pacific	**4422** ± 990 (*n=24)*	**2910** ± 388	**0.09** ± 0.06	**3.2** ± 2.2	**4386** ± 293	**2861** ± 395	**0.09** ± 0.06	**3.2** ± 2.2
Western Equatorial Pacific	**4671** ± 400 (*n=19)*	**3101** ± 360	**0.14** ± 0.05	**3.1** ± 1.0	**4641** ± 269	**3056** ± 366	**0.14** ± 0.05	**3.1** ± 1.0
Central Equatorial Pacific	**4432** ± 386 (*n=18)*	**3178** ± 349	**0.19** ± 0.06	**3.2** ± 1.0	**4412** ± 276	**3152** ± 353	**0.20** ± 0.06	**3.3** ± 1.0
Eastern Equatorial Pacific	**3895** ± 377 (*n=10)*	**2781** ± 408	**0.09** ± 0.04	**0.7** ± 0.3	**3876** ± 331	**2756** ± 412	**0.09** ± 0.04	**0.7** ± 0.3
South West Pacific	**4320** ± 308 (*n=32)*	**3232** ± 341	**0.11** ± 0.06	**4.2** ± 2.2	**4239** ± 287	**3105** ± 359	**0.12** ± 0.06	**4.6** ± 2.2
South East Pacific	**4036** ± 195 (*n=9)*	**3114** ± 359	**0.08** ± 0.05	**1.5** ± 0.9	**3967** ± 308	**3032** ± 370	**0.09** ± 0.05	**1.7** ± 0.9
Philippine Basin	**4077** ± 312 (*n=7)*	**2864** ± 395	**0.10** ± 0.07	**0.5** ± 0.3	**4047** ± 316	**2825** ± 401	**0.10** ± 0.07	**0.5** ± 0.3
Western Indian Ocean	**4765** ± 300 (*n=6)*	**3459** ± 312	**0.12** ± 0.04	**1.6** ± 0.5	**4747** ± 245	**3414** ± 318	**0.13** ± 0.04	**1.7** ± 0.5
Central Indian Ocean	**4439** ± 674 (*n=6)*	**3490** ± 309	**0.10** ± 0.06	**0.9** ± 0.6	**4403** ± 261	**3445** ± 315	**0.11** ± 0.06	**1.0** ± 0.6
Eastern Indian Ocean	**5214** ± 346 (*n=7)*	**3458** ± 313	**0.16** ± 0.04	**2.5** ± 0.7	**5134** ± 231	**3344** ± 328	**0.19** ± 0.04	**2.9** ± 0.7
Southern Indian Ocean	**4346** ± 533 (*n=8)*	**3473** ± 312	**0.07** ± 0.05	**1.4** ± 0.9	**4130** ± 288	**3212** ± 345	**0.10** ± 0.05	**2.0** ± 0.9

Table 5.2 | *Equations used for the computation of standard deviations. This table reports the formulas used to compute the standard deviation associated with each computed variable. For r, the standard deviation was derived using either equations a, b or c reported in this table, depending on the equation used to define r,* ***Eqs. 5.12****,* ***5.13*** *and* ***5.14****, respectively.*

Variable	Standard deviation
F	$\sigma_F = k^* \sqrt{\left(\frac{{K_{sp}}^*}{[Ca^{2+}]}\right)^2 e^{\frac{CCD\ \rho\ g}{p_c}} \left(\frac{\sigma_{CCD}\ \rho\ g}{p_c}\right) \sqrt{\left(\frac{\sigma {K_{sp}}^*}{{K_{sp}}^*}\right)^2 + \left(\frac{\sigma S_p}{S_p}\right)^2} + {\sigma_{[{CO_3}^{2-}]_{SW}}}^2}$
r	a. $\sigma_r = \sigma_F$
	b. $\sigma_r = k^* \sqrt{{[{CO_3}^{2-}]_{eq}}^2 \left(\left(\frac{\sigma {K_{sp}}^*}{{K_{sp}}^*}\right)^2 + \left(\frac{\sigma S_p}{S_p}\right)^2\right) + {\sigma_{[{CO_3}^{2-}]_{SW}}}^2}$
	c. $\sigma_r = \sqrt{{\sigma_F}^2 + (k^*)^2 \left({[{CO_3}^{2-}]_{eq}}^2 \left(\left(\frac{\sigma {K_{sp}}^*}{{K_{sp}}^*}\right)^2 + \left(\frac{\sigma S_p}{S_p}\right)^2\right) + {\sigma_{[{CO_3}^{2-}]_{SW}}}^2\right)}$
Δr	$\sigma_{\Delta r} = \sqrt{{\sigma_{current\ r}}^2 + {\sigma_{preindustrial\ r}}^2}$
$[CO_3^{2-}]_{SW}$	$\sigma_{[{CO_3}^{2-}]_{SW}} = \sqrt{{\sigma_{TA}}^2 + {\sigma_{DIC}}^2}$
$\Delta[CO_3^{2-}]_{SW}$	$\sigma_{\Delta[{CO_3}^{2-}]_{SW}} = \sqrt{{\sigma_{current\ [{CO_3}^{2-}]_{SW}}}^2 + {\sigma_{preindustrial\ [{CO_3}^{2-}]_{SW}}}^2}$

5.5 Supplementary information

5.5.1 Current speed sensitivity

The bottom-ocean velocity field is generally poorly constrained. Significant qualitative and quantitative variations exist across various model output products, e.g., compare the dissipation rates that are proportional to bottom kinetic energy in Figs. 9b and 9c of Arbic et al. (2009), and resolutions, e.g., compare Figs. 2a and 2c of Thoppil et al. (2011). To get a sense of the sensitivity of the beta parameter (β) and dissolution rates to different bottom speed products, we compared the results obtained from the bottom kinetic energy field of a 1/25th degree global configuration of HYCOM, accounting for topographic internal lee-wave drag, with those obtained using a kinetic energy dataset from the same model without the "wave drag" effect, i.e., Fig. 3d and 3b of Trossman et al. (2016), respectively. Here, internal lee-wave drag represents the interaction between the bottom flows and the underlying topography that are not simply due to

bottom friction. This drag is a momentum sink associated with internal lee-wave generation that arises from geostrophic flow impinging upon rough topography and topographic blocking. The results from this comparison are shown in ***Fig. 5.11***. Whereas the world-averaged bottom kinetic energy increases from 0.0066 m^2 s^{-2} using a model taking into account the wave-drag effect to 0.0171 m^2 s^{-2} for a model neglecting this effect (i.e., a 2.6 folds increase), the resulting carbonate ion mass-transfer coefficient (β) and calcite dissolution rate (r) are only moderately affected, as they rise from geometrically world-averaged values of β = 14 m yr^{-1} and r = 0.10 mol m^{-2} yr^{-1} to β = 20 m yr^{-1} and r = 0.13 mol m^{-2} yr^{-1}, respectively (a ~40 and 30% increase, respectively). Thus, our dissolution model, although impacted by the uncertainty in the current speed dataset, tends to attenuate these discrepancies. As shown in ***Fig. 5.11***, our results are not qualitatively affected by the initial bottom kinetic-model choice, as the loci of accelerated anthropogenically-driven dissolution are invariant whether or not the wave-drag effect is included in the initial kinetic energy model.

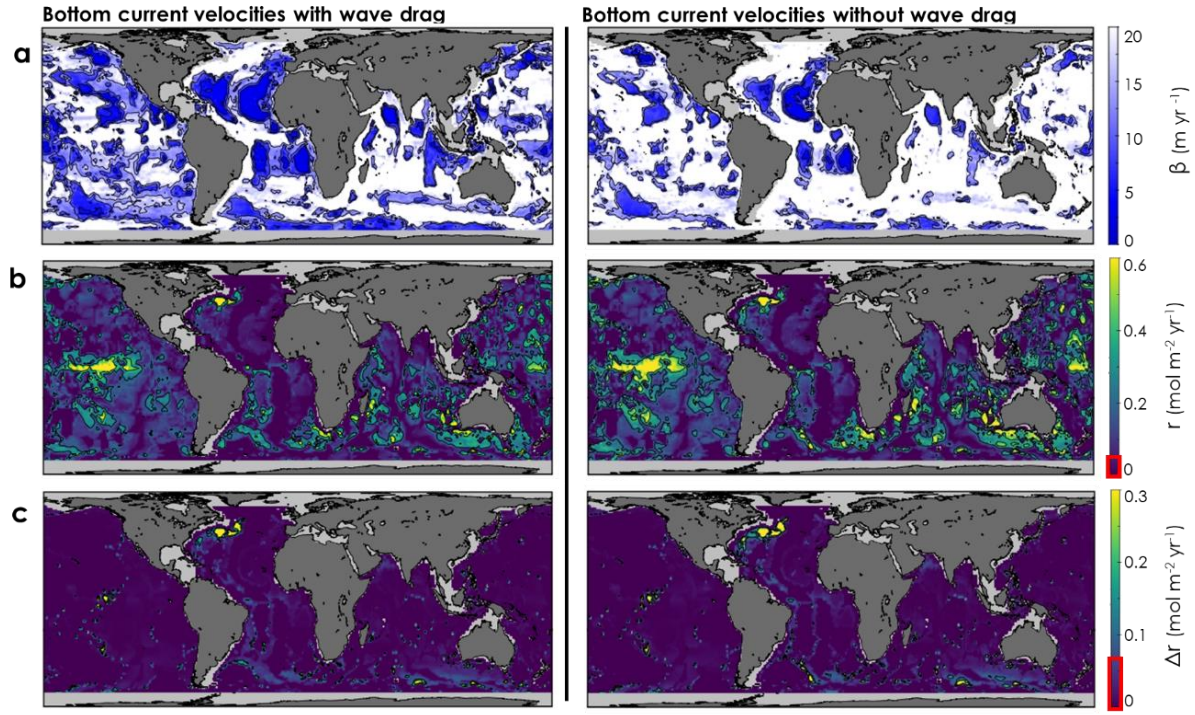

Fig. 5.11 | *Sensitivity of the dissolution rate model to two different initial kinetic energy distribution models. Impact of the "wave drag" effect on (**a**) the water-side CO_3^{2-} mass-transfer coefficient (β), (**b**) the current calcite dissolution rates at the sediment-water interface (r), and (**c**) the difference between pre-industrial and current calcite dissolution rates below 300 m (Δr = current r – pre-industrial r). Uncertainties are indicated by the red outline on the color bars, corresponding to one standard deviation, equal to 0.05 mol m^{-2} yr^{-1} for r and to 0.07 mol m^{-2} yr^{-1} for Δr.*

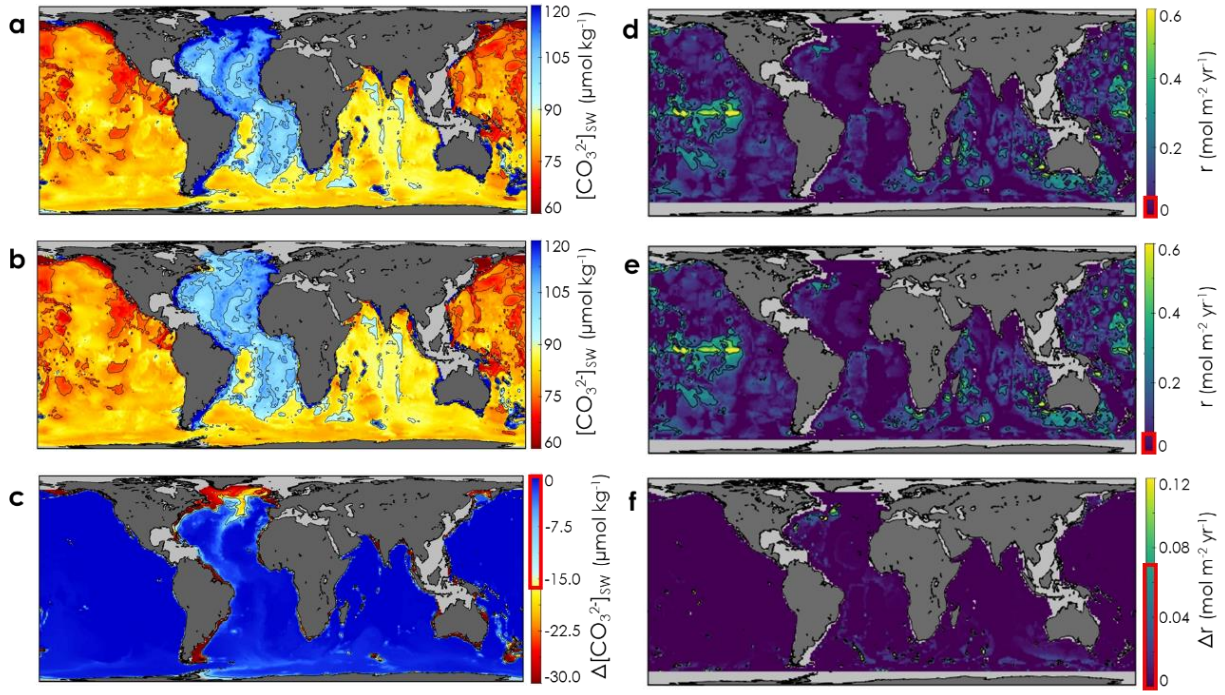

Fig. 5.12 | *Bottom-water [CO_3^{2-}] and calcite dissolution rates estimated from an alternate DIC dataset from Khatiwala et al. (2009). The panels on the left depict (**a**) pre-industrial bottom-water [$CO_3^{2-}]_{SW}$, (**b**) current bottom-water [$CO_3^{2-}]_{SW}$ and (**c**) difference between pre-industrial and current bottom-water [$CO_3^{2-}]_{SW}$ ($\Delta[CO_3^{2-}]_{SW}$ = current bottom-water [$CO_3^{2-}]_{SW}$ minus pre-industrial bottom-water [$CO_3^{2-}]_{SW}$), below 300 m. The panels on the right represent (**d**) pre-industrial, (**e**) current calcite dissolution rates (r) at the sediment-water interface, and (**f**) the difference between pre-industrial and current calcite dissolution rates below 300 m (Δr = current r minus pre-industrial r), i.e., the anthropogenic CO_2-driven calcite dissolution rate. Uncertainties are indicated by the red outline on the color bars, corresponding to one standard deviation, equal to 16.9 µmol kg^{-1} for $\Delta[CO_3^{2-}]_{SW}$, to 0.05 mol m yr^{-1} for r and to 0.07 mol m yr^{-1} for Δr.*

We chose two different bottom current-speed products because it is necessary to put an upper limit on the sensitivity of the dissolution rate changes over time. We focus on the relationship between bottom current-speed changes under a "climate change scenario" and the difference between the two bottom-current speed products used for this sensitivity analysis (i.e., with and without wave drag, see ***Fig. 5.11***). We posit that a comparison of their spatial patterns and magnitudes can inform us about the level of uncertainty in our dissolution rate change estimates. The focus here is on differences between each bottom current speed product because a bias that is consistent over time and space would approximately cancel out when considering its contribution to the changes in dissolution rates. The difference between the bottom current-speed products used here is larger than the simulated bottom current-speed change in climate change

simulations over time (see Fig. 3e of Melet et al. (2015)) and at similar locations (namely, the Southern Ocean and the North Atlantic Ocean). This suggests that our estimates, based on the two bottom current speed products (with and without wave drag), can be used as an upper limit on the uncertainty of our dissolution rate change estimates.

5.5.2 Anthropogenic CO_2 dataset

We have tested the sensitivity of our dissolution rates to the choice of the *DIC* dataset. Resolving or understanding the differences between various *DIC* datasets is beyond the scope of this paper, but we provide a comparison of the results described in the main text of this study, using the *DIC* dataset from Lauvset et al. (2016), with results obtained based on another *DIC* dataset from Khatiwala et al. (2009). Both datasets comprise *DIC* values for the present day, as well as pre-industrial *DIC*, allowing us to compute and compare $\Delta[CO_3^{2-}]_{SW}$ and Δr. First, we note that $[CO_3^{2-}]_{SW}$ values computed with *DIC* from Lauvset et al. (2016), represented in ***Fig. 5.2a-b***, are slightly lower than those derived with DIC from Khatiwala et al. (2009), in ***Fig. 5.12a-b***. These differences are, however, not significant since they are within the error bars. $\Delta[CO_3^{2-}]_{SW}$ from ***Fig. 5.2c***, using the DIC from Lauvset et al. (2016), reveals an anthropogenic $[CO_3^{2-}]_{SW}$ decrease of 4-8 µmol kg^{-1} in most of the bottom waters of the Atlantic and near the Southern Ocean, and the presence of a small anthropogenic signal in most of the bottom waters in the Pacific. On the other hand, $\Delta[CO_3^{2-}]_{SW}$ from ***Fig. 5.12c***, based on the alternative *DIC* dataset from Khatiwala et al. (2009), shows an anthropogenic decrease in bottom $[CO_3^{2-}]_{SW}$ limited to shallow waters, along the Atlantic mid-ocean ridge and in the North Atlantic, while in most bottom waters, including those of the Indian and Pacific Oceans, no anthropogenic DIC seems to have been accumulated since the end of the pre-industrial era.

To examine in further detail the differences between these two datasets, we have plotted depth profiles showing the anthropogenic *DIC* concentration along the 170°W meridian, between 0 and 60°S, for both datasets, along with a depth profile showing the bottom-water CFC-11 concentration along the same section. CFC-11 is a non-reactive anthropogenic trace gas frequently used as an ocean tracer. CFC-11 emission to the atmosphere was virtually nonexistent before the end of World-War II, much later than that of anthropogenic CO_2 (~1950 vs ~1880). There are certainly differences in air-sea equilibration times and solubility, but in general, anywhere CFC-

11 is found in bottom waters there should be anthropogenic *DIC* as well. As it can be seen in ***Fig. 5.13***, both *DIC* datasets show a northward progression of anthropogenic *DIC* in the bottom waters, but the magnitude of that increase varies. In both cases, the patterns of the anthropogenic *DIC* distribution fit those of the CFC-11, also showing a clear northward progression through the bottom waters. In addition, the dataset of Khatiwala et al. (2009), that simulates anthropogenic *DIC* penetration from 1765 AD to 2011 AD, displays an anthropogenic *DIC* concentration of strictly zero for a large portion of the transect (between 2000 and 4000 m-depth, 40 and 0°S), whereas some CFC-11 is found in that area for the year 2009 AD. Anthropogenic *DIC* from Lauvset et al. (2016) is generally higher, and present in concentrations above zero in the entire depth profile, which is closer to the CFC-11 data. These observations support the assumption that the anthropogenic *DIC* dataset from Lauvset et al. (2016) is arguably more accurate than the dataset from Khatiwala et al. (2009) for the purposes of the present study.

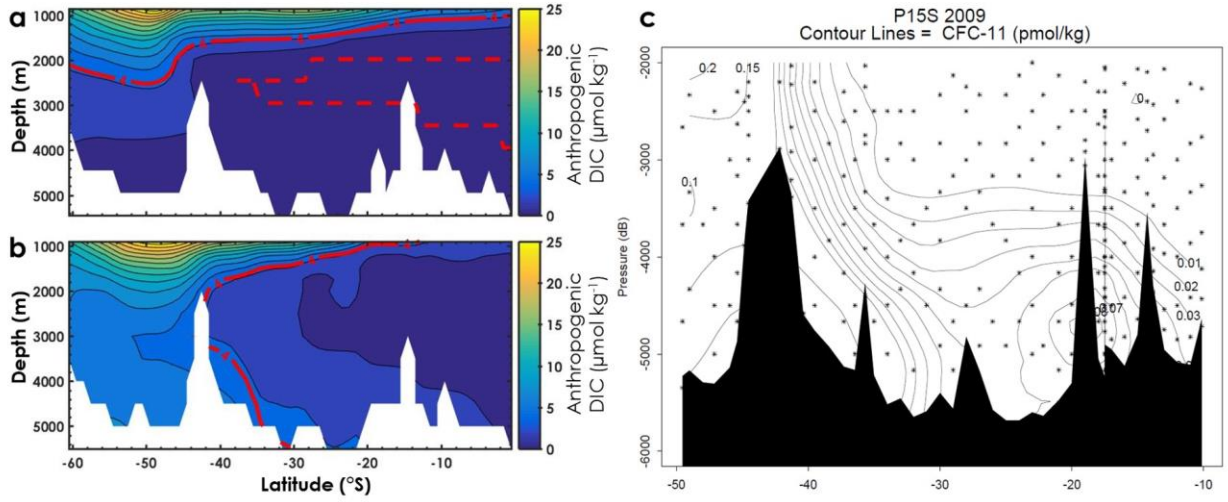

Fig. 5.13 | *Anthropogenic tracers penetration in the ocean bottom waters. Concentration profiles along the 170°W meridian, in the southern hemisphere and below 1000m, of (**a**) anthropogenic DIC from Khatiwala et al. (2009), (**b**) anthropogenic DIC from Lauvset et al. (2016) and (**c**) CFC-11 (note that 2 different contour intervals are used, 0.05 and 0.01 for low concentration areas). The solid red lines in the left panels represent the anthropogenic DIC detection limit that we set to 4 µmol kg^{-1}, below which an anthropogenic DIC addition would not be considered significant, and the red dashed lines delimit the areas where no anthropogenic DIC is found, i.e., its estimated concentration is strictly zero.*

Comparing ***Fig. 5.3c*** with ***Fig. 5.12f***, it can be seen that the loci of anthropogenic dissolution are unaffected by the choice of the anthropogenic *DIC* dataset, with a major anthropogenic dissolution flux observed in the North Atlantic, and the presence of several

dissolution hot spots in the most southern latitudes. Although Δr from Khatiwala et al. (2009) is generally smaller than from Lauvset et al. (2016) and falls for the greater part within the error bars, as shown in ***Fig. 5.12f***, some Δr values remain significant, such as the anthropogenic dissolution hotspots in the North and South Atlantic and in the Pacific. In addition, the CCD in the North West Atlantic rises from 5402 ± 346 m for the pre-industrial to 5086 ± 185 m for today when anthropogenic *DIC* from Lauvset et al. (2016) is used, compared to a rise to 5127 ± 183 m using Khatiwala et al. (2009). These results are statistically identical. Thus, although the magnitudes of the dissolution rates are impacted by the initial choice of the DIC dataset, our results and conclusions are not. There is a clear indication for current anthropogenic dissolution of $CaCO_3$ at the seafloor and a shoaling of $CaCO_3$ marker horizons in the water column.

References

Archer, D. (2005) Fate of fossil fuel CO_2 in geologic time. *Journal of Geophysical Research*, 110(C09S05).

Archer, D., Emerson, S. and Smith, C.R. (1989b) Direct measurement of the diffusive sublayer at the deep sea floor using oxygen microelectrodes. *Nature*, 340, 623-626.

Archer, D., Kheshgi, H. and Maier-Reimer, E. (1998) Dynamics of fossil fuel CO_2 neutralization by marine $CaCO_3$. *Global Biogeochemical Cycles*, 12, 259-276, https://doi.org/10.1029/98GB00744

Armi, L. (1977) The Dynamics of the Bottom Boundary Layer of the Deep Ocean. In: C.J.J. Nihoul (Eds), Bottom turbulence. 8th International Liege Colloquium on Ocean Hydrodynamics. Elsevier, Amsterdam, pp. 153-164.

Battaglia G., Steinacher M. and Joos, F. (2016) A probabilistic assessment of calcium carbonate export and dissolution in the modern ocean. *Biogeosciences*, 13(9), 2823-2848.

Berelson, W.M., Balch, W.M., Najjar, R., Feely, R.A., Sabine, C. and Lee, K. (2007) Relating estimates of $CaCO_3$ production, export, and dissolution in the water column to measurements of $CaCO_3$ rain into sediment traps and dissolution on the sea floor: A revised global carbonate budget. *Global Biogeochemical Cycles* 21(1), https://doi.org/10.1029/2006GB002803

Boudreau, B.P. (2013) Carbonate dissolution rates at the deep ocean floor. *Geophysical Research Letters* 40, 744-748, https://doi.org/10.1029/2012GL054231

Boudreau, B.P. and Jørgensen, B.B. (2001) The Benthic Boundary Layer: Transport Processes and Biogeochemistry. Oxford University Press, Oxford.

Boudreau, B.P., Middelburg, J.J., Hofmann, A.F. and Meysman, F.J.R. (2010a) Ongoing transients in carbonate compensation. *Global Biogeochemical Cycles*, 24(4), https://doi.org/10.1029/2009GB003654

Boudreau, B.P., Middelburg, J.J. and Meysman, F.J.R. (2010b) Carbonate compensation dynamics. *Geophysical Research Letters*, 37, https://doi.org/10.1029/2009GL041847

Boudreau B.P., Luo Y., Meysman F.J.R., Middelburg J.J. and Dickens G.R. (2015) Gas hydrate dissociation prolongs acidification of the Anthropocene oceans. *Geophysical Research Letters*, 42.

Carter B.R., Toggweiler J.R., Key R.M. and Sarmiento J.L. (2014) Processes determining the marine alkalinity and calcium carbonate saturation state distributions. *Biogeosciences* 11, 7349-7362.

Csanady, G.T. (1967) On the "Resistance Law" of a turbulent Ekman layer. *Journal of the Atmospheric Sciences* 24, 467-471, https://doi.org/10.1175/1520-0469(1967)024<0467:OTLOAT>2.0.CO;2

Cui, Y., Kump, L.R., Ridgwell, A.J., Charles, A.J., Junium, C.K., Diefendorf, A.F., Freeman, K.H., Urban, N.M. and Harding, I.C. (2011) Slow release of fossil carbon during the Palaeocene–Eocene Thermal Maximum. *Nature Geosience* 4, 481–485, https://doi.org/10.1038/ngeo1179

Deissler, R.G. (1954) Analysis of turbulent heat transfer, mass transfer, and friction in smooth tubes at high Prandtl and Schmidt numbers. National Advisory Commitee Aerodynamics, Technical Note 3145. U.S. Government Printing Office, Washington D.C.

Doney, S.C., Fabry, V.J., Feely, R.A. and Kleypas, J.A. (2009) Ocean acidification: the other CO_2 problem. Annual Reviews of Marine Science 1, 169-192.

Feely, R.A., Sabine, C.L., Lee, K., Berelson, W., Kleypas, J., Fabry, V.J. and Millero, F.J. (2004) Impact of Anthropogenic CO_2 on the $CaCO_3$ System in the Oceans. *Science* 305(5682), 362-366.

Fukuda, S.Y., Suzuki, Y. and Shiraiwa, Y. (2014) Difference in physiological responses of growth, photosynthesis and calcification of the coccolithophore Emiliania huxleyi to acidification by acid and CO_2 enrichment. *Photosynthesis Research* 121, 299-309.

Gibbs, S.J., Stoll, H.M., Bown, P.R. and Bralower, T.J. (2010) Ocean acidification and surface water carbonate production across the Paleocene–Eocene thermal maximum. *Earth and Planetary Science Letters* 295(3-4), 583-592.

Goff, J.A., Jenkins, C.J. and Williams, S.J. (2008) Seabed mapping and characterization of sediment variability using the usSEABED data base. *Continental Shelf Research* 28(4-5), 614-633.

Gundersen, J.K. and Jørgensen, B.B. (1990) Microstructure of diffusive boundary layers and the oxygen uptake of the sea floor. *Nature* 345, 604-607.

Jenkins, C.J. (1997) Building offshore soils databases. *Sea Technology* 38(12), 25-28.

Keir, R.S. (1983) Variation in the carbonate reactivity of deep-sea sediments: determination from flux experiments. *Deep-Sea Research* 30, 279-296.

Key, R.M., Olsen, A., van Heuven, S., Lauvset, S.K., Velo, A., Lin, X., Schirnick, C., Kozyr, A., Tanhua, T., Hoppema, M., Jutterström, S., Steinfeldt, R., Jeansson, E., Ishi, M., Perez, F.F. and Suzuki, T. (2015) Global Ocean Data Analysis Project, Version 2 (GLODAPv2), ORNL/CDIAC-162, NDP-P093. Carbon Dioxide Information Analysis Center, Oak Ridge National Laboratory, US Department of Energy, Oak Ridge, Tennessee.

Khatiwala, S., Primeau, F. and Hall, T. (2009) Reconstruction of the history of anthropogenic CO_2 concentrations in the ocean. *Nature* 462, 346-349, https://doi.org/10.1038/nature08526

Lauvset, S.K., Key, R.M., Olsen, A., Heuven, S.v., Velo, A., Lin, X., Schirnick, C., Kozyr, A., Tanhua, T., Hoppema, M., Jutterström, S., Steinfeldt, R., Jeansson, E., Ishii, M., Perez, F.F., Suzuki, T. and Watelet, S. (2016) A new global interior ocean mapped climatology: the $1° \times 1°$ GLODAP version 2. *Earth System Science Data* 8, 325-340, https://doi.org/10.5194/essd-8-325-2016

Lewis, E. and Wallace, D.W.R. (1998) Program Developed for CO_2 System Calculations. ORNL/CDIAC-105. Carbon Dioxide Information Analysis Center, Oak Ridge National Laboratory, U.S. Department of Energy, Oak Ridge, Tennessee.

Li, Y.-H. and Gregory, S. (1974) Diffusion of ions in sea water and in deep-sea sediments. *Geochimica et Cosmochimica Acta* 38(5), 703-714.

Maugendre, L., Gattuso, J.-P., Poulton, A.J., Dellisanti, W., Gaubert, M., Guieu, C. and Gazeau, F. (2017) No detectable effect of ocean acidification on plankton metabolism in the NW oligotrophic Mediterranean Sea: results from two mesocosm studies. *Estuarine, Coastal and Shelf Science*, 186(A), 89-99, https://doi.org/10.1016/j.ecss.2015.03.009

Melet, A., Hallberg, R., Adcroft, A., Nikurashin, M. and Legg, S. (2015) Energy Flux into Internal Lee Waves: Sensitivity to Future Climate Changes Using Linear Theory and a Climate Model. *Journal of Climate* 28, 2365-2384.

Monin, A.S. and Yaglom, A.M. (1971) Statistical Fluid Dynamics. Vol. I and II (MIT Press).

Montenegro, A., Brovkin, V., Eby, M., Archer, D. and Weaver, A.J. (2007) Long term fate of anthropogenic carbon. *Geophysical Research Letters* 34(L19707), https://doi.org/10.1029/2007GL030905

Mucci, A. (1983) The solubility of calcite and aragonite in seawater at various salinities, temperatures and one atmosphere total pressure. *American Journal of Science* 283, 780-799, http://doi.org/10.2475/ajs.283.7.780

Olsen, A., Key, R. M., van Heuven, S., Lauvset, S. K., Velo, A., Lin, X., Schirnick, C., Kozyr, A., Tanhua, T., Hoppema, M., Jutterström, S., Steinfeldt, R., Jeansson, E., Ishii, M., Pérez, F. F., and Suzuki, T. (2016) The Global Ocean Data Analysis Project version 2 (GLODAPv2) – an internally consistent data product for the world ocean, *Earth System Science Data*, 8, 297-323, https://doi.org/10.5194/essd-8-297-2016.

Perez, F.F., Fontela, M., Garcia-Ibanez, M.I., Mercier, H., Velo, A., Lherminier, P., Zunino, P., de la Paz, M., Alonso-Perez, F., Guallart, E.F. and Padin, X.A. (2018) Meridional overturning circulation conveys fast acidification to the deep Atlantic Ocean. *Nature* 554, 515-518, https://doi.org/10.1038/nature25493

Pinsonneault, A.J., Matthews, H.D., Galbraith, E.D. and Schmittner, A. (2012) Calcium carbonate production response to future ocean warming and acidification. *Biogeosciences* 9(6), 2351-2364.

Purkey, S.G. and Johnson, G.C. (2013) Antarctic Bottom Water warming and freshening: Contributions to sea level rise, ocean freshwater budgets, and global heat gain. *Journal of Climate* 26, 6105-6122, https://doi.org/10.1175/JCLI-D-12-00834.1

Riebesell, U., Körtzinger, A. and Oschlies, A. (2009) Sensitivities of marine carbon fluxes to ocean change. *Proceedings of the National Academy of Sciences of the United States of America* 106(49), 20602-20609.

Riley, J.P. and Tongudai, M. (1967) The major cation/chlorinity ratios in sea water. *Chemical Geology* 2, 263-269, https://doi.org/10.1016/0009-2541(67)90026-5

Ríos, A.F., Resplandy, L., García-Ibáñez, M.I., Fajar, N.M., Velo, A., Padin, X.A., Wanninkhof, R., Steinfeldt, R., Rosón, G. and Pérez, F.F. (2015) Decadal acidification in the water masses of the Atlantic Ocean. *Proceedings of the National Academy of Sciences of the United States of America* 112, 9950-9955, https://doi.org/10.1073/pnas.1504613112

Santschi, P.H., Anderson, R.F., Fleisher, M.Q. and Bowles, W. (1991) Measurements of diffusive sublayer thicknesses in the ocean by alabaster dissolution, and their implications for the measurements of benthic fluxes. *Journal of Geophysical Research: Oceans* 96, 10641-10657, https://doi.org/10.1029/91JC00488

Schink, D. R., and Guinasso, N. L. (1977) Modelling the influence of bioturbation and other processes on calcium carbonate dissolution at the sea floor. In N. R. Andersen and A. Malahoff [Eds.]. The Fate of Fossil Fuel CO_2 in the Oceans. Plenum Press. p. 375-400.

Shaw, D.A., Hanratty, T.J. (1977) Turbulent mass transfer rates to a wall for large Schmidt numbers. *AIChE Journal* 23(1):28-37.

Smith, H.E.K., Tyrrell, T., Charalampopoulou, A., Dumousseaud, C., Legge, O.J., Birchenough, S., Pettit, L.R., Garley, R., Hartman, S.E., Hartman, M.C., Sagoo, N., Daniels, C.J., Achterberg, E.P. and Hydes, D.J. (2012) Predominance of heavily calcified coccolithophores at low $CaCO_3$ saturation during winter in the Bay of Biscay. *Proceedings of the National Academy of Sciences of the U.S.A* 109, 8845-8849.

Smith, S.V., Mackenzie, F.T. (2016) The role of $CaCO_3$ reactions in the contemporary oceanic CO_2 cycle. *Aquatic Geochemistry* 22, 153-175.

Steinberger, N. and Hondzo, M. (1999) Diffusional mass transfer at sediment-water interface. *Journal of Environmental Engineering* 125, 192-200, https://doi.org/10.1061/(ASCE)0733-9372(1999)125:2(192)

Sulpis, O., Lix, C., Mucci, A. and Boudreau, B.P. (2017) Calcite dissolution kinetics at the sediment-water interface in natural seawater. *Marine Chemistry* 195, 70-83, https://doi.org/10.1016/j.marchem.2017.06.005

Takahashi, T., Sutherland, S.C., Sweeney, C., Poisson, A., Metzl, N., Tilbrook, B., Bates, N., Wanninkhof, R., Feely, R.A., Sabine, C., Olafsson, J. and Nojiri Y. (2002) Global sea–air CO_2 flux based on climatological surface ocean pCO_2, and seasonal biological and temperature effects. *Deep Sea Research Part II: Topical Studies in Oceanography* 49(9-10), 1601-1622, https://doi.org/10.1016/S0967-0645(02)00003-6

Thoppil, P.G., Richman, J.G. and Hogan, P.J. (2011) Energetics of a global ocean circulation model compared to Observations. *Geophysical Research Letters* 38.

Timko, P. G., Arbic, B. K., Richman, J. G., Scott, R. B., Metzger, E. J., & Wallcraft, A. J. (2013). Skill testing a three-dimensional global tide model to historical current meter records. *Journal of Geophysical Research: Oceans*, *118*(12), 6914-6933, https://doi.org/10.1002/2013jc009071

Trossman, D.S., Arbic, B.K., Richman, J.G., Garner, S.T., Jayne, S.R. and Wallcraft, A.J. (2016) Impact of topographic internal lee wave drag on an eddying global ocean model. *Ocean Modelling* 97, 109-128.

van Heuven, S., Pierrot, D., Rae, J.W.B., Lewis, E. and Wallace, D.W.R. (2011) *MATLAB Program Developed for CO2 System Calculations*. ORNL/CDIAC-105b. Carbon Dioxide Information Analysis Center, Oak Ridge National Laboratory, U.S. Department of Energy, Oak Ridge, Tennessee. https://doi.org/10.3334/CDIAC/otg.CO2SYS_MATLAB_v1.1

Waters, C.N., Zalasiewicz, J., Summerhayes, C., Barnosky, A.D., Poirier, C., Galuszka, A., Cearreta, A., Edgeworth, M., Ellis, E.C., Ellis, M., Jeandel, C., Leinfelder, R., McNeill, J.R., Richter, D., Steffen, W., Syvitski, J., Vidas, D., Wagreich, M., Williams, M., Zhisheng, A., Grinevald, J., Odada, E., Oreskes, N. and Wolfe, A.P. (2016) The Anthropocene is functionally and stratigraphically distinct from the Holocene. *Science* 351(6269), https://doi.org/10.1126/science.aad2622

Weatherall, P. (2015) A new digital bathymetric model of the world's oceans. *Earth and Space Science* 2(8), 331-345.

Wood, P.E., Petty, C.A. (1983) New model for turbulent mass transfer near a rigid interface. *AIChE Journal* 29(1), 164-167.

Wootton, J.T., Pfister, C.A., Forester, J.D. (2008) Dynamic patterns and ecological impacts of declining ocean pH in a high-resolution multi-year dataset. *Proceedings of the National Academy of Science of the United States of America* 105(48), 18848-18853.

Zachos, J.C., Röhl, U., Schellenberg, S.A., Sluijs, A., Hodell, D.A., Kelly, D.C., Thomas, E., Nicolo, M., Raffi, I., Lourens, L.J., McCarren, H. and Kroon, D. (2005) Rapid acidification of the ocean during the Paleocene-Eocene Thermal Maximum. *Science* 308(5728), 1611-1615.

Zeebe, R.E., Zachos, J.C., Dickens, G.R. (2009) Carbon dioxide forcing alone insufficient to explain Paleocene–Eocene Thermal Maximum warming. *Nature Geoscience* 2, 576-580.

Zeebe, R.E. (2011) On the molecular diffusion coefficients of dissolved CO_2, HCO_3^-, and CO_3^{2-} and their dependence on isotopic mass. *Geochimica et Cosmochimica Acta* 75, 2483-2498, https://doi.org/10.1016/j.gca.2011.02.010

Preface to Chapter 6

We have seen in ***Chapters 2-4*** that, over most of the seafloor, calcite dissolution at the sediment-water interface is controlled by the presence of a diffusive-boundary layer above the sediment bed. In ***Chapter 5***, we showed that it is possible to derive the rate of calcite dissolution at the seafloor if the bottom-water chemistry and currents are known. We have also shown that anthropogenic ocean acidification has progressed enough to generate significant dissolution fluxes in various areas of the ocean floor. Here, we go further and compute calcite dissolution through the 21st century if all the variables influencing dissolution are allowed to fluctuate in response to climate change.

Results from a range of Earth System and climate models of various resolution, run under high-CO_2 emission scenarios, challenge the paradigm that seafloor $CaCO_3$ dissolution will grow in extent and intensify as ocean acidification persists. Under the "business as usual" RCP8.5 scenario, we find that while $CaCO_3$ dissolution will increase over the 21st century in some areas of the deep ocean, such as the eastern central Pacific Ocean, it is projected to decrease in the Northern Pacific and abyssal Atlantic Ocean. The decrease is due to a reduced $CaCO_3$ delivery to the seafloor as well as a slower bottom-water circulation. The latter leads to thicker diffusive boundary layers above the sediment bed and a consequent stronger kinetic barrier to the dissolution reaction. These results indicate that the neutralization of human-made CO_2 by calcite dissolution at the seafloor may take longer than previously thought.

Chapter 6

Decreasing bottom-current speeds and seafloor $CaCO_3$ dissolution under a business-as-usual scenario*

Olivier Sulpis[1], Carolina O. Dufour[2], David S. Trossman[3], Andrea J. Fassbender[4], Alfonso Mucci[1], Brian K. Arbic[5], Bernard P. Boudreau[6] and John P. Dunne[7]

[1]GEOTOP and Earth and Planetary Sciences Department, McGill University, Montreal QC, Canada

[2]Atmospheric and Oceanic Sciences Department, McGill University, Montreal QC, Canada

[3]Institute of Computational Engineering and Sciences, The University of Texas Austin, Austin TX, USA

[4]Monterey Bay Aquarium Research Institute, Moss Landing CA, USA

[5]Department of Earth and Environmental Sciences, University of Michigan, Ann Arbor MI, USA

[6]Department of Oceanography, Dalhousie University, Halifax NS, Canada

[7]NOAA, Geophysical Fluid Dynamics Laboratory, Princeton NJ, USA

**Under review in Global Biogeochemical Cycles*

Abstract

Results from a range of Earth System and climate models of various resolution run under high-CO_2 emission scenarios challenge the paradigm that seafloor $CaCO_3$ dissolution will grow in extent and intensify as ocean acidification persists. Under the "business as usual" RCP8.5 scenario, we find that while $CaCO_3$ dissolution will increase over the 21st century in some areas of the deep ocean, such as the eastern central Pacific Ocean, it is projected to decrease in the Northern Pacific and abyssal Atlantic Ocean. The decrease is due to reduced $CaCO_3$ delivery to the seafloor as well as slower bottom-water circulation. The latter leads to thicker diffusive boundary layers above the sediment bed and a consequent stronger kinetic barrier to the dissolution reaction. Although a projected weakening of bottom currents is consistent over most of the seafloor into the 21st century, irrespective of the model, strong discrepancies exist in the magnitude of predicted bottom-current speeds. We find that contemporary bottom-current speeds predicted by most models consistently underestimate observations from current meters, and that the discrepancy

between models and observations narrows as the model resolution increases. The poor performance of most models in reproducing bottom velocities, as well as the large disparities across predicted bottom-water chemical variables, reduce our ability to estimate the magnitude and temporal evolution of anthropogenic $CaCO_3$ dissolution rates and the accompanying anthropogenic carbon dioxide neutralization.

6.1 Introduction

Anthropogenic carbon dioxide (CO_2) has been accumulating in the atmosphere since the beginning of the industrial era and, according to projections of future emissions, will continue to do so well beyond the end of this century (Collins et al., 2013; Meinshausen et al., 2011). The atmospheric CO_2 concentration was ~280 parts per million (ppm) in 1750 (Joos and Spahni, 2008), reached 405 ppm in 2017 (Dlugokencky and Tans, 2018), and may exceed 1000 ppm by 2100 according to the "business as usual" Representative Concentration Pathway 8.5 (RCP8.5, van Vuuren et al. (2011)), a high-CO_2 emission scenario in which no specific climate mitigation action is taken (Riahi et al., 2011). Each year about 25% of the anthropogenic carbon emitted into the atmosphere is absorbed by the ocean (Le Quéré et al., 2018). The absorption of CO_2 in seawater leads to a measurable pH decrease which, in turn, reduces the carbonate ion (CO_3^{2-}) concentration and lowers the saturation state of seawater with respect to calcium carbonate minerals ($CaCO_3$, e.g., calcite or aragonite), favouring their dissolution and impeding their precipitation (Mackenzie and Andersson, 2013). These conditions are expected to intensify over the next centuries (Caldeira and Wickett, 2003; Orr et al., 2005). Recent research highlighted the exceptional nature and rate of the present acidification, showing that the rate of anthropogenic carbon release is higher than during any other comparable event over at least the past 66 million years (Zeebe et al., 2016). It is critical that scientists and policy makers obtain accurate estimates of the timescales over which marine ecosystems will be impacted by this anthropogenic acidification.

Two hypothetical pathways can be considered for the evolution of ocean acidification in a high-CO_2 world. In a poorly chemically-buffered ocean, CO_2 accumulation and the resulting seawater-pH decline are rapid, leading to runaway ocean acidification. In contrast, a well-buffered ocean can slow down the pH change through negative feedback mechanisms, whose kinetics then control the ocean recovery time towards its pre-acidification state once anthropogenic CO_2

emissions are curbed. One of these feedback mechanisms, the dissolution of marine $CaCO_3$ minerals, is thought to be the major sink for anthropogenic CO_2 on the time scale of decades to millennia (Archer et al., 2009; Ridgwell and Hargreaves, 2007) and is described by the overall reaction:

$$\mathbf{CaCO_3 + CO_2 + H_2O \leftrightarrow 2HCO_3^- + Ca^{2+}} \quad \textbf{(6.1)}$$

$CaCO_3$-rich (> 30 % of the sediment dry weight) sediments cover a third of the seafloor (Dutkiewicz et al., 2015; Morse and Mackenzie, 1990). The distribution and $CaCO_3$ content of sediment are a function of the $CaCO_3$ production and export from the surface ocean, dilution of sedimentary $CaCO_3$ by authigenic and siliciclastic materials, and, most importantly, the saturation state of overlying waters with respect to $CaCO_3$. The latter is defined as:

$$\mathbf{\Omega = \frac{[Ca^{2+}]_{SW}[CO_3^{2-}]_{SW}}{K_{sp}^*}} \quad \textbf{(6.2)}$$

where the square brackets indicate total concentrations in seawater in mol kg^{-1} and K_{sp}* is the stoichiometric solubility constant of the mineral of interest (mol^2 kg^{-2}) at *in situ* temperature, pressure, and salinity (Millero, 1995; Mucci, 1983). If Ω is lower than 1, seawater is undersaturated with respect to the $CaCO_3$ phase of interest (e.g., calcite or aragonite) and the latter should dissolve if present. Although biogenic aragonite, calcite, and magnesian calcites dominate in the marine environment, only calcite and low magnesian-calcite phases ($MgCO_3$ < 4 % by mole) persist in deep-sea sediments (Morse et al., 2007). As ocean acidification intensifies, the area of the seafloor covered by undersaturated waters will increase, and more dissolution of $CaCO_3$ minerals at the seafloor is expected (Archer et al., 2009; Ridgwell and Hargreaves, 2007; Boudreau et al., 2010a; Alexander et al., 2015). It is this additional dissolution that neutralizes excess CO_2 and allows the ocean to return to its pre-acidification state within a few thousand years (Ciais et al. 2013).

Currently, 55 % of the anthropogenic CO_2 in the ocean is stored in the top 100 m of the water column, while the deep-ocean reservoir (i.e., below 1000 m), which represents 76% of the ocean volume, contains only 4% of the anthropogenic CO_2 (from the data of Khatiwala et al. (2009)). As CO_2 emissions continue over the 21st century, additional anthropogenic CO_2 will be transferred from the surface to the deep ocean, reducing the anthropogenic CO_2 gradient between the shallow and abyssal reservoirs. While most research to date has focused on quantifying

anthropogenic CO_2 invasion in the framework of global carbon budget considerations (e.g., Anderson et al., 1998; Khatiwala et al., 2009) or across targeted surface/intermediate waters (e.g., Bates et al., 2012; Carter et al., 2017), the penetration of anthropogenic CO_2 at the bottom of the ocean and its impact on the pH has not been extensively studied or monitored. An accurate characterization of bottom chemistry and ocean currents is needed to assess the response of carbonate-rich sediments at the seafloor to anthropogenic acidification. The presence of anthropogenic CO_2 has been reported in measurable amounts (i.e., > 4 µmol kg^{-1}) in the bottom waters of the Atlantic (Chen, 1982; Körtzinger et al., 1998; Lauvset et al., 2016; McNeil et al., 2003; Perez et al., 2018; Wanninkhof et al., 2013; Woosley et al., 2016), Pacific (Sabine et al., 2002), Arctic (Vázquez-Rodríguez et al., 2009) and Southern (Chen, 1982; Lauvset et al., 2016) Oceans. Although the presence of anthropogenic CO_2 in bottom waters at various locations is now established, no prediction of future bottom-water acidification is presently available.

In a recent study, Sulpis et al. (2018) showed that anthropogenic bottom-water acidification is now sufficiently advanced to generate significant sedimentary calcite dissolution fluxes in the north-western Atlantic and in the southern extents of the Atlantic, Pacific and Indian Oceans. Here, we use a range of Earth System and climate models to test the paradigm that seafloor calcite dissolution will grow in extent and intensify as acidification persists. To do so, we estimate how global anthropogenic dissolution fluxes at the seafloor will evolve between 2006 and 2100. Subsequently, we test the dependency of benthic dissolution rates to various variables, such as the temperature and current velocities. Finally, we discuss the need for specific observational constraints for model parameterizations.

6.2 Models

Seawater chemical variables spanning the period 2006 to 2100 were extracted from the RCP8.5 simulations of three different models from the Coupled Model Intercomparison Project Phase 5 (CMIP5): the Global Coupled Climate-Carbon Earth System Model ESM2M (Dunne et al., 2012; Dunne et al., 2013) developed at the Geophysical Fluid Dynamics Laboratory (GFDL), the IPSL-CM5A Medium Resolution Earth System Model (Dufresne et al., 2013) developed at the Institut Pierre Simon Laplace (IPSL), and the Hadley Global Environment Model 2 – Carbon Cycle (HadGEM2) (Bellouin et al., 2007; Collins et al., 2011) developed at the UK Met Office Hadley

Centre. Although numerous other CMIP5 models exist, we chose to limit our analysis to these three CMIP5 models for consistency, as they are the only CMIP5 models for which all the bottom-water variables of interest in this study were available. We used annual averages of total alkalinity (TA), dissolved inorganic carbon (DIC), *in situ* temperature (T), practical salinity (S), dissolved inorganic silica concentration ([dSi]), soluble reactive phosphate concentration ([SRP]), sinking calcite flux (F), and seawater velocity (U). We note however, that the variable [SRP] was not available for the HADGEM2C-CC simulation and set to 2 μmol kg^{-1} (Olsen et al., 2016). All model output were horizontally re-gridded onto the 1° x 1° grid of the World Ocean Atlas. For each grid cell, the deepest layer level of the model was considered to be representative of bottom waters. For each model, the bottom-water carbonate ion concentration ($[CO_3^{2-}]_{SW}$) was computed using the MATLAB version of the CO2SYS program (Pierrot et al., 2006; van Heuven et al., 2011), based on bottom-water TA, DIC, T, S, [dSi] and [SRP], using the carbonic acid dissociation constants (K^*_1 and K^*_2) from Lueker et al. (2000) and the HSO_4^- dissociation constant from Dickson (1990), while we kept track of error propagation (Orr et al., 2018). *In situ* temperature and seawater density were computed using the MATLAB version of the GSW Oceanographic Toolbox (McDougall and Barker, 2011). ***Fig. 6.1a-g*** shows the bottom water distribution of T, S, DIC, TA, [SRP], [dSi] and $[CO_3^{2-}]_{SW}$ from the CMIP5 model mean, averaged over the last 30 years of the RCP8.5 simulation (2071-2100).

6.3 Methods

As the salinity of the deep-ocean is nearly invariant and the seawater calcium concentration ($[Ca^{2+}]_{SW}$) is practically conservative (i.e., $[Ca^{2+}]_{SW}$ = f(S)), the saturation state of the deep-ocean water column with respect to calcite (Ω_C, see ***Eq. 6.2***) can simply be represented by $[CO_3^{2-}]_{SW}/[CO_3^{2-}]_{eq}$, where $[CO_3^{2-}]_{eq}$ is the seawater carbonate ion concentration at equilibrium with calcite. $[CO_3^{2-}]_{eq}$ (***Fig. 6.1h***) was estimated from the equations presented in Boudreau et al. (2010b), using $[Ca^{2+}]$ computed from S following Riley and Tongudai (1967) and the calcite stoichiometric solubility constant (K_{sp}^*) at *in situ* T, S (Mucci, 1983) and pressure (P; Millero, 1995).

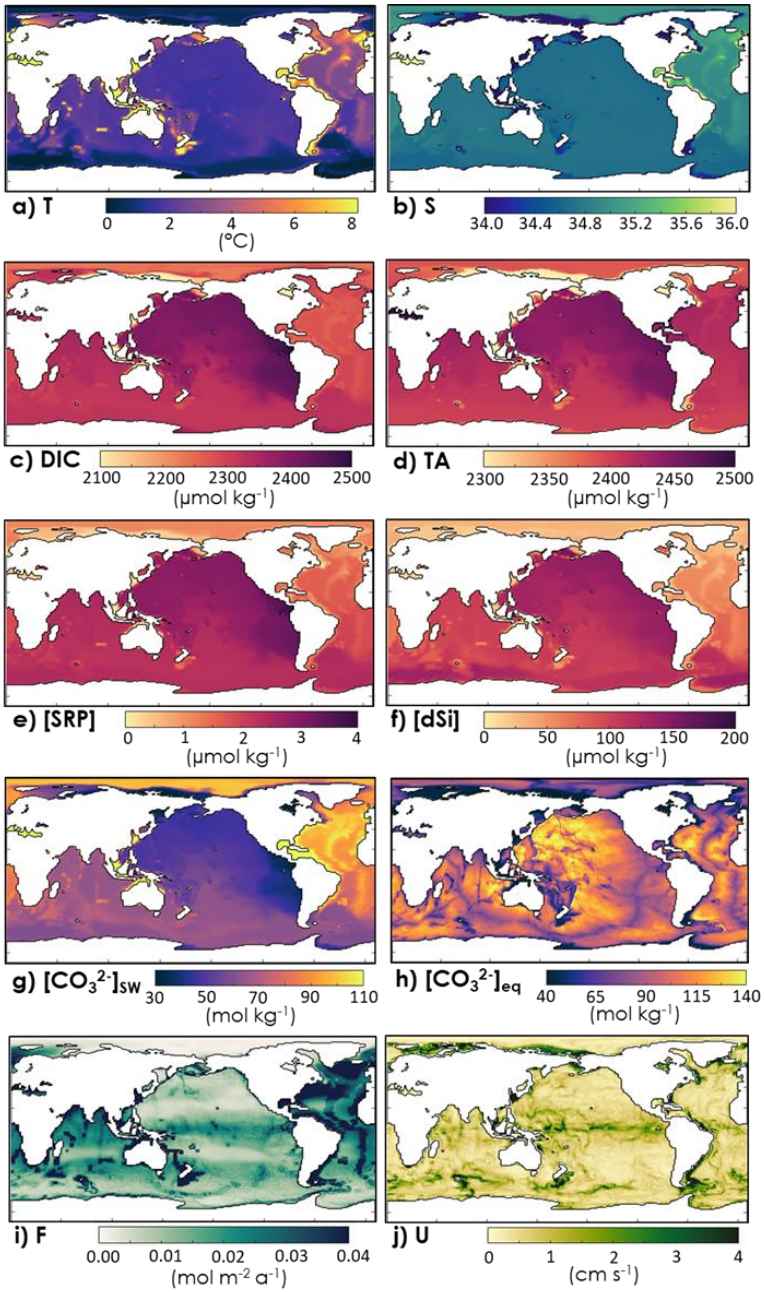

Fig 6.1 | *Modelled bottom-water (a) temperature (T), (b) practical salinity (S), (c) dissolved inorganic carbon concentration (DIC), (d) total alkalinity (TA), (e) soluble reactive phosphate concentration ([SRP]), (f) dissolved inorganic silica concentration ([dSi]), (g) carbonate ion concentration ($[CO_3^{2-}]_{SW}$), (h) carbonate ion concentration in equilibrium with calcite ($[CO_3^{2-}]_{eq}$), (i) calcite flux reaching the seafloor (F) and (j) bottom-current speed (U) averaged over the last 30 years (2071-2100) of the CMIP5 model mean under RCP8.5.*

The depth below which seawater becomes undersaturated with respect to calcite (i.e., $\Omega_C < 1$ or $[CO_3^{2-}]_{SW} < [CO_3^{2-}]_{eq}$), is referred to as the calcite saturation depth (CSD). For each model,

the CSD was computed for each year from 2006 to 2100 using seawater density, $[Ca^{2+}]_{SW}$, $[CO_3^{2-}]_{SW}$, K_{sp}^* and the equations of Boudreau et al. (2010b). Below the CSD, seawater is undersaturated with respect to calcite and dissolution should occur at a rate determined by the slowest step of the overall reaction, according to classical chemical kinetics theory (Morse and Arvidson, 2002; Naviaux et al., 2019). In the case of calcite dissolution at the seafloor, the slowest step or "kinetic barrier" controlling the rate of the reaction, is either diffusion through a diffusive boundary layer (DBL; Schlichting (1979)) at the sediment-water interface, whose thickness increases with decreasing bottom-current speed (Boudreau and Jørgensen, 2001; Dade, 1993; Steinberger and Hondzo, 1999), or processes within the sediment, such as molecular diffusion through the porewaters or reactions at the surface of the mineral grains (Boudreau, 2013; Boudreau and Guinasso, 1982; Sulpis et al., 2017). In the first case, the dissolution reaction is said to be "water-side transport-controlled" and is strongly dependent on the current speed (U) of the overlying waters. Fast bottom currents flatten the DBL and reduce the time necessary for reactants and reaction products to cross the DBL, enhancing the dissolution rate. Conversely, slow bottom currents thicken the DBL and impede the dissolution reaction. When processes within the sediment control the dissolution rate, the reaction is termed "sediment-side controlled" and is independent of the current speed. Currently, calcite dissolution is water-side transport controlled over most of the seafloor, but switches to sediment-side control in areas where sediments are calcite-poor (Boudreau, 2013; Sulpis et al., 2018). Under this formalism, the dissolution rate is expressed as the product of an overall mass transfer coefficient and a concentration gradient, i.e., the deficit in CO_3^{2-} that drives the dissolution reaction.

$$\mathbf{r = k^* \left([CO_3^{2-}]_{eq} - [CO_3^{2-}]_{SW} \right)} \quad \textbf{(6.3)}$$

where k^* is the CO_3^{2-} overall mass transfer coefficient (m a^{-1}), i.e.,

$$\boldsymbol{k^* = (k_S \beta)(k_S + \beta)^{-1}} \quad \textbf{(6.4)}$$

where k_s is the sediment-side CO_3^{2-} mass transfer coefficient (m a^{-1}) and β is the water-side (DBL) CO_3^{2-} mass transfer coefficient (m a^{-1}).

The Calcite Compensation Depth (CCD) is the depth at which the calcite dissolution rate at the sediment-water interface equals the sinking flux of calcite delivered to the seafloor, referred to as the rain rate (F; Bramlette, 1961; Edmond, 1974). At steady state (e.g., pre-industrial

conditions), sediments are calcite-free below the CCD. Since the beginning of the industrial revolution, as anthropogenic CO_2 spreads through the deep oceans, the oceans are no longer at a steady state, and both the CCD and CSD have been shoaling (Boudreau et al., 2010a; Feely et al., 2002; Sulpis et al., 2018). As the CCD shoals, calcitic particles reaching sediments between the rising CCD and the pre-industrial CCD dissolve completely at the sediment-water interface, but the underlying sediments, although now sitting below the CCD, will not become calcite-free for several tens of thousands of years, far beyond the time scale over which this study is focusing (Boudreau and Luo, 2017). Below the CCD, calcite does not accumulate in sediments because F is compensated entirely by dissolution. Thus, below the CCD:

$$\mathbf{r = F}. \qquad \textbf{(6.5)}$$

For sediments between the pre-industrial CCD and the rising CCD, the net dissolution rate is given by the sum of the carbonate rain rate and the dissolution rate of sediments previously deposited or the sum of ***Eqs. 6.3*** and ***6.5***:

$$\mathbf{r = F + } \boldsymbol{k^*} \left(\mathbf{[CO_3^{2-}]_{eq} - [CO_3^{2-}]_{SW}} \right). \qquad \textbf{(6.6)}$$

Above the contemporary CCD, the rate is computed using ***Eq. 6.3***. Here, we use the pre-industrial CCD values from Sulpis et al. (2018), that are based on measured $CaCO_3$ sediment contents, and initially set the 2006 CCD values to the present-day CCD values computed by Sulpis et al. (2018). For each CMIP5 model, the CCD is subsequently allowed to fluctuate freely throughout the 21st century as the simulated seawater chemistry (i.e., $[CO_3^{2-}]_{SW}$), F and k^* evolve in time according to the equations described in Boudreau et al. (2010b). Because the initial CCD values were computed from basin-averaged sediment-$CaCO_3$ content profiles (see Sulpis et al., 2018), CCD predictions are only relevant where the sediment-$CaCO_3$ distribution is controlled by vertical dissolution/deposition fluxes rather than lateral accumulation (i.e., $CaCO_3$ from turbidites or rivers). Because the Southern and Arctic Oceans appear to fall in the category of lateral-transport dominated regions, and because of the lack of data in these regions, we exclude from our analysis the Southern and Arctic Oceans (below 60 °S and above 60 °N, respectively) and the seafloor shallower than 300 m. F, the calcite rain rate (see ***Fig. 6.1i***), was taken as the deepest simulated sinking calcite flux, expressed in mol m^{-2} a^{-1}, that we assume to be representative of the calcite flux reaching the seafloor.

β (see ***Eq. 6.4***) was derived from the *in-situ* diffusion coefficient of CO_3^{2-} (Zeebe, 2011), the *in-situ* molecular kinematic viscosity of seawater and bottom-current speeds (U) for each model, using the equations presented in Sulpis et al. (2018). U was computed from annual averages of the horizontal current velocities in the deepest layer of each CMIP5 model under the RCP8.5 scenario. Models cannot resolve eddies or other oceanic currents that are smaller than a grid cell size (~100 km in most models). Nevertheless, unresolved currents can be parameterized, e.g., by the Gent and McWilliams schemes that most models use (see Gent and McWilliams, 1990; Griffies, 1998). Models simulate the concentration of dissolved species (e.g., DIC) using the sum of both resolved and parameterized oceanic transport. Unfortunately, only resolved current speeds were available in the model output. Thus, the U values reported here represent the velocities as resolved by the models. This point will be addressed in more details in ***section 6.5.2***. The CMIP5 model mean U averaged over the last 30 years of the simulations is presented in ***Fig. 6.1j*** and the resulting β distribution is shown in ***Fig. 6.10***. Since β is dependent on seawater viscosity, it is impacted by seawater T and S changes. β was allowed to evolve as a function of U, T and S between 2006 and 2100, and the impacts of this changing β on the dissolution rates were quantified. k_S, the sediment-side mass transfer coefficient, was computed from the $CaCO_3$ content of the sediments, taken from Sulpis et al. (2018), and set constant throughout the analysis timeframe. The resulting end-of-the-century k_S and the overall mass transfer coefficient k^*, computed from ***Eq. 6.4***, are shown in ***Fig. 6.10***.

6.4 Results

6.4.1 Modeled changes in bottom-water properties under the RCP8.5 scenario

We present the changes (Δ) in bottom-water T, S, DIC, TA, SRP, dSi, U and F between the first 30 years (2006-2035) and the last 30 years (2071-2100) of the CMIP5 model mean, under the RCP8.5 scenario (***Fig. 6.2***). A Mann-Kendall trend test (Kendall, 1975; Mann, 1945) is applied to each CMIP5 model mean time series. This test identifies whether there is a consistently increasing or decreasing monotonic trend. Hence, we wish to note that inter-annual variations or trend changes occurring at the end of the simulation might cause the hypothesis that there is a trend rejected. The sign of the trend for each variable is depicted in ***Fig. 6.2*** and statistics associated with each trend test are reported in ***Table 6.1***.

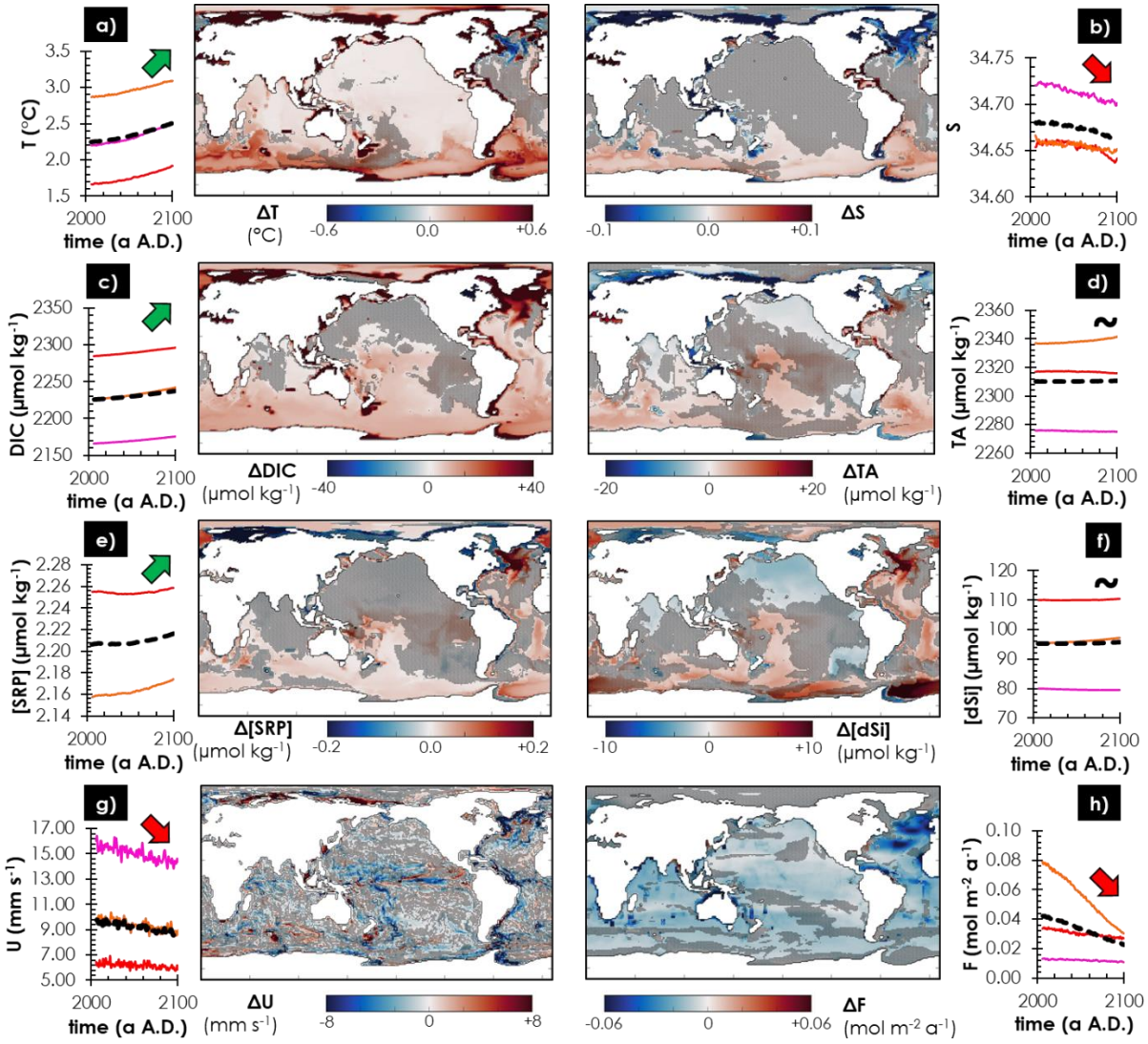

Fig 6.2 | *Changes (Δ) in bottom-water (a) temperature (ΔT), (b) practical salinity (ΔS), (c) dissolved inorganic carbon concentration (ΔDIC), (d) total alkalinity (ΔTA), (e) soluble reactive phosphate concentration (Δ[SRP]), (f) dissolved inorganic silica concentration (Δ[dSi]), (g) bottom-current speed (ΔU) and (h) calcite flux to the seafloor (ΔF) between the first 30 years (2006-2035) and the last 30 years (2071-2100) of the CMIP5 model mean. Each map is associated with an adjacent plot that shows the annual mean of the globally averaged variables in the CMIP5 model mean (black dashed line), ESM2M (orange line), HadGEM2 (pink line) and IPSL (red line) mean value between 2006 and 2100. Qualitative results from Mann-Kendall trend tests performed on the world averaged CMIP5 model mean values between 2006 and 2100 are also shown as green arrows for statistically significant increasing trends, red arrows for statistically decreasing trends, and tilde symbols for diverging trends.*

According to the CMIP5 model mean temperature prediction, an important warming of bottom waters occurs near the continents, where the seafloor is shallow, and in the Southern Ocean. Conversely, the bottom-water temperatures in the northwestern Atlantic display a sharp cooling of ~0.6 °C by the end of this century, which is in agreement with the current abyssal cooling trend in this basin (Desbruyères et al., 2016). We speculate that this is likely attributable to the decline in the meridional overturning circulation strength because the overturning cell becomes shallower, which allows less heat to be transported from the surface to the abyss (Purkey and Johnson, 2010, 2012). Globally, under the RCP8.5 scenario, the mean bottom-water temperature is projected to increase ~ 0.2 °C between the first and the last 30 years of the century. With respect to the salinity, an important freshening of bottom waters is predicted in high boreal latitudes, while bottom-waters in the Southern Ocean become saltier, in line with the results from Heuzé et al. (2015). Recent studies that have reported a current freshening of the Antarctic Bottom Waters (AABW) based on hydrographic data because of glacial melting (Menezes et al., 2017; Purkey and Johnson, 2013). We note that warmer and saltier AABW would be consistent with reduced ventilation in this area, as predicted by ESM2M (***Fig. 6.11***), because deep convection brings relatively cold and fresh waters at the bottom.

Global bottom-water DIC rises by an average of 9 µmol kg^{-1} (i.e., a 0.4% relative to the global CMIP5 model mean) between the first and the last 30 years of simulation. Some of the largest bottom-water DIC increases are predicted to occur in the northern Atlantic, where the bottom waters are youngest (Huiskamp and Meissner, 2012; Matsumoto, 2007) and rich in anthropogenic CO_2. In the Labrador Sea and at the southern edge of Greenland, the DIC increases are as high as +70 µmol kg^{-1} (i.e., a ~3% increase relative to the local CMIP5 model mean). We also note an acute DIC addition along the western fringe of the Atlantic and Pacific Oceans. A weaker but more spatially extended DIC increase (+ ~10 µmol kg^{-1}) in the southern half of the globe is predicted, that we attribute partly to the northward spreading of the dense and young Antarctic Bottom Waters (de Lavergne et al., 2017; Gebbie and Huybers, 2012). The elongated positive DIC anomaly in the low latitudes of the Pacific Ocean (i.e., between Peru and Melanesia) is driven by an accumulation of metabolic CO_2, as an increase in both the age of bottom waters (see ***Fig. 6.11***) and the particulate organic carbon sinking flux (see ***Fig. 6.12***) is predicted in this area. Older bottom waters may reflect weakened bottom currents (discussed later) and/or reduced bottom-water renewal. Older bottom waters accumulate more metabolic products (nutrients, DIC)

resulting from the oxic catabolism of material sinking from above, explaining the positive anomaly in TA, DIC, [SRP] and [dSi] in the equatorial Pacific, Southern Ocean and Northern Atlantic.

Under the RCP8.5 scenario, the global mean bottom-water TA is stable, increasing by only ~0.5 µmol kg^{-1} during the 21st century. Potential sources for TA include $CaCO_3$ dissolution and the addition of nutrients (SRP or dSi) to seawater. In fact, bottom-water SRP and dSi concentrations strongly increase in the Atlantic Ocean, while they decrease in the Arctic Ocean, as seen in ***Fig. 6.1e-f***, and the relative changes in TA, SRP and dSi are highly correlated in most of the bottom waters, as shown in ***Fig. 6.13***.

The modelled changes in U are spatially highly heterogeneous, as displayed in ***Fig. 6.1g***, making it challenging to identify coherent regional changes. Nevertheless, in a warm and high-CO_2 world, the CMIP5 model mean U globally declines by ~8% by the end of the century. Bottom currents weaken notably near the Equator and Northern Atlantic, and by up to 70% by the end of the century off-shore Newfoundland. Finally, the downward flux of calcite reaching the seafloor, F, is predicted to show a ubiquitous decline. The CMIP5 model mean F value decreases by 35% by the end of the 21st century. We attribute this abated F to a reduced surface export and increased water-column $CaCO_3$ dissolution. Although the absolute F drop is stronger at low latitudes, where the $CaCO_3$ rain rate is highest, the relative F decline is more important at high latitudes.

Excluding high latitudes, we find that at the end of this century (i.e., average 2071-2100), the CMIP5 model mean CSD will be 2041 m, 146 m shallower than the 2006-2035 averaged value. In comparison, Sulpis et al. (2018) computed a CSD rise of 142 m between the end of the preindustrial period (i.e., 1800) and 2002. These results suggest that the CSD rise is accelerating as we go further into the Anthropocene.

6.4.2 Calcite dissolution rate

At the end of the 21st century, the fastest benthic $CaCO_3$ dissolution occurs in the equatorial Pacific (***Fig. 6.3a***), where bottom waters are strongly undersaturated with respect to calcite, sediments are rich in $CaCO_3$ and bottom currents are fast (see ***Fig. 6.1*** and ***Fig. 6.10***). In the eastern equatorial Pacific, meridional shifts in bottom currents cause abrupt changes in the benthic dissolution rates. In the northern half of the central Pacific, between the Fiji Plateau and the

Aleutian Trench, we observe a large area of reduced r, explained primarily by a drop in F (***Fig. 6.4b***). In this area, except for the Hawaiian archipelago, the seafloor is located below the CCD. Thus, the calcite dissolution rate at the seafloor is constrained by the calcite rain rate, according to ***Eq. 6.5***, regardless of any DBL limitation and, thus, independent of bottom currents. The same is true for the southern extents of the Atlantic, Pacific and Indian Oceans, where most of the seafloor is below the CCD, and seafloor dissolution depends only on rain rate changes. The deep Atlantic Ocean does not display, according to our computed dissolution rates, any increase in benthic calcite dissolution rate between 2006-2035 and 2071-2100 (***Fig. 6.3b***) but, instead, a dissolution rate decrease in the abyssal plains on each side of the Atlantic ridge, in the Argentinian continental shelf and in the Gulf of Mexico, attributed to a bottom-current slowdown and an associated decrease in β. Although a large amount of anthropogenic CO_2 enters the deep ocean in the North Atlantic, this CO_2 does not spread in the deepest layers of the abyssal Atlantic (see ***Fig. 6.2***). In fact, most of the seafloor in this basin is covered by colder and denser AABW (Johnson, 2008; Morozov et al., 2010), nearly devoid of anthropogenic CO_2 except for its most southern extent (Ríos et al., 2015). It may take several centuries for the AABW to reach the Equator in the Atlantic Ocean basin (Huiskamp and Meissner, 2012).

Isolating the effect of each of the variables on the overall benthic dissolution rate (***Fig. 6.4a***), we see that while increasing bottom-water DIC globally drives the dissolution rate up during the 21st century, bottom-water total alkalinity (TA), bottom-current speeds (U) and calcite rain rates (F) lower the dissolution rate. A reduction in the calcite flux reaching the deep-ocean (F) leads to a lower dissolution rate below the CCD, according to ***Eqs. 6.5*** and ***6.6***, and causes the CCD to rise much faster (Boudreau et al., 2010b). We estimate that the CMIP5 model mean world-averaged CCD will rise from 4465 ± 396 m at the beginning of the 21st century to 3742 ± 811 m by the end of the century - a 723 ± 902 m shoaling in less than a century. Changes in F dominate the 21st century benthic dissolution rate variations mainly over high latitudes and deep abyssal plains, as these areas are for the most part below the CCD. DIC- and TA-driven dissolution rate changes are more important is shallower areas, corresponding to topographic highs or coastal areas, as shown in ***Fig. 6.4b***. Finally, the global decrease in CMIP5 model mean bottom-current speeds increases the average DBL thickness and leads to a general slowdown of the calcite dissolution rate at the seafloor. Dissolution rate reduction due to bottom-current changes is important at low latitudes and in the Atlantic Ocean (***Fig. 6.4b***), where the bottom-current

slowdown is greatest (***Fig. 6.2g***). Globally, throughout the 21st century and under RCP8.5, the calcite rain rate (F) and bottom-current speed (U) govern the seafloor calcite dissolution rate changes over 47% and 36% of the dissolving seafloor (i.e., the area of the seafloor overlain by undersaturated bottom waters), respectively. Other factors, such as DIC and TA, predominate the calcite dissolution changes over much smaller portions of the seafloor (11% and 6%, respectively). Isolating the effect of T, S, [SRP] and [dSi], we note that none of these factors exert a strong enough influence on the benthic dissolution rate to influence its global value, as each impact the rate by less than 1% throughout the 21st century.

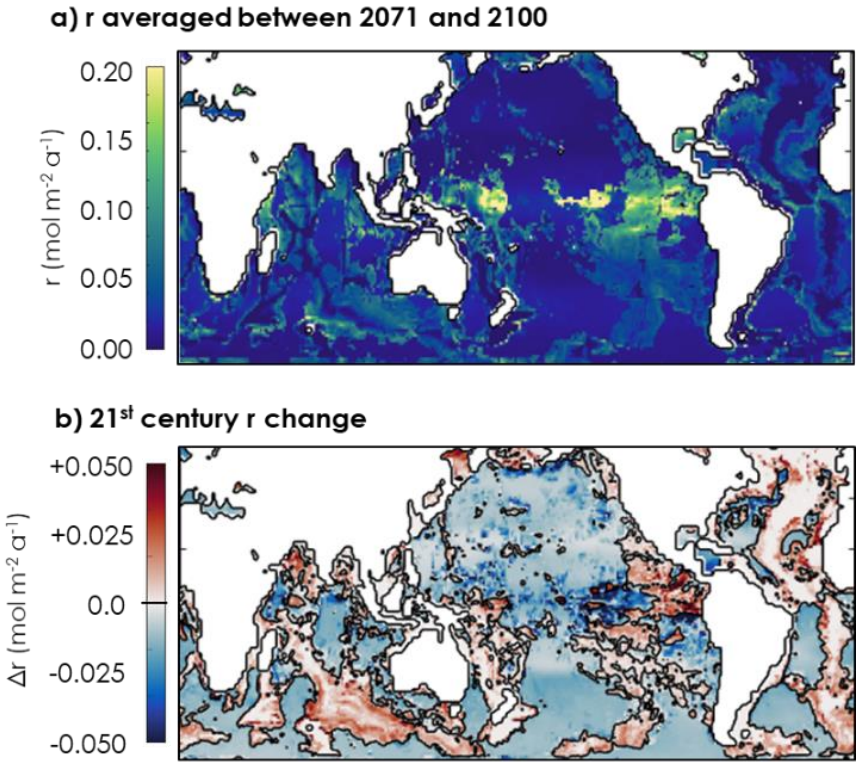

Fig 6.3 | *Predicted (a) calcite dissolution rate (r) at the sediment-water interface averaged between 2071 and 2100 and (b) change in the dissolution rate (Δr) between the first 30 years and the last 30 years of the simulation.*

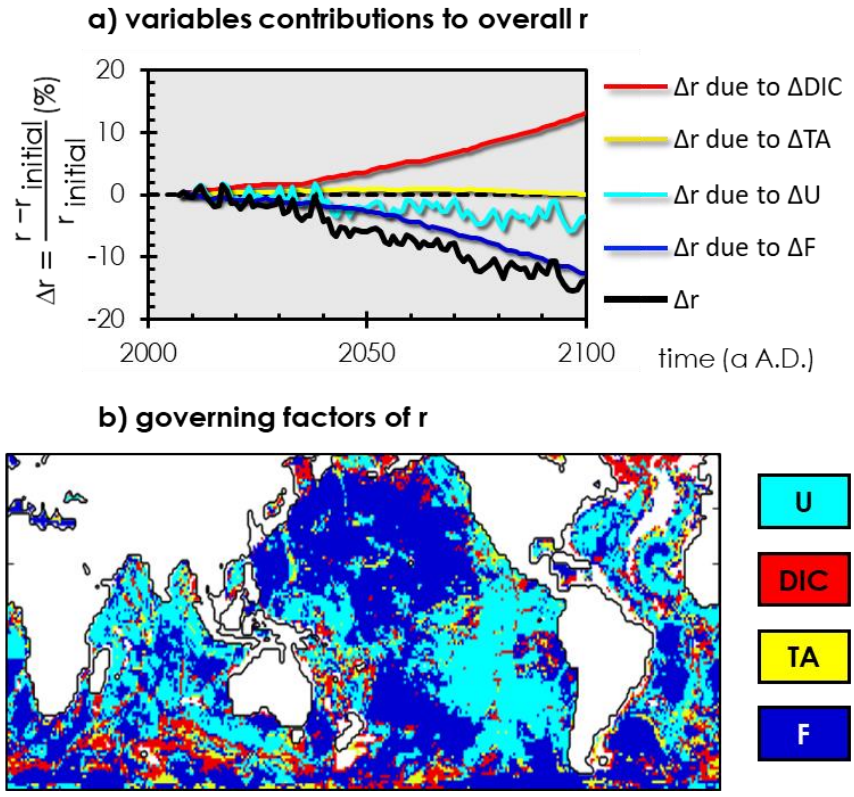

Fig 6.4 | *Modelled (a) Temporal evolution of the CMIP5 model mean global-averaged benthic dissolution rate anomaly (Δr) and the respective contribution of U (light blue), DIC (red), TA (yellow) and F (dark blue) to the dissolution rate anomaly. Respective contributions of each variable were estimated by computing the dissolution rate through time when all variables are kept constant throughout the 21st century, except the variable whose contribution is to be isolated. The dashed, black line represents the dissolution rate in 2006, at the beginning of the simulation. (b) Geographical distribution of primary driver of the benthic dissolution rate, i.e., variables with the highest correlation coefficient (R^2) resulting from a multiple multivariate linear regression of r over U, DIC, TA and F.*

6.5 Discussion

6.5.1 Formulating calcite dissolution in sediments

Our dissolution rate model does not include oxic or anoxic respiration-driven dissolution. In ***Fig. 6.5***, we provide a comparison of our 2006-2035 dissolution rates with those obtained by Dunne et al. (2012). The model developed by Dunne et al. (2012) accounts for organic matter respiration within the sediments (and metabolic CO_2 production), which can locally reduce the porewater calcite saturation state and trigger dissolution regardless of the water column chemistry (Archer, 1996; Mekik et al., 2002; Hales, 2003). As our dissolution rate computations do not

consider metabolic dissolution, our model underestimate dissolution relative to the results of Dunne et al. (2012) in areas of high organic carbon fluxes to the bottom (***Fig. 6.5d***). In such areas, changes in organic carbon fluxes in the future (e.g., see ***Fig. 6.12***) could affect calcite dissolution in sediments. Similarly, other factors such as changes in bottom-water temperature or oxygen concentration could influence the activity of burrowing organisms, enhancing or impeding bioirrigation or bioturbation, processes that can locally exert a strong control on porewater solute distribution and fluxes across the sediment-water interface (Boudreau and Jørgensen, 2001; Meysman et al., 2006; Teal et al., 2008). Regrettably, due to the absence of observations on ongoing changes in deep-sea burrowing organism activity and/or in benthic organic carbon fluxes, we are unable to go expand further without speculation. On the other hand, the model of Dunne et al. (2012) does not take into consideration the presence of a DBL above the sediment-water interface, irrespective of the overlaying current speed. Most sediment models published to date either ignore the presence of a DBL above the sediment-water interface (van Cappellen and Wang, 1996; Archer et al., 2002; Hales, 2003; Munhoven, 2007; Tschumi et al., 2011) or consider a DBL with a thickness set to a constant arbitrary value (Boudreau, 1996; Heinze et al., 1999). Instead, the DBL thickness should be expressed as a function of current-speed, as formulated by various authors (Boudreau and Guinasso 1982; Levich 1962; Higashino and Stefan 2004; Sulpis et al., 2019) and confirmed by experimentalists (Larkum et al. 2003; Lorke et al. 2003; Santschi et al. 1983; Santschi et al. 1991). As shown in ***Fig. 6.5***, the present study, which uses a current-speed dependent DBL thickness, predicts dissolution rates that are higher than those from Dunne et al. (2012) in areas of fast bottom currents. Future research efforts should focus on developing sediment modules representing both organic carbon degradation and mass transfer through a DBL of variable thickness.

Integrating our beginning-of-the-century dissolution rates (***Fig. 6.5a***) over the seafloor surface, we find that 8.71 Tmol of $CaCO_3$ dissolve each year at the sediment-water interface, while using the data of Dunne et al. (2012; see ***Fig. 6.5b***), we estimate that 12.96 Tmol of $CaCO_3$ are dissolved each year within marine sediments. These values represent only 7.1 and 10.6 %, respectively, of the total pelagic $CaCO_3$ dissolution estimated by Smith and Mackenzie (2016). In comparison, Berelson et al. (2007) and Sulpis et al. (2018) estimated the modern seafloor calcite dissolution flux at 33 ± 25 and 32 ± 12 Tmol a^{-1}, respectively. Based on CMIP5 bottom current speed, the CMIP5 model mean DBL thickness is ~1.3 cm. This is 10 to 20 times thicker than for

typical deep-sea DBLs (Santschi et al., 1991; Boudreau and Jørgensen, 2001; Sulpis et al., 2018). A possible cause for this DBL thickness overestimation would be an underestimation of the benthic bottom current speeds simulated by models. Overestimating the DBL thickness in a model where the dissolution is limited by diffusion through the DBL, such as ours, implies underestimating the true dissolution rate, and may explain the discrepancy in the magnitude of the global $CaCO_3$ dissolution identified here. In the following discussion, we investigate the bottom current representation in models and correct our dissolution rate estimates accordingly.

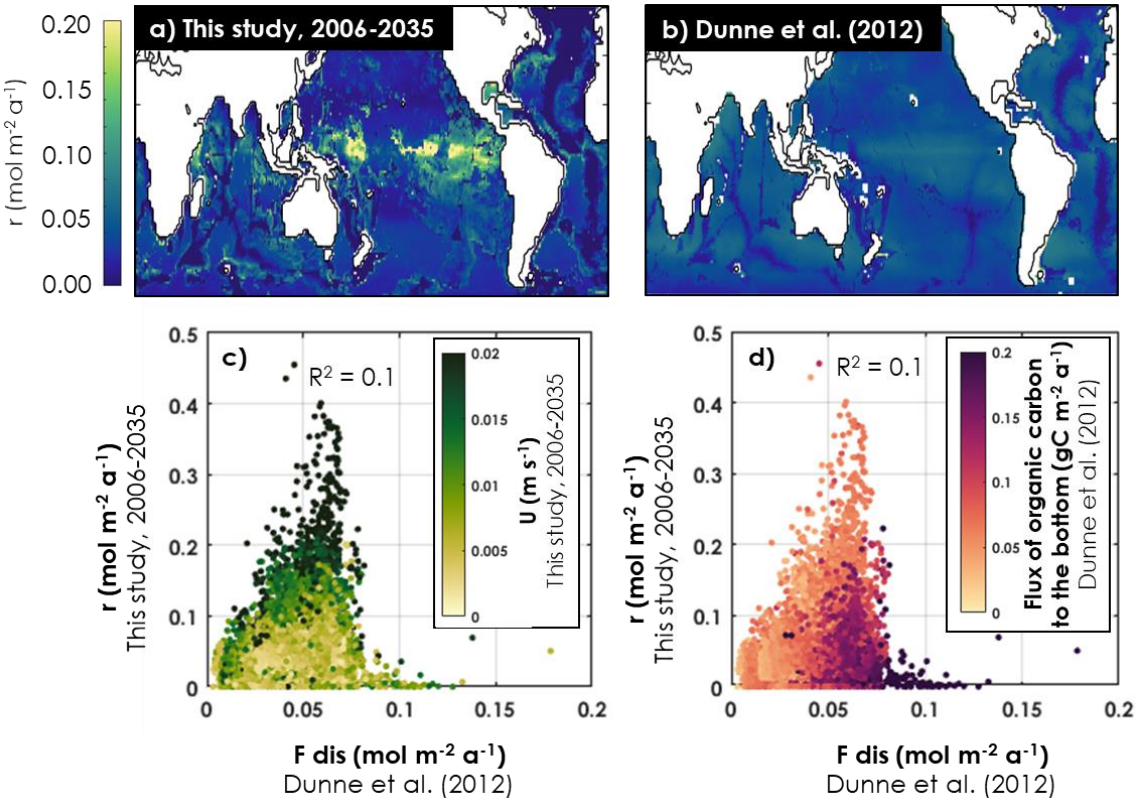

Fig. 6.5 | *Comparison between (a) the CMIP5 model mean dissolution rate from this study (r) averaged between 2006 and 2035, with (b) the dissolution rates from Dunne et al. (2012) that we term F_{dis}. The F_{dis} values from Dunne et al. (2012) were computed by subtracting their final modelled calcite burial flux to their final modelled calcite bottom flux. Hence, F_{dis} does not necessarily represents the dissolution rate of calcite at the sediment-water interface, but rather the fraction of the calcite flux to the bottom that is being dissolved either at the sediment-water interface, or within the sediment porewaters. Scatter plots compare (c) r values from this study with (d) F_{dis} values from Dunne et al. (2012). U is from the CMIP5 model mean. The flux of organic carbon to the bottom is taken from Dunne et al. (2012). The correlation coefficients (R^2) describing the agreement between r and F_{dis} values are also shown.*

6.5.2 Bottom currents

In order to accurately estimate the response of the seafloor to future climate changes, a reliable representation and prediction of the bottom-current speeds is required in models. To get a sense of the accuracy of the bottom-current speeds predicted by models, we use a new compilation of current meter data that we compare to model-predicted bottom currents. To compare the bottom-current evolution throughout the 21st century across different coarse resolution (~1° x ~1°) models, we used the bottom-current speeds under RCP8.5 from HadGEM2, IPSL CM5A-MR and GFDL ESM2M, as shown in ***Figs. 6.1j*** and ***6.2g***. The current-speed spread between these models is thereafter termed CMIP5-intermodel spread. In addition, to evaluate the impact of model horizontal resolution on the representation of bottom-current speeds, we compared results from three climate models of different resolution, namely CM2.6 (Griffies et al., 2015; Winton et al., 2014), which uses a 1/10th degree horizontal resolution, CM2.5 model (Delworth et al., 2012), with a 1/4th degree horizontal resolution, and CM2-1deg (Griffies et al., 2015), with a 1 degree horizontal resolution. The CM2-O models are run under an atmospheric partial pressure of CO_2 (pCO_2) increase of 1% per year for 70 years starting at 286 ppm. This idealized CO_2 concentration scenario is similar to the RCP8.5 scenario used in the three CMIP5 models used in this study. Finally, we also used four simulations from the HYbrid Coordinate Ocean Model (HYCOM; Trossman et al., 2016 - note that these simulations are of the present-day ocean only). Two of the HYCOM simulations were run in a 1/12th degree global configuration, and two were run in a 1/25th degree configuration, with each configuration comprising one simulation that included a parameterized topographic internal lee wave drag, and another simulation without it, as described in Trossman et al. (2016). "Wave drag" here refers to the momentum sink associated with the generation of internal lee waves, and accounts for a possible blocking effect when the geostrophic flow impinges upon rough topography, based on the theory of Garner (2005) and applied as described in Trossman et al. (2013).

The current-meter dataset contains measurements obtained from Trossman et al. (2016) and Luecke et al. (2017). A low-pass filter was applied to each current-meter record, and only records containing a minimum of 105 days of observations were considered, following Timko et al. (2013). In each unique location, measurements within 500 meters of the seafloor were averaged and considered to be representative of bottom currents, for comparison with bottom-current values

simulated by models. We chose to average current-meter measurements over the bottom 500 meters because these values are close to the vertical resolution in the deepest layers of the models, where the current speed comparison takes place. There is a trade-off between the number of observations available, decreasing as we get closer to the seafloor, and the representativeness of the current speeds farther from the seafloor. An upper boundary at 500 meters above the seafloor allows us to resolve an entire model layer as well as to have a reasonably large number of current-meter observations. Using only the data at locations where at least 2 instruments were available within the bottom 500 meters, with seafloor depths exceeding 1000 meters, our current-meter dataset comprises measured current speeds over 378 locations.

Fig. 6.6a-b summarizes the results of the inter-comparison of bottom-current predictions in the 6 models run under an increasing atmospheric pCO_2 scenario. A Mann-Kendall trend test (Kendall, 1975; Mann, 1945) reveals a statistically significant negative world-averaged bottom-current speed trend for all the models (see ***Table 6.2***), for bottom waters deeper than 1 km and between 60°S and 60°N. On average, the six models simulated the world-averaged U to drop by 6.8 ± 3.9 % when reaching a doubling of preindustrial atmospheric pCO_2. As shown in ***Fig. 6.6b***, all models predict a bottom-current slowdown in several areas of the North Atlantic, the Equatorial Atlantic and most of the Pacific Ocean, consistent with the results of Cheng et al. (2013). Recent studies have reported a weakening of the Atlantic meridional overturning circulation (AMOC) and a reduced ventilation in the North Atlantic (Caesar et al., 2018; Pérez et al., 2013; Steinfeldt et al., 2009; Thornalley et al., 2018; Wanninkhof et al., 2010; Zhang, 2008). Collins et al. (2013) estimated that the strength of the AMOC will drop by 12-54% during the 21st century under RCP8.5. Likewise, it has been shown that anthropogenic-driven surface-water freshening in the Southern Ocean might cause a weakening in the production of AABW (de Lavergne et al., 2014).

Although the trend of decreasing bottom-current over this century is a consistent feature across CMIP5 and CM2-O models, a comparison of these modelled bottom velocities with current-meter observations shows that below 1 km-depth, where most calcite dissolution occurs, these models consistently underestimate bottom-current speeds (***Fig. 6.7***). Only the HYCOM simulations successfully reproduce bottom-current speeds with a magnitude similar to the observations (***Fig. 6.7***). Nevertheless, the correlation coefficients of the simulated U to the measurements for the HYCOM simulations are lower than for the CMIP5 and CM2-O models

(***Fig. 6.8***). The correlations between the higher resolution models and the current meter observations are not expected to be as high as for the coarser resolution models because of the increasing difficulty of locating intensified currents exactly where they really occur. In fact, the correlations between the higher resolution models and the current meter observations increase when the higher resolution model output is smoothed and placed on the same grid as the coarser resolution models.

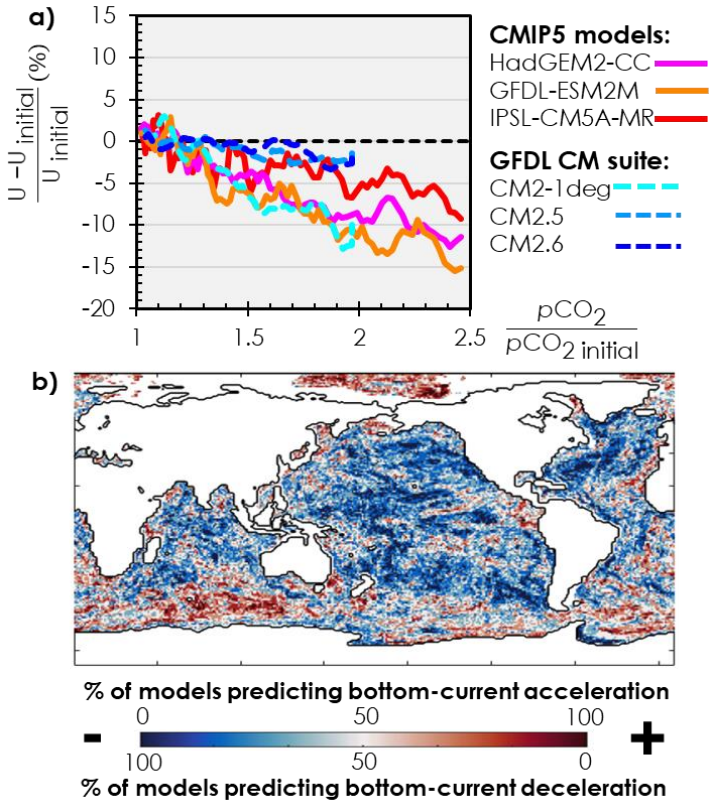

Fig 6.6 | *Inter-comparison of the modelled resolved bottom-current speed response of 6 Earth System and climate models to atmospheric pCO_2 accumulation. (a) Modelled, world-averaged relative bottom-current speed changes as a function of relative change to increasing atmospheric pCO_2 for bottom waters deeper than 1 km and between 60°S and 60°N. $U_{initial}$ is the average over the 30 first years for each model. U is the CMIP5 model mean bottom-current speed. $pCO_{2\,initial}$ is the world-averaged atmospheric pCO_2 for the first year of each simulation. pCO_2 values for the models under the RCP8.5 scenario are taken from Meinshausen et al. (2011). The solid lines represent running averages over a 5-year period. The dashed black line indicates the baseline. (b) Sign of the bottom-current speed change between the first 30 years and the 30 last years of the 6 simulations. The dark blue end of the colorbar represents a case where all 6 models predict a bottom-current speed decrease and the dark red end is for a case where all 6 models predict a bottom-current speed increase.*

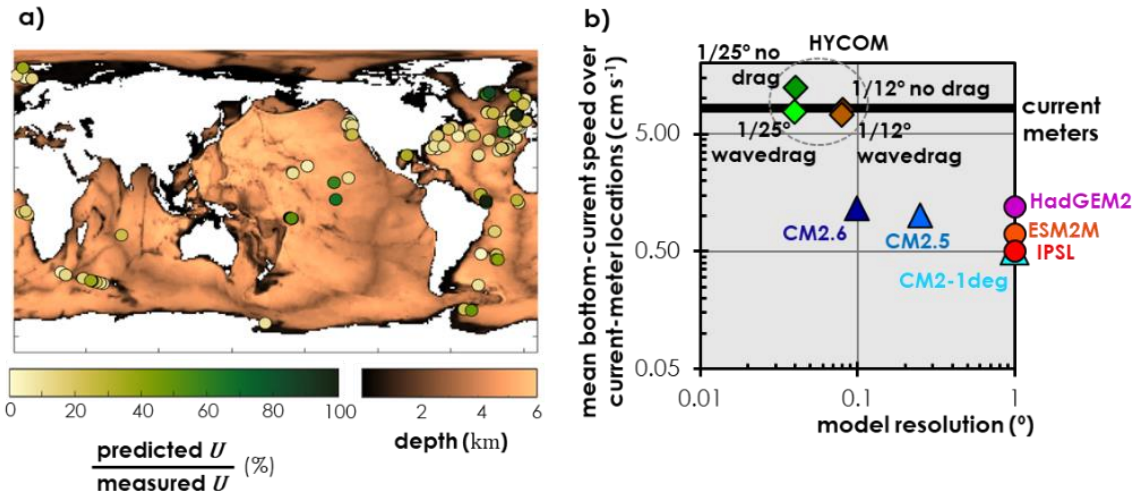

Fig 6.7 | *Comparison of the resolved bottom-current speeds between models and observations. (a) Ratio of the current speed from CMIP5 model mean by that from current-meters. (b) Bottom current speeds averaged over 378 current-meter locations deeper than 1 km in the three CMIP5 models, three CM2-O models and four configurations of the HYCOM model (see* ***section 6.5.2*** *for description of the models) as a function of the model resolution. The black thick line represents the current-meter average. For simplicity, the CMIP5 models are considered to be of the order of 1° x 1° resolution.*

Mesoscale eddies carry a large proportion of the flow from the surface to the bottom and these are only resolved for ocean models with horizontal resolution higher than about 1/5th degree at ~30 °N or S, 1/10th degree at ~60 °N or S (Hecht and Hasumi, 2008; Hallberg, 2013). Thus, the three CMIP5 models used in this study have a horizontal resolution that is too coarse to resolve explicitly these eddies and, instead, these models rely on a parameterization to represent the mesoscale eddy transport (see Gent and McWilliams, 1990; Griffies, 1998). In addition, the use of geopotential height vertical coordinates requires additional schemes to accurately represent bottom-following flows (e.g., (Adcroft et al., 1997)) and can result in their misrepresentations (Dunne et al., 2012). In ***Fig. 6.14***, we show that, in CM2-1deg, the parameterized bottom-current speeds associated with the mesoscale are generally less than 5% of the resolved current speeds, except in high latitudes. Thus, it is unlikely that the unresolved, parameterized flows account for the order of magnitude discrepancy between the coarse resolution models and the current-speed observations. Pearson et al. (2017) found that reduced water viscosity in models leads to stronger bottom currents. The bottom-current speed underestimation by CM2.6 is surprising, given its relatively high resolution, and we speculate, based upon the Pearson et al. (2017) results, that the differences between CM2.6 and the HYCOM simulations might be due to different viscosity

coefficients (see e.g., Griffies and Hallberg (2000) and Wallcraft et al. (2005)), or methods of applying bottom-drag. We also note an increasing trend in the world-averaged resolved bottom-current speed as model resolution is refined in the CM2-O suite, i.e., the higher the resolution, the faster the bottom currents, as shown in ***Fig. 6.7b***.

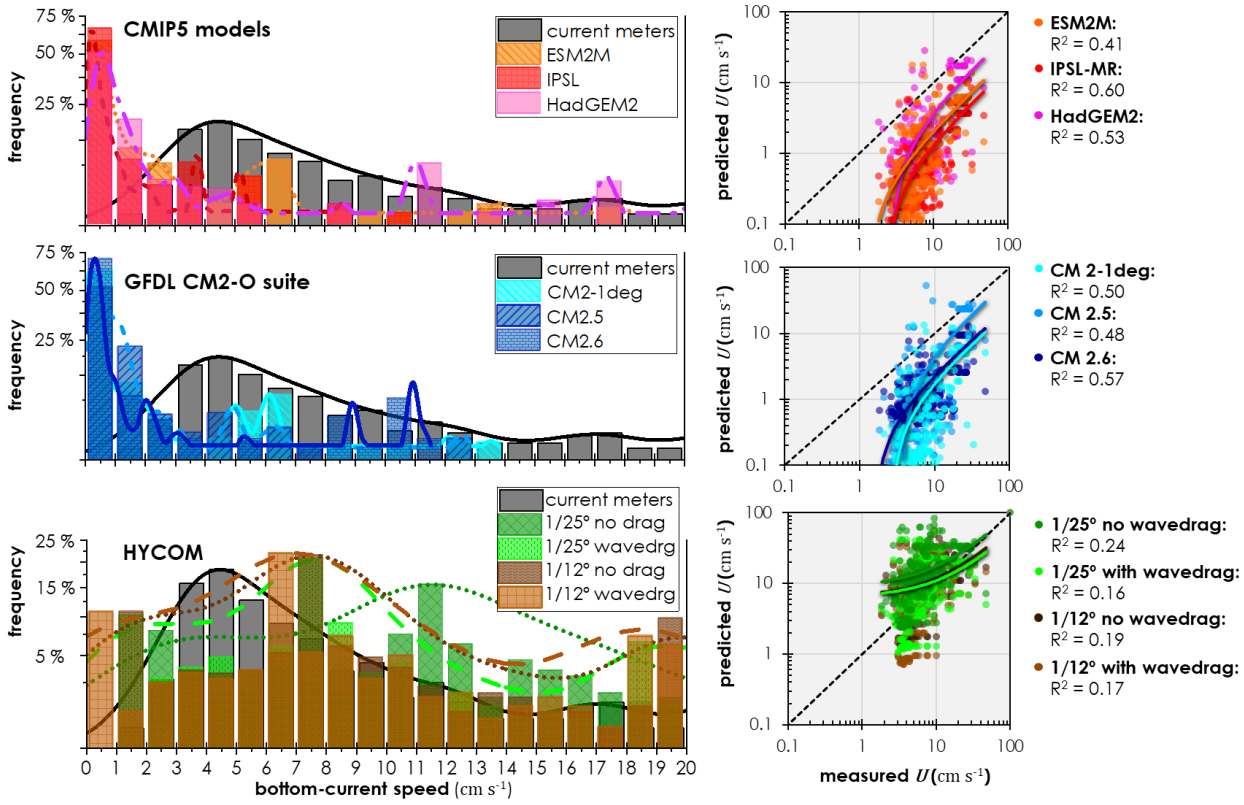

Fig. 6.8 | *(Left) Histograms of the distribution of resolved bottom-current speeds corresponding to the 378 current-meter sites deeper than 1 km. Lines represent kernel density functions. (Right) Correlation diagrams between measured bottom-current speeds (U) and model-simulated values. Correlation coefficients (R^2) are shown for each model.*

6.5.3 Global $CaCO_3$ estimates

The strong underestimation of bottom-current speeds provided by the models directly impact the representation of the benthic DBL and, hence, the calcite dissolution rate. Scaling up or down the CMIP5 model mean bottom-current speeds by a constant factor, we evaluate the sensitivity of the global modelled seafloor calcite dissolution rate to the world-averaged bottom-current speed (***Fig. 6.9a***). When the CMIP5 model mean U is scaled up to the current-meter level,

the estimated amount of calcite dissolved at the seafloor rises from 8.7 Tmol a^{-1} to 30.4 Tmol a^{-1} when averaged over the first 30 years of the simulation, which is in good agreement with the results of Berelson et al. (2007) and Sulpis et al. (2018).

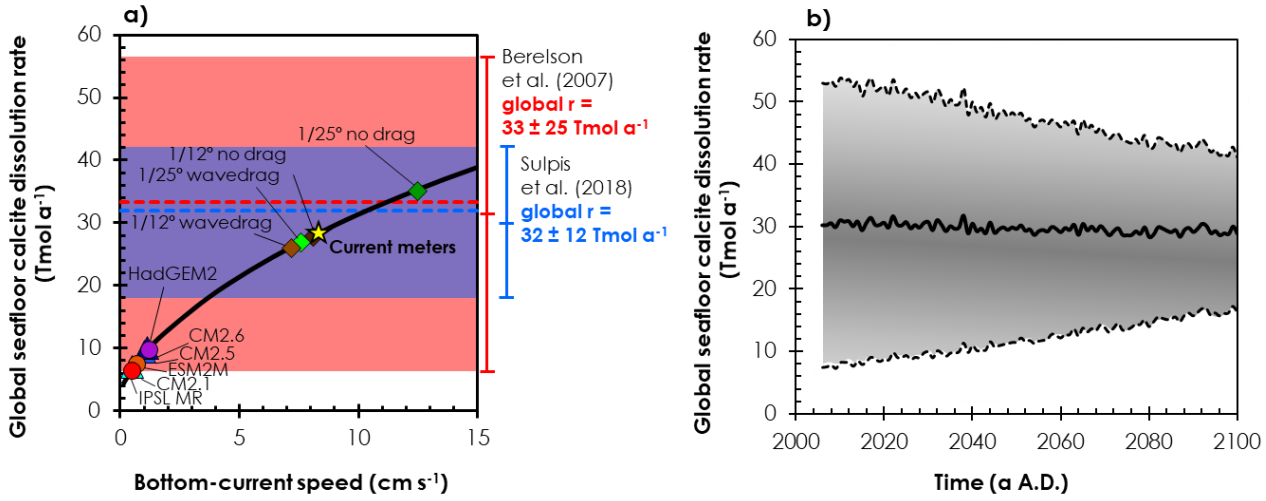

Fig 6.9 | *(a) Global seafloor CMIP5 model mean calcite dissolution rate as a function of the world-averaged bottom-current speed from scaling up or down CMIP5 bottom current speed. Symbols represents the theoretical dissolution rates corresponding to the current-speed means presented in* ***Fig. 6.7b****. The dashed horizontal lines and shaded areas represent the contemporary seafloor calcite dissolution and the related uncertainty as estimated by Berelson et al. (2007) (in red) and Sulpis et al. (2018) (in blue). (b) Global seafloor calcite dissolution rate as a function of time simulated by the CMIP5 model mean under the RCP8.5 scenario (black line), taking into account the uncertainties associated with each CMIP5 model mean variable (CMIP5-intermodel spread) and their propagation into the computed dissolution rates (grey shaded area).*

Fig. 6.9b represents the global 21st century calcite dissolution rate, computed from the CMIP5 model variables shown in ***Figs. 6.1*** and ***6.2***, where CMIP5 current speeds have been scaled up to correspond to the current-meter average, and the standard deviation has been computed using standard error propagation rules following Sulpis et al. (2018). The uncertainty associated with the computed $[CO_3^{2-}]_{SW}$ was derived using the code of Orr et al. (2018). In year 2100, the scaled-up seafloor calcite dissolution rate is 29.1 ± 13.8 Tmol a^{-1}, statistically indistinguishable than the 2006-2035 averaged rate of 30.4 ± 21.6 Tmol a^{-1}, due to the wide error bar. As can be seen in ***Fig. 6.2***, the modelled values of many bottom-water variables are very heterogeneous depending on the model. From the three CMIP5 models used in this study, the world-averaged intermodel standard deviations for TA and DIC are 40 and 66 µmol kg^{-1}, respectively, which represents more than 10

times the usual measurement errors (Millero, 2007; Olsen et al., 2016). The computed bottom-water CO_3^{2-} concentration is thus highly dependent on the model, which inhibits our ability to simulate accurate dissolution rates in the present or in the future. Similarly, the world-averaged standard deviation for the calcite flux to the bottom is larger than its mean value throughout the entire century. These results highlight the need for a better representation of both physical and chemical bottom-water variables in the next generation of Earth System and climate models. We note, however, that despite large cumulative errors that hinder accurate future calcite dissolution predictions, a Mann-Kendall trend test reveals that the global seafloor calcite dissolution rate evolves during the 21st century under RCP8.5 with a statistically significant decreasing trend ($p = 1 \times 10^{-9}$).

6.6 Conclusion

Calcite dissolution rates at the seafloor are dictated by a variety of processes that will evolve in the future. Whereas ocean acidification controls the thermodynamic potential of the dissolution reaction, widening the gap between $[CO^{2-}]_{SW}$ and $[CO^{2-}]_{eq}$, and driving calcite towards dissolution, the dissolution rate at the seafloor also depends on kinetic processes independent of solution chemistry, such as the resistance caused by the presence of a diffusive boundary layer above the seafloor, whose thickness is dependent on bottom-current speed. Traditionally, the balance of $CaCO_3$ fluxes at the sediment-water interface has been expected to shift towards enhanced dissolution in response to any acidification event (Archer et al., 1998; Boudreau, 2013; Broecker and Peng, 1982; Eyre et al., 2018; Sulpis et al., 2018). Our results show that within the 21st century, when various processes affecting the calcite dissolution rate at the seafloor are considered, the dissolution rate will not increase in response to ocean acidification but, instead, will globally decrease. The general slowdown of bottom-currents and decreasing $CaCO_3$ flux to the seafloor counteract the effect of ocean acidification on the calcite dissolution rate at the seafloor, which might prevent this mechanism to act as a significant anthropogenic carbon sink within the 21st century. Even though models strongly underestimate modern bottom-current speeds relative to observations, partly due to the low-resolution of the ocean component, all models tested in this study consistently predict a global decrease in the strength of bottom circulation. This suggests that calcite dissolution in response to the ongoing acidification event may be delayed and,

therefore, its associated CO_2 sink. To accurately predict the magnitude and loci of calcite dissolution at the seafloor, models must better represent bottom-water chemistry, bottom currents, and integrate a diffusive boundary layer module in which thickness fluctuates according to the hydrodynamics at the seafloor. This study highlights the need to adopt an integrative approach when computing seafloor calcite dissolution rates through time, and has important implications in our understanding of calcite dissolution and preservation on geological time scales.

6.7 Supplementary figures and tables

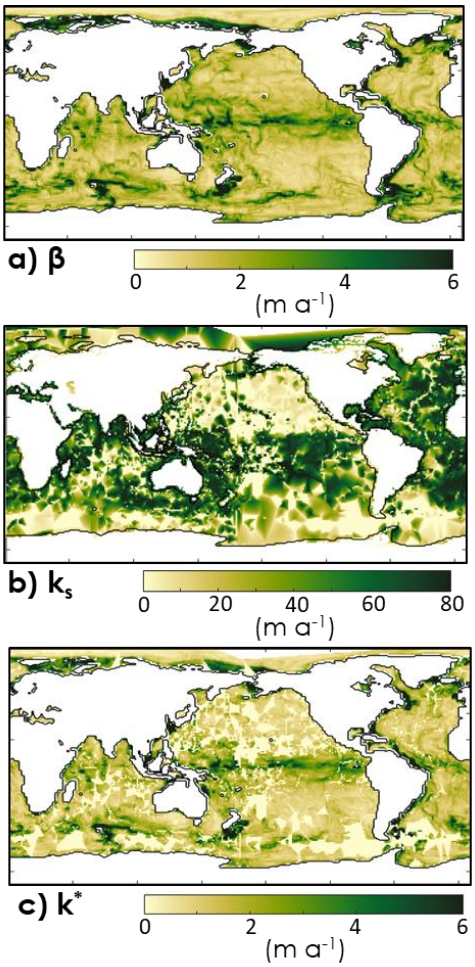

Fig 6.10 | *CMIP5 ensemble average predicted (a) water-side CO_3^{2-} mass transfer coefficient (β), (b) sediment-side CO_3^{2-} mass transfer coefficient (k_S) and (c) overall CO_3^{2-} mass transfer coefficient (k^*) under RCP8.5 and averaged over the last 30 years of the simulation (2071-2100).*

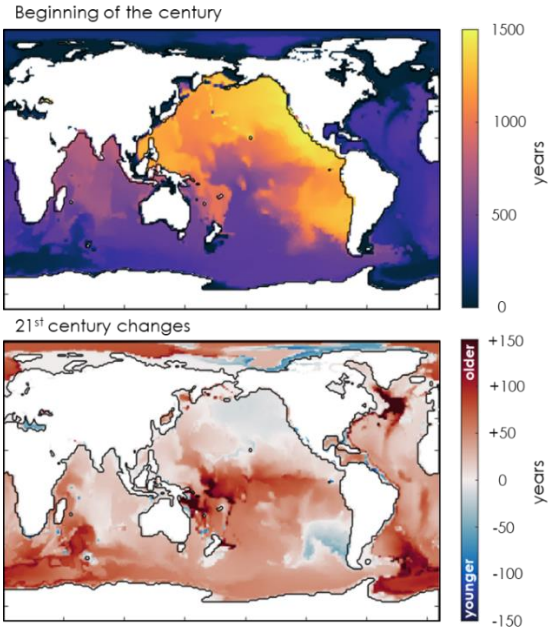

Fig 6.11 | *Bottom-water age since the last contact with the surface, as simulated by the ESM2M model under the RCP8.5 scenario. The top panel represents the 2071-2100 averaged value and the bottom panel depicts the change between the 2006-2035 average and the 2071-2100 average. Output of the age tracer were not available in HadGEM2-CC and IPSL-CM5A-MR.*

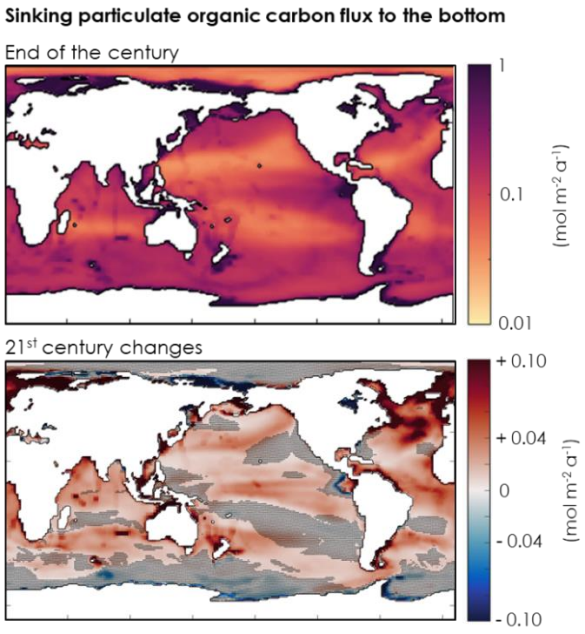

Fig 6.12 | *CMIP5 model mean (top) sinking fluxes of particulate organic carbon (POC) at the bottom, averaged over the last 30 years of simulation and (bottom) POC sinking flux to the bottom changes between the first 30 years and the last 30 years of simulation.*

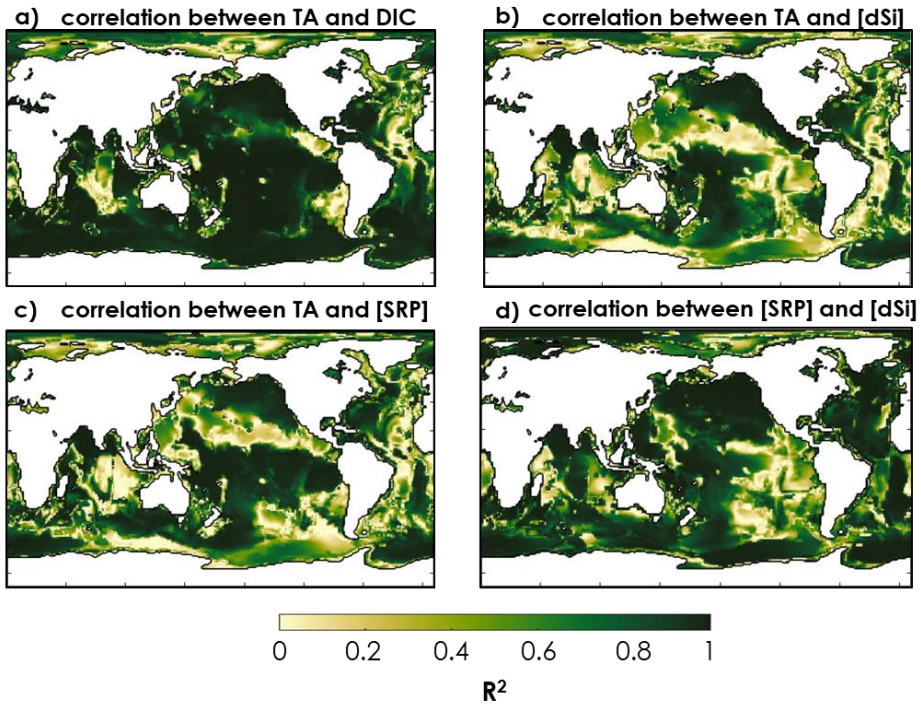

Fig. 6.13 | *CMIP5 model mean correlation coefficient of a linear regression between (a) TA and DIC, (b) TA and [dSi], (c) TA and [SRP] and (d) [SRP] and [dSi] between 2006 and 2100.*

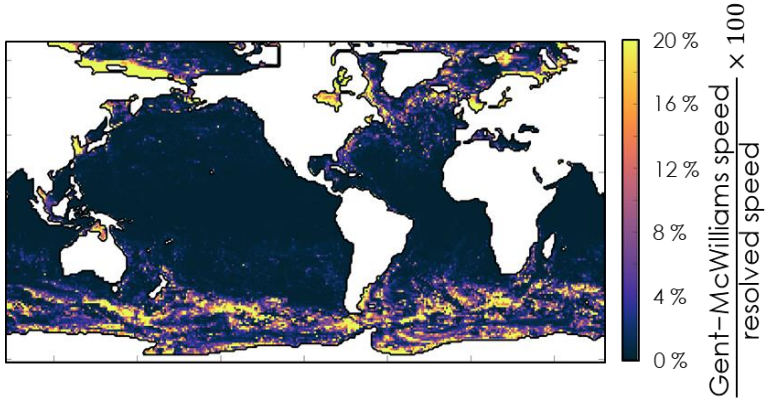

Fig. 6.14 | *Ratio of the parameterized bottom current speed to the resolved bottom-current speeds in CM2-1deg. The parameterized current speed has been calculated from the parameterized mass transport and represents the mesoscale eddy transport (Griffies et al., 1998). The data used in this map is an averaged of the 30 first years of a simulation where the atmospheric partial pressure of CO2 (pCO_2) increases by 1% per year.*

Table. 6.1 | *p-values of a Mann-Kendall trend test on the world-averaged CMIP5 model mean variables presented in* ***Fig. 6.2****. p-values smaller than 0.05 (in red) indicate that the bottom-current time series shows a statistically significant monotonic decreasing trend over the corresponding timeframe (i.e., from 2006 to 2100). Green color indicates a statistically significant monotonic increasing trend. p-values higher than 0.05 indicate no specific trend.*

Variable	GFDL-ESM2M	HadGEM2-CC	IPSL-CM5A-MR	CMIP5 ensemble average
T	4×10^{-43}	2×10^{-44}	1×10^{-43}	7×10^{-46}
S	1×10^{-22}	1×10^{-33}	1×10^{-18}	2×10^{-36}
DIC	4×10^{-46}	1×10^{-46}	2×10^{-46}	1×10^{-46}
TA	4×10^{-41}	2×10^{-32}	1×10^{-19}	6×10^{-36}
[SRP]	8×10^{-42}	-	3×10^{-5}	9×10^{-29}
[dSi]	2×10^{-46}	5×10^{-36}	2×10^{-18}	9×10^{-30}
U	2×10^{-21}	2×10^{-24}	2×10^{-7}	4×10^{-25}
F	2×10^{-45}	2×10^{-28}	5×10^{-33}	1×10^{-44}

Table. 6.2 | *p-values of a Mann-Kendall trend test on the bottom-current speeds (U) time series presented in* ***Fig. 6.6a****. p-values smaller than 0.05 (in red) indicate that the bottom-current time series shows a statistically significant monotonic decreasing trend over the corresponding timeframe (i.e., from 2006 to 2100).*

model	doubling atmospheric pCO_2 over 80 years	RCP8.5 from 2006 to 2100
GFDL-ESM2M	-	2×10^{-21}
HadGEM2-CC	-	2×10^{-24}
IPSL-CM5A-MR	-	2×10^{-7}
CM2.1	2×10^{-23}	-
CM2.5	2×10^{-10}	-
CM2.6	1×10^{-9}	-

References

Adcroft, A., Hill, C. and Marshall, J. (1997) Representation of Topography by Shaved Cells in a Height Coordinate Ocean Model. *Monthly Weather Review*, 125, 2293-2315, https://doi.org/10.1175/1520-0493(1997)125<2293:ROTBSC>2.0.CO;2

Alexander, K., J. Meissner, K., & J. Bralower, T. (2015). Sudden spreading of corrosive bottom water during the Palaeocene–Eocene Thermal Maximum. *Nature Geoscience, 8*(6), 458-461. doi:10.1038/ngeo2430, https://doi.org/10.1038/NGEO2430

Anderson, L.G., Olsson, K., Jones, E.P., Chierici, M. and Fransson, A. (1998) Anthropogenic carbon dioxide in the Arctic Ocean: Inventory and sinks. *Journal of Geophysical Research: Oceans* 103, 27707-27716, https://doi.org/10.1029/98JC02586

Archer, D. (1996) A data-driven model of the global calcite lysocline. *Global Biogeochemical Cycles* 10: 511-526, https://doi.org/10.1029/96GB01521.

Archer, D., Kheshgi, H. and Maier-Reimer, E. (1998) Dynamics of fossil fuel CO_2 neutralization by marine $CaCO_3$. *Global Biogeochemical Cycles* 12, 259-276, https://doi.org/10.1029/98GB00744

Archer, D.E., Morford, J.L. and Emerson, S.R. (2002) A model of suboxic sedimentary diagenesis suitable for automatic tuning and gridded global domains. *Global Biogeochemical Cycles* 16(1), 17-1-17-21, https://doi.org/10.1029/2000GB001288

Archer, D., Eby, M., Brovkin, V., Ridgwell, A., Cao, L., Mikolajewicz, U., Caldeira, K., Matsumoto, K., Munhoven, G., Montenegro, A. and Tokos, K. (2009) Atmospheric Lifetime of Fossil Fuel Carbon Dioxide. *Annual Review of Earth and Planetary Sciences* 37, 117-134, https://doi.org/10.1146/annurev.earth.031208.100206

Bates, N.R., Best, M.H.P., Neely, K., Garley, R., Dickson, A.G. and Johnson, R.J. (2012) Detecting anthropogenic carbon dioxide uptake and ocean acidification in the North Atlantic Ocean. *Biogeosciences* 9, 2509-2522, https://doi.org/10.5194/bg-9-2509-2012

Bellouin N., O. Boucher, J. Haywood, C. Johnson, A. Jones, J. Rae, and S. Woodward. (2007) *Improved representation of aerosols for HadGEM2*. Meteorological Office Hadley Centre, Technical Note 73, March 2007

Berelson, W.M., Balch, W.M., Najjar, R., Feely, R.A., Sabine, C. and Lee, K. (2007) Relating estimates of $CaCO_3$ production, export, and dissolution in the water column to measurements of $CaCO_3$ rain into sediment traps and dissolution on the sea floor: A revised global carbonate budget. *Global Biogeochemical Cycles* 21, https://doi.org/10.1029/2006GB002803

Boudreau, B.P. (1996) A method-of-lines code for carbon and nutrient diagenesis in aquatic sediments. *Computers & Geosciences* 22(5), 479-496, https://doi.org/10.1016/0098-3004(95)00115-8

Boudreau, B.P. (2013) Carbonate dissolution rates at the deep ocean floor. *Geophysical Research Letters* 40, 744-748, https://doi.org/10.1029/2012GL054231

Boudreau, B.P. and Guinasso, N.L., Jr. (1982) The influence of a diffusive boundary layer on accretion, dissolution, and diagenesis at the sea floor, in: Fanning, K.A., Manheim, F.T. (Eds.), *The Dynamic Environment of the Ocean Floor*. Lexington Books, Lexington, pp. 115-145.

Boudreau, B.P. and Jørgensen, B.B. (2001) *The Benthic Boundary Layer: Transport Processes and Biogeochemistry*. Oxford University Press, Oxford.

Boudreau, B.P. and Luo, Y. (2017) Retrodiction of secular variations in deep-sea $CaCO_3$ burial during the Cenozoic. *Earth and Planetary Science Letters* 474, 1-12, https://doi.org/10.1016/j.epsl.2017.06.005

Boudreau, B.P., Middelburg, J.J., Hofmann, A.F. and Meysman, F.J.R. (2010a) Ongoing transients in carbonate compensation. *Global Biogeochemical Cycles* 24, https://doi.org/10.1029/2009GB003654

Boudreau, B.P., Middelburg, J.J. and Meysman, F.J.R. (2010b) Carbonate compensation dynamics. *Geophysical Research Letters* 37, https://doi.org/10.1029/2009GL041847

Bramlette, M.N. (1961) Pelagic sediments, in: Sears, M. (Ed.), Oceanography. *Publications of the American Association for the Advancement of Science*, 67, pp. 345-366.

Broecker, W.S. and Peng, T.H. (1982) *Tracers in the Sea*. Lamont-Doherty Geological Observatory, Columbia University, Palisades, New York.

Caesar, L., Rahmstorf, S., Robinson, A., Feulner, G. and Saba, V. (2018) Observed fingerprint of a weakening Atlantic Ocean overturning circulation. *Nature* 556, 191-196, https://doi.org/10.1038/s41586-018-0006-5

Caldeira, K. and Wickett, M.E. (2003) Anthropogenic carbon and ocean pH. *Nature* 425, 365-365, https://doi.org/10.1038/425365a

Carter, B.R., Feely, R.A., Mecking, S., Cross, J.N., Macdonald, A.M., Siedlecki, S.A., Talley, L.D., Sabine, C.L., Millero, F.J., Swift, J.H., Dickson, A.G. and Rodgers, K.B. (2017) Two decades of Pacific anthropogenic carbon storage and ocean acidification along GO-SHIP sections P16 and P02. *Global Biogeochemical Cycles*, https://doi.org/10.1002/2016GB005485

Chen, C.-T.A. (1982) On the distribution of anthropogenic CO_2 in the Atlantic and Southern oceans. *Deep Sea Research* 29, 563-580, https://doi.org/10.1016/0198-0149(82)90076-0

Cheng, W., Chiang, J.C.H. and Zhang, D. (2013) Atlantic Meridional Overturning Circulation (AMOC) in CMIP5 Models: RCP and Historical Simulations. *Journal of Climate* 26, 7187-7197, https://doi.org/10.1175/JCLI-D-12-00496.1

Ciais, P., Sabine, C., Bala, G., Bopp, L., Brovkin, V., Canadell, J., Chhabra, A., DeFries, R., Galloway, J., Heimann, M., Jones, C., Le Quéré, C., Myneni, R.B., Piao, S. and Thornton, P. (2013) Carbon and Other Biogeochemical Cycles. In: Stocker, T.F., D. Qin, G.-K. Plattner, M. Tignor, S.K. Allen, J. Boschung, A. Nauels, Y. Xia, V. Bex and P.M. Midgley [Eds.] Climate Change 2013: The Physical Science Basis. Contribution of Working Group I to the Fifth Assessment Report of the Intergovernmental Panel on Climate Change. Cambridge University Press, Cambridge, United Kingdom and New York, NY, USA.

Collins, M., Knutti, R., Arblaster, J., Dufresne, J.-L., Fichefet, T., Friedlingstein, P., Gao, X., Gutowski, W.J., Johns, T., Krinner, G., Shongwe, M., Tebaldi, C., Weaver, A.J. and Wehner, M. (2013) Long-term Climate Change: Projections, Commitments and Irreversibility, in: Stocker, T.F., Qin, D., Plattner, G.-K., Tignor, M., Allen, S.K., Boschung, J., Nauels, A., Xia, Y., Bex, V., Midgley, P.M. (Eds.), *Climate Change 2013: The Physical Science Basis. Contribution of Working Group I to the Fifth Assessment Report of the Intergovernmental Panel on Climate Change*. Cambridge University Press, Cambridge, United Kingdom and New York, NY, USA, https://doi.org/10.1017/CBO9781107415324.024

Collins, W.J., Bellouin, N., Doutriaux-Boucher, M., Gedney, N., Halloran, P., Hinton, T., Hughes, J., Jones, C.D., Joshi, M., Liddicoat, S., Martin, G., O'Connor, F., Rae, J., Senior, C., Sitch, S., Totterdell, I., Wiltshire, A. and S. Woodward (2011) Development and evaluation of an Earth-System model – HadGEM2. *Geosci. Model Dev.*, 4, 1051-1075, https://doi.org/10.5194/gmd-4-1051-2011

Dade, W.B. (1993) Near-bed turbulence and hydrodynamic control of diffusional mass transfer at the sea floor. *Limnology and Oceanography* 38, 52-69, https://doi.org/10.4319/lo.1993.38.1.0052

de Lavergne, C., Madec, G., Roquet, F., Holmes, R.M. and McDougall, T.J. (2017) Abyssal ocean overturning shaped by seafloor distribution. *Nature* 551, 181-186, https://doi.org/10.1038/nature24472

de Lavergne, C., Palter, J.B., Galbraith, E.D., Bernardello, R. and Marinov, I. (2014) Cessation of deep convection in the open Southern Ocean under anthropogenic climate change. *Nature Climate Change* 4, 278-282, https://doi.org/10.1038/nclimate2132

Delworth, T.L., Rosati, A., Anderson, W., Adcroft, A.J., Balaji, V., Benson, R., Dixon, K., Griffies, S.M., Lee, H.-C., Pacanowski, R.C., Vecchi, G.A., Wittenberg, A.T., Zeng, F. and Zhang, R. (2012) Simulated Climate and Climate Change in the GFDL CM2.5 High-Resolution Coupled Climate Model. *Journal of Climate* 25, 2755-2781, https://doi.org/10.1175/JCLI-D-11-00316.1

Desbruyères, D.G., Purkey, S.G., McDonagh, E.L., Johnson, G.C. and King, B.A. (2016) Deep and abyssal ocean warming from 35 years of repeat hydrography. *Geophysical Research Letters* 43(19): 10,356-10,365, https://doi.org/10.1002/2016GL070413

Dickson, A.G. (1981) An exact definition of total alkalinity and a procedure for the estimation of alkalinity and total inorganic carbon from titration data. *Deep Sea Research Part A. Oceanographic Research Papers*, 28, 609-623, https://doi.org/10.1016/0198-0149(81)90121-7

Dickson, A.G. (1990) Standard potential of the reaction: $AgCl(s)+1/2H_2(g) = Ag(s)+HCl(aq)$, and the standard acidity constant of the ion HSO_4^- in synthetic sea water from 273.15 to 318.15 K. *The Journal of Chemical Thermodynamics* 22, 113-127, https://doi.org/10.1016/0021-9614(90)90074-Z

Dlugokencky, E. and Tans, P. (2018) *Trends in atmospheric carbon dioxide*. National Oceanic and Atmospheric Aministration, Earth System Research Laboratory (NOAA/ESRL).

Dufresne, J.L., Foujols, M.A., Denvil, S., Caubel, A., Marti, O., Aumont, O., Balkanski, Y., Bekki, S., Bellenger, H., Benshila, R., Bony, S., Bopp, L., Braconnot, P., Brockmann, P., Cadule, P., Cheruy, F., Codron, F., Cozic, A., Cugnet, D., de Noblet, N., Duvel, J.P., Ethé, C., Fairhead, L., Fichefet, T., Flavoni, S., Friedlingstein, P., Grandpeix, J.Y., Guez, L., Guilyardi, E., Hauglustaine, D., Hourdin, F., Idelkadi, A., Ghattas, J., Joussaume, S., Kageyama, M., Krinner, G., Labetoulle, S., Lahellec, A., Lefebvre, M.P., Lefevre, F., Levy, C., Li, Z.X., Lloyd, J., Lott, F., Madec, G., Mancip, M., Marchand, M., Masson, S., Meurdesoif, Y., Mignot, J., Musat, I., Parouty, S., Polcher, J., Rio, C., Schulz, M., Swingedouw, D., Szopa, S., Talandier, C., Terray, P., Viovy, N. and Vuichard, N. (2013) Climate change projections using the IPSL-CM5 Earth System Model: from CMIP3 to CMIP5. *Climate Dynamics* 40, 2123-2165, https://doi.org/10.1007/s00382-012-1636-1

Dunne, J.P., Hales, B. and Toggweiler, J.R. (2012) Global calcite cycling constrained by sediment preservation controls. Global Biogeochemical Cycles 26, https://doi.org/10.1029/2010GB003935.

Dunne, J.P., John, J.G., Adcroft, A.J., Griffies, S.M., Hallberg, R.W., Shevliakova, E., Stouffer, R.J., Cooke, W., Dunne, K.A., Harrison, M.J., Krasting, J.P., Malyshev, S.L., Milly, P.C.D., Phillipps, P.J., Sentman, L.T., Samuels, B.L., Spelman, M.J., Winton, M., Wittenberg, A.T. and Zadeh, N. (2012) GFDL's ESM2 Global Coupled Climate–Carbon Earth System Models. Part I: Physical Formulation and Baseline Simulation Characteristics. *Journal of Climate* 25, 6646-6665, https://doi.org/10.1175/JCLI-D-11-00560.1

Dunne, J.P., John, J.G., Shevliakova, E., Stouffer, R.J., Krasting, J.P., Malyshev, S.L., Milly, P.C.D., Sentman, L.T., Adcroft, A.J., Cooke, W., Dunne, K.A., Griffies, S.M., Hallberg, R.W., Harrison, M.J., Levy, H., Wittenberg, A.T., Phillips, P.J. and Zadeh, N. (2013) GFDL's ESM2 Global Coupled Climate–Carbon Earth System Models. Part II: Carbon System Formulation and Baseline Simulation Characteristics. *Journal of Climate* 26, 2247-2267, https://doi.org/10.1175/JCLI-D-12-00150.1

Dutkiewicz, A., Müller, R.D., O'Callaghan, S. and Jónasson, H. (2015) Census of seafloor sediments in the world's ocean. *Geology* 43, 795-798, https://doi.org/10.1130/G36883.1

Edmond, J.M. (1974) On the dissolution of carbonate and silicate in the deep ocean. *Deep Sea Research* 21, 455-480, https://doi.org/10.1016/0011-7471(74)90094-1

Eyre, B.D., Cyronak, T., Drupp, P., Carlo, E.H.D., Sachs, J.P. and Andersson, A.J. (2018) Coral reefs will transition to net dissolving before end of century. *Science* 359, 908-911, https://doi.org/10.1126/science.aao1118

Feely, R.A., Sabine, C.L., Lee, K., Millero, F.J., Lamb, M.F., Greeley, D., Bullister, J.L., Key, R.M., Peng, T.H., Kozyr, A., Ono, T. and Wong, C.S. (2002) In situ calcium carbonate dissolution in the Pacific Ocean. *Global Biogeochemical Cycles* 16, 91-91-91-12, https://doi.org/10.1029/2002GB001866

Garner, S.T. (2005) A Topographic Drag Closure Built on an Analytical Base Flux. *Journal of the Atmospheric Sciences* 62, 2302-2315, https://doi.org/10.1175/JAS3496.1

Gebbie, G. and Huybers, P. (2012) The Mean Age of Ocean Waters Inferred from Radiocarbon Observations: Sensitivity to Surface Sources and Accounting for Mixing Histories. *Journal of Physical Oceanography* 42, 291-305, https://doi.org/10.1175/JPO-D-11-043.1

Gent, P. R. and McWilliams, J. C. (1990) Isopycnal Mixing in Ocean Circulation Models. *Journal of Physical Oceanography* 20, 150-155, https://doi.org/10.1175/1520-0485(1990)020<0150:IMIOCM>2.0.CO;2

Giorgetta, M.A., Jungclaus, J., Reick, C.H., Legutke, S., Bader, J., Böttinger, M., Brovkin, V., Crueger, T., Esch, M., Fieg, K., Glushak, K., Gayler, V., Haak, H., Hollweg, H.-D., Ilyina, T., Kinne, S., Kornblueh, L., Matei, D., Mauritsen, T., Mikolajewicz, U., Mueller, W., Notz, D., Pithan, F., Raddatz, T., Rast, S., Redler, R., Roeckner, E., Schmidt, H., Schnur, R., Segschneider, J., Six, K.D., Stockhause, M., Timmreck, C.,

Wegner, J., Widmann, H., Wieners, K.-H., Claussen, M., Marotzke, J. and Stevens, B. (2013) Climate and carbon cycle changes from 1850 to 2100 in MPI-ESM simulations for the Coupled Model Intercomparison Project phase 5. *Journal of Advances in Modeling Earth Systems* 5, 572-597, https://doi.org/10.1002/jame.20038

Griffies, S.M. (1998) The Gent–McWilliams Skew Flux. *Journal of Physical Oceanography* 28, 831-841, https://doi.org/10.1175/1520-0485(1998)028<0831:TGMSF>2.0.CO;2

Griffies, S. M. and R. W. Hallberg. (2000) Biharmonic friction with a Smagorinsky-like viscosity for use in large-scale eddy-permitting ocean models. *Monthly Weather Review* 128, 2935-2946.

Griffies, S.M., Winton, M., Anderson, W.G., Benson, R., Delworth, T.L., Dufour, C.O., Dunne, J.P., Goddard, P., Morrison, A.K., Rosati, A., Wittenberg, A.T., Yin, J. and Zhang, R. (2015) Impacts on Ocean Heat from Transient Mesoscale Eddies in a Hierarchy of Climate Models. *Journal of Climate* 28, 952-977, https://doi.org/10.1175/JCLI-D-14-00353.1

Gruber, N., Clement, D., Carter, B.R., Feely, R.A., Heuven, S.v., Hoppema, M., Ishii, M., Key, R.M., Kozyr, A., Lauvset, S.K., Monaco, C.L., Mathis, J.T., Murata, A., Olsen, A., Perez, F.F., Sabine, C.L., Tanhua, T. and Wanninkhof, R. (2019) The oceanic sink for anthropogenic CO2 from 1994 to 2007. *Science*, 363, 1193-1199, https://doi.org/10.1126/science.aau5153

Hales, B. (2003) Respiration, dissolution, and the lysocline. *Paleoceanography and Paleoclimatology* 18: https://doi.org/10.1029/2003PA000915.

Hallberg, R. (2013) Using a resolution function to regulate parameterizations of oceanic mesoscale eddy effects. *Ocean Modelling* 72, 92-103.

Hecht and Hasumi (2008) AGU Monograph. Hecht, M. W., and H. Hasumi, Eds., 2008: Ocean Modeling in an Eddying Regime. *Geophys. Monogr*., Vol. 177, Amer. Geophys. Union, 409 pp, https://doi.org/10.1029/GM177

Heinze, C., Maier-Reimer, E., Winguth, A.M.E. and Archer, D. (1999) A global oceanic sediment model for long-term climate studies. *Global Biogeochemical Cycles* 13(1), 221-250, https://doi.org/10.1029/98GB02812

Heuzé, C., Heywood, K.J., Stevens, D.P. and Ridley, J.K. (2015) Changes in Global Ocean Bottom Properties and Volume Transports in CMIP5 Models under Climate Change Scenarios. *Journal of Climate* 28, 2917-2944, https://doi.org/10.1175/JCLI-D-14-00381.1

Higashino, M., and Stefan, H. G. (2004) Diffusive boundary layer development above a sediment-water interface. *Water Environment Research* 76: 292-300, https://doi.org/10.2175/106143004X141870.

Huiskamp, W.N. and Meissner, K.J. (2012) Oceanic carbon and water masses during the Mystery Interval: A model-data comparison study. *Paleoceanography* 27, https://doi.org/10.1029/2012PA002368

Johnson, G.C. (2008) Quantifying Antarctic Bottom Water and North Atlantic Deep Water volumes. *Journal of Geophysical Research* 113, https://doi.org/10.1029/2007JC004477

Joos, F. and Spahni, R. (2008) Rates of change in natural and anthropogenic radiative forcing over the past 20,000 years. *Proceedings of the National Academy of Sciences* 105, 1425-1430, https://doi.org/10.1073/pnas.0707386105

Kendall, M.G. (1975) *Rank Correlation Methods*. Charles Griffin, London, UK.

Khatiwala, S., Primeau, F. and Hall, T. (2009) Reconstruction of the history of anthropogenic CO_2 concentrations in the ocean. *Nature* 462, 346-349, https://doi.org/10.1038/nature08526

Körtzinger, A., Mintrop, L. and Duinker, J.C. (1998) On the penetration of anthropogenic CO_2 into the North Atlantic Ocean. *Journal of Geophysical Research: Oceans* 103, 18681-18689, https://doi.org/10.1029/98JC01737

Larkum, A.W.D., Koch, E.M.W., and Kühl, M. (2003) Diffusive boundary layers and photosynthesis of the epilithic algal community of coral reefs. *Marine Biology* 142: 1073-1082, https://doi.org/10.1007/s00227-003-1022-y.

Lauvset, S.K., Key, R.M., Olsen, A., Heuven, S.v., Velo, A., Lin, X., Schirnick, C., Kozyr, A., Tanhua, T., Hoppema, M., Jutterström, S., Steinfeldt, R., Jeansson, E., Ishii, M., Perez, F.F., Suzuki, T. and Watelet, S. (2016) A new global interior ocean mapped climatology: the 1° × 1° GLODAP version 2. *Earth System Science Data* 8, 325-340, https://doi.org/10.5194/essd-8-325-2016

Le Quéré, C., Andrew, R.M., Friedlingstein, P., Sitch, S., Pongratz, J., Manning, A.C., Korsbakken, J.I., Peters, G.P., Canadell, J.G., Jackson, R.B., Boden, T.A., Tans, P.P., Andrews, O.D., Arora, V.K., Bakker, D.C.E., Barbero, L., Becker, M., Betts, R.A., Bopp, L., Chevallier, F., Chini, L.P., Ciais, P., Cosca, C.E., Cross, J., Currie, K., Gasser, T., Harris, I., Hauck, J., Haverd, V., Houghton, R.A., Hunt, C.W., Hurtt, G., Ilyina, T., Jain, A.K., Kato, E., Kautz, M., Keeling, R.F., Klein Goldewijk, K., Körtzinger, A., Landschützer, P., Lefèvre, N., Lenton, A., Lienert, S., Lima, I., Lombardozzi, D., Metzl, N., Millero, F., Monteiro, P.M.S., Munro, D.R., Nabel, J.E.M.S., Nakaoka, S.-i., Nojiri, Y., Padin, X.A., Peregon, A., Pfeil, B., Pierrot, D., Poulter, B., Rehder, G., Reimer, J., Rödenbeck, C., Schwinger, J., Séférian, R., Skjelvan, I., Stocker, B.D., Tian, H., Tilbrook, B., Tubiello, F.N., van der Laan-Luijkx, I.T., van der Werf, G.R., van Heuven, S., Viovy, N., Vuichard, N., Walker, A.P., Watson, A.J., Wiltshire, A.J., Zaehle, S. and Zhu, D. (2018) Global Carbon Budget 2017. *Earth System Science Data* 10, 405-448, https://doi.org/10.5194/essd-10-405-2018

Levich, V. G. (1962) *Physicochemical Hydrodynamics*, Prentice-Hall.

Lorke, A., Müller, B., Maerki, M., and Wüest, A. (2003) Breathing sediments: The control of diffusive transport across the 530 sediment-water interface by periodic boundary-layer turbulence. *Limnology and Oceanography* 48: 2077-2085, https://doi.org/10.4319/lo.2003.48.6.2077.

Luecke, C.A., Arbic, B.K., Bassette, S.L., Richman, J.G., Shriver, J.F., Alford, M.H., Smedstad, O.M., Timko, P.G., Trossman, D.S. and Wallcraft, A.J. (2017) The Global Mesoscale Eddy Available Potential Energy Field in Models and Observations. *Journal of Geophysical Research: Oceans* 122, 9126-9143, https://doi.org/10.1002/2017JC013136

Lueker, T.J., Dickson, A.G. and Keeling, C.D. (2000) Ocean pCO_2 calculated from dissolved inorganic carbon, alkalinity, and equations for K_1 and K_2: validation based on laboratory measurements of CO_2 in gas and seawater at equilibrium. *Marine Chemistry* 70, 105-119, https://doi.org/10.1016/S0304-4203(00)00022-0

Mackenzie, F. and Andersson, A. (2013) The Marine Carbon System and Ocean Acidification during Phanerozoic Time. *Geochemical Perspectives*, 1-227, https://doi.org/10.7185/geochempersp.2.1

Mann, H.B. (1945) Nonparametric tests against trend. *Econometrica* 13, 245-259.

Matsumoto, K. (2007) Radiocarbon-based circulation age of the world oceans. *Journal of Geophysical Research* 112, https://doi.org/10.1029/2007JC004095

McDougall, T.J. and Barker, P.M. (2011) *Getting started with TEOS-10 and the Gibbs Seawater (GSW) Oceanographic Toolbox*. SCOR/IAPSO WG127, p. 28.

McNeil, B.I., Matear, R.J., Key, R.M., Bullister, J.L. and Sarmiento, J.L. (2003) Anthropogenic CO_2 Uptake by the Ocean Based on the Global Chlorofluorocarbon Data Set. *Science* 299, 235-239, https://doi.org/10.1126/science.1077429

Meinshausen, M., Smith, S.J., Calvin, K., Daniel, J.S., Kainuma, M.L.T., Lamarque, J.F., Matsumoto, K., Montzka, S.A., Raper, S.C.B., Riahi, K., Thomson, A., Velders, G.J.M. and van Vuuren, D.P.P. (2011) The RCP greenhouse gas concentrations and their extensions from 1765 to 2300. *Climatic Change* 109, 213-241, https://doi.org/10.1007/s10584-011-0156-z

Mekik F. A., P. W. Loubere, and D. E. Archer, Organic carbon flux and organic carbon to calcite flux ratio recorded in deep-sea carbonates: Demonstration and a new proxy. *Global Biogeochemical Cycles* 16, https://doi.org/10.1029/2001GB001634.

Menezes, V.V., Macdonald, A.M. and Schatzman, C. (2017) Accelerated freshening of Antarctic Bottom Water over the last decade in the Southern Indian Ocean. *Science Advances* 3, https://doi.org/10.1126/sciadv.1601426

Meysman, F.J.R., Galaktionov, O.S., Gribsholt, B. and Middelburg, J.J. (2006) Bioirrigation in permeable sediments: Advective pore-water transport induced by burrow ventilation. *Limnology and Oceanography* 51: 142-156, https://doi.org/10.4319/lo.2006.51.1.0142.

Millero, F.J. (1995) Thermodynamics of the carbon dioxide system in the oceans. *Geochimica et Cosmochimica Acta* 59, 661-677, https://doi.org/10.1016/0016-7037(94)00354-O

Millero, F.J. (2007) The Marine Inorganic Carbon Cycle. *Chemical Reviews*, 107: 308-341, https://doi.org/10.1021/cr05557.

Morozov, E.G., Demidov, A.N., Tarakanov, R.Y. and Zenk, W. (2010) *Deep Water Masses of the South and North Atlantic, Abyssal Channels in the Atlantic Ocean*. Springer, Dordrecht. https://doi.org/10.1007/978-90-481-9358-5_2

Morse, J.W. and Arvidson, R.S. (2002) The dissolution kinetics of major sedimentary carbonate minerals. *Earth-Science Reviews* 58, 51-84, https://doi.org/10.1016/S0012-8252(01)00083-6

Morse, J.W., Arvidson, R.S. and Lüttge, A. (2007) Calcium Carbonate Formation and Dissolution. *Chemical Reviews* 107, 342-381, https://doi.org/10.1021/cr050358j

Morse, J.W. and Mackenzie, F.T. (1990) *Geochemistry of Sedimentary Carbonates*. Elsevier, Amsterdam.

Mucci, A. (1983) The solubility of calcite and aragonite in seawater at various salinities, temperatures and one atmosphere total pressure. *American Journal of Science* 283, 780-799, http://doi.org/10.2475/ajs.283.7.780

Munhoven, G. (2007) Glacial–interglacial rain ratio changes: Implications for atmospheric CO_2 and ocean–sediment interaction. *Deep Sea Research Part II: Topical Studies in Oceanography* 54(5-7), 722-746, https://doi.org/10.1016/j.dsr2.2007.01.008

Naviaux, J.D., Subhas, A.V., Rollins, N.E., Dong, S., Berelson, W.B. and Adkins, J.F. (2019). Temperature dependence of calcite dissolution kinetics in seawater. *Geochimica et Cosmochimica Acta* 246: 363-384, https://doi.org/10.1016/j.gca.2018.11.037

Orr, J.C., Fabry, V.J., Aumont, O., Bopp, L., Doney, S.C., Feely, R.A., Gnanadesikan, A., Gruber, N., Ishida, A., Joos, F., Key, R.M., Lindsay, K., Maier-Reimer, E., Matear, R., Monfray, P., Mouchet, A., Najjar, R.G., Plattner, G.K., Rodgers, K.B., Sabine, C.L., Sarmiento, J.L., Schlitzer, R., Slater, R.D., Totterdell, I.J., Weirig, M.F., Yamanaka, Y. and Yool, A. (2005) Anthropogenic ocean acidification over the twenty-first century and its impact on calcifying organisms. *Nature* 437, 681-686, https://doi.org/10.1038/nature04095

Orr, J.C., Epitalon, J.-M., Dickson, A.G. and Gattuso, J.-P. (2018) Routine uncertainty propagation for the marine carbon dioxide system. *Marine Chemistry* 207: 84-107, https://doi.org/10.1016/j.marchem.2018.10.006

Olsen, A., Key, R. M., van Heuven, S., Lauvset, S. K., Velo, A., Lin, X., Schirnick, C., Kozyr, A., Tanhua, T., Hoppema, M., Jutterström, S., Steinfeldt, R., Jeansson, E., Ishii, M., Pérez, F. F., and Suzuki, T. (2016) The Global Ocean Data Analysis Project version 2 (GLODAPv2) – an internally consistent data product for the world ocean, *Earth System Science Data*, 8, 297-323, https://doi.org/10.5194/essd-8-297-2016.

Pearson, B., Fox-Kemper, B., Bachman, S.D. and Bryan, F.O. (2017) Evaluation of scale-aware subgrid mesoscale eddy models in a global eddy-rich model. *Ocean Modelling* 115: 42–58, https://doi.org/10.1016/j.ocemod.2017.05.007

Perez, F.F., Fontela, M., Garcia-Ibanez, M.I., Mercier, H., Velo, A., Lherminier, P., Zunino, P., de la Paz, M., Alonso-Perez, F., Guallart, E.F. and Padin, X.A. (2018) Meridional overturning circulation conveys fast acidification to the deep Atlantic Ocean. *Nature* 554, 515-518, https://doi.org/10.1038/nature25493

Pérez, F.F., Mercier, H., Vázquez-Rodríguez, M., Lherminier, P., Velo, A., Pardo, P.C., Rosón, G. and Ríos, A.F. (2013) Atlantic Ocean CO_2 uptake reduced by weakening of the meridional overturning circulation. *Nature Geoscience* 6, 146-152, https://doi.org/10.1038/ngeo1680

Pierrot, D., Lewis, E. and Wallace, D. (2006) *MS Excel Program Developed for CO_2 System Calculations*. ORNL/CDIAC-105a, Carbon Dioxide Information Analysis Center, Oak Ridge National Laboratory, U.S. Department of Energy, Oak Ridge, Tennessee.

Purkey, S.G. and Johnson, G.C. (2010) Warming of Global Abyssal and Deep Southern Ocean Waters between the 1990s and 2000s: Contributions to Global Heat and Sea Level Rise Budgets. *Journal of Climate* 23, 6336-6351, https://doi.org/10.1175/2010JCLI3682.1

Purkey, S.G. and Johnson, G.C. (2012) Global Contraction of Antarctic Bottom Water between the 1980s and 2000s. *Journal of Climate* 25, 5830-5844 https://doi.org/10.1175/JCLI-D-11-00612.1

Purkey, S.G. and Johnson, G.C. (2013) Antarctic Bottom Water Warming and Freshening: Contributions to Sea Level Rise, Ocean Freshwater Budgets, and Global Heat Gain. *Journal of Climate* 26, 6105-6122, https://doi.org/10.1175/JCLI-D-12-00834.1

Riahi, K., Rao, S., Krey, V., Cho, C., Chirkov, V., Fischer, G., Kindermann, G., Nakicenovic, N. and Rafaj, P. (2011) RCP 8.5-A scenario of comparatively high greenhouse gas emissions. *Climatic Change* 109, 33-57, https://doi.org/10.1007/s10584-011-0149-y

Ridgwell, A. and Hargreaves, J.C. (2007) Regulation of atmospheric CO_2 by deep-sea sediments in an Earth system model. *Global Biogeochemical Cycles* 21, https://doi.org/10.1029/2006GB002764

Riley, J.P. and Tongudai, M. (1967) The major cation/chlorinity ratios in sea water. *Chemical Geology* 2, 263-269, https://doi.org/10.1016/0009-2541(67)90026-5

Ríos, A.F., Resplandy, L., García-Ibáñez, M.I., Fajar, N.M., Velo, A., Padin, X.A., Wanninkhof, R., Steinfeldt, R., Rosón, G. and Pérez, F.F. (2015) Decadal acidification in the water masses of the Atlantic Ocean. *Proceedings of the National Academy of Sciences of the United States of America* 112, 9950-9955, https://doi.org/10.1073/pnas.1504613112

Sabine, C.L., Feely, R.A., Key, R.M., Bullister, J.L., Millero, F.J., Lee, K., Peng, T.H., Tilbrook, B., Ono, T. and Wong, C.S. (2002) Distribution of anthropogenic CO_2 in the Pacific Ocean. *Global Biogeochemical Cycles* 16, 30-31-30-17, https://doi.org/10.1029/2001GB001639

Santschi, P. H., Bower, P., Nyffeler, U. P., Azevedo, A., and Broecker, W. S. (1983) Estimates of the resistance to chemical transport posed by the deep-sea boundary layer. *Limnology and Oceanography* 28: 899-912, https://doi.org/10.4319/lo.1983.28.5.0899.

Santschi, P.H., Anderson, R.F., Fleisher, M.Q. and Bowles, W. (1991) Measurements of diffusive sublayer thicknesses in the ocean by alabaster dissolution, and their implications for the measurements of benthic fluxes. *Journal of Geophysical Research: Oceans* 96, 10641-10657, https://doi.org/10.1029/91JC00488

Schlichting, H. (1979) *Boundary Layer Theory*. McGraw-Hill, New York.

Smith, S.V. and Mackenzie, F.T. (2016). The role of $CaCO_3$ reactions in the contemporary CO_2 cycle. *Aquatic Geochemistry* 22(2), 153-175, https://doi.org/10.1007/s10498-015-9282-y

Steinberger, N. and Hondzo, M. (1999) Diffusional Mass Transfer at Sediment-Water Interface. *Journal of Environmental Engineering* 125, 192-200, https://doi.org/10.1061/(ASCE)0733-9372(1999)125:2(192)

Steinfeldt, R., Rhein, M., Bullister, J.L. and Tanhua, T. (2009) Inventory changes in anthropogenic carbon from 1997-2003 in the Atlantic Ocean between 20°S and 65°N. *Global Biogeochemical Cycles* 23, https://doi.org/10.1029/2008GB003311

Sulpis, O., Boudreau, B.P., Mucci, A., Jenkins, C.J., Trossman, D.S., Arbic, B.K. and Key, R.M. (2018) Current $CaCO_3$ dissolution at the seafloor caused by anthropogenic CO_2. *Proceedings of the National Academy of Sciences* 115, 11700-11705, https://doi.org/10.1073/pnas.1804250115

Sulpis, O., Lix, C., Mucci, A. and Boudreau, B.P. (2017) Calcite dissolution kinetics at the sediment-water interface in natural seawater. *Marine Chemistry* 195, 70-83, https://doi.org/10.1016/j.marchem.2017.06.005

Teal, L.R., Bulling, M.T., Parker, E.R. and Solan, M. (2008) Global patterns of bioturbation intensity and mixed depth of marine soft sediments. Aquatic Biology 2: 207-218, https://doi.org/10.3354/ab00052.

Thornalley, D.J.R., Oppo, D.W., Ortega, P., Robson, J.I., Brierley, C.M., Davis, R., Hall, I.R., Moffa-Sanchez, P., Rose, N.L., Spooner, P.T., Yashayaev, I. and Keigwin, L.D. (2018) Anomalously weak Labrador Sea convection and Atlantic overturning during the past 150 years. *Nature* 556, 227-230, https://doi.org/10.1038/s41586-018-0007-4

Timko, P. G., Arbic, B. K., Richman, J. G., Scott, R. B., Metzger, E. J., & Wallcraft, A. J. (2013). Skill testing a three-dimensional global tide model to historical current meter records. *Journal of Geophysical Research: Oceans*, *118*(12), 6914-6933, https://doi.org/10.1002/2013jc009071

Trossman, D.S., Arbic, B.K., Garner, S.T., Goff, J.A., Jayne, S.R., Metzger, E.J. and Wallcraft, A.J. (2013) Impact of parameterized lee wave drag on the energy budget of an eddying global ocean model. *Ocean Modelling* 72, 119-142, http://doi.org/10.1016/j.ocemod.2013.08.006

Trossman, D.S., Arbic, B.K., Richman, J.G., Garner, S.T., Jayne, S.R. and Wallcraft, A.J. (2016) Impact of topographic internal lee wave drag on an eddying global ocean model. *Ocean Modelling* 97, 109-128, https://doi.org/10.1016/j.ocemod.2015.10.013

Tschumi, T., Joos, F., Gehlen, M. and Heinze, C. (2011) Deep ocean ventilation, carbon isotopes, marine sedimentation and the deglacial CO_2 rise. *Climate of the Past* 7(3), 771-800, https://doi.org/10.5194/cp-7-771-2011

van Heuven, S., Pierrot, D., Rae, J.W.B., Lewis, E. and Wallace, D.W.R. (2011) *MATLAB Program Developed for CO_2 System Calculations*. ORNL/CDIAC-105b. Carbon Dioxide Information Analysis Center, Oak Ridge National Laboratory, U.S. Department of Energy, Oak Ridge, Tennessee. https://doi.org/10.3334/CDIAC/otg.CO2SYS_MATLAB_v1.1

Van Cappellen, P. and Wang, Y. (1996) Cycling of iron and manganese in surface sediments; a general theory for the coupled transport and reaction of carbon, oxygen, nitrogen, sulfur, iron, and manganese. *American Journal of Science* 296(3), 197-243, https://doi.org/10.2475/ajs.296.3.197

van Vuuren, D.P., Edmonds, J., Kainuma, M., Riahi, K., Thomson, A., Hibbard, K., Hurtt, G.C., Kram, T., Krey, V., Lamarque, J.-F., Masui, T., Meinshausen, M., Nakicenovic, N., Smith, S.J. and Rose, S.K. (2011) The representative concentration pathways: an overview. *Climatic Change* 109, 5-31, https://doi.org/10.1007/s10584-011-0148-z

Vázquez-Rodríguez, M., Touratier, F., Monaco, C.L., Waugh, D.W., Padin, X.A., Bellerby, R.G.J., Goyet, C., Metzl, N., Ríos, A.F. and Pérez, F.F. (2009) Anthropogenic carbon distributions in the Atlantic Ocean: data-based estimates from the Arctic to the Antarctic. *Biogeosciences* 6, 439-451, https://doi.org/10.5194/bg-6-439-2009

Voldoire, A., Sanchez-Gomez, E., Mélia, D.S.y., Decharme, B., Cassou, C., Sénési, S., Valcke, S., Beau, I., Alias, A., Chevallier, M., Déqué, M., Deshayes, J., Douville, H., Fernandez, E., Madec, G., Maisonnave, E., Moine, M.-P., Planton, S., Saint-Martin, D., Szopa, S., Tyteca, S., Alkama, R., Belamari, S., Braun, A., Coquart, L. and Chauvin, F. (2013) The CNRM-CM5.1 global climate model: description and basic evaluation. *Climate Dynamics* 40, 2091-2121, https://doi.org/10.1007/s00382-011-1259-y

Wallcraft, A. J., A. B. Kara, and H. E. Hurlburt. (2005) Convergence of Laplacian diffusion versus resolution of an ocean model. *Geophysical Research Letters* 32, L07604, https://doi.org/doi:10.1029/2005GL022514

Wanninkhof, R., Doney, S.C., Bullister, J.L., Levine, N.M., Warner, M. and Gruber, N. (2010) Detecting anthropogenic CO_2 changes in the interior Atlantic Ocean between 1989 and 2005. *Journal of Geophysical Research* 115, https://doi.org/10.1029/2010JC006251

Wanninkhof, R., Park, G.-H., Takahashi, T., Feely, R.A., Bullister, J.L. and Doney, S.C. (2013) Changes in deep-water CO_2 concentrations over the last several decades determined from discrete pCO_2 measurements. *Deep Sea Research Part I* 74, 48-63, https://doi.org/10.7916/D8QJ7T4F

Winton, M., Anderson, W.G., Delworth, T.L., Griffies, S.M., Hurlin, W.J. and Rosati, A. (2014) Has coarse ocean resolution biased simulations of transient climate sensitivity? *Geophysical Research Letters* 41, 8522-8529, https://doi.org/10.1002/2014GL061523

Woosley, R.J., Millero, F.J. and Wanninkhof, R. (2016) Rapid anthropogenic changes in CO_2 and pH in the Atlantic Ocean: 2003-2014. *Global Biogeochemical Cycles* 30, 70-90, https://doi.org/10.1002/2015GB005248

Zeebe, R.E. (2011) On the molecular diffusion coefficients of dissolved CO_2, HCO_3^-, and CO_3^{2-} and their dependence on isotopic mass. *Geochimica et Cosmochimica Acta* 75, 2483-2498, https://doi.org/10.1016/j.gca.2011.02.010

Zeebe, R.E., Ridgwell, A. and Zachos, J.C. (2016) Anthropogenic carbon release rate unprecedented during the past 66 million years. *Nature Geoscience* 9, 325-329, https://doi.org/10.1038/ngeo2681

Zhang, R. (2008) Coherent surface-subsurface fingerprint of the Atlantic meridional overturning circulation. *Geophysical Research Letters* 35, https://doi.org/10.1029/2008GL035463

Preface to Chapter 7

In this final Chapter, I explore the marine $CaCO_3$ system in the Anthropocene and how results presented in this thesis contribute to our understanding - or misunderstanding - of the various $CaCO_3$ marine sinks. The vision of the $CaCO_3$ cycle that has prevailed throughout this thesis is somewhat simplistic, in part because of the scientific background of its authors, as it only focuses on abiotic processes. Here, I attempt to highlight the possible role of biologically-mediated processes in the marine $CaCO_3$ cycle.

Chapter 7

Implications and general conclusions

7.1 The marine $CaCO_3$ cycle in the Anthropocene

In ***Chapters 2-4***, we presented experimental evidence that in addition to bottom-water chemistry, i.e., Ω_C, bottom-water physics, i.e., bottom-current speeds and their control on the diffusive boundary layer (DBL) thickness, control the dissolution rate of $CaCO_3$ at the sediment-water interface (SWI). Yet, to my knowledge, all models simulating $CaCO_3$ dissolution or accumulation in sediments either explicitly disregard the presence of a DBL (e.g., Van Cappellen and Wang, 1996; Archer et al., 2002; Hales, 2003; Munhoven, 2007; Tschumi et al., 2011), or consider a DBL with a constant value, irrespective of the bottom hydrodynamics (Boudreau, 1996; Heinze et al., 1999). In the recent years, Bernard P. Boudreau and his colleagues showed in a number of papers (Boudreau et al., 2010a, b; Boudreau, 2013; Boudreau et al., 2015; Luo and Boudreau, 2016; Luo et al., 2016; Boudreau and Luo, 2017; Boudreau et al., 2018; Luo et al., 2018; Boudreau et al., 2019) that a simple model assuming diffusive transport control through a DBL of the $CaCO_3$ dissolution rate at the SWI can successfully reproduce both the average position of the CCD and its evolution through time as well as the $CaCO_3$ content of surface sediments. Notwithstanding, these papers treated the marine $CaCO_3$ system as a one-dimensional problem, using a global, average value for the water-side mass transfer coefficients (β) that describes the rate at which CO_3^{2-} ions diffuse through the DBL. In ***Chapters 5*** and ***6***, we showed that it is possible to estimate β and the DBL thickness in a four-dimensional framework, across latitude, longitude, seafloor depth and time, by deriving the DBL thickness from the benthic current speeds.

Throughout the work presented in this thesis, we have consistently discarded all biologically-mediated dissolution, in our experimental reactors or in our field models. On one hand, laboratory $CaCO_3$ dissolution kinetics studies, whether on sediment beds or suspended particles, provide insights on the abiotic mechanisms that control marine dissolution and allow the development of straightforward $CaCO_3$ dissolution models. On the other hand, biological processes may also affect dissolution, whether it is in the porewaters by microbial organic matter degradation and metabolic CO_2 production (Emerson and Bender, 1981; Archer et al., 1989a;

Jahnke et al., 1997; Wenzhöfer et al., 2001; Mekik et al., 2002; Steiner et al., 2019) or in the water column through dissolution in the guts of grazing organisms or their fecal pellets (Bishop et al., 1986; Penry and Jumars, 1986; Harris, 1994; Milliman et al., 1999; Jansen and Wolf-Gladrow, 2001; Berelson et al., 2007). Note, however, that the relative importance of the aforementioned biologically-mediated calcite dissolution processes remains controversial and no consensus has been reached among the marine geochemical community so far (van der Wal, 1995; Pond et al., 1995; Jahnke and Jahnke, 2004; Friis et al., 2006; Gehlen et al., 2007; Bisset et al., 2011). This biological component constitutes the cryptic component of the marine $CaCO_3$ cycle. Here, I use datasets and equations from various authors to compute abiotically-driven $CaCO_3$ fluxes in the marine environment, in an attempt to locate and quantify this cryptic component of the marine $CaCO_3$ sink.

7.1.1 $CaCO_3$ Surface export

Upon their death or grazing, the calcitic and aragonitic shells/exoskeleton of $CaCO_3$-secreting marine organisms are exported, individually or within fecal pellets, from the surface ocean to the deep ocean. This flux (F_{surf}) is vertical and expressed in moles of sinking $CaCO_3$ per m^2 of ocean surface per year. Various estimates of the $CaCO_3$ export rates from the surface ocean have been published, ranging from 33 Tmol a^{-1} (Moore et al., 2004) to 150 Tmol a^{-1} (Murnane et al., 1999), as well as the average export fluxes, are compiled in ***Table 7.1***.

The $CaCO_3$ export flux from the surface ocean, F_{surf}, expressed in moles per square meter of ocean surface and per year, can be conceptualized as a continuous shower of solid material from the surface ocean. The solid grains are falling through the water column with an associated velocity, which is a function of the density and shape of the falling particle and can range from 10 cm d^{-1} for a single coccolith (Honjo, 1976) to 200 m d^{-1} for $CaCO_3$ particles within a fecal pellet (Riley et al., 2012). For the purpose of this discussion, we will consider the $CaCO_3$ export data from Dunne et al. (2007; represented in ***Fig. 7.1***), assuming that all exported $CaCO_3$ is calcite. Dunne et al. (2007) used a dataset of satellite chlorophyll and photosynthetically active radiation from which they inferred the particulate organic carbon (POC) export. From the POC export, the $CaCO_3$ export was derived using a fitted $CaCO_3$ to TOC export ratio that is specific to each basin and latitude range, as explained in Sarmiento et al. (2002). The global average molar export ratio

is 0.06 ± 0.03 (Sarmiento et al., 2002). That different export ratios are used for different ranges of latitudes explains the sharp latitudinal difference in F_{surf} observed at ~ 45 °S in ***Fig. 7.1***.

Table. 7.1 | *$CaCO_3$ global export flux as estimated by various authors.*

Reference	$CaCO_3$ global export rate (Tmol a^{-1})	$CaCO_3$ average export flux (mol m^{-2} a^{-1})
Moore et al. (2004)	33	0.09
Moore et al. (2002)	42	0.12
Sarmiento and Gruber (2006)	42	0.12
Dunne et al. (2007)	**48.5**	0.13
Milliman (1993)	50	0.14
Yamanaka and Tajika (1996)	50-67	0.14-0.19
Gnanadesikan et al. (2004)	56-65	0.16-0.18
Garcon and Minster (1988)	50-125	0.14-0.35
Sarmiento et al. (2002)	50	0.14
Bacastow and Maier Reimer (1990)	58	0.16
Milliman (1999)	60	0.17
Battaglia et al. (2016)	60-87	0.17-0.24
Jin et al. (2006)	70	0.19
Shaffer (1993)	75	0.21
Lee (2001)	75-92	0.21-0.26
Ridgwell et al. (2007)	100	0.28
Chuck et al. (2005)	117	0.33
Balch et al. (2007)	130	0.36
Smith and Mackenzie (2016)	133	0.37
Berelson et al. (2007)	> 133	> 0.37
Heinze et al. (2003)	137	0.38
Archer et al. (1998)	138	0.38
Heinze et al. (1999)	150	0.42
Murnane et al. (1999)	150	0.42

Here, I assume a uniform settling rate of 200 m d^{-1} for all falling particles (Riley et al., 2012). Dividing a flux (mol m^{-2} yr^{-1}) by a velocity (m yr^{-1}) gives a concentration (mol m^{-3}). In a world without dissolution, the vertical distribution of $CaCO_3$ would be vertically homogeneous throughout the water column. In reality, however, because of dissolution in the water column, the $CaCO_3$ concentration decreases with water depth.

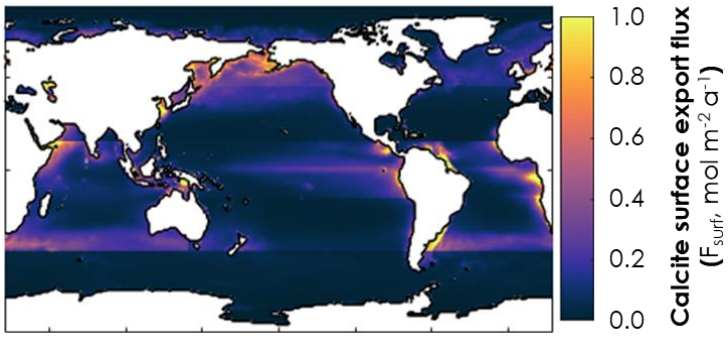

Fig. 7.1 | *$CaCO_3$ surface export expressed per square meter of ocean surface, from Dunne et al. (2007).*

7.1.2 $CaCO_3$ water-column and SWI dissolution

The fate of these falling particles will either be dissolution or, for the remaining fraction, accumulation in sediments. In this section, I use the state-of-the-art empirical description of calcite dissolution kinetics in seawater from the research group of Jess. F. Adkins and William M. Berelson (Subhas et al, 2015, 2017, 2018; Dong et al., 2018; Naviaux et al., 2019) to compute dissolution of $CaCO_3$ particles in the water column. These publications all describe the dissolution kinetics of $CaCO_3$ particles enriched in ^{13}C and kept in suspension in bags placed on a shaker table maintained at a fixed temperature and, thus, are more appropriate to describe the dissolution kinetics of particles sinking through the water column than our sediment disk-based experiments presented in ***Chapters 2-4***. Naviaux et al. (2019) reported calcite dissolution rate constants (*k*, see ***Eq. 1.21***) and reactions orders (*n*, see ***Eq. 1.21***) for four different temperatures, between 5 °C and 37 °C. They derived rate constants and reaction orders for two separate regions of the (1 - Ω_C) spectrum, and the Ω_C threshold value dividing these two regions was Ω_C = 0.75-0.8. Above this value, dissolution is believed to be limited to the retreat of pre-existing steps, kinks and adatoms on the calcite surface, or defect-assisted dissolution, whereas below this value, undersaturation is believed to be high enough to allow dissolution to occur homogeneously across the mineral surface (Naviaux et al., 2019). Here, based on the results of Naviaux et al. (2019) at 5 °C, I use k = 0.027 mol m^{-2} a^{-1} and n = 0.34 for $\Omega_C > 0.75$ and k = 30.84 mol m^{-2} a^{-1} and n = 4.81 for $\Omega_C \leq 0.75$.

The dissolution rate constants taken from Naviaux et al. (2019) are expressed as a function of the surface area of the dissolving calcite grains. In this discussion, I use a surface area of 500 m^2 mol^{-1}, in the middle of the range of BET surface areas measured by Keir (1980; between ~100 and 1000 m^2 mol^{-1}) on natural coccoliths and foraminifera. I also assume that pellets act as pure "spheres" of $CaCO_3$. In reality, pellets have a complex geometry, are surrounded by a diffusive boundary layer and are a mixture of clay, organic matter and $CaCO_3$. Thus, this calculation is very idealistic and is will provide *maximum* estimates of dissolution. Using GLODAPv2 seawater-chemistry data, as in ***Chapter 5***, the modern and preindustrial *in situ* seawater Ω_C can be estimated, and the dissolution rate of $CaCO_3$ (expressed in mol per m^3 of seawater) computed using ***Eqs. 7.1-7.4*** for both preindustrial (i.e., 1800) and modern (i.e., 2002) times. Results of these calculations are shown for a transect along the meridian 166 ° west of Greenwich in ***Figs. 7.2a*** and ***7.2b***. The difference between the modern dissolution rate and that estimated for preindustrial times, that we

attribute to anthropogenic forcing, is represented in ***Fig. 7.2c*** (note that F_{surf} is considered the same for preindustrial and modern times). Interestingly, in regions where strong water-column dissolution occurs, such as in the Northern Pacific where more anthropogenic CO_2 invades, less dissolution occurs at depth, simply because fewer $CaCO_3$ particles survive shallow-water dissolution and are delivered to the deep sea.

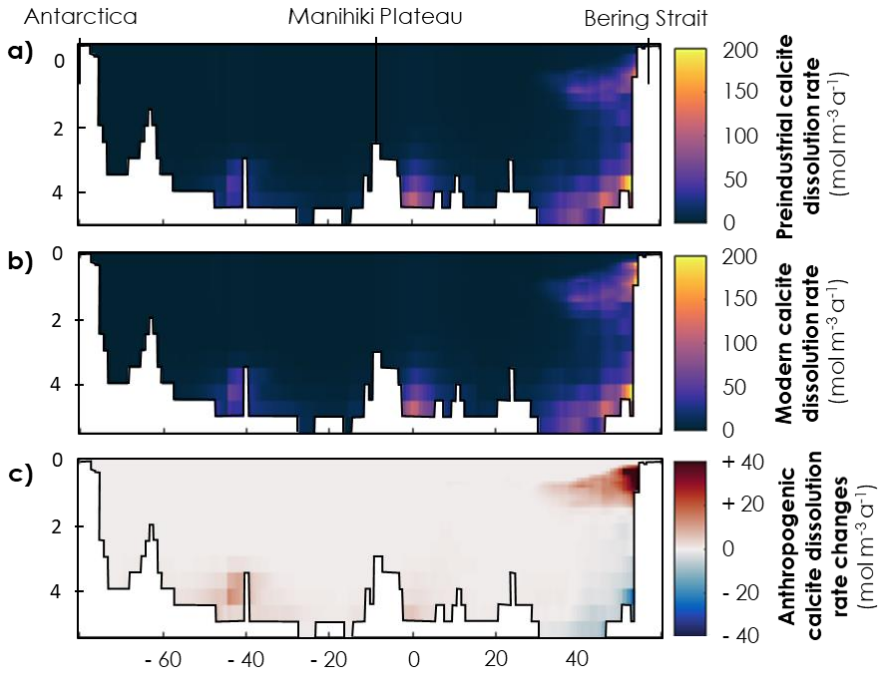

Fig. 7.2 | *(**a**) Preindustrial, (**b**) modern and (**c**) anthropogenic water-column $CaCO_3$ dissolution along the meridian 166°W of Greenwich.*

The $CaCO_3$ flux at the seafloor can be estimated by subtracting the amount of $CaCO_3$ particles dissolved, as they fall through the water column, from the surface production (F_{surf}). Integrating over the water-column depth, the amount of $CaCO_3$ dissolved in the water-column by the action of corrosive waters for each square meter of ocean surface, that I will call R_{SW}, and its anthropogenic component, ΔR_{SW}, are shown in ***Fig. 7.3***. The modern fraction of F_{surf} that makes it to the seafloor, and its anthropogenic component, are depicted in ***Fig. 7.4***. Most water-column dissolution occurs in the North Pacific, where the CSD is shallowest (Feely et al., 2004), and in the very deep Argentine Basin (***Fig. 7.3a***). In both regions, less than 10 % of the surface $CaCO_3$ export currently reaches the seafloor, whereas this value stands at between 70 and 100 % for most of the seafloor's surface (***Fig. 7.4a***). Whereas the strongest anthropogenic water-column

dissolution currently takes place in coastal environments and in the Argentine Basin, the largest decrease in the fraction of the $CaCO_3$ export flux reaching the seafloor is found in the Southern Ocean, where the anthropogenic DIC concentration is high at all depths (Chen, 1982; Lauvset et al., 2016; Gruber et al., 2019) and the $CaCO_3$ surface export flux is very small (***Fig. 7.1***). For instance, in the Enderby Abyssal Plain, close to the Antarctic Circle, assuming a fixed $CaCO_3$ surface export flux, the fraction of the $CaCO_3$ reaching the seafloor has dropped by a *maximum* value of ~30 % since the end of the preindustrial era, solely due to anthropogenic water-column dissolution.

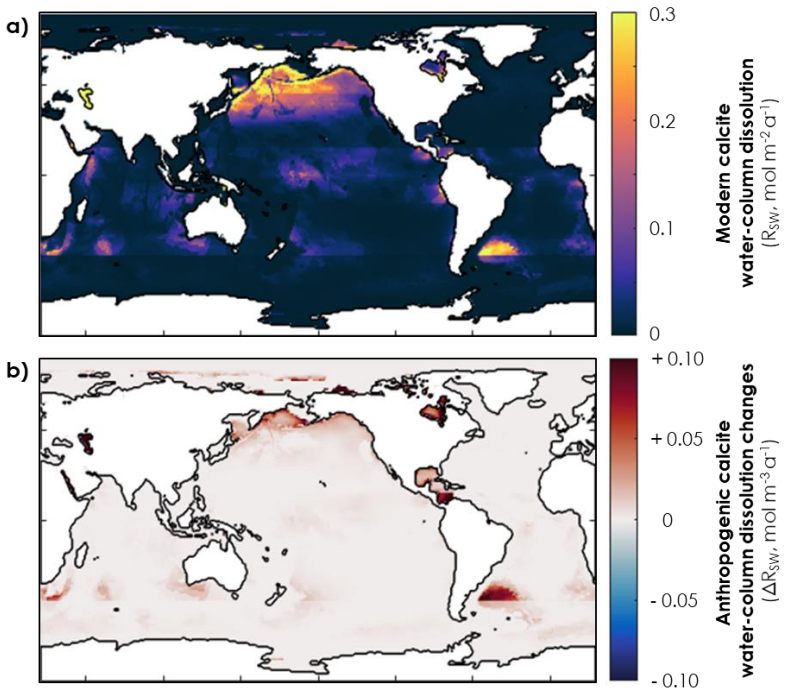

Fig. 7.3 | *(**a**) Modern and (**b**) anthropogenic water-column $CaCO_3$ dissolution integrated over the whole water column.*

Next, using the methodology described in ***Chapter 5***, bottom current speeds derived from HYCOM and the $CaCO_3$ flux reaching the bottom computed above, the $CaCO_3$ dissolution rate at the SWI can be computed. Results are represented in ***Fig. 7.5a*** for modern times, whereas ***Fig. 7.5b*** represents anthropogenic changes. As can be noted when comparing ***Fig. 7.5*** with ***Fig. 5.3***, whether we assume that the $CaCO_3$ flux to the seafloor corresponds to the flux of $CaCO_3$ that must reach the CCD in order to explain the observed $CaCO_3$ contents in surficial sediments (as we did

in ***Chapter 5***) or we use the flux of $CaCO_3$ reaching the seafloor as computed here, no noticeable difference can be observed in the magnitude or location of $CaCO_3$ dissolution at the seafloor.

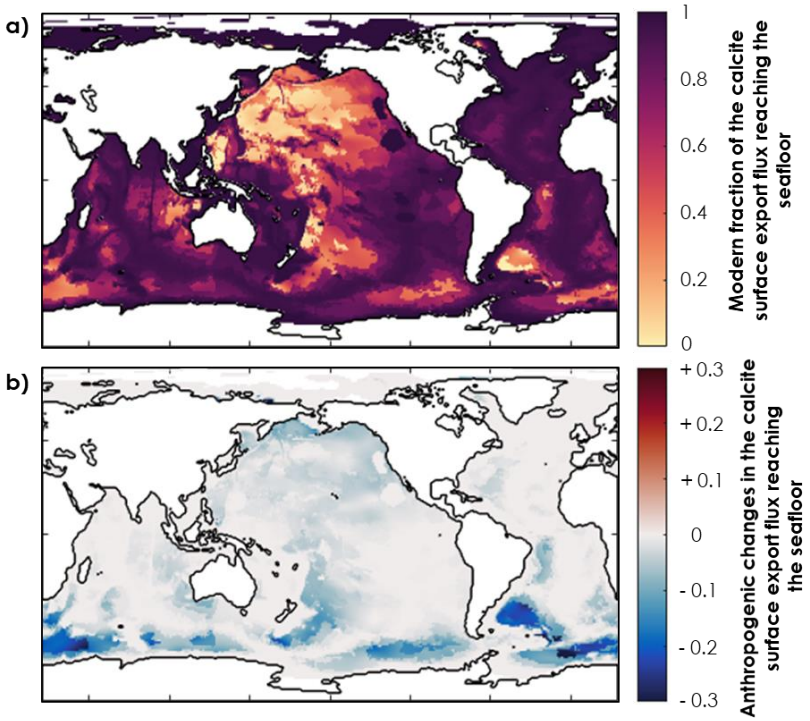

Fig. 7.4 | *(**a**) Modern fraction of the $CaCO_3$ surface export flux that reaches the seafloor. (**b**) Changes in the fraction of surface $CaCO_3$ that reaches the seafloor between the end of the preindustrial period and modern times.*

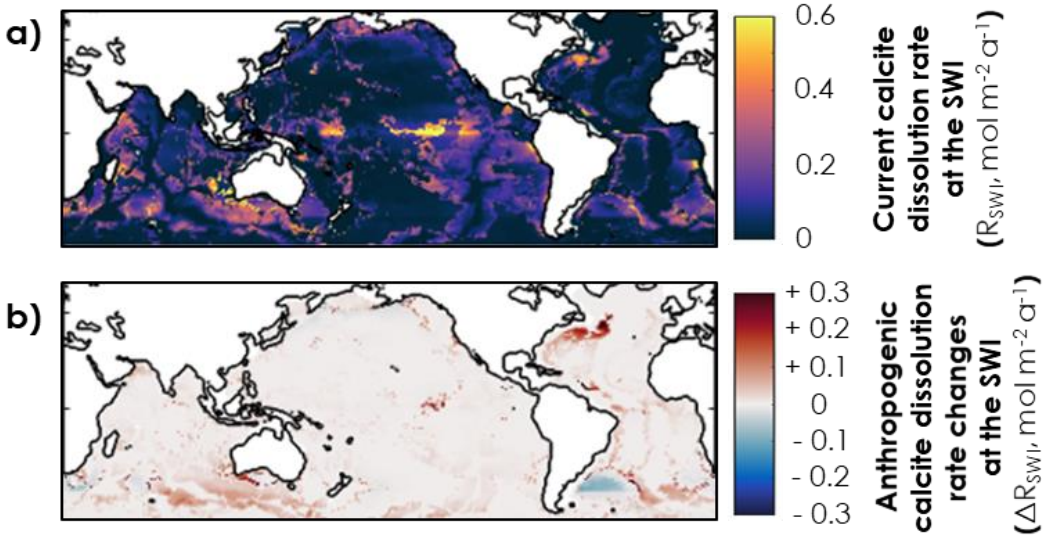

Fig. 7.5 | *(**a**) Modern and (**b**) anthropogenic $CaCO_3$ dissolution rate at the sediment-water interface.*

7.1.3 $CaCO_3$ accumulation at the seafloor and the missing sink

An ocean-wide compilation of total sediment accumulation rates has been published before (Sarmiento and Gruber, 2006), but the corresponding $CaCO_3$ accumulation rates are unknown. Here, I use the total sediment accumulation rate dataset of Sarmiento and Gruber (2006), based on the original data of Jahnke (1996), and the $CaCO_3$ content of marine sediments extracted from the dbSEABED database of Jenkins (1997, shown in ***Fig. 5.6a***) to compute $CaCO_3$ accumulation rates according to:

$$A_{CaCO_3} = X_{CaCO_3} \times A_{tot} \quad \textbf{(7.1)}$$

where X_{CaCO3} is the weight fraction of $CaCO_3$ in surface sediments and A_{tot} is the total sediment accumulation rate from Sarmiento and Gruber (2006). A_{CaCO3} is presented in ***Fig. 7.6***.

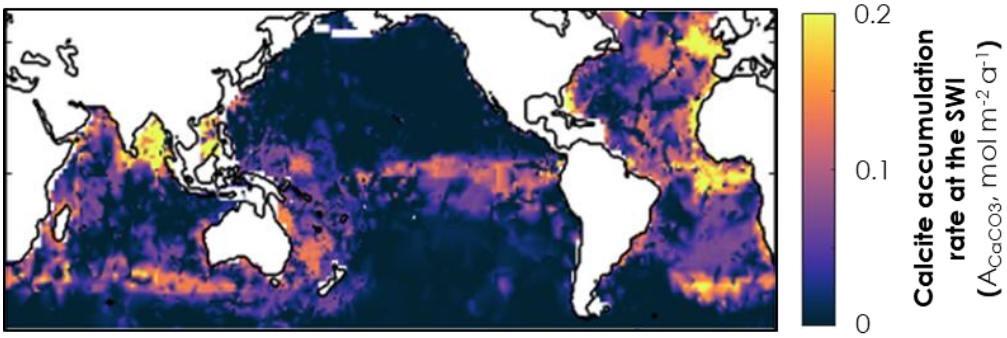

Fig. 7.6 | *$CaCO_3$ accumulation rates in sediments. White zones are areas where no data is available.*

Assuming that biogenic $CaCO_3$ produced in surface waters is the only source of solid $CaCO_3$ to the seafloor, thus neglecting the contribution of rivers or lithogenic sources, a simple mass balance equation describing the $CaCO_3$ cycle can be written as:

$$F_{surf} = R_{SW} + R_{SWI} + A_{CaCO_3} + R_{missing} \quad \textbf{(7.2)}$$

where F_{surf} is the $CaCO_3$ surface export flux from ***Fig. 7.1***, R_{SW} is the water-column dissolved $CaCO_3$ flux from ***Fig. 7.3a***, R_{SWI} is the $CaCO_3$ flux dissolved at the SWI from ***Fig. 7.4a***, A_{CaCO3} is the accumulation flux of $CaCO_3$ in sediments shown in ***Fig. 7.6*** and $R_{missing}$ is the fraction of the $CaCO_3$ export that is neither dissolved abiotically nor accumulated in sediments (i.e., the surplus of $CaCO_3$). Thus, $R_{missing}$ can represent dissolution that occurs in the guts of grazing organisms

living in the water column, or within sediments, due to oxic diagenesis and the accumulation of metabolic CO_2 production that acidifies the porewaters. I should note that since $R_{missing}$ is obtained by a difference rather than a measurement, it is associated with a probably large uncertainty that will depend on the uncertainties of F_{surf}, R_{SW}, R_{SWI} and A_{CaCO3}, which cannot be readily quantified.

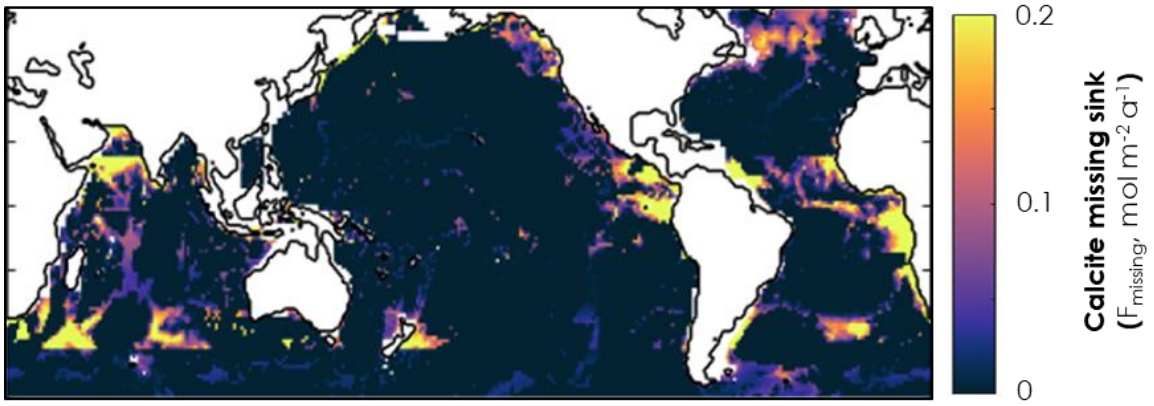

Fig. 7.7 | *$CaCO_3$ missing sink, what is left from the $CaCO_3$ surface export flux after water-column dissolution, dissolution at the SWI, and accumulation in sediments.*

Globally, this analysis shows that while 48.5 Tmol of $CaCO_3$ are exported from the surface ocean each year, 7.9 Tmol (16 %) are dissolved in the water column, 23.5 Tmol (48 %) are dissolved at the SWI, 11.3 Tmol (23 %) accumulate in the sediments and 5.8 Tmol (12 %) constitute the missing sink. The global $CaCO_3$ accumulation rate derived here (11.3 Tmol a^{-1}) is close to values reported in previous studies, e.g., 13.5 Tmol a^{-1} (Boudreau and Luo, 2017), 12 Tmol a^{-1} (Mackenzie and Morse, 1992) and 15 Tmol a^{-1} (Davies and Worsley, 1981). In response to anthropogenic changes, since the end of the preindustrial period, water-column and seafloor $CaCO_3$ dissolution have increased by 8.2 and 10.3 %, respectively, and the flux of $CaCO_3$ reaching the bottom has decreased by 1.5 %.

$R_{missing}$, shown in ***Fig 7.7***, appears to be higher near the coast, and is correlated with both the $CaCO_3$ surface export and the total organic carbon (TOC) content of the sediment, taken from Sarmiento and Gruber (2006) based on the original dataset of Seiter et al. (2004)) (***Fig. 7.8***). What mechanism hides behind this $CaCO_3$ missing sink? The fact that more $CaCO_3$ is missing in areas of high TOC sedimentary content would imply that this missing $CaCO_3$ sink could be attributed to

dissolution caused by oxic diagenesis and metabolic CO_2 accumulation in porewaters (Froelich et al., 1979; Jahnke et al., 1997; Mucci et al., 2000; Wenzhöfer et al., 2001; Steiner et al., 2019). Nevertheless, no correlation was found between the $R_{missing}$ and bottom-water oxygen contents from GLODAPv2, that are usually narrowly linked to sediment carbon remineralization (Emerson et al., 1985). Alternatively, $R_{missing}$ may be independent of the sediment TOC content, as correlation does not imply causation. $R_{missing}$ could simply be an artefact of the high carbon export from the surface, the latter affecting both shallow-water biotic dissolution and sediment TOC. Let us remember that the $CaCO_3$ export dataset used in this discussion is derived from satellite surface chlorophyll concentration measurements, from which both the POC and $CaCO_3$ export fluxes are derived as they are assumed to be correlated. If $CaCO_3$ is dissolving within the guts of grazing organisms or within fecal pellets while settling through the water column (Bishop et al., 1986; Penry and Jumars, 1986; Milliman et al., 1999; Jansen and Wolf-Gladrow, 2001; Berelson et al., 2007), this dissolution is not in any way taken into account in most models, including this one, which could explain the apparent missing $CaCO_3$ sink. Alternatively, this missing sink could also be attributed to shallow-water (i.e., above the calcite saturation depth, CSD) dissolution of more soluble phases, such as aragonite or high-Mg calcites (Betzer et al., 1984; Byrne et al., 1984).

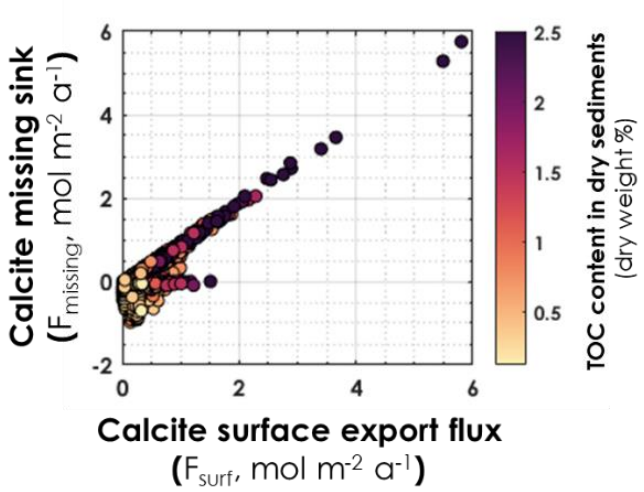

Fig. 7.8 | *Calcite missing sink as derived in this study as a function of the calcite surface export from Dunne et al. (2007). The color represents the total organic carbon (TOC) content in dry sediments taken from Sarmiento and Gruber (2006) based on the original dataset of Seiter et al. (2004).*

From this discussion, it appears that a significant fraction of the marine $CaCO_3$ sink is neither abiotic dissolution, nor accumulation in sediments. Biotic dissolution occurring above the

CSD has been hypothesized or reported by several authors (Bishop et al., 1986; Milliman and Droxler, 1996; Milliman et al., 1999; Wilson et al., 2008; Steiner et al., 2019). It is also known that porewater acidification during oxic diagenesis takes place in organic matter-rich sediments (Emerson and Bender, 1981; Archer et al., 1989a; Mekik et al., 2002), which is also strongly influenced by the amount of oxygen in the bottom waters (Cai and Reimers, 1995; Cai and Sayles, 1996), or by the action of burrowing organisms (Meysman et al., 2006; Teal et al., 2008). If anthropogenic changes can enhance abiotically-driven dissolution in both the water column and at the SWI through the invasion of anthropogenic DIC in the oceans, can the anthropogenic influence on the bottom-water O_2 content or on the activity of burrowing organisms affect $CaCO_3$ dissolution as well? How would the DBL control on the benthic dissolution rates highlighted throughout this thesis differ if strong metabolic $CaCO_3$ dissolution occurs within marine sediments? Irrespective, we have seen in ***Chapter 6*** that, under a business-as-usual scenario, a changing $CaCO_3$ export will be the main driver on the 21st century $CaCO_3$ dissolution rates at the SWI. How would changes in surface primary production impact water-column $CaCO_3$ dissolution as well as the delivery of $CaCO_3$ and TOC to the seafloor? It is clear that more research is required on the biologically-mediated $CaCO_3$ cycle and on the potential anthropogenic component. In the following section, I present my recommendations for future research in tackling these timely questions.

7.2 Recommendations for future research

Water-column $CaCO_3$ research has a very bright future. Whereas detailed mechanisms of $CaCO_3$ dissolution in seawater are slowly being unraveled (Lüttge et al., 2013; Fischer et al., 2014; Arvidson et al., 2015; Dong et al., 2018; Naviaux et al., 2019), the implementation of these latest, more accurate, kinetic laws in global-scale models still awaits. Furthermore, as mentioned in Section 7.1 of this Chapter, the mystery of shallow-water $CaCO_3$ dissolution highlighted by Milliman et al. (1999) still prevails. Mesocosms or laboratory studies should focus on quantifying the amount of $CaCO_3$ dissolution occurring in zooplankton guts, and its dependency on the species or environmental variables, to predict how this "gut" dissolution could evolve with time. Finally, it is implicit in most carbonate budgets, including the one presented in this Chapter, that $CaCO_3$ exported from the ocean surface to the seafloor is mostly calcite (Buitenhuis et al., 2019). Yet, recent work has revealed that pteropods, which precipitate an aragonitic shell, dominate surface

$CaCO_3$ production and export (Buitenhuis et al., 2013; Buitenhuis et al., 2019). These more soluble phases, if present in important quantities, could account for the $CaCO_3$ missing sink. In addition, as noted by Berelson et al. (2007), the literature can be confusing regarding the difference between surface $CaCO_3$ "production" and "export", which might explain some of the variability in the export fluxes reported in ***Table 7.1***. This confusion betrays our lack of understanding of the shallow-water (i.e., above the CSD) $CaCO_3$ cycle.

One of the main tasks of future studies on the dissolution kinetics of $CaCO_3$ in marine sediments at the seafloor will be to improve our understanding of the link between organic matter and $CaCO_3$ fluxes and preservation. Dissolution experiments carried out on sediments containing $CaCO_3$ and organic matter of variable concentrations and lability (reactivity, see for instance Middelburg (1989), Boudreau and Ruddick (1991), Arndt et al. (2013) or Stolpovsky et al. (2018)) will help reach this goal. Of particular interest, although challenging to reproduce in the laboratory, would be a study of the impact of pulses of organic matter delivery to the seafloor and its consumption by benthic meio- or macro-fauna (Witte et al., 2003; Nascimento et al., 2012) on the structure and chemistry of sediments. Future experimental work could focus on characterizing changes through time in organic matter reactivity and content, as well as changes in $CaCO_3$ mineralogy. Although only low-Mg calcite phases persist in deep-sea sediments (Morse and Mackenzie, 1990), shallow sediments can contain more soluble $CaCO_3$ phases, such as aragonite (Mucci, 1983) and/or high-Mg calcites (Bischoff et al., 1987), that Morse et al. (2006) predicted to be the "first responder" to ocean acidification (see ***section 1.2.2***). On the other hand, a progressive recrystallization of biogenic Mg-calcites into calcite cements of lower Mg content (undefined precisely) has been described during long-term equilibration experiments (Tribble and Mackenzie, 1998) and was associated with a decrease in carbonate mineral solubility. Changing $CaCO_3$ mineralogy might also be significant in deep-sea sediments, as Sun and Turchyn (2014) reported that at least 10 % of the global $CaCO_3$ accumulation is accounted for by authigenic $CaCO_3$ precipitation.

Given that dissolution driven by organic matter remineralization in sediments can occur well below the SWI (Archer et al., 1989a; Jourabchi et al., 2008), the analysis of solids and porewater solutes profiles will be necessary to document the interaction between organic matter and $CaCO_3$. For this purpose, characterization of the stable carbon isotopic composition of the

porewater DIC would be particularly useful. If the ^{13}C signature of $CaCO_3$ and TOC are known, the fraction of porewater DIC originating from $CaCO_3$ dissolution and that coming from TOC degradation can be established by a Keeling plot (Pataki et al., 2003). pH (Archer, 1989a; Cai and Reimers, 1993; Zhao and Cai, 1999; Cai et al., 2000), pCO_2 (Zhao and Cai, 1997; Cai et al., 2000), CO_3^{2-} (de Beer et al., 2008; Han et al., 2014; Cai et al., 2016), O_2 (Reimers, 1987; Archer et al., 1989a; Sosna et al., 2007), and even dissolved Fe, Mn or S(-II) (Brendel and Luther, 1995) microelectrodes have been developed during the past decades. These microelectrodes would provide unique insights on the role of organic matter in the fate of $CaCO_3$ particles within a context of early diagenesis. As raised in the literature review in ***Chapter 5***, important porewater acidification due to organic carbon remineralization, for instance, could generate deep CO_3^{2-} gradients within the sediment, reducing the DBL control on the diffusive CO_3^{2-} highlighted in this thesis. To validate or refute this hypothesis, solute profiles through the sediment-water interface need to be determined precisely with microelectrodes, under various DBL thicknesses and organic matter contents.

Most, if not all, of the above future research recommendations and potential analytical insights could be achieved using a modified version of the rotating-disk reactor described in ***Chapter 3***, in which microelectrodes could be inserted from above and below the sediment disk. However, as demonstrated by Glud et al. (1994) using early microelectrodes, deeper sediment O_2 penetration depths are measured when electrodes are inserted into sediments from the water-side of the SWI than when electrodes are inserted from below and moved upward. The sediment disk should also be made thicker in order to visualize deeper solute and solid gradients caused by organic carbon remineralization.

On the modelling side, sediment modules integrating several carbonate polymorphs (e.g., Ahm et al., 2018), multiple POC pools (e.g., Stolpovsky et al., 2018), a full set of diagenetic reactions (e.g., Couture et al., 2010), bioturbation and irrigation (e.g., Boudreau et al., 1996) and variable DBL thicknesses (e.g., Sulpis et al., 2018) have all been described in the literature, but are yet to be merged into a single model. Such a model would certainly help to identify new climate feedback mechanisms. In ***Chapter 6***, we showed that bottom-current flowpaths and speeds may display strong changes within a century, thereby affecting the DBL thickness and the $CaCO_3$ dissolution patterns. Similarly, it has been shown that changes in bioturbation through geological

times has played a important role in the evolution of the sulfur (Canfield and Farquhar, 2009), oxygen and carbon (van de Velde, 2018) biogeochemical cycles. How will bioturbation evolve in the next centuries, however, is unknown. Notwithstanding, based on the predicted increase POC flux to the seafloor predicted to occur in the 21st century (***Fig. 6.12***), one can speculate that in a high CO_2 world, with the exception of $CaCO_3$-secreting organisms, life at the seafloor will thrive.

References

Ahm, A.-S. C., Bjerrum, C.J., Blättler, C.L., Swart, P.K. and Higgins, J.A. (2018) Quantifying early marine diagenesis in shallow-water carbonate sediments. *Geochimica et Cosmochimica Acta*, 236, 140-159, https://doi.org/doi:10.1016/j.gca.2018.02.042

Archer, D., Emerson, S. and Reimers, C. (1989a) Dissolution of calcite in deep-sea sediments: pH and O_2 microelectrode results. *Geochimica et Cosmochimica Acta*, 53(11), 2831-2845.

Archer, D., Kheshgi, H. and Maier-Reimer, E. (1998) Dynamics of fossil fuel CO_2 neutralization by marine $CaCO_3$. *Global Biogeochemical Cycles*, 12, 259-276, https://doi.org/10.1029/98GB00744

Archer, D.E., Morford, J.L. and Emerson, S.R. (2002) A model of suboxic sedimentary diagenesis suitable for automatic tuning and gridded global domains. *Global Biogeochemical Cycles*, 16(1), 17-1-17-21, https://doi.org/10.1029/2000GB001288

Arndt, S., Jørgensen, B.B., LaRowe, D.E., Middelburg, J.J., Pancost, R.D. and Regnier, P. (2013) Quantifying the degradation of organic matter in marine sediments: A review and synthesis. *Earth-Science Reviews*, 123, 53-86. https://doi.org/10.1016/j.earscirev.2013.02.008

Arvidson, R.S., Fischer, C. and Luttge, A. (2015) Calcite dissolution kinetics. *Aquatic Geochemistry*, 21, 415-422.

Bacastow, R., and Maier-Reimer, E. (1990). Ocean-circulation model of the carbon cycle, *Climate Dynamics*, 4, 95-125.

Balch, W.M., Drapeau, D.T., Bowler, B.C. and Booth, E. (2007) Prediction of pelagic calcification rates using satellite-measurements, *Deep Sea Research Part II: Topical Studies in Oceanography*, 54(5-7), 478-495.

Battaglia G., Steinacher M. and Joos, F. (2016) A probabilistic assessment of calcium carbonate export and dissolution in the modern ocean. *Biogeosciences*, 13(9), 2823-2848.

Berelson, W.M., Balch, W.M., Najjar, R., Feely, R.A., Sabine, C. and Lee, K. (2007) Relating estimates of $CaCO_3$ production, export, and dissolution in the water column to measurements of $CaCO_3$ rain into sediment traps and dissolution on the sea floor: A revised global carbonate budget. *Global Biogeochemical Cycles* 21(1), https://doi.org/10.1029/2006GB002803

Betzer, P.R., Byrne, R.H., Acker, J.G., Lewis, C.S., Jolley, R.R. and Feely, R.A. (1984) The oceanic carbonate system: a reassessment of biogenic controls. *Science*, 226(4678), 1074-1077.

Bischoff, W.D., Mackenzie, F.T. and Bishop, F.C. (1987) Stabilities of synthetic magnesian calcites in aqueous solution: Comparison with biogenic materials. *Geochimica et Cosmochimica Acta*, 51(6): 1413-1423.

Bishop, J.K.B., Stepien, J.C. and Wiebe, P.H. (1986) Particulate matter distributions, chemistry and flux in the panama basin: response to environment forcing. *Progress in Oceanography* 17, 1-59.

Bissett, A., Neu, T.R. and Beer, D. (2011). Dissolution of calcite in the twilight zone: bacterial control of dissolution of sinking planktonic carbonates is unlikely. *PLoS One*, 6(11), e26404, https://doi.org/10.1371/journal.pone.0026404

Boudreau, B.P. (1996) A method-of-lines code for carbon and nutrient diagenesis in aquatic sediments. *Computers & Geosciences*, 22(5), 479-496, https://doi.org/10.1016/0098-3004(95)00115-8

Boudreau, B.P. (2013) Carbonate dissolution rates at the deep ocean floor. *Geophysical Research Letters* 40, 744-748, https://doi.org/10.1029/2012GL054231

Boudreau, B.P. and Ruddick, B.R. (1991) On a reactive continuum representation of organic matter diagenesis. *American Journal of Science*, 291(5), 507-538.

Boudreau, B.P., Middelburg, J.J., Hofmann, A.F. and Meysman, F.J.R. (2010a) Ongoing transients in carbonate compensation. *Global Biogeochemical Cycles*, 24(4), https://doi.org/10.1029/2009GB003654

Boudreau, B.P., Middelburg, J.J. and Meysman, F.J.R. (2010b) Carbonate compensation dynamics. *Geophysical Research Letters*, 37, https://doi.org/10.1029/2009GL041847

Boudreau B.P., Luo Y., Meysman F.J.R., Middelburg J.J. and Dickens G.R. (2015) Gas hydrate dissociation prolongs acidification of the Anthropocene oceans. *Geophysical Research Letters*, 42.

Boudreau, B.P. and Luo, Y. (2017) Retrodiction of secular variations in deep-sea CaCO 3 burial during the Cenozoic. *Earth and Planetary Science Letters*, 474, 1-12, https://doi.org/10.1016/j.epsl.2017.06.005

Boudreau, B.P., Middelburg, J.J. and Luo, Y. (2018) The role of calcification in carbonate compensation. *Nature Geoscience*, 11, 84-890,

Boudreau, B.P., Middelburg, J.J., Sluijs, A. and van der Ploeg, R. (2019) Secular variations in the carbonate chemistry of the oceans over the Cenozoic. *Earth and Planetary Science Letters*, 512, 194-206, https://doi.org/10.1016/j.epsl.2019.02.004

Brendel, P.J. and Luther, G.W.I. (1995) Development of a gold amalgam voltammetric microelectrode for the determination of dissolved Fe, Mn, O_2, and S(-II) in porewaters of marine and freshwater sediments. *Environmental Science & Techmology*, 29(3), 751-761.

Buitenhuis, E.T., Vogt, M., Moriarty, R., Bednaršek, N., Doney, S.C., Leblanc, K., Le Quéré, C., Luo, Y.-W., O'Brien, C., O'Brien, T., Peloquin, J., Schiebel, R., and Swan, C. (2013) MAREDAT: towards a world atlas of MARine Ecosystem DATa, *Earth System Science Data*, 5, 227-239, https://doi.org/10.5194/essd-5-227-2013

Buitenhuis, E.T., Le Quéré, C., Bednaršek, N. and Schiebel, R. (2019) Large contribution of pteropods to shallow $CaCO_3$ export. *Global Biogeochemical Cycles*, in press. https://doi.org/10.1029/2018GB006110

Byrne, R.H., Acker, J.G., Betzer, P.R., Feely, R.A. and Cates, M.H. (1984). Water column dissolution of aragonite in the Pacific Ocean. *Nature*, 312, 321-326.

Cai, W.-J. and Reimers, C.E. (1993) The development of pH and pCO_2 microelectrodes for studying the carbonate chemistry of pore waters near the sediment-water interface. *Limnology and Oceanography* 38, 1762-1773.

Cai, W.-J. and Reimers, C.E. (1995) Benthic oxygen flux, bottom water oxygen concentration and core top organic carbon content in the deep northeast Pacific Ocean. *Deep Sea Research Part I: Oceanographic Research Papers* 42, 1681-1699.

Cai, W.-J. and Sayles, F.L. (1996) Oxygen penetration depths and fluxes in marine sediments. *Marine Chemistry* 52, 123-131.

Cai, W.-J., Zhao, P. and Wang, Y. (2000) pH and pCO_2 microelectrodes measurement and diffusive behavior of carbon dioxide species in coastal marine sediments. *Marine Chemistry*, 70, 133–148.

Cai, W.-J., Ma, Y., Hopkinson, B. M., Grottoli, A. G., Warner, M. E., Ding, Q., Hu, X., Yuan, X., Schoepf, V., Xu, H., Han, C., Melman, T.F., Hoadley, K.D., Pettay, D.T., Matsui, Y., Baumann, J.H., Levas, S., Ying, E. and Wang, Y. (2016) Microelectrode characterization of coral daytime interior pH and carbonate chemistry. *Nature Communications*, 7, 11144. http://doi.org/10.1038/ncomms11144

Canfield, D.E. and Farquhar, J. (2009) Animal evolution, bioturbation, and the sulfate concentration of the oceans. *Proceedings of the National Academy of Science of the United States of America* 106(20), 8123-8127.

Chen, C.-T.A. (1982) On the distribution of anthropogenic CO_2 in the Atlantic and Southern oceans. *Deep Sea Research* 29, 563-580, https://doi.org/10.1016/0198-0149(82)90076-0

Chuck, A., Tyrrell, T., Totterdell, I.J. and Holligan, P.M. (2005), The oceanic response to carbon emissions over the next century: investigation using three ocean carbon cycle models, *Tellus, Ser. B* 57,70– 86.

Couture, R.-M., Shafei, B., Van Cappellen, P., Tessier, A. and Gobeil, C. (2010) Non-steady state modeling of arsenic diagenesis in lake sediments. *Environmental Science & Technology* 44(1), 197-203, https://doi.org/10.1021/es902077q

Davies, T.A. and Worsley, T.R. (1981). Paleoenvironmental implications of oceanic carbonate sedimentation rates. *SEPM Special Publication* 32, 169-179.

de Beer, D., Bissett, A., de Wit, R., Jonkers, H., Köhler-Rink, S., Nam, H., Kim, B.H., Eickert, G. and Grinstain, M. (2008) A microsensor for carbonate ions suitable for microprofiling in freshwater and saline environments. *Limnology and Oceanography Methods* 6(10), 532–541, https://doi.org/10.4319/lom.2008.6.532

Dong, S., Subhas, A.V., Rollins, N.E., Naviaux, J.D., Adkins, J.F. and Berelson, W.M. (2018) A kinetic pressure effect on calcite dissolution in seawater. *Geochimica et Cosmochimica Acta* 238, 411-423.

Dunne, J.P., Sarmiento, J.L. and Gnanadesikan, A. (2007) A synthesis of global particle export from the surface ocean and cycling through the ocean interior and on the seafloor. *Global Biogeochemical Cycles*, 21(4), https://doi.org/10.1029/2006gb002907

Emerson, S. and Bender, M. (1981) Carbon fluxes at the sediment-water interface of the deep-sea: calcium carbonate preservation. *Journal of Marine Research* 39, 139-162.

Emerson, S., Fischer, K., Reimers, C. and Heggie, D. (1985). Organic carbon dynamics and preservation in deep-sea sediments. *Deep Sea Research Part A. Oceanographic Research Papers* 32(1), 1-21.

Feely, R.A., Sabine, C.L., Lee, K., Berelson, W., Kleypas, J., Fabry, V.J. and Millero, F.J. (2004) Impact of Anthropogenic CO_2 on the $CaCO_3$ System in the Oceans. *Science* 305(5682), 362-366.

Fischer, C., Kurganskaya, I., Schäfer, T. and Lüttge, A. (2014). Variability of crystal surface reactivity: What do we know? *Applied Geochemistry* 43, 132-157, https://doi.org/10.1016/j.apgeochem.2014.02.002

Friis, K., Najjar, R.G., Follows, M.J. and Dutkiewicz, S. (2006). Possible overestimation of shallow-depth calcium carbonate dissolution in the ocean. *Global Biogeochemical Cycles* 20(4), https://doi.org/10.1029/2006gb002727

Froelich, P.N., Klinkhammer, G.P., Bender, M.L., Luedtke, N.A., Heath, G.R., Cullen, D., Dauphin, P., Hammond, D., Hartman, B. and Maynard, V. (1979) Early oxidation of organic matter in pelagic sediments of the eastern equatorial Atlantic: suboxic diagenesis. *Geochimica et Cosmochimica Acta* 43, 1075-1090.

Garcon, V. C., and J.-F. Minster (1988), Heat, carbon and water fluxes in a 12-box model of the world ocean. *Tellus, Serie B* 40, 161–177.

Gehlen, M., Gangstø, R., Schneider, B., Bopp, L., Aumont, O. and Ethe, C. (2007) The fate of pelagic $CaCO_3$ production in a high CO_2 ocean: a model study. *Biogeosciences* 4(4), 505-519.

Glud, R.N., Gundersen, J.K., Revsbech, N.P. and Jørgensen, B.B. (1994) Effects on the benthic diffusive boundary layer imposed by microelectrodes. *Limnology and Oceanography* 39, 462-467.

Gnanadesikan, A., Dunne, J.P., Key, R.M., Matsumoto, K., Sarmiento, J.L., Slater, R.D. and Swathi, P.S. (2004), Oceanic ventilation and biogeochemical cycling: Understanding the physical mechanisms that produce realistic distributions of tracers and productivity. *Global Biogeochemical Cycles* 18(GB4010), https://doi.org/10.1029/2003GB002097

Gruber, N., Clement, D., Carter, B.R., Feely, R.A., Heuven, S.v., Hoppema, M., Ishii, M., Key, R.M., Kozyr, A., Lauvset, S.K., Monaco, C.L., Mathis, J.T., Murata, A., Olsen, A., Perez, F.F., Sabine, C.L., Tanhua, T. and Wanninkhof, R. (2019) The oceanic sink for anthropogenic CO_2 from 1994 to 2007. *Science* 363, 1193-1199.

Hales, B. (2003) Respiration, dissolution, and the lysocline. *Paleoceanography and Paleoclimatology* 18: https://doi.org/10.1029/2003PA000915.

Han, C., Cai, W.-J., Wang, Y. and Ye, Y. (2014) Calibration and evaluation of a carbonate microsensor for studies of the marine inorganic carbon system. *Journal of Oceanography* 70, 425–433.

Harris, R. P. (1994) Zooplankton grazing on the coccolithophore Emiliania huxleyi and its role in inorganic carbon flux. *Marine Biology* 119, 431-439.

Heinze, C., Maier-Reimer, E., Winguth, A.M.E. and Archer, D. (1999) A global oceanic sediment model for long-term climate studies. *Global Biogeochemical Cycles* 13(1), 221-250, https://doi.org/10.1029/98GB02812

Heinze, C., Hupe, A., Maier-Reimer, E., Dittert, N. and Ragueneau, O. (2003) Sensitivity of the marine biospheric Si cycle for biogeochemical parameter variations. *Global Biogeochemical Cycles* 17(3), 1086, https://doi.org/10.1029/2002GB001943

Honjo, S. (1976) Coccoliths: Production, transportation and sedimentation. *Marine Micropaleontology* 1, 65-79.

Jahnke, R.A. (1996). The global ocean flux of particulate organic carbon: Areal distribution and magnitude. *Global Biogeochemical Cycles*, 10(1), 71-88. https://doi.org/10.1029/95gb03525

Jahnke, R.A., Craven, D.B., McCorkle, D.C. and Reimers, C.E. (1997) $CaCO_3$ dissolution in California continental margin sediments: The influence of organic matter remineralization. *Geochimica et Cosmochimica Acta* 61, 3587-3604.

Jahnke, R.A. and Jahnke, D.B. (2004) Calcium carbonate dissolution in deep sea sediments: reconciling microelectrode, pore water and benthic flux chamber results. *Geochimica et Cosmochimica Acta* 68(1), 47-59.

Jansen, H. and Wolf-Gladrow, D.A. (2001). Carbonate dissolution in copepod guts: a numerical model. *Marine Ecology Progress Series* 221, 199-207.

Jenkins (1997

Jenkins, C.J. (1997) Building offshore soils databases. *Sea Technology* 38(12), 25-28.

Jourabchi, P., Meile, C., Pasion, L.R. and Van Cappellen, P. (2008). Quantitative interpretation of pore water O_2 and pH distributions in deep-sea sediments. *Geochimica et Cosmochimica Acta* 72(5), 1350-1364, https://doi.org/10.1016/j.gca.2007.12.012

Keir, R.S. (1980) The dissolution kinetics of biogenic calcium carbonates in seawater. *Geochimica et Cosmochimica Acta* 44(2), 241-252.

Lauvset, S.K., Key, R.M., Olsen, A., Heuven, S.v., Velo, A., Lin, X., Schirnick, C., Kozyr, A., Tanhua, T., Hoppema, M., Jutterström, S., Steinfeldt, R., Jeansson, E., Ishii, M., Perez, F.F., Suzuki, T. and Watelet, S.

(2016) A new global interior ocean mapped climatology: the 1° × 1° GLODAP version 2. *Earth System Science Data* 8, 325-340, https://doi.org/10.5194/essd-8-325-2016

Lee, K. (2001), Global net community production estimated from the annual cycle of surface water total dissolved inorganic carbon. *Limnology and Oceanography* 46, 1287–1297.

Luo, Y. and Boudreau, B. P. (2016). Future acidification of marginal seas: A comparative study of the Japan/East Sea and the South China Sea. *Geophysical Research Letters* 43(12), 6393-6401.

Luo, Y., Boudreau, B. P., Dickens, G. R., Sluijs, A., & Middelburg, J. J. (2016). An alternative model for $CaCO_3$ over-shooting during the PETM: Biological carbonate compensation. *Earth and Planetary Science Letters* 453, 223-233, https://doi.org/10.1016/j.epsl.2016.08.012

Luo, Y., Kienast, M. and Boudreau, B. P. (2018). Invariance of the carbonate chemistry of the South China Sea from the glacial period to the Holocene and its implications to the Pacific Ocean carbonate system. *Earth and Planetary Science Letters* 492, 112-120, https://doi.org/10.1016/j.epsl.2018.04.005

Lüttge, A., Arvidson, R.S. and Fischer, C. (2013). A stochastic treatment of crystal dissolution kinetics. *Elements* 9(3), 183-188.

Mackenzie, F. T. and Morse, J. W. (1992). Sedimentary carbonates through Phanerozoic time. *Geochimica et Cosmochimica Acta* 56(8), 3281-3295.

Mekik F. A., P. W. Loubere, and D. E. Archer, 2002 Organic carbon flux and organic carbon to calcite flux ratio recorded in deep-sea carbonates: Demonstration and a new proxy. *Global Biogeochemical Cycles* 16, https://doi.org/10.1029/2001GB001634.

Meysman, F.J.R., Galaktionov, O.S., Gribsholt, B. and Middelburg, J.J. (2006) Bioirrigation in permeable sediments: Advective pore-water transport induced by burrow ventilation. *Limnology and Oceanography* 51: 142-156, https://doi.org/10.4319/lo.2006.51.1.0142.

Middelburg, J. J. (1989) A simple rate model for organic matter decomposition in marine sediments. *Geochimica et Cosmochimica Acta* 53(7), 1577-1581.

Milliman, J. D. (1993), Production and accumulation of calcium carbonate in the ocean: Budget of a nonsteady state. *Global Biogeochemical Cycles* 7, 927–957.

Milliman, J.D. and Droxler, A.W. (1996) Neritic and pelagic carbonate sedimentation in the marine environment: ignorance is not bliss. *Geologische Rundschau* 85, 496-504.

Milliman, J. D., Troy, P. J., Balch, W. M., Adams, A. K., Li, Y.-H. and Mackenzie, F. T. (1999). Biologically mediated dissolution of calcium carbonate above the chemical lysocline? *Deep Sea Research I* 46, 1653-1669.

Moore, J. K., Doney, S.C., Glover, D.M. and Fung, I.Y. (2002) Iron cycling and nutrient limitation patterns in surface waters of the world ocean, *Deep Sea Research Part II* 49, 463–508.

Moore, J. K., Doney, S.C. and Lindsay, K. (2004) Upper ocean ecosystem dynamics and iron cycling in a global three-dimensional model. *Global Biogeochemical Cycles* 18(GB4028), https://doi.org/10.1029/2004GB002220

Morse, J. W., Andersson, A. J. and Mackenzie, F. T. (2006) Initial responses of carbonate-rich shelf sediments to rising atmospheric pCO_2 and "ocean acidification": Role of high Mg-calcites. *Geochimica et Cosmochimica Acta* 70(23), 5814-5830.

Morse, J.W. and Mackenzie, F.T. (1990) Geochemistry of Sedimentary Carbonates. Elsevier, Amsterdam.

Mucci, A. (1983) The solubility of calcite and aragonite in seawater at various salinities, temperatures and one atmosphere total pressure. *American Journal of Science* 283, 780-799, http://doi.org/10.2475/ajs.283.7.780

Mucci, A., Sundby, B., Gehlen, M., Arakaki, T., Zhong, S. and Silverberg, N. (2000) The fate of carbon in continental shelf sediments of eastern Canada: a case study. *Deep-Sea Research Part II: Topical Studies in Oceanography* 47, 733-760.

Munhoven, G. (2007) Glacial–interglacial rain ratio changes: Implications for atmospheric CO_2 and ocean–sediment interaction. *Deep-Sea Research Part II: Topical Studies in Oceanography* 54(5-7), 722-746, https://doi.org/10.1016/j.dsr2.2007.01.008

Murnane, R. J., J. L. Sarmiento, and C. Le Quéré (1999), Spatial distribution of air-sea CO_2 fluxes and the interhemispheric transport of carbon by the oceans. *Global Biogeochemical Cycles* 13, 287–305.

Nascimento, F.J.A., Naslund, J. and Elmgren, R. (2012) Meiofauna enhances organic matter mineralization in soft sediment ecosystems. *Limnology and Oceanography* 57, 338-346.

Naviaux, J.D., Subhas, A.V., Rollins, N.E., Dong, S., Berelson, W.B. and Adkins, J.F. (2019). Temperature dependence of calcite dissolution kinetics in seawater. *Geochimica et Cosmochimica Acta* 246: 363-384, https://doi.org/10.1016/j.gca.2018.11.037

Pataki, D.E., Ehleringer, J.R., Flanagan, L.B., Yakir, D., Bowling, D.R., Still, C.J., Buchmann, N., Kaplan, J.O. and Berry, J.A. (2003) The application and interpretation of Keeling plots in terrestrial carbon cycle research. *Global Biogeochemical Cycles* 17(1), https://doi.org/10.1029/2001GB001850

Penry, D. L. and Jumars, P. A. (1986) Chemical reactor analysis and optimal digestion. *BioScience* 36(5), 310-315.

Pond, D.W., Harris, R.P. and Brownlee, C. (1995) A microinjection technique using a pH-sensitive dye to determine the gut pH of Calanus helgolandicus. *Marine Biology* 123, 75-79.

Reimers, C.E. (1987) An in situ microprofiling instrument for measuring interfacial pore water gradients: methods and oxygen profiles from the North Pacific Ocean. *Deep-Sea Research Part A. Oceanographic Research Papers* 34, 2023-2035.

Ridgwell, A. and Hargreaves, J.C. (2007) Regulation of atmospheric CO_2 by deep-sea sediments in an Earth system model. *Global Biogeochemical Cycles* 21, https://doi.org/10.1029/2006GB002764

Riley, J. S., Sanders, R., Marsay, C., Le Moigne, F. A. C., Achterberg, E. P. and Poulton, A. J. (2012). The relative contribution of fast and slow sinking particles to ocean carbon export. *Global Biogeochemical Cycles* 26(1), https://doi.org/10.1029/2011gb004085

Sarmiento, J. L., Dunne, J., Gnanadesikan, A., Key, R. M., Matsumoto, K. and Slater, R. (2002) A new estimate of the $CaCO_3$ to organic carbon export ratio. *Global Biogeochemical Cycles* 16(4), 54-51-54-12.

Sarmiento, J.L. and Gruber, N. (2006) Ocean Biogeochemical Dynamics. Princeton University Press, Princeton, NJ.

Seiter, K., Hensen, C., Schröter, J. and Zabel, M. (2004). Organic carbon content in surface sediments - defining regional provinces. *Deep Sea Research Part I: Oceanographic Research Papers* 51(12), 2001-2026, https://doi.org/10.1016/j.dsr.2004.06.014

Shaffer, G. (1993), Effects of the marine biota on global carbon cycling, in The Global Carbon Cycle, NATO ASI Ser., vol. I15, Global Environmental Change, edited by M. Heimann, pp. 431–455, Springer, New York.

Smith, S.V., Mackenzie, F.T. (2016) The role of $CaCO_3$ reactions in the contemporary oceanic CO_2 cycle. *Aquatic Geochemistry* 22, 153-175.

Sosna, M., Denuault, G., Pascal, R. W., Prien, R. D., & Mowlem, M. (2007). Development of a reliable microelectrode dissolved oxygen sensor. *Sensors and Actuators B: Chemical* 123(1), 344-351, https://doi.org/10.1016/j.snb.2006.08.033

Steiner, Z., Lazar, B., Reimers, C.E. and Erez, J. (2019) Carbonates dissolution and precipitation in hemipelagic sediments overlaid by supersaturated bottom-waters – Gulf of Aqaba, Red Sea. *Geochimica et Cosmochimica Acta* 246, 565-580.

Stolpovsky, K., Dale, A. W. and Wallmann, K. (2018). A new look at the multi-G model for organic carbon degradation in surface marine sediments for coupled benthic–pelagic simulations of the global ocean. *Biogeosciences* 15(11), 3391-3407. https://doi.org/10.5194/bg-15-3391-2018

Subhas, A.V., Rollins, N.E., Berelson, W.M., Dong, S., Erez, J. and Adkins, J.F. (2015) A novel determination of calcite dissolution kinetics in seawater. *Geochimica et Cosmochimica Acta* 170, 51-68.

Subhas, A.V., Adkins, J.F., Rollins, N.E., Naviaux, J., Erez, J. and Berelson, W.M. (2017) Catalysis and chemical mechanisms of calcite dissolution in seawater. *Proceedings of the National Academy of Sciences of the U.S.A* 114(31), 8175-8180.

Subhas, A.V., Rollins, N.E., Berelson, W.M., Erez, J., Ziveri, P., Langer, G. and Adkins, J.F. (2018) The dissolution behavior of biogenic calcites in seawater and a possible role for magnesium and organic carbon. *Marine Chemistry* 205, 100-112.

Sulpis, O., Boudreau, B.P., Mucci, A., Jenkins, C.J., Trossman, D.S., Arbic, B.K. and Key, R.M. (2018) Current $CaCO_3$ dissolution at the seafloor caused by anthropogenic CO_2. *Proceedings of the National Academy of Sciences of the United States of America* 115, 11700-11705, https://doi.org/10.1073/pnas.1804250115

Sun, X. and Turchyn, A.V. (2014) Significant contribution of authigenic carbonate to marine carbon burial. *Nature Geoscience* 7(3), 201-204.

Teal, L.R., Bulling, M.T., Parker, E.R. and Solan, M. (2008) Global patterns of bioturbation intensity and mixed depth of marine soft sediments. *Aquatic Biology* 2: 207-218, https://doi.org/10.3354/ab00052.

Tribble, J. S. and Mackenzie, F. T. (1998). Recrystallization of magnesian calcite overgrowths on calcite seeds suspended in seawater. *Aquatic Geochemistry* 4, 337-360.

Tschumi, T., Joos, F., Gehlen, M. and Heinze, C. (2011) Deep ocean ventilation, carbon isotopes, marine sedimentation and the deglacial CO_2 rise. *Climate of the Past* 7(3), 771-800, https://doi.org/10.5194/cp-7-771-2011

Van Cappellen, P. and Wang, Y. (1996) Cycling of iron and manganese in surface sediments; a general theory for the coupled transport and reaction of carbon, oxygen, nitrogen, sulfur, iron, and manganese. American Journal of Science 296(3), 197-243, https://doi.org/10.2475/ajs.296.3.197

van de Velde, S., Mills, B. J. W., Meysman, F. J. R., Lenton, T. M. and Poulton, S. W. (2018). Early Palaeozoic ocean anoxia and global warming driven by the evolution of shallow burrowing. *Nature Communication* 9(1), 2554, https://doi.org/10.1038/s41467-018-04973-4

Van der Wal, P., Kempers, R.S. and Veldhuis, M.J.W. (1995) Production and downward flux of organic matter and calcite in a North Sea bloom of the coccolithophore Emiliania huxleyi. *Marine Ecology Progress Series* 126.

Wenzhöfer, F., Adler, M., Kohls, O., Hensen, C., Strotmann, B., Boehme, S. and Schulz, H.D. (2001) Calcite dissolution driven by benthic mineralization in the deep-sea: in situ measurements of Ca^{2+}, pH, pCO_2 and O_2. *Geochimica et Cosmochimica Acta* 65, 2677-2690.

Wilson, M.E.J. (2008) Global and regional influences on equatorial shallow-marine carbonates during the Cenozoic. *Palaeogeography, Palaeoclimatology, Palaeoecology* 265, 262-274.

Witte, U., Wenzhofer, F., Sommer, S., Boetius, A., Heinz, P., Aberle, N., Sand, M., Cremer, A., Abraham, W.-R., Jørgensen, B.B. and Pfannkuche, O. (2003) In situ experimental evidence of the fate of a phytodetritus pulse at the abyssal sea floor. *Nature* 424, 763-766.

Yamanaka, Y. and Tajika, E. (1996), The role of the vertical fluxes of particulate organic matter and calcite in the ocean carbon cycle.: Studies using an ocean biogeochemical model. *Global Biogeochemical Cycles* 10, 361–382.

Zhao, P. and Cai, W.-J. (1997) An improved potentiometric pCO_2 microelectrode. *Analytical Chemistry* 69(24), 2052-5058.

Zhao, P. and Cai, W.-J. (1999) pH polymeric membrane microelectrodes based on neutral carriers and their application in aquatic environments. *Analytical Chimica Acta* 395, 285–291.